Developing a Biodegradable Electrospun Membrane as a Periosteum Substitute for Critical Size Bone Defect Repair

Heather Elizabeth Owston

Submitted in accordance with the requirements for the degree of
PhD in Tissue Engineering and Regenerative Medicine

The University of Leeds

Institute of Medical and Biological Engineering,

School of Mechanical Engineering

and

Leeds Institute of Rheumatic and Musculoskeletal Medicine,

Faculty of Medicine and Health

May 2019

The candidate confirms that the work submitted is her own and that appropriate credit has been given where reference has been made to the work of others.

Acknowledgements

I would firstly like to thank the patients of Leeds General Infirmary (LGI) that donated tissue samples that enabled this project and to Peter Giannoudis, lead trauma orthopaedic surgeon at the LGI, for harvesting the samples.

My primary supervisor, Elena Jones has been the greatest mentor anyone could hope for, eternally supportive, positive, empathetic and most importantly innately intellectually curious. I thank you for all of your guidance and wisdom, and hope to work with you again in the future. Thank you to the rest of my multidisciplinary supervisory team, Peter Giannoudis keeping us clinically focused and Steve Russell and Giuseppe Tronci for guiding me with patience and positivity through the materials side of the project.

The MSC group has been the best place to carry out my PhD, never to take life to seriously, but always there to provide advice, guidance or most importantly a G&T. Thank you to Thomas Baboolal, Richard Cuthbert and Ola Altaie for all your mentorship in the lab and hilarious antics out of the lab. A special mention to the fabulous lady Ola, you have become the very best of friend. Payal, you are always so happy and optimistic, thank you for coming on the HoloMonitor adventure with me and for always taking photos. Dragos, thank you for helping me with PCR, stay grumpy. Last but not least, Kat, without whom the long days spent electrospinning would not have been so fun, thank you for being there for me.

Friendships solidified through Thursday dinner club and my hockey team have kept me sane through this whole process. Zoe was always there for chats and tea, and also Halina and Cat for Coffee and SaniTea during our write up. Mum and dad kept me supplied with a never ending supply of mini eggs and support on the end of the phone. Hazel, Jim and TJ have always welcomed me to their house whenever I needed them and Steve, Maria and Milo, thank you for the phone calls and ‘big brotherly advice’. Finally, to Simon for proof reading this whole thesis, I cannot believe you actually read it all for me, thank you.

I would like to thank certain individuals that have provided training for me throughout this project, Adam Davison and Liz Straszynski (flow cytometry, confocal microscopy and orchestrating the HoloMonitor equipment demo),

Jackie Hudson (SEM and confocal microscopy), Mohammad Tausif (Electrospinning and textiles characterisation equipment) and Mike Shires (Histology).

The research of Chapter 5 has been carried out in partnership with *Katrina Moisley*. Whose contributions have been as follows, to jointly develop and manufacture the free surface electrospun barrier membranes (Chapter 5), jointly characterise the 'optimisation membranes' (Section 5.3.1) and to provide laser cutting of the membranes (Section 6.2.3). My own contributions, fully and explicitly indicated in the thesis, have been Chapter's 1-4, Chapter 5 (Section 5.3.2 onwards) and Chapter 6-7.

Abstract

Critical size bone defects (CSBD) are too large (>1-2 cm) for spontaneous repair. Here, a new concept of a 'hybrid graft' CSBD reconstruction was investigated, whereby a barrier membrane to contain graft material and support periosteal regrowth was developed alongside examination into periosteum and bone marrow (BM) as mesenchymal stem cell (MSC) sources.

To create a 'bioinspired' substitute membrane, human and porcine periosteum samples were analysed for thickness and tissue architecture. Free surface electrospun membranes containing poly(ε-caprolactone) (PCL) (M3%-PCL) and collagen-PCL (M6%-CP70:30) were developed and characterised, followed by barrier function testing and MSC attachment and proliferation.

'Clinically relevant' human periosteum samples generally lacked a cambium layer, but were positive for CD271, an MSC marker throughout the collagenous fibrous layer. Porcine periosteum was variable in thickness (127-2310 μm). MSCs were significantly more frequent in periosteum (2% vs 0.0008%, P=0.004), but formed significantly smaller colonies *in vitro* 6.1 mm^2 vs 15.5 mm^2, P=0.0006), compared to BM MSCs. Whilst osteogenic and chondrogenic potential was similar, periosteum MSCs were significantly less adipogenic. Live cell imaging showed that BM MSCs were more migratory than periosteum MSCs in early culture (<3 weeks). M3%-PCL and M6%-CP70:30 were made of nano-scale randomly aligned fibres, forming small pore diameters (mean, 1.4 μm and 0.4 μm respectively). M6%-CP70:30 supported significantly lower (P<0.01) MSC attachment and proliferation than M3%-PCL, potentially due to a 'burst' release of collagen. Significant spontaneous alignment of MSCs on M3%-PCL was seen over 4 weeks. Spontaneous MSC migration through both membranes was prevented for up to a week *in vitro*.

In summary, two free surface electrospun membranes have been developed with the potential for supporting, to different extents, MSC proliferation, whilst acting as a barrier to cell migration, suitable for CSBD repair. Periosteum was shown to be at least equivalent and possibly, superior source of MSCs to BM for membrane colonisation.

Table of Contents

List of Tables

List of Figures

List of Equations

List of Abbreviations

ALP – alkaline phosphatase

APC – allophycocyanin

ATMP – advanced therapy medicinal product

AT MSC – adipose tissue derived mesenchymal stem cell

β-TCP – beta-tricalcium phosphate

BGLAP – bone gamma-carboxyglutamate (gla) protein

BM – bone marrow

BMA – bone marrow aspirate

BMAC – bone marrow aspirate concentrate

BM MSC – bone marrow mesenchymal stem cell

BMP – bone morphogenetic protein

BSA – bovine-serum albumin

CD – circular dichroism (Chapter 6)

CD – cluster of differentiation (Chapter 3 and Chapter 4)

CD14 – monocyte differentiation antigen

CD19 – B-lymphocyte antigen

CD31 – platelet endothelial cell adhesion molecule-1

CD34 – haematopoietic progenitor cell antigen

CD45 – lymphocyte common antigen

CD73 – ecto-5'-nucleotidase

CD90 – thy-1

CD105 – endoglin

CD146 – melanoma cell adhesion molecule

CD271 – Low-affinity Nerve Growth Factor Receptor

Cebpβ – CCAAT/enhancer-binding protein beta

CFSE – 5(6)-Carboxyfluorescein N-hydroxysuccinimidyl ester

CFU-F – colony forming unit-fibroblast

cN – centinewton

CO_2 – carbon dioxide

COL2A1 – collagen, type II, alpha 1

CSBD – critical size bone defect

DAB – 3,3'diaminobenzidine

dH_2O – distilled water

DAPI – 4',6-diamidino-2-phenylindole

DMEM – Dulbecco's modified eagle medium

DMSO – dimethyl sulfoxide

DPX – distyrene plasticizer xylene

e-PFTE – expanded polytetrafluoroethylene

ECM – extracellular matrix

EDTA – ethylenediaminetetraacetic acid

EDX – energy dispersive X-Ray

EtOH - ethanol

ESC – embryonic stem cell

F – female

FABP4 – fatty acid binding protein 4

FACS – fluorescence-activated cell sorting

FCS – fetal calf serum

FITC – fluorescein isothiocyanate

FWHM – full width at half maximum

G – g force

GAG – glycosaminoglycan

GFP – green fluorescent protein

GMP – good manufacturing processes

H – hour

H&E – haematoxylin and eosin

HA – hydroxyapatite

HCl – hydrochloric acid

HFIP – 1,1,1,3,3,3-Hexafluoro-2-propanol

HLA – human leukocyte antigen

HLA-DR – human leukocyte antigen–DR isotype

HPRT1 – hypoxanthine phosphoribosyltransferase 1

HRP – horseradish peroxidase

HUVEC – human umbilical vein endothelial cells

IgG – immunoglobulin G

IL – interleukin

ISCT – international society for cellular therapies

kPa – kilo pascals

kV – kilovolts

M – male

M3%-PCL – membrane (3% w/v)-PCL

M6%-CP(x:y) – membrane (6% w/v)-Collagen and PCL(ratio of collagen:PCL)

MHC – major histocompatibility complex

MMP – matrix metalloproteinase

MPa – mega pascals

MRW – mean residue weight

MSC – mesenchymal stem or stromal cell

MSCA-1 – mesenchymal stromal cell antigen-1

NCC – nucleated cell

NP – non passaged

P0 – passage 0

Pa – pascals

PBS – phosphate buffered saline

PCL – poly (ε-caprolactone)

PD – population doublings

PDGF – platelet derived growth factor

PE – R-phycoerythrin

PECy7 – R-phycoerythrin/Cyanine7

PLGA – poly(lactic-co-glycolic acid)

PLLA – poly(L-lactic acid)

P MSC – periosteum mesenchymal stem cell

PP – polypropylene

PPAR-γ – peroxisome proliferator-activated receptor gamma

PRP – platelet rich plasma

PS – penicillin streptomycin

PSR – Picro Sirius red

PSU – polysulfone

RBC – red blood cell

Reg 1 – regenerating gene 1

RIA – reaming irrigator aspirator

RT – room temperature

RT-PCR – real time PCR

RUNX2 – runt-related transcription factor 2

S3%-C-F – solution (3% w/v)-Collagen, cast as a film

S3%-PCL – solution (3% w/v)-PCL

S3%-PCL-F – S3%-PCL-F, cast as a film

S6%-CP(x:y) – solution (6% w/v)-Collagen and PCL(ratio of collagen:PCL)

S6%-CP(x:y)-F – S6%-CP(x:y), cast as a film

SBF – simulated body fluid

SDF-1 – stromal derived factor-1

SEM – scanning electron microscopy

SEM – standard error of the mean

Sox9 – SRY (sex determining region Y)-box 9

Stro-1 – mesenchymal stem cell marker-1

SUSD2 – sushi domain containing 2

TBS – tris buffered saline

TGF-β - transforming growth factor-β

TiO_2 – titanium oxide

TNF-α – tumour necrosis factor-α

TRAP – tartrate-resistant acid phosphatase

UCB MSC – umbilical cord blood derived mesenchymal stem cell

v/v – volume to volume

VEGF – vascular endothelial growth factor

w/v – weight to volume

Chapter 1: Introduction

This project aims to improve bone regeneration of critical size bone defects (CSBD), therefore factors surrounding the biology of bone and fracture healing will be investigated. The suitability and uses of a subset of adult stem cells, mesenchymal stem cells (MSCs) involved in bone regeneration will also be reviewed. Finally, the concept behind the development of a biodegradable barrier membrane to aid in CSBD repair will be discussed.

The annual rate of bone fracture in the UK is estimated to be 73.3 per 10,000 for 18-49 year olds, increasing to 116.3 per 10,000 for 50 year olds and above (Curtis et al. 2016). The rate of fracture non-union is reported to be between 2-10%, and is dependent on the fracture location, fracture type and patient demographics (Tzioupis & Giannoudis 2007; Mills, Aitken & Simpson 2017). Treatment strategies for fracture non-union are costly to the National Health Service, ranging from £7000 to £79000 (Mills & Simpson 2013) and averaging at £29,204 per patient (Hak et al. 2014). However, there are great indirect costs through loss of productivity for the patient, high rates of depression and opioid use, all of which will have a detrimental effect on patient quality of life (Antonova et al. 2013). Therefore, improvements to treatment of bone fracture repair is important, the diamond concept was developed to tackle this issue, providing a framework for bone fracture repair (Giannoudis, Einhorn & Marsh 2007). This draws attention to the importance of a fracture site containing osteogenic cells and growth factors important for aiding in the bone healing process, as well as the use of bone scaffolds with an osteoconductive nature and finally that the mechanical environment is stabilised (Giannoudis, Einhorn & Marsh 2007).

1.1 Bone Repair

To understand how bone regeneration fails due to bone infection or non-union or is in fact not possible due to the loss of bone, a knowledge of how bone remodels or heals uneventfully must be covered.

1.1.1 Bone Characteristics and Remodelling

The typical clinical scenario this project will investigate are CSBDs to long bones – rather than short, flat, sesamoid or irregular – which classically occur in the femur and tibia. Cortical or compact bone forms the outer shell of long bones; mainly composed of osteons. These are cylindrical in shape, made of concentric layers (lamellae) of bone tissue that wraps around a central canal called a Haversian canal. Within these canals lies the blood supply for bone, which connects the blood supply from the periosteum, the outermost layer of bone, to blood vessels found in the medullary region via perforating canals. Within this shell of cortical bone lies a layer of cancellous (spongy) bone which forms a network of trabeculae forming columns, that allows stress to be transferred down the longitudinal axis of bone. The shaft of the bone is hollow, allowing for this compartment to be filled with bone marrow (BM). Endosteum lines the medullary cavity and periosteum lines the outermost part of the bone, which allows for a blood and nervous supply to enter bone (Dwek 2010).

To describe the composition of bone it is often split into two phases, mineral and organic. The mineral phase refers to hydroxyapatite (HA) and the organic phase consists of predominately collagen type I (90%), non-collagenous proteins (~5%), lipids (~2%) and water (Boskey 2013). This composition differs depending on the location in the body but it is also affected by factors such as age, gender and disease (Boskey 2013). The structure and integrity of bone is maintained by various cell types, also located within bone that work together in a constant state of bone remodelling, these include osteoblasts, osteoclasts and osteocytes. Osteoblasts are derived from MSCs and are known as bone forming cells responsible for bone matrix deposition and mineralisation. Extracellular matrix (ECM) is synthesised and secreted from osteoblasts, consisting mainly of collagen type I and various proteins, including but not limited to osteocalcin and sialoprotein (Lerner 2012). In contrast osteoclasts are derived from the haematopoietic stem cell lineage and work in opposition to osteoblasts to degrade mineralised bone tissue (Santos, Bakker & Klein-Nulend 2009). Mature osteoclasts are multinucleated giant cells, which attach to bone surfaces via a ‘sealing zone’, a classical feature of these cells is the cell membrane in contact with bone becoming

extensively folded (Lerner 2012). Here, expression of proton pumps and chloride channels allow for extracellular acidification resulting in bone demineralisation, following this bone matrix can be degraded by proteolytic enzymes released from osteoclasts (Lerner 2012).

The third cell type are osteocytes, these are mature osteoblasts that have become entrapped and embedded within crevices of bone called lacunae, situated between lamellae, whereas osteoblasts form a single cell layer covering bone (Buckwalter, Glimcher & Becker 1995). Morphologically, osteocytes are different to osteoblasts as they have long dendritic processes, extending towards and connecting to fellow osteocytes via gap junctions, through tunnels called canaliculi and extending to osteoblasts on the bone surface. Recently osteocytes have become known for their mechanotransduction properties, when bone is put under stress, i.e. during movement or activity it deforms. This deformation causes movement of interstitial fluid surrounding osteocytes from areas of high pressure to low pressure, causing direct deformation of osteocytes amplifying tissue strain, which results in increased signalling from osteocytes (Santos, Bakker & Klein-Nulend 2009). Osteocytes are thought to orchestrate bone remodelling through signalling osteoblasts and osteoclasts to lay down bone or reabsorb bone in response to mechanical cues (Caetano-Lopes, Canhão & Fonseca 2007). In addition this fine balance is kept in check by osteoblasts, which are able to regulate the differentiation of osteoclasts (Lerner 2012).

1.1.2 Periosteum Anatomy

As previously mentioned periosteum refers to the outermost layer of bone. Periosteum is made up of two distinct layers named the outer (fibrous) and the inner (cambium) layer (Figure 1.1). The outer layer is thought to be formed of two parts, the most superficial layer is collagen predominant with elastic fibres running through it, this is also considered to be the most vascularised area of periosteum (Dwek 2010). Just underneath this is the second fibrous layer, also collagenous but containing many elastic fibres, giving periosteum its elasticity. However, the elastin content of periosteum will be debated during Chapter 3. The outer layer is considered to have a poor cellular content,

however, the lack of cellularity and collagen fibre dominance to the architecture could act as a barrier, controlling the flow of fluid and cell transport in and out of bone (Evans et al. 2013). In contrast, the inner cambium layer is highly cellular, it is here that MSCs, osteogenic progenitor cells and fibroblasts are contained. The cambium layer also contains collagen fibres, interestingly blood vessel density, fibroblast number and thickness have been shown to decrease with age, which could explain the decrease in the osteoblastic potential of periosteum with age. Periosteum is also attached tightly to bone through Sharpey's fibres, making it difficult to remove without tearing the cell rich cambium layer. This poses a problem with surgeons and scientists looking to utilise periosteum as a cell source of MSCs or osteoblastic cells in surgery or laboratory experiments (Chang & Knothe Tate 2012).

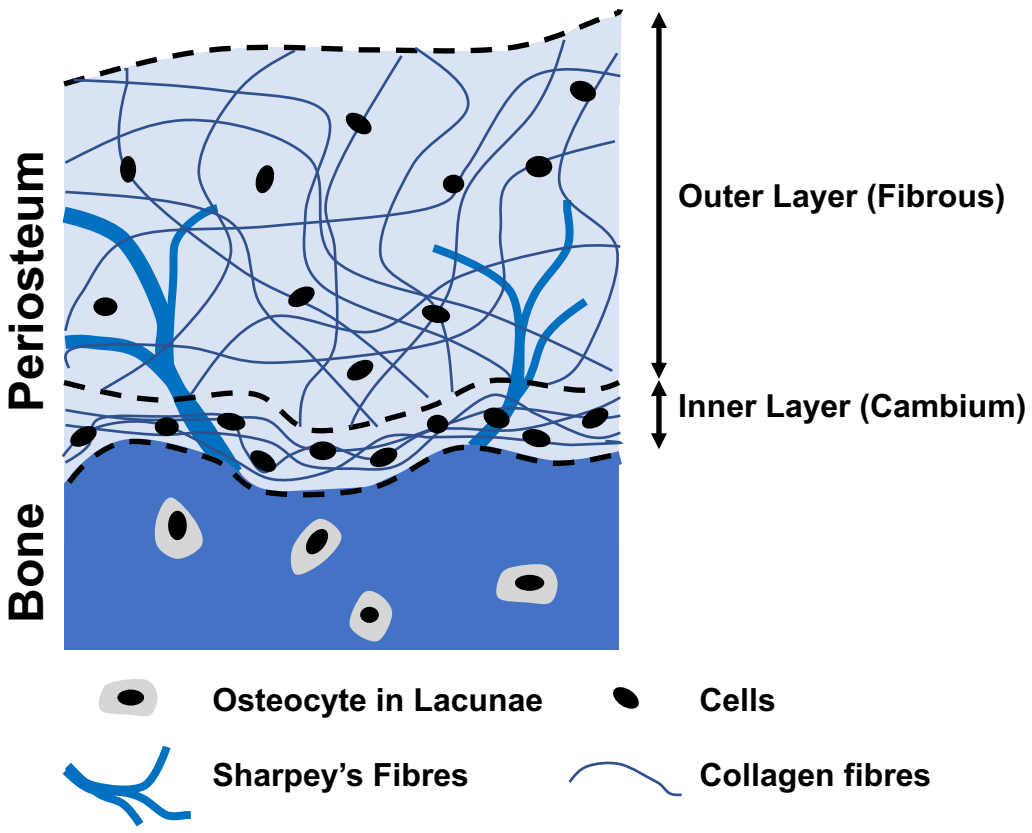

Figure 1.1: The anatomy of periosteum. Schematic representation of the composition of periosteum in relation to bone. Periosteum can be split into two layers, the inner and outer layer. The inner layer, also known as the cambium layer lies closest to the bone surface, it is the main reservoir of stem cells. The outer layer acts as a protective layer, composed mainly of collagen and elastin with poor cellular content. Image reproduced and adapted from: Chang & Knothe Tate (2012).

1.1.3 Fracture Healing

Now that the characteristics of bone and periosteum have been described, it is important to understand the mechanism of how a bone fracture heals. Fracture healing allows for injured tissue to repair, unlike most tissues in the body, bone has the ability to repair and regenerate to regain its former biochemical and biomechanical properties without scar formation (Panteli et al. 2015). There are two mechanisms for bone healing, which are 'direct' and 'indirect', both of which will be described below.

Direct bone healing is reached through direct re-establishment of connection of the Haversian system, lamellar bone and blood vessels (Marsell & Einhorn 2011). Here 'cutting cones' bridge the gap, protruding from the end of osteons at the fracture site, which contain osteoclasts, creating longitudinal tunnels, later filled with bone by osteoblasts, restoring the Haversian systems (Kaderly 1991). These 'bridging osteons' later mature into lamellar bone by direct bone remodelling. The gap healing process results in perpendicular, not longitudinal, lamellar bone filling the fracture site, which over time is replaced by longitudinal osteons that are vascularised so therefore transport a source of osteoprogenitor cells to the fracture site (Schenk & Hunziker 1994). Direct or primary fracture healing is not the common path for natural fracture healing, but can be the goal after open fracture reduction or internal fixation surgery (Marsell & Einhorn 2011). It can occur if adequate stability and connection of the fracture site is achieved, which allows for reduction of interfragmentary strain. Rigid fixation that does not allow for micromovement at the fracture is needed. If the fracture gap and interfragmentary strain is below 0.01 mm and 2% respectively then contact healing can occur, whereas, if the gap is less than 0.8 mm to 1.0 mm then gap healing occurs (Shapiro 1988; Kaderly 1991).

Indirect or secondary fracture repair is the process that most likely occurs post fracture. Unlike with direct healing the fracture does not need to be rigidly stable, and is in fact enhanced by micromotion and weight bearing (Marsell & Einhorn 2011). It is a three step process starting with the inflammatory phase, reparative phase and finally the remodelling phase, involving multiple tissues including periosteum, cortical bone, BM and external soft tissue (Dimitriou, Tsiridis & Giannoudis 2005). The acute inflammatory stage is triggered by

haematoma formation immediately post injury at the fracture site which consists of BM cells, peripheral and intramedullary blood which coagulates into a clot which will be the basis of future callus formation (Marsell & Einhorn 2011). Cells at the fracture site become nutrient deprived and as a result descend into necrosis, resulting in an acute inflammatory response, peaking at 24 hours post injury and lasting for up to seven days (Cho, Gerstenfeld & Einhorn 2002). Specifically, tumour necrosis factor-α (TNF-α), IL-1 (interleukin), IL-6, IL-11 and IL-18 recruit inflammatory cells and promote angiogenesis (Gerstenfeld, Cullinane, et al. 2003). Pro-inflammatory cytokine levels are increased during the acute inflammatory phase.

The reparative stage begins with MSC recruitment to the fracture site, where their ability to differentiate into osteoblasts and chondrocytes is important for fracture healing, in particular bone morphogenetic protein-2 (BMP-2) has been suggested to be critical to this process (Knight & Hankenson 2013). Current knowledge points towards recruitment of MSCs from BM and periosteum upon fracture, *in vivo* studies have shown that fracture healing is reduced or delayed upon BM or periosteum removal at the fracture site, proving their importance to the process (Dimitriou et al. 2012; Mercurio et al. 2012). MSCs themselves could also perpetuate MSC homing through release of various chemoattractant molecules and expression of chemokine receptors has been shown, suggestive that MSC homing is attractant and receptor dependent (Shao, Zhang & Yang 2015). There is an additional role in completing the inflammatory stage, where MSCs have immunomodulatory effects at the site of trauma, working to reduce levels of IL-1β, IL-6 and TNF-α (Granero-Moltó et al. 2012). Also of importance is the ability of MSCs to reduce TNF-α levels, which have been found to be elevated at fracture sites, therefore MSCs can act to limit inflammation (Scotti et al. 2013). Interestingly TNF-α can recruit MSCs and osteoclasts to trauma sites, allowing for chondrocyte apoptosis and endochondral ossification (Gerstenfeld, Cho, et al. 2003). MSCs have also been shown to stimulate proliferation of regulatory T cells, but also inhibit the proliferation of neutrophils, natural killer cells, B cells, CD4+ (cluster of differentiation 4 positive) and CD8+ T cells (Shao, Zhang & Yang 2015).

There are spatial differences in fracture healing with respect to the type of ossification that occurs. The medullary canal and intercortical areas generate a soft callus that undergoes endochondral ossification and a hard callus is formed, however, subperiosteally and with the immediate soft tissue, intramembranous ossification occurs (Phillips 2005). The difference being that endochondral ossification involves the laying down of cartilage that is replaced over time by bone, whereas, intramembranous ossification allows for bone formation without prior cartilage formation. Callus formation relies on the recruitment of MSCs, where collagen can be produced which appears to be dependent on transforming growth factor-β (TGF-β) (Marsell & Einhorn 2011). In contrast BMP-5 and -6 could induce intramembranous ossification at the periosteum (Cho, Gerstenfeld & Einhorn 2002; Colnot et al. 2003).

Revascularisation of the fracture site is important for successful bone repair as replacement of the cartilaginous callus into bone requires invasion of new blood vessels. Here, matrix metalloproteinases (MMP) degrade the ECM allowing for angiogenesis to occur, where new capillaries sprout from existing blood vessels, most likely from the periosteum (Weiss et al. 2009). This process appears to be under the control of vascular endothelial growth factor (VEGF), basic fibroblast growth factor, angiogenin, angiopoietin 2, platelet derived growth factor AB (PDGF-AB) and pleiotrophin, which have been found to be upregulated during fracture healing (Lehmann et al. 2005; Bourque, Gross & Hall 1993). Angiogenesis can also be modulated by MSCs, which release angiogenic factors, a process believed to be increased upon trauma (Shao, Zhang & Yang 2015). Over time the cartilaginous callus formed by endochondral ossification becomes mineralised, as chondrocytes mature and proliferate they become hypertrophic and calcified. Further recruitment of MSCs to the area allows for calcified cartilage to be replaced by woven bone, resulting in a more mechanically rigid callus (Gerstenfeld et al. 2006). The final stage of fracture repair is the bone remodelling stage, where the hard callus is remodelled into lamellar bone with a medullary cavity. Osteoclasts reabsorb the hard callus while osteoblasts work to deposit lamellar bone (Lerner 2012). This process can begin after 3-4 weeks post fracture and last for years for full bone remodelling to take place, where age is thought to lengthen the process (Boskey & Coleman 2010).

1.1.4 Critical Size Bone Defects

Bone defects form a subset of fractures where bone loss occurs, these become critical size or ‘large bone defects’ when they are above a certain size that will not completely heal over time (Spicer et al. 2012). This can also be described physically as a defect of greater than 1-2 cm in length with a greater than 50% loss of the circumference of the bone (Schemitsch 2017). Bone loss can refer to structural defects or regions of missing bone, bought about by external factors primarily caused through open fractures, gunshot wounds or osteoclastic tumours. Alternatively, bone loss could be due to secondary causes such as tumour resection or infection and non-union, where infected or ‘dead’ bone needs to be removed. Another classification of bone loss is a structural loss from within an existing bone caused by osteopenia, osteoporosis or metabolic disease (Wiese & Pape 2010). The most common cause of CSBDs occurs through traumatic injury, followed by tumour resection, infection and non-union fracture (Wiese & Pape 2010).

In addition, it is estimated that between 5-10% of all fractures result in non-union (Calori et al. 2007), which are classified as fractures that have not healed within nine months and have not shown radiographic progression in three months (Panagiotis 2005). Although, it should not be ignored that approximately 9 in 10 of all fractures will heal uneventfully. However, when fractures fail to unite, the effect on patients’ lives is catastrophic. Factors thought to contribute to and increase the risk of non-union are gender (females >55), age, muscle mass, smoking, diabetes, osteoporosis, nonsteroidal anti-inflammatory drugs, local risk factors, vascular damage, infection, multiple trauma or fractures (Calori et al. 2007). As previously mentioned a subset of these can develop into CSBDs, often coupled with infection which will need to be debrided prior to repair (Hossain & Barry 2011).

1.1.5 Challenges and Complications of Critical Size Bone Defects

CSBDs pose multiple issues to orthopaedic surgeons, therefore limb salvage method must be carefully and thoughtfully assessed for each case. The ideal outcome for a CSBD is to allow for “bone union, acceptable [bone] alignment, equal limb length and restoration of function” (Hossain & Barry 2011). Once

debridement of soft tissue and bone has occurred the surgeon can stabilise the fracture and decide on the best course of action. External fixators can be used for stabilisation and alignment of CSBDs, however in the case of small bone loss internal fixation can be considered. From here a decision must be made whether to maintain limb length or to shorten the limb, this is dependent on the size, position and length of the bone defect and soft tissue loss. Limb shortening allows the fracture to be brought together in order to encourage fracture union, later bone distraction can be used to restore limb length.

The Ilizarov technique, exploits the ability for bone regeneration to occur through distraction (Rozbruch et al. 2008). External ring fixators are built around the affected limb and fixed above and below the fracture site using pins. The top ring allows for force to be transferred to the external frame during early weight bearing, thus bypassing the defect site. However, this technique is contraindicated by limb length inequality, donor site morbidity, pin infection and the need for multiple surgeries (Maini et al. 2000). These issues with treatment are heightened by the increased chance of complication such as infection, low quality vascular supply and a low quality soft tissue envelope seen with these type of bone defects (Wiese & Pape 2010). In addition, there are individual patient factors that can affect their ability to heal, including but not limited to diabetes, ageing, neoplastic lesions, infection and impaired blood supply (Bigham et al. 2011).

1.1.6 Current Grafting Techniques

Traditionally, when approaching impaired fracture healing the ‘triangular concept’ has been implemented, where the combination of growth factors, bone scaffolds and MSCs have been thought to aid restoration of bone. However, as previously mentioned this has been re-evaluated to be considered the ‘diamond concept’, whereby thought is given to the input of the mechanical environment of the fracture site also (Figure 1.2), which forms the basis of how to approach surgical repair of CSBDs (Giannoudis, Einhorn & Marsh 2007). The ideal bone substitute or ‘scaffold’ for CSBDs has been described as ‘osteoconductive, osteoinductive, osteogenic, without risk of transferring disease, readily available, manageable, biocompatible and

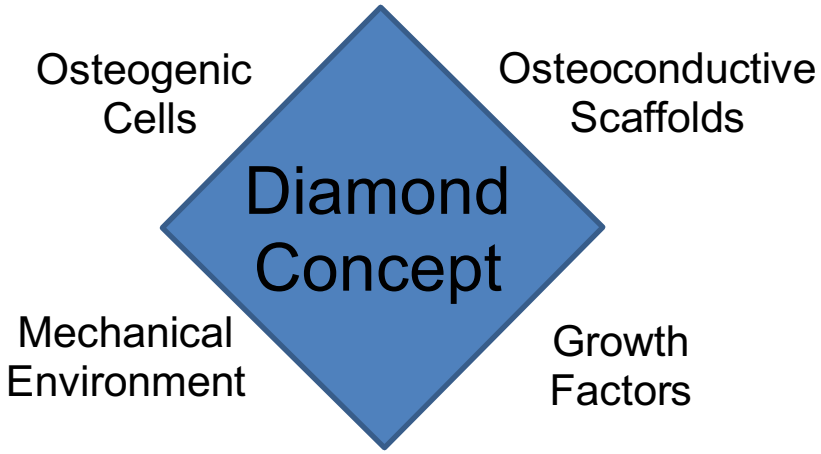

Figure 1.2: The Diamond Model of bone fracture healing interactions. Reproduced from (Giannoudis, Einhorn & Marsh 2007).

bioresorbable' (Calori et al. 2011). Osteoconductivity is determined by graft or scaffold porosity and whether or not it allows for colonisation and in growth of new bone cells and capillaries (Panteli et al. 2015; Calori et al. 2011). Osteoinductivity refers to whether the graft can stimulate or promote bone formation and osteogenicity is the presence of osteogenic cells in the bone graft (Panteli et al. 2015; Calori et al. 2011).

The use of a bone graft or scaffold to fill a defect site is an alternative to the Ilizarov technique as it mitigates the need to undergo lengthy and painful distraction therapy (Rozbruch et al. 2008). Bone scaffolds are porous solid biomaterials that can be designed to fulfil the following four functions. Firstly, to promote cell to biomaterial interactions through adhesion and ECM deposition, secondly by allowing for sufficient transport of nutrients and waste products, thirdly by being biodegradable, at a known rate in line with the target tissues regeneration rate and finally the biomaterial must aim to provoke minimal inflammatory reactions or toxicity (Dhandayuthapani et al. 2011).

There are many options available to an orthopaedic surgeon for grafting material, currently, the gold standard is an autograft, typically taken from the iliac crest. Other options include allograft, xenografts, decellularised or demineralised grafts and synthetic grafts, each have their own merits and drawbacks, summarised in Table 1.1. Autografts have advantages over other grafting materials as they do not elicit an immune response, unlike allografts and xenografts, however, issues involve lack of volume of graft that can be

harvested, a factor especially important for the larger subset of bone defects and risk donor site morbidity. Having a second surgical site also increases the time needed in surgery and therefore cost. Here allografts, xenografts and synthetic grafts are advantageous as availability and volume is not an issue. The more processing that allografts, xenografts and demineralised grafts undergo increases the immunocompatibility, availability, shelf life and cost, however this usually results in reduction of osteogenicity, osteoinductivity and graft strength (Shibuya & Jupiter 2015). Although there are advantages to allografts and xenografts, recently their use has been replaced with synthetic grafts, which on their own are lacking in osteoinductiveness and osteogenicity. However, synthetic grafts can be easily modified either post manufacture or just prior to surgical implantation. Modifications include, but are not limited to the addition of growth factors like BMP-2, known to be important for bone regeneration or platelet rich plasma (PRP) an autologous source of growth factors and collagen, important for improving cell attachment and growth onto scaffolds (El-Jawhari et al. 2016).

It is important to understand the grafting materials available to a surgeon, as these form the type of materials MSCs will interact with following surgical intervention for CSBD repair. The pros and cons of different types of bone grafting materials, whether autogenic, allogenic, xenogenic or synthetic are discussed (Table 1.1). Autografts are currently considered to be the gold standard for treatment as they offer the best osteoconductive, osteogenic and osteoinductive properties (Zimmermann & Moghaddam 2011). Therefore, in order to remove or reduce the need for iliac crest autografting a suitable and effective replacement or adjuvant must be developed.

A recent study investigated three bone scaffolds, a ‘bare’ scaffold made from HA, a collagen coated HA based scaffold and a synthetic collagen coated β-tricalcium phosphate (β-TCP) scaffold. It was found that when unprocessed bone marrow aspirate (BMA) was loaded onto these scaffolds enhancement in BM MSC attachment and proliferation were seen with the scaffolds that also contained collagen (El-Jawhari et al. 2016). Naked bone scaffolds are known to have low cellular attachment, which supports the theory that collagen increases MSC attachment (Zimmermann & Moghaddam 2011).

Table 1.1: Summary of the different graft material options for critical size bone defect repair (CSBD), listing the advantages and disadvantages of each material or tissue source.

	Description	Advantages	Disadvantages
Autograft (Gold Standard for CSBD)	Sample of bone taken from the patient, usually the iliac crest, to fill the defect site.	Mitigates risk of immune response and is histocompatible to the bone it aims to replace (Dimitriou et al. 2011). Considered ' living' with intrinsic osteogenic activity, as it contains MSCs, osteocytes and osteoblasts (Kovar & Wozasek 2011).	Limited by harvestable bone volume, therefore may need to take multiple donor graft sites (Kovar & Wozasek 2011). Also, adds cost and time to surgery, as will need to be harvested prior to implantation. Risk of donor site morbidity and increased pain or site inflammation (Oryan, Alidadi & Moshiri 2013). Associated with approximately 10% minor complication and major complication rate (Kovar & Wozasek 2011) and with faster implant resorption (Zimmermann & Moghaddam 2011).
Autograft & Reaming Irrigator Aspirator	A method to harvest intramedullary bone grafts, one step procedure that reduces intramedullary pressure and temperature to help prevent fat embolism, primarily used prior to nail insertion (Kovar & Wozasek 2011). The reamed bone marrow can be collected, compacted and used as grafting material.	RIA taken when intramedullary nails are used already. RIA material contains MSCs that appear to be ' viable and osteogenic' (Uppal et al. 2013). Reported complication rate is lower than iliac crest bone graft harvesting, 6% compared to 19% (Dimitriou et al. 2011). Can harvest larger volumes of grafting material in comparison to autografts (Dimitriou et al. 2011).	Could require second surgical exposure site if fracture site does not allow for access to the medullary cavity (Seagrave et al. 2014).

(Table 1.1 continued)

	Description	Advantages	Disadvantages
Allograft	Sample of bone taken from the patient, usually the iliac crest, to fill the defect site.	No donor site morbidity. Readily available and in larger quantities than autograft, which is needed for larger bone defects (Giannoudis, Dinopoulos & Tsiridis 2005).	Risk of inducing an immune response and disease transmission (hepatitis, HIV) (Zimmermann & Moghaddam 2011). Graft viability may not be ideal, could result in graft resorption and a host immune response (Oryan, Alidadi & Moshiri 2013). Lengthy recovery period to allow for graft incorporation, associated with re-fracture and non-union (Hossain & Barry 2011). Could be lacking in osteogenic properties due to absence of viable cells (Zimmermann & Moghaddam 2011).
Xenograft	Bone taken from another species, typically bovine or porcine origin. Goes through an extensive sterilisation process (Shibuya & Jupiter 2015).	No donor site morbidity. Low cost and tissue is readily available. Long shelf life due to extensive sterilisation process (Shibuya & Jupiter 2015). Due to this often used for the production of tissue engineered biomaterials (decellularised/demineralised).	Risk of inducing an immune response (Badylak & Gilbert 2008). Processing of graft removes cells, therefore reducing the osteoinductive nature of the graft (Badylak & Gilbert 2008). Risk of disease transmission (bovine spongiform encephalitis, rabies, Epstein–Barr virus) (Oryan, Alidadi & Moshiri 2013). Can have higher reabsorption rate than autografts and allografts (Oryan, Alidadi & Moshiri 2013).

(Table 1.1 continued)

	Description	Advantages	Disadvantages
Decellularised or Demineralised	Can be derived from allograft or xenograft. Tissue processed with various detergents and enzymes to remove cellular and DNA material. Left with porous extracellular matrix in the form or chips or bone blocks.	Readily available, can be used in large volumes, can be sterilised and packaged for surgery easily. No second surgical site or donor site morbidity. Can be used as a scaffolding material to grow MSCs onto it or for attachment of growth factors (Kouroupis et al. 2013).	Can lack osteoinductivity and osteogenicity due to the removal of cells during processing.
Synthetic Graft	Made from ceramics, hydroxyapatite (HA) or tri-calcium phosphate (TCP). Often used to make up the bone volume in conjunction with autograft.	Hard and porous material, ideal for cellular infiltration, can be made in different forms to suit use (Zimmermann & Moghaddam 2011). Can be osteoconductive, no risk of disease transmission as can be sterilised (Zimmermann & Moghaddam 2011). Biocompatible and HA chemically similar to mineralised bone (Smith & Grande 2015).	Can lack osteoinductivity and osteogenicity when used on their own. Ceramics are known to be brittle (Giannoudis, Dinopoulos & Tsiridis 2005). HA not as easily reabsorbed by osteoclasts in comparison to TCP (Zimmermann & Moghaddam 2011).

1.2 Utilising Mesenchymal Stem Cells for Bone Regeneration

Stems cells can be defined as cells with the ability to “perpetuate themselves through self-renewal” combined with the ability to generate “mature cells of a particular tissue through differentiation” (Reya et al. 2001). Multipotent stem cells also known as adult stem cells or tissue specific stem cells can differentiate into the specialist tissue of the fetus or adult and are only able to form into a restricted number of mature cell types. For example, MSCs are a type of adult stem cell that can differentiate into osteogenic, chondrogenic and adipogenic lineages whereas haematopoietic stem cells differentiate into myeloid and lymphoid lineages of blood cells.

For the application of tissue engineered bone regeneration the source of cells to aid this is important. As previously outlined, the terminally differentiated cell types of MSCs, chondrocytes (cartilage) and osteoblasts (bone) are needed for the indirect and direct pathways of bone healing, therefore, it would be logical to target MSCs as the cell source for this application. It could be argued that embryonic stem cells (ESC) are a superior choice to adult stem cells as they have a greater differentiation capacity (Jung & Kleinheinz 2014). However, as embryonic stem cells are generally derived from *in vitro* fertilisation treatment this causes ethical concerns for their use and the harvesting and isolation of ESCs is under strict control (Jung & Kleinheinz 2014). Therefore, in comparison adult stem cells are a more favourable source of cells and can be harvested from different tissues with little to no donor site morbidity (Table 1.2). In addition the use of autologous adult stem cells could be easier to drive down the desired cell lineage, by allowing the cell type introduced to the treated area to be more selective in comparison to ESCs (Jung & Kleinheinz 2014).

Table 1.2: The pros and cons for different sources of mesenchymal stem cells (MSC) for the application of bone regeneration, as well as the ethical considerations surrounding each source.

	Pros	Cons	Is Autologous Cell Harvesting Ethical?
Bone Marrow Aspirate (BMA)	Established harvesting technique, broadly used in orthopaedic surgery currently (Hernigou et al. 2005). Known osteogenic potential, aiding non-union repair when injected into fracture site (Garg, Gaur & Sharma 1993). Whole BMA include growth factors from platelets, which could be beneficial for bone regeneration (Muschler et al. 2003). BM MSCs show higher *in vitro* mineralisation, higher levels of osteocalcin and alkaline phosphate compared to adipose MSCs (Knight & Hankenson 2013).	BM MSCs are a rare population, with lower colony frequency compared to adipose and periosteal derived MSCs (Knight & Hankenson 2013). MSC count in BMA varies (0.001%-0.01% of total nucleated BM cells), known to decrease with age (Bernardo, Locatelli & Fibbe 2009). MSC characteristics affected by age (senescence, migration, differentiation, proliferation) (Fehrer & Lepperdinger 2005). Risks harvest site morbidity (Hernigou et al. 2005) and requires patient to be under general anaesthesia. Technique variation effects MSC frequency (Cuthbert et al. 2012). MSC numbers harvested could be too low, therefore concentration of BMA to overcome this is often needed (Jackson, Nesti & Tuan 2010).	Yes, BMA can be taken while the patient is under anaesthesia for their orthopaedic surgery. However, patient should be aware that there could be associated harvest site pain or morbidity.
Periosteum	Periosteal MSCs differentiate into osteoblasts and chondrocytes, important to fracture healing (Colnot 2009). Lower adipogenic differentiation capacity at different seeding densities in comparison to BM MSCs (Eyckmans, Lin & Chen 2012).	Hard to source human samples ethically, as it is an invasive procedure and removal could impair fracture healing (Dimitriou et al. 2012). Periosteum thins with age, therefore could be more difficult to source from elderly patients (Lin et al. 2014).	Debatable, dependent on how much tissue is needed to be effective.

(Table 1.2 continued)

	Pros	Cons	Is Autologous Cell Harvesting Ethical?
Periosteum (continued)	Higher cell mass per unit of harvested tissue in comparison to BM and adipose tissue, in canines, therefore higher frequency of MSCs than BM (Kisiel et al. 2012).	Cambium level strongly attached to bone, making it hard to harvest (Knight & Hankenson 2013).	Stripping of periosteum from fracture site impedes healing (Gerstenfeld, Cullinane, et al. 2003).
Trabecular Bone Chips	Similar numbers of nucleated cells to BM, forms more MSC colonies following enzymatic treatment, suggestive of there being more MSCs present attached to bone (Sakaguchi et al. 2009). Cells isolated are capable of tri-lineage differentiation and self-renewal.	Have to harvest a bone chip to isolate these cells.	Yes, bone samples are taken for autografts already, but harvestable volume is limited due to potential to create defect.
Endosteum	MSCs migrate from the endosteum into the fracture site upon injury, known to be involved in the bone healing process (Calori et al. 2007). Evidence suggests MSCs from the endosteal niche may be involved in maintaining haematopoietic stem cells *in vivo* in mice (Nakamura et al. 2010).	Hard to specifically isolate endosteum MSCs for the use of regenerative surgical techniques, will need to take a bone chip sample for this to occur.	Would need to harvest a bone sample, and is a specific area to target for cellular removal.
Skeletal Muscle	Sample can be taken during orthopaedic surgery, can be retrieved from surgical waste post debridement of soft tissue.	Controversy about whether there are a subset of MSCs located in skeletal muscle or whether tissue specific progenitors are driven to skeletal lineages *in vitro* or *in vivo* (Colnot 2011). MSCs found are in lower numbers than BM (Nesti 2008).	Would need to harvest a bone sample, and is a specific area to target for cellular removal.

(Table 1.2 continued)

	Pros	Cons	Is Autologous Cell Harvesting Ethical?
Adipose Tissue	Easy and safe to access and isolate (liposuction waste) (Jung & Kleinheinz 2014). Can harvest greater volumes in comparison to BM, therefore more MSCs (500x more MSCs per gram of fat to equivalent BMA (Hass et al. 2011).	Could be more committed down the adipogenic lineage due to tissue source, have not been shown to contribute to bone repair *in vivo* (Colnot 2011).	Yes, can take via liposuction or aspiration, however, some patients are unsuitable for this procedure.
Peripheral Blood	MSCs have been isolated from whole blood of various mammalian species as well as humans, (Kuznetsov et al. 2001). Some evidence that MSCs can be mobilised into blood following injury but the numbers remain low.	Limited knowledge on MSCs mobilisation into peripheral blood, however, recent evidence shows that MSCs were not mobilised into blood following orthopaedic injury (Tan et al. 2015). Pharmaceutical intervention needed to mobilise MSCs into blood. MSC frequency in blood is significantly lower than BM and most likely will not be high enough for efficient colony formation (He, Wan & Li 2007).	Yes, blood sample can be taken, however, probably will not produce clinically relevant numbers of MSCs. Also, contradictory evidence of whether MSCs can be mobilised into the blood stream.
Dental Pulp	Can be taken from wisdom teeth (by product of a necessary surgery) and banked. Known to be able to differentiate into the osteogenic lineage (Rajendran et al. 2013).	Prior harvesting, banking and storage is needed, resulting in increased costs. For MSC release grind up the teeth or use enzymatic release, therefore would need to be culture expanded.	Debatable, only if the patient needs to have wisdom teeth removed, there are better harvesting sites.
Synovium	MSCs from synovium have higher proliferation and colony forming potential that adipose derived MSCs. MSC numbers are higher compared to BMA and similar to adipose tissue (Mochizuki et al. 2006).	Upon single cell analysis synovial MSCs were shown to be not as osteogenic as donor matched periosteal MSCs (De Bari et al. 2008).	No, this subset of patients would have long bone defects so not ethical to taken from joints.

(Table 1.2 continued)

	Pros	Cons	Is Autologous Cell Harvesting Ethical?
Umbilical Cord Tissue & Blood	It is considered to be a waste material and banking procedures are well established.	Low numbers in blood (higher numbers in umbilical cord tissue), both require prolonged storage for autologous use and therefore is costly. Hard to isolate MSCs and needs to be processed quickly to improve yield. Differentiation to osteoblasts is lower compared to BM and appears to have preferential adipogenic differentiation (Sibov et al. 2012).	No, unless the patient has their umbilical cord frozen (rare in this country, but could be more common place in the future).

1.2.1 Mesenchymal Stem Cells

MSCs are a multipotent self-renewing population of cells with the potential to differentiate down several cell lineages (Marsell & Einhorn 2011; Jing et al. 2013). In order to characterise human MSCs experimentally a predetermined criteria must be met, set out by the Mesenchymal and Tissue Stem Cell Committee of the International Society for Cellular Therapy (ISCT) (Dominici et al. 2006). MSCs must adhere to tissue culture plastic, when cultured under standard conditions, they must form fibroblastic like cells. Furthermore, the cells should be seen to be able to be 'colony forming', easily tested through the use of a colony forming unit-fibroblast (CFU-F) assay. When analysed using flow cytometry, over 95% of the cell population must express cell surface markers, CD105, CD73 and CD90, as well as show an absence of cell markers for haematopoietic progenitor cells, CD45, CD34, CD14, CD19 and human leukocyte antigen (HLA) class II expression should be below 2% (Dominici et al. 2006). Finally, the MSCs must have the capacity for tri-lineage differentiation into osteogenic, chondrogenic and adipogenic cell lineages when using standard differentiating culture conditions *in vitro* (Ma 2010). This definition will form the basis of comparing different MSC types derived from BM and periosteum during Chapter 4.

MSCs have been isolated from different human tissue sources including: BM, adipose tissue, periosteum, peripheral blood, dental pulp, synovial membrane and fluid, umbilical cord, skeletal and cardiac muscle (Hass et al. 2011; Mafi et al. 2011; Marsell & Einhorn 2011). Table 1.2 considers in detail the pros, cons and ethical issues surrounding the harvesting of MSCs for the application of bone regeneration. Relevant sources of MSCs involved in bone regeneration are believed to be from the BM, periosteum and endosteum (Shao, Zhang & Yang 2015). This project will focus on two different MSC sources, BM and periosteum. Each source has been selected for varying reasons that will be covered in the following section.

1.2.1.1 Bone Marrow Derived MSCs

BM refers to the tissue filling the voids of vascular sinuses and bone surfaces of the pores from cancellous bone (Sakaguchi et al. 2009). MSCs from this

area can be aspirated from patients as a BMA, typically the anterior or posterior iliac crest is used as the site of BM harvesting in orthopaedic surgeries. It was first shown in 1997 that aspiration volume has an effect on the CFU-F formation and therefore must affect the number of MSCs in BMA. It was concluded that volumes over 2 mL resulted in reduced CFU-F formation, which could be partially attributed to peripheral blood dilution in the sample (Muschler, Boehm & Easley 1997). Another study agreed with this theory but suggested it was important to aspirate BM in fractions up to 10 mL and potentially aspirate from multiple sites in order to maximise the level of harvested MSCs (Hernigou et al. 2005). MSC numbers in BM have been reported to have large donor variation, which could be due to either, or a combination of, aspiration technique and the donor. A more recent study concluded that MSC frequency dropped 7 fold and 9 fold upon performing flow cytometry analysis and CFU-F assays, respectively when comparing the first 5mL of BMA in comparison to the following 15 mL (Cuthbert et al. 2012).

Current research on skeletal tissue regeneration using MSCs involves the use of culture expanded MSCs, as this is a sure way of being able to amplify numbers of implantable MSCs. Also, culture expanded MSCs seeded onto various bone scaffolds have been used for the treatment of non-union and bone defects (Undale et al. 2009). The use of culture expanded cells in surgery is under regulation as ‘advanced therapy medicinal products’ (ATMP), this regulatory pathway is not only lengthy but expensive. A more appealing solution would be to bypass this regulatory pathway and use uncultured samples like BMA. The use of BMA during orthopaedic surgeries is considered to be ‘minimally manipulated’ by the FDA, as long as process methods are ‘non-enzymatic’ and used within the ‘same medical intervention’ (Gee 2018). Harvesting BMA containing MSCs directly from the patient during surgery to mix with a bone scaffold to fill the bone defect could act as a ‘living’ regenerative scaffold. When mixed with bone grafts or scaffolds, this can be regulated as a ‘class III medical device’ with a shorter and cheaper regulatory route. Recently, this theory has been investigated *in vitro*, showing successful MSC attachment, derived from fresh BMA onto a bone scaffold followed by MSC growth and differentiation (Kouroupis et al. 2013). In addition, the idea that taking a BMA from a patient to add to a bone scaffold could replace the

current practice of autograft harvesting is an attractive concept as it comes with less risk, shown through the BM aspiration procedure having a lower and less severe complication rate than autograft harvesting (P. Hernigou et al. 2014).

Although expanded MSCs allow for a known number of MSCs to be added to a defect site or seeded onto a scaffold, with the increasing knowledge of optimal BMA harvesting to reduce peripheral blood dilution, new techniques for quick MSC enumeration from BM using fast flow cytometry assays and the development of BMA concentrates (BMAC), this can be mitigated (El-Jawhari et al. 2017). BMACs can be achieved through density gradient centrifugation, reducing a volume of 60 mL BMA to approximately 8 mL, this can then either be injected into sites of non-union fractures or combined with bone scaffolds and implanted into defect sites and was seen to help improve healing (Jäger et al. 2011). *In vitro* analysis of BMAs showed a 5 fold concentration of white blood cells following centrifugation, producing BMAC, also larger colony size was seen following CFU-F assays in BMAC samples (Jäger et al. 2011). In addition, PRP injections into the iliac crest have been shown to increase MSC levels in BM, this poses an interesting prospect for the future where 3 days prior to an operation patients can have a PRP injection, allowing for BMA samples, taken during an operation to contain larger amounts of MSCs (Philippart et al. 2014). As most of the surgeries for CSBD repairs occur once ‘non-union’ has been diagnosed, known to take up to a year post trauma, this method could be helpful as surgery and therefore PRP injections can be planned in advance.

A further avenue for investigation will be utilising BMA as not only a source of MSCs but also autologous platelets. Typically BMA is collected in heparin to prevent coagulation, however, previous studies have shown that if coagulation of BMA is allowed when combining with a bone scaffold improved results for bone regeneration for spinal fusion can be seen *in vivo* (Muschler et al. 2003). It is thought that the fibrin clot produced in the coagulation cascade can provide stability to the graft site whilst serving as a site for osteogenic cell attachment and migration (Muschler et al. 2003). Degranulation of platelets within the BMA could also occur, allowing for growth factor release into the

graft site, known to enhance wound healing and regeneration (Rubio-azpeitia & Andia 2014). This creates an exciting opportunity to manipulate not only the contents of BMA but also the clotting cascade to aid bone regeneration. This overarching aim is to be able to work towards producing a single stage surgical procedure that is compatible with real operating times, by removing the time taken to culture MSCs, thus reducing the need for further surgeries for the patient.

The theory of fibrin clot manipulation has been used in other areas of tissue engineering. Fibrin gels, formed from fibrinogen, have been used to mimic the coagulation cascade of blood that results in a fibrin clot and used for the application of wound repair (Li et al. 2015). Proliferation of MSCs has been seen to be enhanced within 3D fibrin clots *in vitro*, which again supports the idea of manipulating the natural clotting cascade of BM (Ho et al. 2006).

1.2.1.2 Periosteum Derived MSCs

Early studies showed that the osteogenic potential of the periosteum is limited to the inner or cambium layer, closest to the bone, therefore, the process for periosteum removal becomes very important with respect to retaining this layer (Eyre-Brook 1984). Different techniques have been developed for removal of periosteum typically, forceps, scalpels or periosteal elevators are used. However, the use of forceps can result in tearing or the loss of the cambium layer and potentially should only be used for periosteal retrieval from young patients as it is thicker and has looser attachment to the bone (Chang & Knothe Tate 2012). With older patients the periosteum becomes thinner and a scalpel can be used to scrape periosteum from the bone. Periosteal elevators give the advantage of allowing for Sharpey's fibres, which anchor periosteum to the bone, to be cut during removal. However, the specific technique of periosteal elevation varies and can also result in failure to fully remove the cambium layer. Brownlow et al. (2000) performed a comparison study of four types of periosteum removal, a scalpel was used to outline the piece of tissue followed by 1) forcep removal (pulled), 2) sharp dissection using scalpel, 3) use of a periosteal elevator or removal of corticoperiosteal chips using chisel elevation. It was found that the tissue site did not make a difference to the results, but the degree of damage to the cambium layer

varied between method of periosteum removal (Brownlow et al. 2000). It should be noted that this paper's results focused on the ability to retain the cambium layer to the bone sample taken, rather than the quality of the cambium layer in the detached periosteum sample. The use of either a periosteal elevator or chisel elevation resulted in the most complete removal of the cambium layer of periosteum (Brownlow et al. 2000).

Although BM MSCs are considered to have the greatest osteogenic differentiation capacity, recent evidence has shown periosteum to have equal to or greater bone regeneration properties (Chang & Knothe Tate 2012). Seeding density in tissue culture of human periosteal MSCs has been shown to influence cell marker expression for differentiation. Eyckmans et al. (2012) reported that limitation of cell spreading by high cell seeding density seemed to promote adipogenesis and chondrogenesis, whereas promotion of cell spreading (low seeding density) supports osteogenesis (Eyckmans, Lin & Chen 2012).

As periosteum is a more precious tissue to obtain, due to its importance in bone regeneration, human sources of periosteal derived MSCs have been investigated less than BM MSCs. A recent paper investigated the growth kinetics, colony formation capacity and MSC marker expression of human periosteum MSCs. It was shown that MSC colony formation was possible up to passage 15, which is potentially longer than BM MSCs, where passage is known to reduce the multipotency and growth rate of BM MSCs (Jin Jin et al. 2013; Ball et al. 2011). It was also seen that in tissue culture, 40% of the cells could be described as a 'mature osteoblastic phenotype' with a further 10% being at an 'intermediate stage', seen through phenotypic expression profiles using flow cytometry. This is suggestive of there being mixed populations of MSCs in periosteum at different stages of differentiation, although this conclusion cannot be taken as definitive (Ball et al. 2011). A limitation to this study is sample number and that comparison was not made to matched BM samples, which is more ideal with respect to allowing for comparisons to be made. De Bari et al. (2006) showed the multipotency of single cell derived clonal populations of human periosteum MSCs. It was shown that linear growth rates for at least 30 population doublings (PD) could be achieved,

suggestive that the heterogenicity of periosteum digest, seen in Ball et al. (2011) not only affects marker presentation but also growth kinetics. This project has ethical approval to obtain human periosteum and BM samples, so direct, donor matched comparisons with respect to cell surface marker expression, PDs, growth kinetics and differentiation potential can be made.

1.2.2 Comparison of MSC Characteristics

Gaps in current research surrounding BM, periosteum and skeletal muscle derived MSCs have been highlighted in Table 1.3, with respect to *in vivo* input into bone regeneration, migration, proliferation, differentiation and immunoregulation. It is apparent that the majority of research has been carried out on BM MSCs, leaving gaps in the research with respect to confirming periosteal MSC involvement. This is particularly apparent with immunomodularity effects of periosteum MSCs, where research appears to have been carried out on BM MSCs. This makes sense as it is the most easily available source of MSCs that are known to have direct input into bone regeneration, unlike adipose sources, which may be predisposed to adipogenic differentiation. However, this does leave a good area to target research at. It is particularly apparent being able to collect donated human periosteum and BMA from patients is difficult, therefore this project is in a unique position to compare and contrast donor matched samples, as will be covered in Chapter 4.

Table 1.3: Comparison of two sources of MSCs, bone marrow and periosteum with respect to the main functions of MSCs.

	BM MSC	Periosteal MSC
Input for *in vivo* Bone Regeneration	Known to have input in intramembranous ossification, during fracture healing (Colnot 2009). *In vivo* studies showed that reaming of BM negatively effects bone regeneration (Dimitriou et al. 2012; Mercurio et al. 2012).	Known to have input in endochondral ossification as part of the bone regeneration process (Colnot 2009). Removal of periosteum results in reduced capacity for fracture callus development (Dimitriou et al. 2012; Mercurio et al. 2012).
Migration	Mouse BM MSCs have been shown to migrate into fracture sites (Granero-Moltó et al. 2012).	Can migrate into fracture site. High expression of SDF-1 in periosteum during acute fracture healing. SDF-1 blockage inhibits MSC migration to fracture site (Kitaori et al. 2009).
Proliferation	In tissue culture, loss of multipotency as BM MSCs age, become quiescent, seen by lower PDs.	Single cell analysis showed rapid growth rates up to passage 30 (De Bari, Dell'Accio, Vanlauwe, Eyckmans, Ilyas M. Khan, et al. 2006). Recent studies have shown proliferation up to passage 15 in tissue culture (heterogenous population) (Ball et al. 2011). Periosteal MSCs proliferate faster than BM MSCs at low seeding densities (5000 cells/cm^2) (Eyckmans, Lin & Chen 2012).
Differentiation	Apart from synovium, has the highest capacity for chondrogenic differentiation (Mochizuki et al. 2006). Well established osteogenic potential (Yoshimura et al. 2007). Shown to have high ALP levels at early time points, which is a marker for early osteoblast differentiation (Ito et al. 2008).	Also known to have chondrogenic differentiation as well as osteogenic differentiation (Mochizuki et al. 2006). Involved in endochondral ossification, which involves the production of cartilage. Used in cartilage repair, to cover defect site in matrix autologous chondrocyte transplantation surgeries (Gooding et al. 2006).
Immuno-regulation	By releasing factors can recruit macrophages and endothelial lineage cells (Chen et al. 2008). May be involved with switching off the inflammatory stage of fracture healing.	Not reported

SDF-1 - stromal cell derived factor-1, BM – bone marrow, BM MSC – BM mesenchymal stem cells, PD – population doubling

1.3 Engineering Periosteum Using a Biodegradable Barrier Membrane

A key objective of this project is the development of a biodegradable barrier membrane that can be used in surgery to wrap around CSBD sites. The membrane will need to allow for periosteal regrowth along the membrane and migration of periosteal cells on or through the material, which will depend on the membrane porosity. The barrier function of this membrane will act to prevent tissue ingrowth from 'outside' the defect site, this refers to fibroblastic infiltration from surrounding soft tissue which is thought to impede bone regeneration (Ogiso et al. 1991). Another advantage to this barrier is that muscle has also been seen to physically infiltrate bone defect sites, thus taking up room that is needed for bone regeneration (Schenk et al. 1997). This also allows for selective cellular repopulation of the defect area from only the periosteum and bone fracture sites, allowing for slower migrating osteogenic cells to repopulate the defect area (Froum, Cho & Pariente 2012). By creating this environment of a 'contained' defect site filled with autograft or 'loaded' bone scaffold also allows for MSCs within the autograft or loaded onto the scaffold (most likely via fresh BMA) to remain within the defect site. Without this membrane there is the potential for MSCs to be lost via diffusion, thus an increased concentration of MSCs will remain within the defect when a membrane is used.

1.3.1 Current Commercial Barrier Membranes

The creation of a so called 'barrier membrane' is not new, it originates from dental research where hard scaffolds combined with a barrier membrane cover jaw defects during tooth reconstruction (Naung, Shehata & Van Sickels 2019). Early investigations involved the use of a non-resorbable expanded polytetrafluoroethylene (e-PTFE) membrane to cover bone fenestrations within the jaw, whereby the use of the membrane proved to increase bone formation compared to control (Dahlin, Andersson & Linde 1991). This concept is a similar, but smaller scale concept to that of this Thesis, where a CSDB will be filled with grafting material and then wrapped in a barrier membrane. Current commercial membranes used are non-resorbable, usually

e-PTFE as previously described or resorbable made from collagen, either non-crosslinked or cross linked and aliphatic polyesters (Omar et al. 2019). This thesis will not investigate non-resorbable membranes as the aim of the project is to reduce the amount of surgeries needed for CSBD repair, thus making the use of a non-resorbable membrane redundant if it would then require another surgery for retrieval.

The most popular commercial membrane is BioGide® (Geistlich), a resorbable non-crosslinked bilayer membrane made from type I and III porcine skin collagen (Wang et al. 2016). It is placed with the compact, low porosity smooth layer facing outwards to the soft tissue, to prevent downgrowth of epithelial cells and the more porous spongy layer facing into the defect, allowing for bone regeneration. BioGide® in combination with BioOss® (deproteinised bovine bone mineral, Geistlich) was shown to improve the treatment of intrabony defects after a 2.5 year follow up (Irokawa et al. 2017). Another study showed that implants treated with BioGide® and an e-PTFE membrane (Goretex®) coverage had comparable implant survival over a 12-14 year follow up to implants with intact surrounding bone (Jung et al. 2013). Thus, BioGide® is a clinically proven membrane, that is approximately 440 µm thick and shows quick tissue integration and vascularisation, while remaining intact for 2-4 weeks *in vivo* (Willershausen et al. 2014; Rothamel et al. 2005).

Another bilayered non-crosslinked membrane is Tutodent® (Tutogen), made from bovine type I collagen, which is shown to maintain thickness *in vivo* for longer than BioGide® (16 weeks compared to 4 weeks) (Rothamel et al. 2005). However, Tutodent® is more compact (less porous) and therefore was more resistant to *in vivo* blood vessel invasion and showed potential for an inflammatory response during biodegradation (Rothamel et al. 2005; Siar et al. 2011).

BioMend® (Zimmer Dental) and Ossix® Plus (Datum Dental) are both bovine type I collagen membranes, crosslinked using glutaraldehyde or an enzymatic method, respectively. Compared to non-crosslinked membranes, these showed slower *in vivo* vascularisation and biodegradation, whereby the use of glutaraldehyde to crosslink could result in cytotoxic effects that reduce biocompatibility (Rothamel et al. 2005). Clinically, Ossix® Plus was shown to

be comparable to BioGide® for the treatment of dehiscence defects, despite differing degradation profiles, where Ossix® Plus maintains a barrier function for 4-6 months, suggestive that crosslinking with a native metabolite can prevent the potential for cytotoxicity (Lee et al. 2015).

The main drawback of a collagen membrane is their mechanical competency and relatively fast degradation, resulting in low space maintenance (Iviglia, Kargozar & Baino 2019). Thus, aliphatic polymers have been utilised to develop synthetic resorbable membranes, with tuneable degradation patterns. Guidor® (Sunstar Americas Inc) is a blended poly(lactic acid) and citric acid ester bilayer membrane, where there is internal space between the two layers allowing for tissue ingrowth. This membrane can be resorbed in 6-7 months, shows malleability which aids clinical handling as well as providing a barrier function (for approximately 6 weeks) that allows for guided bone regeneration (Lundgren et al. 1994; Wang et al. 2016).

The commercially available barrier membranes on the market are currently designed for dental applications, thus are not ‘tuned’ to the CSBD application that requires the membrane to be intact as a barrier for approximately 12 weeks. Collagen based membranes degrade quickly in vivo, this can be prolonged through crosslinking, however, the method of crosslinking can result in cytotoxicity. In comparison resorbable polymers have been developed to overcome rapid degradation times, however therefore risk resorbing too slowly.

The development and optimisation of the barrier membrane will be clinically led (Table 1.4). From conception, thought will be put into the suitability of the membrane as an ‘orthopaedic product’, with respect to handling and whether the membrane is scalable for larger bone defects (>10 cm long). Also, biocompatible materials must be used and a known degradation profile is needed, suggested by surgeons as being approximately 12 weeks. In addition to this, supporting periosteal regrowth whilst preventing cellular migration through the membrane is needed.

Periosteum can be thought of as a natural barrier membrane for bone, in addition to the cellular involvement of periosteum in fracture repair.

Table 1.4: Summary key characteristics and specification for the collagen based barrier membrane

Characteristic	Specification
Barrier Function	Act as a barrier to prevent soft tissue invasion of defect site
	Act as a 'containment' factor, prevent loss of MSCs from 'loaded' scaffold filling the defect site
Support Cell Growth	Allow for periosteal MSCs to migrate into membrane
	Support growth of periosteum from fracture sites
Suitability as Orthopaedic Product	Membrane must be suitable for handling during orthopaedic surgeries
	Must be scalable to be suitable for small and CSBD (defects larger than 20 mm in length)
Other Properties	Provide mild mechanical support to the defect area
	Degradation profile - must be intact for 12 weeks
	Must be biocompatible

Interestingly, recent descriptions of periosteum have eluded to it having the 'hallmarks of semipermeable epithelial barrier membranes', where samples of ovine periosteum have shown 'directional dependent' permeability (Evans et al. 2013). During homeostasis it has been suggested that periosteum may act as a barrier separating bone and muscle but upon trauma becomes more permeable due to increased pressure and flow rates, allowing for more communication between the two tissues (Evans et al. 2013).

A recent paper has shown periosteum to have an approximate thickness of 500 μm, however, this is known to be variable, depending on location and age of the patient (Evans, Chang & Knothe Tate 2013). Therefore, this project will investigate this further through samples of periosteum collected from orthopaedic patients. Histological analysis into collagen content, orientation and density will give basic information about periosteum that will be replicated in the structure of the biodegradable barrier membrane, this will be covered in Chapter 3.

1.3.2 Creation of the Biodegradable Barrier Membrane

As the main functions of the membrane require support of periosteal regrowth as well as a known *in vivo* degradation profile, manufacturing a barrier membrane based on collagen harnesses the bioresorbable nature of collagen as well as its known biomimetic advantages. Collagen type I is known to be important for the regulation of an osteoblastic phenotype that aids bone

regeneration (Shi, Kirk & Kahn 1996). Collagen brings an advantage over conventional polymer materials as it is biodegradable, where degradation rate is dependent on the degree to which collagen molecules are cross linked (Meyer, Baltzer & Schwikal 2010). Collagen is also biocompatible and can be purified *ex vivo* in order to present minimal antigenicity (Lynn, Yannas & Bonfield 2004). As a biological material, collagen also allows for cell attachment, proliferation and differentiation (Lee, Singla & Lee 2001).

There are 28 members of the collagen superfamily split into fibrillar or non-fibrillar types, collagen accounts for one-third of all protein in humans, making it the most abundant of all proteins (Ricard-Blum 2011). The majority of collagen in humans consists of fibre forming collagen types I, II and III, each of which form a particular interest in this thesis due to their involvement in bone regeneration, cartilage formation and presence in rat tail collagen (alongside collagen type I, which is the dominant collagen type), respectively (Karsdal 2016; Bell, Ivarsson & Merrill 1979). On a molecular scale, collagen displays great diversity in structure, the most common of which is the triple helix domain which dependent on collagen type can form 10-96% of the overall structure (Ricard-Blum 2011).

The collagen molecule is made up of three polypeptide α chains, which can all be identical (homotrimer) as with collagen type II, made up of three α_1(II) chains (denoted as) $[\alpha_1(II)]_3$ and collagen type III with three α_1(III) chains (denoted $[\alpha_1(III)]_3$. In contrast, collagen type I forms a heterotrimer, composed of two identical α_1(II) chains (denoted as $[\alpha_1(I)]_2$ and one α_2(I) chain. To take collagen type I as a fibril forming collagen example, the α chains, which are left-handed polyproline II helices, twist to form right handed triple helixes that are staggered and form supercoils around a central axis (Arafat et al. 2015). The triple helices, approximately 300 nm long, are formed of Gly-X-Y amino acid repeats, whereby X and Y are often proline and hydroxyproline, respectively (Ricard-Blum 2011; Varma, Orgel & Schieber 2016). Once extracellular, triple helices assemble to form fibrils, which then assemble into fibril bundles and fibres through combining with other collagen types or non-collagenous molecules, such as proteoglycans (Varma, Orgel & Schieber 2016).

Initially rat tail tendons will be used as the source of collagen, mostly containing collagen type I, as well as type III (Bell, Ivarsson & Merrill 1979). However, a long-term aim would be to use medical (GMP) grade collagen if this membrane were to be approved for clinical use. Isolation of rat tail collagen involves the four tendons found in the tail to be stripped and placed into 17.4 mM acetic acid for three days (50 mL per tail). Here, the supernatant will be centrifuged and freeze dried to obtain a source of collagen (Arafat et al. 2015). Importantly, this process of collagen extraction has been shown to maintain the helical structure of collagen, described above (Tronci, Russell & Wood 2013).

This prototype will be based on a synthetic membrane core, to provide mechanical stability, e.g. poly (ε-caprolactone) (PCL), will be blended with collagen as the biomimetic phase. A polymer, such as PCL is selected in light of its wide availability and fibre-forming properties, thus hopefully improving the ease of manufacture of collagen into a material, discussed in more detail in Chapter 5. Here, the aim is to develop a membrane with a porosity or pore sizes that will block cellular infiltration from outside of the defect site, while simultaneously allowing for periosteal MSC migration on the inside of the membrane (Table 1.4). It is hypothesised that the presence of collagen will allow for a cell homing functionality.

1.3.3 Manufacturing Process

Now that the material basis of the barrier membrane has been discussed it is important to consider the use of an appropriate manufacturing process. Nonwoven structures can be briefly described as fibres, filaments or chopped yarns that have been formed into webs by any process bar interlacing of these into a woven fabric (Turbak 1993; Mao 2016). Nonwoven manufacturing processes are well established and include: wet spinning, melt spinning and electrospinning; all with their own merits and pitfalls.

Wet spinning has been used in the textile industry in order to produce long fibres of polymers that can be used to make nonwoven materials. This process involves extrusion of a polymer solution, using a spinneret to form continuous filaments or fibres. As the name suggests, melt spinning or extrusion involves

heating a polymer solution to rapidly cool it following extrusion to form fibres, often used with polymers that can be melted. However, collagen would not withstand the high temperatures needed for this process so is not suitable (Isenberg & Wong 2006). Electrospinning has become a popular technique for collagen fibre manufacture for tissue engineering applications, which involves passing a voltage through a polymer solution and drawing charged threads to a grounding collector.

Wet spinning and electrospinning processes require solubilisation or dissolving of the polymer (collagen and PCL) in various solvents. However, certain solvents can denature the native collagen structure, resulting in structure instability even after cross linking (Jha et al. 2011; Yang et al. 2008). As the commercialisation of the developed membrane in this project is at the forefront of the design process, electrospinning, especially free surface electrospinning was chosen as manufacturing process, which will be described in more detail below.

1.3.3.1 Electrospinning

Electrospinning allows for the formation of nonwoven nanofiber webs and fabrics. A voltage is applied to a charged polymer solution, at a certain voltage electrostatic charges overcome the surface tension of a polymer droplet causing elongation into nano-fibres which are laid down on a grounded collector. There are many forms of electrospinning, but the two most common are ‘needle’ based and ‘free surface’ (needleless). Needle electrospinning consists of a spinneret (hollow metallic needle), connected to a syringe pump that injects the polymer spinning solution at a controllable rate and a voltage is applied to the spinneret. As the droplet emerges from the end of the needle it deforms into a conical shape (Taylor cone), due to effects of surface tension and electrostatic repulsion of surface charges. When the surface tension is overcome, a charged liquid jet extends from the Taylor cone, if using a solvent based system, this will evaporate leaving solidification of polymer fibres which are deposited onto a grounded collector (Uyar & Kny 2017). Free surface electrospinning relies on the same principle described for needle based electrospinning. However, instead of generating a droplet from the end of a needle, the polymer solution is either added to the end of a ‘spike’ electrode

or introduced to a rotating wire or metal-based cylindrical electrode, to which a voltage is applied (Lukas, Sarkar & Pokorny 2008). Multiple Taylor cones are formed on the surface of the chosen electrode rather than the tip of a needle, thus allowing many more electrospinning jets to be created at one time, enabling scalable membrane manufacture.

Fibre architecture can be tuned and controlled by different parameters involved in the electrospinning process. Changes to the spinning solution include solvent type, conductivity, polymer molecular weight and concentration. Changes to the electrospinning process include distance from collector, type of collector and voltage applied (DeFrates et al. 2018). Specific parameters to needle based electrospinning include – spinneret diameter and shape and rate of the syringe pump, whereas for free surface electrospinning the type of electrode used (spike or rotatory wire electrode) can be altered (DeFrates et al. 2018).

Unlike free surface electrospinning, there are drawbacks when using a needle based system, e.g. clogging of the needle with the polymer solution, which has knock-on effect by restricting continuous fibre production (Persano et al. 2013). To increase the yield of fibre deposition, multi-needle spinnerets have also been designed in addition to the previously described free surface electrospinning set up. The latter circumvents the issue of clogging of the needle and has an increased capacity for generating multiple electrospinning jets along the length of the wire electrode, apposed from the tip of a needle, allowing for larger polymer solution volumes to be electrospun. It was for this reason that free surface electrospinning was chosen as the manufacturing process of choice for the barrier membrane, to allow for scalable manufacture and industrial technology uptake for future commercialisation.

1.4 The Hybrid Graft – Bringing the Diamond Concept Together

This project looks to reinvent the current surgical strategies for CSBD repair through the concept of wrapping a large bone defect in a biodegradable barrier membrane to prevent soft tissue infiltration. This will be combined with filling the defect site with autograft or a synthetic bone scaffold loaded with patient's own MSCs, creating a 'hybrid graft'. This aims to increase the osteogenic regenerative potential at the defect site, therefore aiding bone healing of CSBDs.

The diamond concept (Figure 1.2) formed the basis of this idea. Whereby a source of osteogenic cells, either the current gold standard of BMA or potentially in the future periosteal tissue, is introduced to the defect site. This would be in combination with autograft or a synthetic bone scaffold, that will form a structure and environment mimicking bone, for MSCs to grow onto and repopulate. The biodegradable barrier membrane, to be developed as part of this project, can also be considered to be a scaffold as it will not only contain the defect site, but also to support periosteal regrowth from either fracture end.

Through the use of BMA or autograft, a natural supply of growth factors will be provided to the defect site, the presence of platelets allows for the potential of growth factors to be released that could enhance the local environment to encourage bone regeneration. Finally, there is potential that the loaded bone scaffold as a 'hard scaffold' could provide mechanical support to the area, however, the majority of mechanical support to the defect site is likely to come from external fixation or use of metal plates.

This project cannot cover all corners of this new surgical strategy, so will focus on the development of a new biodegradable barrier membrane to be wrapped around CSBDs. In addition, investigation into periosteal tissue to inform the development of said membrane, as well as a source of osteogenic cells in comparison to the gold standard BM MSCs.

1.5 Rationale for the Study

As current treatments for CSBD repair remain suboptimal, a new approach involving a regenerative medicine and tissue engineering could result in improved treatment outcomes. Here a 'hybrid graft' would combine autografting material or synthetic bone scaffold with a source of patients' MSCs. This 'MSC loaded' grafting material would be contained to the defect site by a biodegradable membrane which aims to mimic the periosteum as well as acting as a barrier to cellular infiltration.

1.5.1 Hypothesis

The combination of a biodegradable membrane with a commercially available bone scaffold or autograft material loaded with MSCs from periosteum or BM will enhance bone regeneration for CSBDs.

1.5.2 Project Aim

To ascertain whether periosteum derived MSCs are a desirable source of MSCs and if a biodegradable membrane can block cellular infiltration while supporting periosteal regrowth to enhance bone regeneration for CSBDs.

1.5.3 Objectives

The objectives of this work were to:

1. Investigate the architecture and cellular content of human and porcine periosteum.
2. Generate and characterise cultures for BM and periosteal MSCs.
3. Develop and manufacture biodegradable membranes to use as a containment factor for CSBD repair.
4. Investigate the interactions between MSCs and the biodegradable membranes in short and long term culture.

Chapter 2: General Materials and Methodology

The following methodology is a collation of general methods used in more than one chapter. Detailed descriptions of the research methodology carried out for each part of the investigation is detailed in each chapter. A comprehensive list of reagents, details of solutions used, lab consumables and equipment can be found throughout Appendix 1.

2.1 Human Tissue Collection and Ethics

Human samples of periosteum, BMA (aspirated from the iliac crest) and iliac crest trabecular bone were obtained from patients being treated at the Trauma Orthopaedic Unit at Leeds General Infirmary, Leeds, UK for the surgical repair of lower limb CSBDs or fracture non-union. Informed written consent was given by all patients and ethical approval was granted by the National Research Ethics Committee – Leeds East, with ethical approval number 06/Q1206/127 (See Appendix 5).

Periosteum was harvested by an operating surgeon from the femur, near to the fracture site. Tissue was taken using a scalpel and collected in sterile saline, samples collected were approximately 20 mm^2 in size and 0.3 g in weight. BMA was harvested as part of the patients' standard care, whereby as part of the procedure BMAC was used for bone defect reconstruction. Donor matched BM was aspirated from the iliac crest using a flushed trocar with 1000 U/mL solution of sodium heparin, to prevent clotting and collected in sterile ethylenediaminetetraacetic acid (EDTA) blood tubes. Volumes collected ranged from 4 mL to 20 mL. Samples were stored at 4°C and processed within 24 hours. Additionally, iliac crest bone was taken if the patient was undergoing autograft procurement and collected in sterile saline.

2.2 Processing Bone Marrow and Periosteum Samples

Tubes of BMA were pooled and any existing clots were removed through a 70 µm cell strainer. Nucleated cells (NCC) were isolated via ammonium chloride (Stem Cell Technologies) induced red blood cell (RBC) lysis. Briefly, 4 mL of ammonium chloride solution was added per 1 mL of BMA and incubated for

10 mins on ice. Cells were concentrated via centrifugation (650 g (g force), 5 mins) and re-suspended in 20 mL (dependent on the size of cell pellet) of Dulbecco's Modified Eagle Medium (DMEM), supplemented with 10% fetal calf serum (FCS) and 1% Penicillin Streptomycin (PS) (referred to hereafter as supplemented DMEM) and counted as described below (Section 2.3.1).

Periosteum samples were washed with sterile phosphate buffered saline (PBS), weighed in a sterile universal container using a balance (Mettler Toledo), macerated and digested in collagenase (600 U/mL, Stem Cell Technologies) at a ratio of 0.1 g of tissue to 0.5 mL of collagenase, for 4 h, incubated at 37°C, 5% CO_2, with agitation every 30 mins. After digestion, the cell suspension was passed through a 70 µm cell strainer to further break up the tissue and remove large debris. The cell suspension was concentrated via centrifugation (650 g, 5 mins), the cell pellet was re-suspended in supplemented DMEM and counted as described below (Section 2.3.1).

2.3 Tissue Culture Techniques

2.3.1 Cell Counting

Cells in solution were counted with the use of a haemocytometer. A 10 µL volume of the cell suspension was added to 10 µL of trypan blue (dye for dead cells). A haemocytometer was loaded (via pipette) with 10 µL of the cell suspension and live cells were counted under a light microscope. To calculate the total number of cells in a solution, the mean number of cells counted in four squares, of the haemocytometer, was counted and applied to Equation 2.1.

Equation 2.1: Calculating total number of cells in a known suspension volume

Total cells = average counted cells x 2 (trypan dilution) x cell suspension volume in mL x (1×10^4)

2.3.2 Cell Passaging and Trypsinisation

Following initial processing (Section 2.2), NCCs obtained from BMA and periosteal tissue were plated into 25 cm^2 tissue culture treated flasks at a

density of 2-4 x 10^5 per cm^2 (5-10 x 10^6 per flask) and 1 x 10^4 per cm^2 (2.5 x 10^5 per flask), respectively. Samples were incubated at 37°C, 5% CO_2, with 5 mL of StemMACS MSC expansion medium (supplemented with 1% PS, herein referred to as StemMACS media).

After 48 h the culture media was removed and flasks were washed once with 5 mL of sterile PBS to remove non adherent cells, 5 mL of fresh StemMACS media was then added. Biweekly half media changes were carried out for two weeks or until 60-80% confluent, as seen under light microscopy.

At this point flasks were trypsinised and the culture media removed, flasks were washed once with sterile PBS and 1 mL of trypsin (0.1%) was added and incubated at 37°C, 5% CO_2 for 4-8 mins. Once cells were seen to detach from the bottom of the flask, the cell solution was transferred to a sterile centrifuge tube and with the addition of 8 mL supplemented DMEM, where the presence of FCS inactivated the trypsin.

The cell suspension was centrifuged (650 g, 5 mins), the supernatant removed and re-suspended in 1 mL supplemented DMEM to be counted (Section 2.3.1). Cells were reseeded into new 25 cm^2 flasks at cell densities of 1.25 x 10^5 for periosteum (Eyckmans, Lin & Chen 2012) and 2.5 x 10^5 for BM (Fossett & Khan 2012), this was repeated until at least passage 6 was reached.

2.3.3 Freezing of Cells

At initial cell isolation and at each cell passage, excess cells that were not carried forward to the next passage were frozen for use in future experiments. Cell suspensions to be frozen were centrifuged (650 g, 5 mins) and the supernatant removed. The cell pellet was re-suspended in freezing media (10% dimethylsulfoxide (DMSO), 90% FCS), kept on ice, at a ratio of 1 mL per 5-20 x 10^6 NCCs (freshly isolated samples) or 1-10 x 10^5 cells (passaged BM or periosteum samples), dependent on the cell yield of the sample. Cells in 1 mL freezing media solution were transferred to cryovials, placed in a freezing container and stored at -80°C. After two days, cryovials were transferred to liquid nitrogen tanks for long term storage.

2.3.4 Thawing Cells

When needed for future experiments (carried out in Chapter 4 and Chapter 6), frozen cells were thawed and recovered in tissue culture. Cryovials were retrieved from liquid nitrogen tanks, on dry ice and thawed in a water bath (37°C) and slowly pipetted into a separate falcon tube of pre-warmed (37°C) supplemented DMEM. The cell suspension was centrifuged (400 g, 5 mins) and re-suspended in 1 mL supplemented DMEM. Cells were counted (Section 2.3.1) and seeded into 25 cm^2 flasks (Section 2.3.2).

Chapter 3: Characterisation of Periosteum as a Stem Cell Source and a Biomaterial

Periosteum is the focus of this thesis in more ways than one, firstly as a new potential cellular source of MSCs to aid bone regeneration during CSBD repair (covered in Chapter 4). Secondly, from a biomaterial perspective as the tissue we aim to emulate when developing a barrier membrane for the surgical treatment of CSBD (Chapter 5). Therefore, this chapter will cover what is known of the architecture of periosteum from a cellular and materials perspective.

3.1 Introduction

Periosteum covers the outer layer of most bones, except intra-articular surfaces and is made up of two main layers, the bone lining cambium layer and the outer fibrous layer. The cambium layer is thought to become thinner and more tightly attached onto the underlying bone, with age (Malizos & Papatheodorou 2005). It is highly cellular, and contains MSCs, pre-osteoblastic cells and osteoblasts (Colnot 2009). However, the collagen within this layer is highly aligned along the direction of bone growth (Foolen et al. 2008). In comparison, the fibrous layer has low cellularity and mostly consists of organised collagen fibres of random orientation (Chang & Knothe Tate 2012). Attachment onto the underlying bone is achieved by Sharpey's Fibres, which act as collagen based anchors, thought to be continuations of periosteum collagen fibres that become encapsulated in cortical lamellae, thus making periosteum hard to remove (Malizos & Papatheodorou 2005). Periosteum is highly vascularised, which decreases with age, providing the blood supply to cortical bone. The fibrous layer is thought to be the most vascularised area of periosteum, and nerve fibres travel along blood vessels through the cortex and cambium layer (Dwek 2010).

During childhood, the cambium layer is at its thickest, contributing to appositional bone growth (Bisseret et al. 2015). However, when entering into adulthood, periosteum thins, becomes less active, loses elasticity and attaches onto cortical bone more tightly (Bisseret et al. 2015). The periosteum

works in conjunction to the endosteum (lining the medullary cavity of long bones), compensating for endosteum resorption to maintain bone strength and cortical bone thickness. Thus, as periosteum becomes less active in replacing cortical thickness with age and endosteum remains active, this can result in thinning of cortical bone (Roberts et al. 2015).

Conversely, following trauma or infection, the periosteum reactivates and is seen to thicken in response (Colnot 2009). Periosteum is considered to be anisotropic as a material, thus subject to strain stiffening and therefore acts to cushion the bone upon impact, absorbing energy (Knothe Tate et al. 2016). In addition, periosteum is under tension when attached to underlying bone, achieved through the attachment of the aforementioned Sharpey's Fibres, which during trauma can become damaged, affecting the intrinsic stress of periosteum during injury (Knothe Tate et al. 2016). The permeability of periosteum is found to be directional, whereby following trauma, permeability is significantly higher in the direction of bone to muscle, thus allowing for increased communication between bone and muscle upon injury (Evans et al. 2013).

3.1.1 Current Periosteum Histology Literature

The architecture of periosteum as a source of bone regenerating cells as well as a material lining the bone is particularly interesting. Histology is used to develop understanding of certain tissues through various staining regimes that can unveil the tissue architecture. In addition, immunohistochemistry can be used to target particular cell types or molecules using antibodies to further reveal the presence and locations of certain cells within the tissue. Although of great importance, periosteum is under-researched histologically, especially with respect to human samples, due to difficulties obtaining said samples. Therefore, the current literature surrounding animal and human periosteum was evaluated to ascertain the current knowledge of periosteum histology.

3.1.1.1 Animal Periosteum Histology

Various animal sources of periosteum have been researched, including rat, rabbit, ovine, porcine and canine samples. Femoral periosteum of 7 week, 7

month and 2 year old rats were compared for thickness, cellularity and the presence of certain cell types. The cambium layer and fibrous layer of diaphyseal periosteum were seen to be similar thicknesses (6-27 μm and 7-22 μm, respectively), reducing with age and in comparison to matched metaphyseal periosteum (Fan, Crawford & Xiao 2008). In addition, not only did cellularity reduce with age, it was seen to be reduced from the cambium to the fibrous layer (Fan, Crawford & Xiao 2008). Differences were seen in the distribution of cell type between age groups, where there was a loss of stem cells (Stro1+, MSC marker) but an increase in osteoclasts (tartrate-resistant acid phosphatase (TRAP) positive) with age from 7 weeks to 2 years, macrophage levels remained high irrespective of age (Fan, Crawford & Xiao 2008). In a follow up publication, Fan et al. (2010) compared 7-month old femoral periosteum of osteoporotic rats, having undergone ovariectomies with age matched controls. Osteoporotic rats were found to have similar cambium layer thickness (11-12 μm) but a significantly thinner fibrous layer (10 μm compared to 17 μm) of periosteum compared to control. TRAP+ cells were not found within the fibrous layer, but TRAP+ cells and von Willebrand Factor (marker for endothelial cells) stained blood vessels were found in significantly higher numbers in the cambium layer of osteoporotic periosteum, which could lead to increased osteoclastic and bone resorption activity (Fan et al. 2010).

These papers back up the earlier findings of Hosoya et al. (2005), that found when imaging rat femoral bone, the cambium layer was seen to be particularly thin at a couple of cells thick and Filgueira (2004) that imaged osteoclasts (TRAP stained) within the cambium layer of rat tibial periosteum. In addition, a recent paper carried out histology on 10 week old rat femoral periosteum, whereby the majority of cells were seen to be proliferating, blood vessels were located mainly within the outer fibrous layer and in agreement with previous papers, Stro1+ and alkaline phosphatase (ALP) positive cells were located in the cambium layer (Henrich et al. 2016).

Periosteal reaction following fracture was shown with a rat femoral fracture model. Here, regenerating gene I (Reg I), postulated to be involved in cell proliferation and differentiation and therefore tissue regeneration, was not expressed during health in the periosteum. Levels were increased post

fracture, however Reg I expression was not seen within bone, BM or muscle prior to or post fracture (Tohma et al. 2017). As IL-7 was shown to induce further Reg I expression, this suggests a specific IL-7/Reg pathway in the response of periosteum to fracture repair. In addition to this, thickening and increased cellularity of the periosteum overlying newly formed bone was seen visually following fracture repair at 4 weeks (Tohma et al. 2017).

Collagen was shown to be the main component of rabbit tibial periosteum following histological analysis and quantification, where collagen made up 100 µg per mg (10%, dry weight), compared to 4-5 µg per mg (0.4-0.5%, dry weight) for glycosaminoglycans (GAG) (K. Chen et al. 2015). Under polarised light, no difference was seen between the cambium and fibrous layer, however, using SEM the collagen fibres were shown to be randomly aligned, with the potential to being more randomly aligned throughout the cambium (K. Chen et al. 2015).

The effect of maintaining the *in vivo* tension of ovine femoral periosteum whilst imaging collagen and the embedded cells was investigated by Yu et al. (2017). Shrinkage of periosteal tissue was seen upon removal from the femur, as previously reported by Evans, Chang & Knothe Tate (2013), this also resulted in increased crimping of collagen within the fibrous layer and an increase in the roundness of nuclei within the cambium layer, whereby the change in the nucleus shape could have an effect on periosteal quiescence (Yu et al. 2017).

As previously mentioned, the permeability of ovine periosteum was found to be directional. During homeostasis, where periosteum is under pre-tension, it acts as a barrier to allow equal but low bidirectional levels of molecular communication between bone and muscle (Evans et al. 2013). However, following trauma or injury increased bidirectional permeability is seen, but more so from bone to muscle, potentially allowing for pressure release from the bone due to fluid build-up (Evans et al. 2013).

Al-Qtaitat, Shore & Aaron (2010) characterised the periosteum of young (1 year) and old (3 years) porcine mandibles, showing that even though cortical thickness increased from 4.9 to 9.3 mm, periosteum became significantly thinner (180 µm to 129 µm) with age (Table 3.1). This reduction in periosteum

Table 3.1: Summary of periosteum characteristics from different animal species.
N – normal, OP – osteoporotic, NR – not reported. Mean shown ± standard deviation, unless stated otherwise.

Species	Location	Sample Age	Periosteum Thickness (μm)	Cambium Layer Thickness (μm)	Fibrous Layer Thickness (μm)	Reference
Rat	Femur	7 weeks 7 months 2 years	~49 ~31 ~13	27 13 6	22 18 7	(Fan, Crawford & Xiao 2008)
Rat	Femur	7 months – N 7 months – OP	~29 ~21	12 11	17 10	(Fan et al. 2010)
Rat	Femur	10 weeks	47	26	21	(Henrich et al. 2016)
Rabbit	Tibia	6 months	~290	NR	NR	(K. Chen et al. 2015)
Ovine	Femur Tibia	3-4 years 2 years 3 years	160 ± 23 417 ± 12 371 ± 16	NR	NR	(Evans et al. 2013)
Porcine	Mandible Zygomatic Arch Mandible	Unknown	300 ± 100 1200 ± 300 500 ± 100	NR	NR	(Popowics, Zhu & Herring 2002)
Porcine	Mandible	1 year 3 years	161 ± 34 120 ± 7	NR	NR	(Al-Qtaitat, Shore & Aaron 2010)
Canine	Palate Skull	2-3 months	70-150 (range)	10-20 (range) 20-80 (range)	20-80 (range)	(Squier, Ghoneim & Kremenak 1990)

thickness with age is in agreement with 'skeletally mature' ovine studies (>2 years) that showed reductions from 417 μm (2 years) to 371 μm (3 years) in the tibia (Table 3.1), it should also be noted that tibial periosteum was found to be thicker than femoral periosteum, which was 146 μm (Evans et al. 2013).

The ultrastructure of canine periosteum from the palate and skull revealed three 'zones', the thinnest of the zones lined bone (zone 1), at 10-20 μm thick it consisted of mainly osteoblasts (Squier, Ghoneim & Kremenak 1990). Vascularisation was reported to be greatest at 'zone 2' (middle layer) (Squier, Ghoneim & Kremenak 1990), in agreement with rat periosteum, where most blood vessels were also found to run through the fibrous layer (Henrich et al. 2016). Zone 3, representing the fibrous layer, where collagen was the majority, in addition elastin was found in very low levels (1 ± 1 mm^3/cm^3) within palate periosteum, but not in skull periosteum (Squier, Ghoneim & Kremenak 1990).

To summarise the histological evidence of periosteum from various species, it was found that periosteum thickens with increase in the size of the animal investigated. Whereby, the thickness of rat periosteum is 13-49 μm, compared to porcine, which ranges from 120-1200 μm (Table 3.1). When examined, periosteum thickness reduces with age, but also varies in thickness dependent on the type of bone, irrespective of species (Table 3.1). Additionally, although the literature usually points to the cambium layer being thinner than the fibrous layer, the papers that describe said differences use rat periosteum, which is known to be particularly thin, here the two layers appear to be of similar thicknesses. Periosteum also is made out of collagen for the majority, with evidence of low level elastin content within the fibrous layer of certain canine bone types.

3.1.1.2 Human Periosteum Histology

Allen, Hock & Burr (2004) showed images of a thin layer of periosteum covering a midshaft human femur, whereby a thin but highly cellular layer of cambium in contact with cortical bone could be seen, with the outer fibrous layer showing low cellularity and staining for collagen. As a continuance, Allen & Burr (2005) compared human femoral neck and midshaft periosteum, which

again showed that the fibrous layer appears to have a higher collagen content than the cambium. In addition, it was shown that mid shaft periosteum contained lower levels of mineralisation and higher cambium coverage of the cortical bone in comparison to femoral neck periosteum (Allen & Burr 2005). Suggestive that even though the cambium layer was found to cover 40-80% of the total bone surface, there is donor variance and the whole circumference of the femur may not have a visibly distinguishable cambium layer.

Seminal papers on human periosteum histology that many review articles and journal articles refer to are the two previously described papers – Allen, Hock & Burr (2004) and Allen & Burr (2005). Inconsistencies in interpretation of these papers can be picked up within the periosteum literature, many articles use these papers as their reference for human periosteum containing collagen, as well as elastin. However, neither paper mentions elastin or stains for elastin. Thus, many review articles appear to be perpetuating information about the elastin content of human periosteum without any substantial evidence of this in the literature. So far the only evidence of elastin within periosteum was found by Squier, Ghoneim & Kremenak (1990), at very low levels (1 ± 1 mm^3/cm^3) in canine palate.

Cuthbert et al. (2013) compared the histological differences of long bone periosteum to induced membrane, taken from patients undergoing a second stage Masquelet technique orthopaedic surgery. Here, two distinct layers were seen, containing CD31+ (Platelet endothelial cell adhesion molecule-1) blood vessels associated with CD146+ (melanoma cell adhesion molecule) pericytes and CD271+ (Low-affinity Nerve Growth Factor Receptor) MSCs. In addition, BMP-2 was found at the luminal edge of blood vessels, along with VEGF and stromal cell derived factor-1 (SDF-1) (Cuthbert et al. 2013).

Another study took samples of human tibial periosteum and used fluorescent imaging to show the increased cellular density within the cambium layer (Frey et al. 2013). Although cells within the fibrous layer were found to be fibroblastic, the cambium layer contained a heterogenous cell population (Frey et al. 2013). The majority of which were stromal cells (Stro-1+), which increased in frequency closer to the cortical bone border, followed by osteoblastic lineage cells (Core-binding factor alpha 1/runt-related

Table 3.2: Summary of human periosteum characteristics.
NR – not reported. Means shown ± standard deviation.

Location	Sample Age	Periosteum Thickness (μm)	Cambium Layer (μm)	Fibrous Layer (μm)	Reference
Femur (*Cadaver*)	81	~119	~41	~78	Allen, Hock & Burr (2004)
Femur Shaft Femur Neck (*Cadaver*)	81	~104 ~258	~52 ~82	~52 ~176	Allen & Burr (2005)
Various Sources* (*Resected*)	18-80	860 (468–1019)	129	387	(Cuthbert et al. 2013)
Tibia (*Resected*)	18-62	NR	~53	NR	Frey et al. (2013)
Femur Tibia (*Cadaver or Amputee)*	68-99	~100 ~101	23 ± 2.5 29 ± 3.1	77 ± 8.8 72 ± 5.1	Moore, Milz & Knothe Tate (2014)
Fibular (*NR*)	NR	NR	~62	NR	(Roberts et al. 2015)

*Femur, Tibia, Radius or Ulna

factor 2 (RUNX2)), as well as osteoclasts (TRAP+) and immature dendritic cells (major histocompatibility complex (MHC) Class II+). Gene expression confirmed the presence of these cell types, as well as the presence of chondroblastic lineage through SOX9 (SRY (sex determining region Y)-box 9) detection (Frey et al. 2013). These findings of osteoclastic lineage cells close to cortical bone are in agreement with Fan et al. (2010), using rat samples.

Moore, Milz & Knothe Tate (2014) showed no correlation between the thickness of cambium or fibrous layer thickness or cellularity with age and body mass, from samples of tibial and femoral periosteum. However, the cambium layer of the bending axis of the tibia was found to be significantly thicker and more cellular than corresponding donor matched periosteum from the femur, showing the differences in periosteum taken from different sites (Moore, Milz & Knothe Tate 2014).

The majority of the literature surrounding human periosteum has been carried out on elderly samples (>60 years), with only three studies looking at younger

and middle aged samples. However, as previously mentioned, human periosteum is difficult to obtain, sourced from cadavers and patients undergoing orthopaedic surgery, both are likely to be elderly. Therefore, this leaves a good opportunity for human periosteum of all ages to be looked into in detail. Table 3.2 summarises the characteristics of human periosteum, there appears to be reasonable agreement that the cambium layer is 40-80 μm thick and that the fibrous layer is the same or thicker at 50-180 μm. However, evidence for the elastin content within adult human periosteum is lacking.

3.1.2 Chapter Aims and Objectives

The aims of this chapter are to analyse human periosteum samples, surgically removed using a scalpel from patients undergoing orthopaedic surgeries and find common features to further understand the architecture and stem cell presence in this tissue. In addition, a porcine sample of periosteum will be obtained, still attached onto the underlying bone to compare to the human samples, which will be stripped from the bone.

3.1.2.1 Objectives

The objectives of this work were to:

1. To assess porcine periosteum intact to bone to further characterise the differences between the cambium and fibrous layer and to act as control tissue to compare to human periosteum.
2. To assess the architecture of clinically relevant samples of human periosteum.
3. Identify the presence of the cambium layer and ascertain the thickness of human periosteum.
4. Characterise and image the collagen and elastin content of human periosteum.
5. Quantify the vascularity of human periosteum as a measure of porosity to inform the biomaterial design process.
6. To detect the presence of stem cells within human periosteum, surgically removed from underlying bone.

3.2 Specific Materials and Methodology

In order to investigate the architecture of periosteum to further understand the tissue as a 'biomaterial' as well as a source of stem cells various histological methods have been employed to investigate this. As the BM within iliac crest bone is a known location for MSCs, this was used as control tissue for human periosteum antibody staining for MSCs using immunohistochemistry (Section 3.2.4.4). Porcine femoral samples were also obtained to compare the periosteum architecture to human samples.

3.2.1 Sample Collection and Processing

Human periosteum and iliac crest samples, collected from surgery (Section 2.1), were washed in sterile PBS to remove excess blood and clots. Samples were fixed in 3.75% formaldehyde for at least a week and then used for histological analysis. Details of all donors used within this chapter can be found in Table 3.3.

Table 3.3: Patient sample details of periosteum and bone.
None – sample harvested during first orthopaedic surgery. M – male, F – female, NU – non-union, IMN – intermedullary nailing, NR – not reported. * patient also donated iliac crest bone sample.

	Donor Gender, Age (Years)	Harvested From	Time Since Injury (Weeks)	Number of Previous Surgeries	Surgery
Periosteum	M, 23	Femur	57	2	NU, IMN nailing
	M, 35	Humerus	108	None	NU, bone grafting with MSCs
	M, 47	Femur	19	None	NU, RIA
	M, 61*	Iliac Crest	0.5	None	Unknown
	F, 74	Femur	49	2	NU, IMN, bone graft
	F, 80	Femur	17	2	Masquelet,
Bone	F, 39	Iliac Crest	NR	NR	NR
	M, 49	Iliac Crest	NR	NR	NR
	M, 61	Iliac Crest	0.5	None	Unknown

A porcine hindleg was obtained by the Faculty of Biological Sciences, University of Leeds for research already being carried out, where the femur and surrounding muscle was going to be waste. The porcine leg was from the food chain and therefore was not subject to requiring ethical approval. A cross section of femoral bone with surrounding muscle attached was taken using a scalpel and bone saw, washed in PBS and fixed for a month in 3.75% formaldehyde.

3.2.2 Fixation and Decalcification of Samples

Iliac crest bone and porcine femoral samples were decalcified using an EDTA solution, to chelate calcium from the samples. Iliac crest bone samples were weighed and placed in 0.5 M EDTA, at a volume 40x weight of sample (1 g to 40 mL). EDTA solutions were changed daily for the first week and then weekly. Samples were subjected to X-Ray (0.129 mA, 70 kV (kilovolts)) (Carestream Dental CS2200) until complete decalcification was confirmed (see Figure 3.1). Due to the size and weight of the porcine samples, EDTA changes were made weekly for the first month and then monthly for the following year. X-Rays were taken monthly until complete decalcification was seen.

3.2.3 Tissue Processing and Cutting of Samples

Periosteum, decalcified iliac crest bone and decalcified porcine bone were processed (see Appendix 2 for full protocol) and embedded in paraffin wax, this was carried out by Mike Shires, Leeds Institute of Molecular Medicine, University of Leeds. 5 µm slices were taken using a Leica RM2255 Microtome, placed onto SuperFrost Plus histology slides and dried using a hot plate set to 45°C. Mike Shires also cut the slides for the porcine bone samples.

3.2.4 Histological Staining

Excess wax was removed and the slides were hydrated. Dewaxing was carried out using four changes of xylene (3 mins each). Afterwards slides were subjected to gradual hydration of four changes of 100% ethanol (EtOH) (3 mins each), followed by changes in 75% EtOH (3 mins), 50% EtOH (3 mins), 25% EtOH (3 min) and finally tap water (1 min).

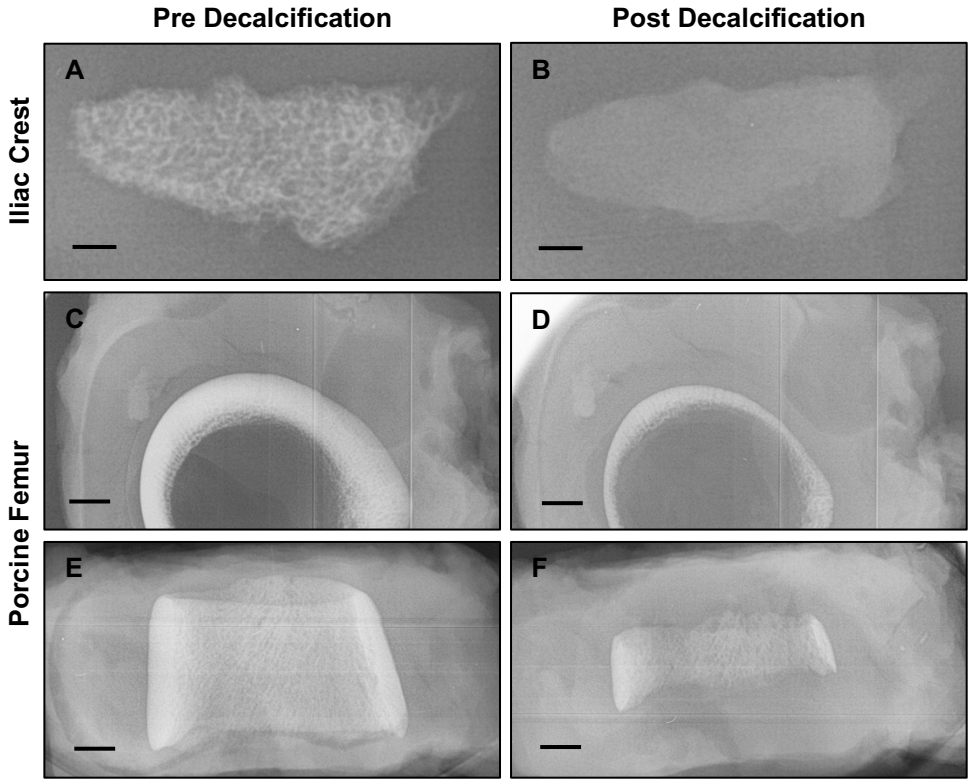

Figure 3.1: Confirmation of decalcification of iliac crest and porcine bone using X-Ray. A-B) Pre and post decalcification X-Rays of human iliac crest. **C-F)** Pre and mid decalcification images of porcine femoral bone, taken in cross section (C-D) and longitudinally (E-F). Pre decalcification X-Ray images (left column), compared to decalcified images (right column). Loss of 'white' in the sample, showing removal of mineralisation of the samples. Black scale bar represents 0.25 mm (A-B) and 0.5 mm (C-F).

Once hydrated, iliac crest bone samples were stained for Haematoxylin and Eosin (H&E). Periosteum samples were stained for H&E, Picro Sirius Red (PSR), Masson's Trichrome and Miller's Elastin. Periosteum and iliac crest bone samples were also stained using immunohistochemistry, with the antibodies CD271 and CD73 (ecto-5′-nucleotidase), to locate and compare MSC location throughout the two tissue sources. Porcine bone samples were stained with H&E, PSR and Masson's Trichrome.

3.2.4.1 Haematoxylin and Eosin

H&E staining was used to look at general tissue architecture, as blood vessels and nuclei locations could be easily visualised. H&E dyes nuclei (haematoxylin) and cytoplasm or ECM structures (eosin). Sections were stained for 2 mins in haematoxylin, rinsed in Scott's Tap Water to remove excess dye and then placed in eosin for 2 mins.

3.2.4.2 Picro Sirius Red and Miller's Elastin

As collagen is known to be a large component of periosteum, histological stains specific for collagen were used to investigate the density and orientation of collagen fibres throughout human periosteum. PSR stains for collagen and nuclei (Wiegert's haematoxylin). Slices were stained in haematoxylin for 8 mins followed by a 10 min wash in tap water. Sections were then placed in PSR for 1 h before being washed in acidified water (0.5% glacial acetic acid, in dH_2O).

Another component of periosteum is thought to be elastin, which can be stained for using Miller's Elastin. This is a modification of the PSR stain, whereby slides were stained with potassium permanganate (5 mins), rinsed with dH_2O, decolourised with oxalic acid (1 min), and washed again with several changes of dH_2O. Slides are then stained with Millers Elastin for 3 hours, rinsed with 95% alcohol, followed by dH_2O and then counterstained with PSR (however for 10 mins) following the above protocol.

3.2.4.3 Masson's Trichrome

In addition to PSR, Masson's Trichrome was used to also look at the collagen content of periosteum. As this also stains muscle and erythrocytes this allowed for identification of muscle fibres and blood clots in the samples. Masson's Trichrome stains for collagen (methyl blue), nuclei (Wiegert's haematoxylin) and muscle, cytoplasm and erythrocytes (Ponceau Fuchsin). Sections were dyed in Wiegert's haematoxylin for 10 mins, washed in tap water and differentiated (removal of excess dye) using 1% acid alcohol (0.1% HCl, in 70% EtOH) and rinsed in tap water again. Ponceau Fuchsin was used to stain for 5 mins and then sections were washed in dH_2O, followed by 15 min in 1% phosphotungstic acid to differentiate samples. Sections were immediately transferred to methyl blue for 1 min and then rinsed in dH_2O.

3.2.4.4 Immunohistochemistry

The presence and location of CD271 positive MSCs and CD73 (another candidate MSC marker) throughout human periosteum was investigated using immunohistochemistry (Table 3.4). Hydrated slides were subjected to antigen

Table 3.4: Antibodies used for Immunohistochemistry

Antibody	Clone, Manufacturer	Antigen Retrieval Method	Working Concentration
CD73 – ecto-5′-nucleotidase	1D7, Novus Biologicals	10 mM/L Citrate Buffer	1:200
CD271 – Low-affinity Nerve Growth Factor Receptor	NGFRS, Abcam	10 mM/L Citrate Buffer	1:200

retrieval (see Table 3.4), by being heated at full power in a 900 W microwave for 10 mins in citrate buffer (10 mM/L, pH 6.0). After cooling for a further 10 mins, slides were transferred to tap water for 5 mins. Dual enzyme blocking solution (Dako EnVision kit, Dako) was used to block endogenous peroxidase activity followed by a 1 min and 5 min Tris Buffered Saline (TBS) wash.

Non-specific antibody binding activity was blocked by applying antibody diluent for 30 min at room temperature (RT), this was also used as a negative control. After removal of the antibody diluent, the primary antibody, diluted in antibody diluent (see Table 3.4 for concentrations) was incubated with the slide for 1 h, at RT. Sections were washed in TBS for 1 min, followed by a 5 min TBS wash. Polymer-HRP (horseradish peroxidase) (Dako EnVision kit) was then applied to the sections for 30 min at RT. Slides were washed in TBS for 1 min, followed by a 5 min TBS wash. To visualise the stain, DAB (3,3'diaminobenzidine) reagent (Dako EnVision kit) was incubated with the slides for 10 mins at RT. Slides were washed in running tap water for 10 mins and counter stained with haematoxylin for 5 mins.

3.2.4.5 Dehydration and Mounting of Slides

Post-staining slides were dehydrated in 100% EtOH for 11 mins and cleared with xylene (9 mins). Coverslips were placed over slides, adhered using distyrene plasticizer xylene mounting medium (DPX) and left to dry overnight.

3.2.5 Imaging of Slides

Slides were scanned using the University of Leeds Virtual Pathology Service, to give an online digital image of the slides at increasing magnification from x1 to x20. Where needed, images were taken at x40 magnification using a Zeiss Microscope (AxioCam MRc5). PSR slides were also imaged under polarised light, using a Zeiss Microscope (AxioCam MRc5) with a polariser fitted. All periosteum images were taken with the following parameters to allow for consistency – 0.65 gamma, 30.5% light (LED Transmitted Light) and 700 ms exposure. The images were processed using Zeiss Zen Pro software.

3.2.6 Semi Quantitative Scoring of Tissue Architecture

In order to form a design rationale for the barrier membrane (developed in Chapter 5), semi quantitative analysis of porcine and human periosteum was carried out, with respect to blood vessel content and periosteum thickness. Cross sections of porcine femurs were imaged and quantified using digital scans, through the software – ImageScope. Measurements every 200 μm were taken for the thickness of periosteum, cambium and cortical bone around the circumference of the femur (See Figure 3.2, insert), and exported into Excel for analysis. In addition, the surface area of periosteum was measured, as was the surface area and diameter of blood vessels found within the periosteum to allow for the frequency of blood vessels to be analysed.

Human periosteum samples were also analysed, whereby 30 measurements for each donor were taken for periosteum and cambium thickness. Blood vessel frequency, periosteum surface area and blood vessel lumen surface area and diameter was also quantified.

3.2.7 Statistical Analysis

Where necessary statistical analysis was carried out, comparison of porcine and human periosteum values was done using a non-parametric Mann Whitney test ($P<0.05$). Comparison of human periosteum donors was carried out using a non-parametric Kruskal-Wallis multiple comparisons test ($P<0.05$). Data presented as mean ± standard deviation.

3.3 Results

3.3.1 Porcine Femoral Histology

In order to investigate the architecture of periosteum a cross section of mid shaft porcine femur, with full surrounding muscle attachment was obtained (approximately 4 months old). Due to the size of the sample (40 x 55 mm) being too large to fit onto a histology slide, the porcine femur was cut in half longitudinally and processed separately. Cross sectional slides were stained with H&E and scanned to allow for analysis to be carried out (Figure 3.2A). Measurements of the thickness of the cortex, periosteum and cambium layer of the periosteum were taken every 200 μm along the circumference of the femur (Figure 3.2B).

Cortical thickness of the porcine femur ranged from 1.9–7.9 mm (mean 3.9 ± 0.1 mm) and was shown to increase and decrease along the circumference of the femur (Figure 3.2A-B). The overall periosteal thickness was also measured (both the fibrous and cambium layer), taken to start at the cortical-periosteal interface (Figure 3.2A, insert) towards the outer edge of the periosteum. The trajectory was taken from a central point, through the centre of the bone cross section. Here, the mean periosteal thickness was measured at 524 ± 533 μm, however as with cortical thickness, periosteal thickness was found to vary dependent on anatomical position along the circumference of the femur and was therefore split into 4 separate regions as depicted in Figure 3.2A-B. In addition to this, periosteum and cambium layer thickness was not found to correlate with cortical bone thickness, with low r^2 values of 0.28 and 0.27, respectively.

Region 1 (blue – position 0-15), showed periosteal thickness to reduce sharply from 2310 μm (the thickest measured area of periosteum) to 689 μm (Figure 3.2A & C) and cortical thickness increased from 6329 μm to 7915 μm (the thickest measured area of cortex). This was followed by region 2 (green - position 16-45), where thickness remained constant at a mean of 887 ± 146 μm, with a linear drop in cortical thickness from 7580 μm to 2852 μm (Figure 3.2A & C). Region 3 (yellow – position 46-60) saw periosteal thickness quickly increase to 1641 μm and then immediately reduce down to 177 μm,

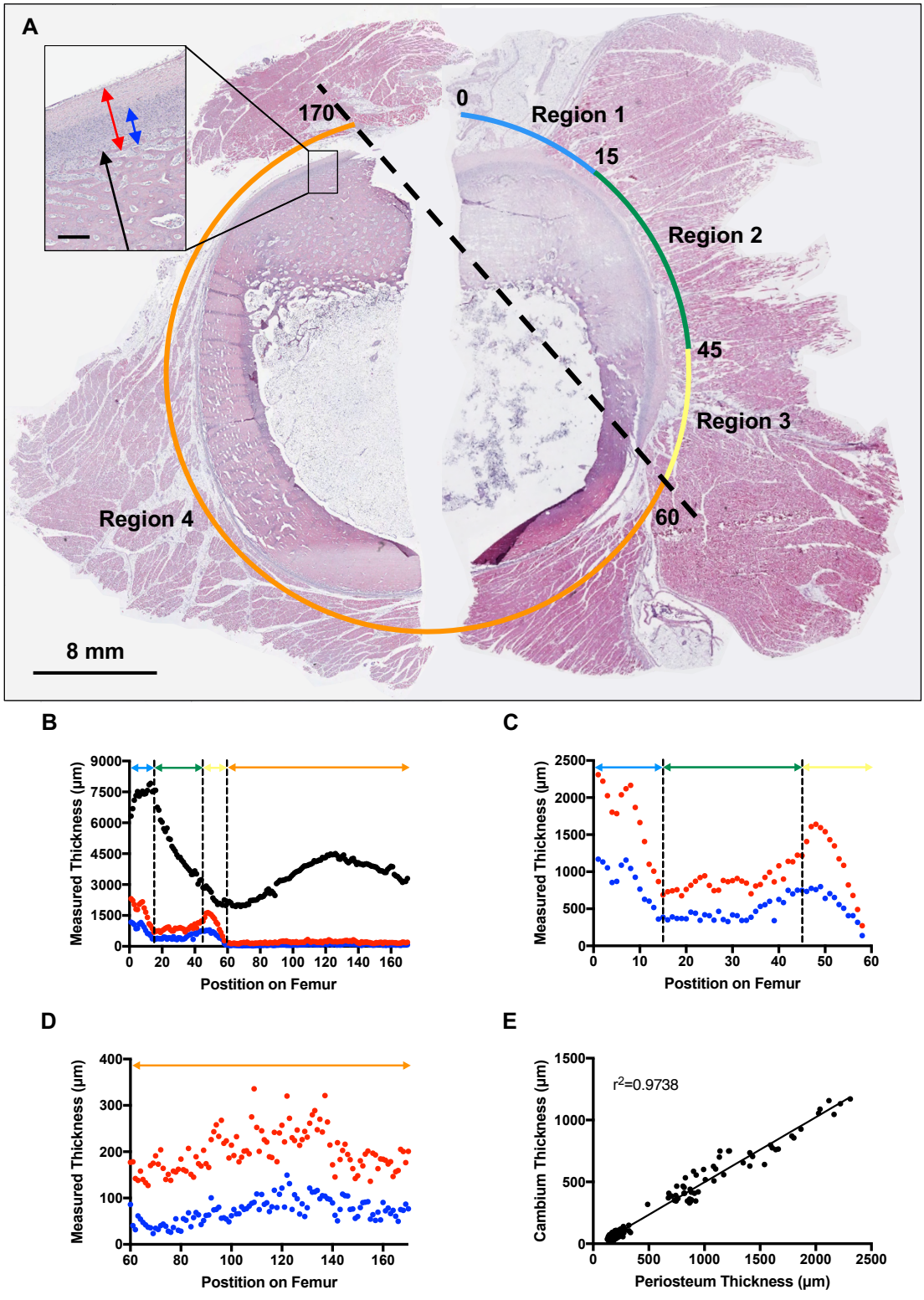

Figure 3.2: Cross sectional histological imaging of porcine mid shaft femur, with intact muscles to show periosteum thickness throughout the circumference of the femur. A) Light microscope gross image stained with H&E, annotated to show areas of consistent periosteum thickness (orange and green) and increasing or decreasing periosteum thickness (blue and yellow). Insert, exemplar measurements of cortex (black), periosteum (red)

and cambium (blue) thickness. **B)** The thickness of the femur cortex, periosteum and the cambium layer of the periosteum was quantified every 200 µm around the circumference of the femur. **C-D)** The thickness of the periosteum and the cambium layer (as in B) around the circumference of the porcine femur for regions 1-3 (C) and region 4 (D). **E)** Correlation between periosteum and cambium thickness. Black – cortex, red - periosteum and blue – cambium. Scale bar of insert – 400 µm.

Table 3.5: Summary of cross-sectional cortical bone, periosteum and cambium thicknesses around the circumference of a mid-shaft porcine femur. Colours and regions refer to that of Figure 3.2, R – region. Values reported as mean ± standard deviation. * Percentage cambium makes up of overall periosteum thickness, $ Percentage the periosteum makes up of overall cortical and periosteum thickness.

Position on Femur	Cortex Thickness (µm)	Periosteum Thickness (µm)	Cambium Thickness (µm)	Cambium: Periosteum* (%)	Periosteum: Cortex$ (%)
All (R1-4) (0-170)	3883 ± 1482	524 ± 533	247 ± 284	41 ± 11	13 ± 13
R1-3 (0-60)	4726 ± 2002	1119 ± 505	568 ± 261	51 ± 7	27 ± 15
R1 (0-15)	7361 ± 406	1671 ± 530	837 ± 280	50 ± 4	23 ± 8
R2 (16-45)	4596 ± 1221	887 ± 146	465 ± 136	52 ± 9	21 ± 9
R3 (46-60)	2351 ± 344	1031 ± 547	505 ± 255	50 ± 6	42 ± 20
R4 (61-170)	3423 ± 795	200 ± 44	73 ± 26	36 ± 9	6 ± 1

here cortical thickness was also reducing from 2932 µm to 1985 µm (Figure 3.2A & C).

Region 4 (orange 61-170) accounts for the majority of the rest of the femur circumference, where the thickness of the periosteum remained constant at a mean thickness of 200 ± 44 µm despite changes of cortical thickness throughout this region, with a mean of 3423 ± 795 µm (Figure 3.2A-D).

The periosteum is made up of two distinct layers (Figure 3.2A, insert), the cambium (inner layer in contact with cortical bone) and fibrous layer (outer layer, next to the musculature). When looking at the 'consistent thickness' areas of periosteum (regions 2 and 4) the cambium layer made up 52 ± 9% (465 ± 136 µm) and 36 ± 9% (73 ± 26 µm) of the overall periosteum thickness, respectively. In the areas of variable periosteum thickness (regions 1 and 3) the cambium layer was seen to make up a similar percentage of the overall

thickness as region 2 at 50 ± 4% (837 ± 280 μm) and 50 ± 6% (505 ± 255 μm) respectively. When linear regression was carried out on periosteum thickness against cambium layer thickness a r^2 value of 0.97 was seen, showing high correlation between the two values (Figure 3.2E).

Areas of 'thin' periosteum from region 4 (Figure 3.3) and areas of 'thicker' periosteum from region 1-3 (Figure 3.3), stained with H&E, Masson's Trichrome and PSR were investigated to compare the architecture of periosteum throughout the circumference of the femur. Periosteum was found to be in tight connection with the underlying cortical bone (Figure 3.3A-G), apart from in one area at the transition from region 3 to 4 (Figure 3.2A) where the periosteum had detached (Figure 3.3C & N) during the histology process. Close to the outer edge of the periosteum, skeletal muscle was clearly imaged from flattened nuclei surrounding distinctive muscle bundles (Figure 3.3A, B & E). Porcine periosteum showed two distinct layers, the inner cambium layer was clearly more cellular (Figure 3.3D), whilst the outer fibrous layer was less cellular but showed higher levels of staining for collagen (Figure 3.3E-G).

Masson's Trichrome is a stain used to distinguish between collagen and muscle, whereby collagen typically stains blue, and muscle, cytoplasm and erythrocytes stain red. The fibrous layer was stained blue by Masson's Trichrome, whereas the cambium layer was stained purple, due to a combination of lower collagen levels and increased cellularity, thus more cytoplasm (Figure 3.3B & E). This was also found with PSR, an anionic dye that increases collagen's natural birefringence under polarised light as well as staining collagen red under light microscopy. As with Masson's Trichrome, the cambium layer stained lighter than the fibrous layer, the difference of which was particularly stark under polarised light where the fibrous layer showed increased birefringence (Figure 3.3C & F-G).

When 'thicker' areas of periosteum were stained (Figure 3.3H-N), a similar architecture was seen, however, the bilayer nature of periosteum was more pronounced, further showing the differing thicker collagen fibrils throughout the fibrous layer and the increased cellularity of the cambium layer.

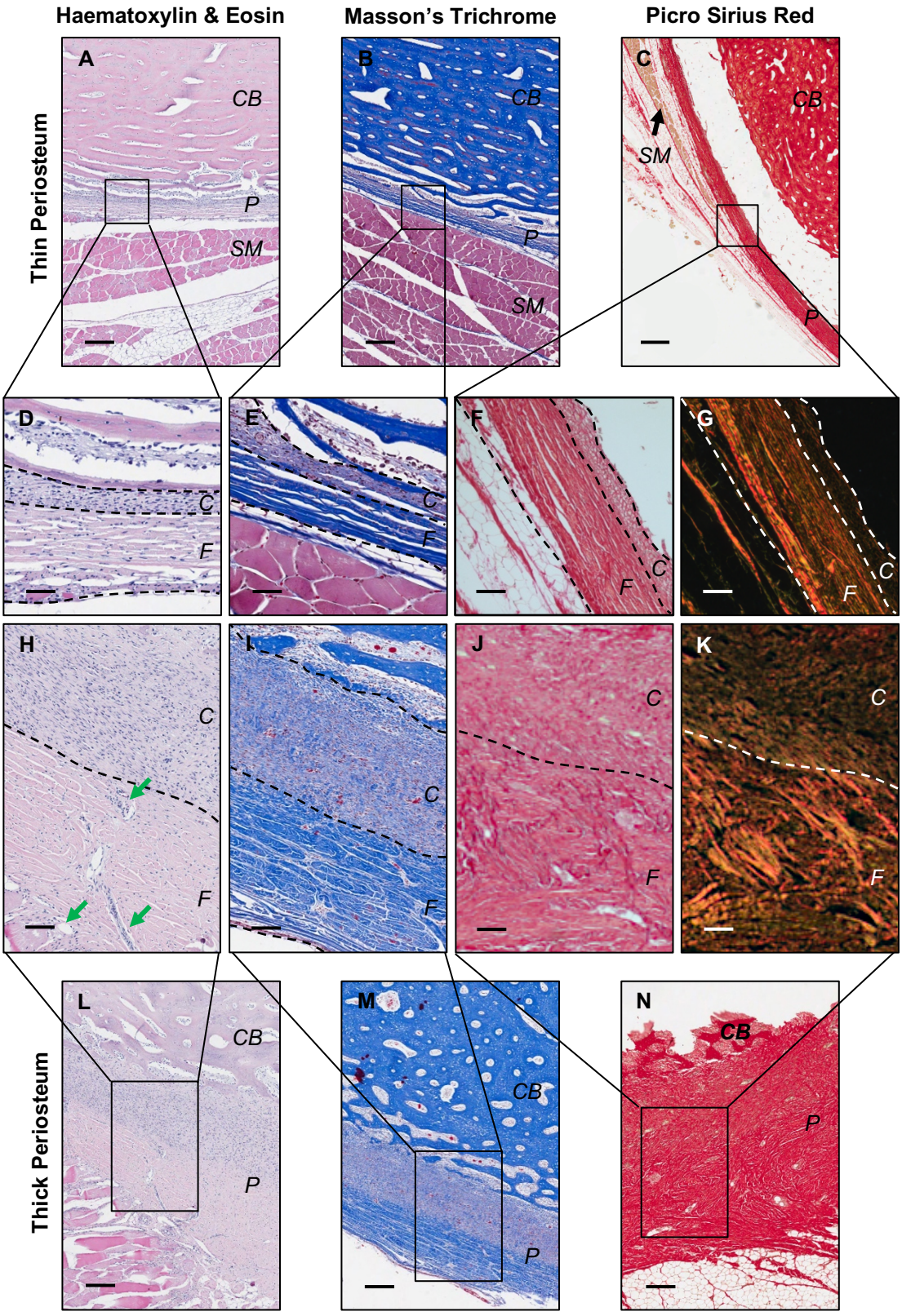

Figure 3.3: Histological imaging of porcine femoral periosteum. Showing areas of 'thin' (A-G) and 'thick' (H-N) periosteum from region 4 and region 1-3, respectively. A, L) H&E staining for an overview of periosteum architecture and cellularity at x4 mag, with magnified region at x20 mag (D, H). B, M) Masson's Trichrome staining for collagen and skeletal muscle, at x4 mag, with magnified region at x20 mag (E, I). C, N) Picro Sirius Red staining for collagen

at x4 mag, with a magnified region at x20 mag imaged using light microscopy (F, J) and with polarised light (G, K). Scale bars represent 250 μm (A-C, L-N) and 50 μm (D-G). Annotations: *CB* – cortical bone, P – periosteum, *SM* – skeletal muscle, *C* – cambium layer of periosteum, *F* – fibrous layer of periosteum and green arrows – blood vessels.

In summary, periosteum thickness was found to be very variable around the circumference of porcine bone, shown by a ten-fold difference in the thinnest and thickest areas. Therefore, this should be kept in mind with the human samples, that are only going to be a 'snap shot' and potentially not representative of the whole bone. Also, the thickness of periosteum does not correlate to cortical bone thickness, thus cannot be used to predict periosteum thickness. However, cambium layer thickness correlates highly with periosteum thickness. The distinction between the two periosteum layers was most apparent for thicker areas of periosteum.

3.3.2 Human Periosteal Histology

Six human periosteum samples were obtained from patients undergoing orthopaedic surgeries related to fracture repair, of these samples 4 were from the femur and the other two were from the humerus (Male, 35) and iliac crest (Male, 61) (Table 3.3). A scalpel was used to separate the periosteum sample from the underlying bone and this method is known to leave the cambium attached to the bone (Brownlow et al. 2000). The donors ranged from 23 to 80 years old in age, with 4 male and 2 female samples (Figure 3.4). All samples were stained with H&E, Masson's Trichrome and PSR and then certain samples were taken forward for immunohistochemical staining for locating MSCs within the periosteum.

3.3.2.1 Overall Characteristics and Stem Cell Location

Common characteristics were noted between samples, all were highly vascular, which was to be expected as periosteum is known to be a highly vascularised tissue (Simpson 1985) and four samples had 'muscle-like' areas and three samples had 'tendon-like' areas. The cambium layer was confirmed for certain on one sample, due to the periosteum being removed with a layer of underlying bone, enabling for the cambium layer to be located. Potential areas of cambium were also located on two other samples and compared to

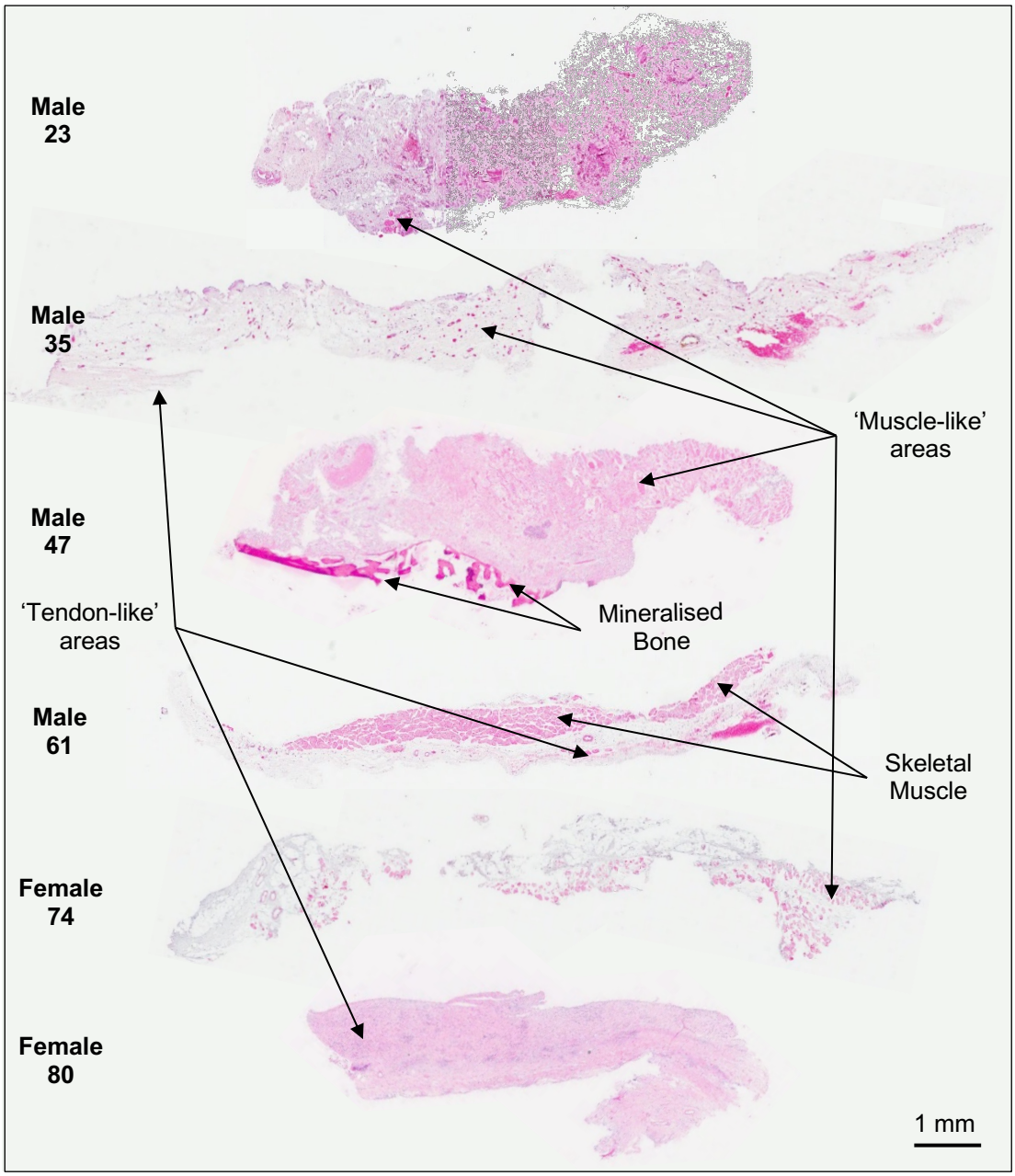

Figure 3.4: Gross light microscopy images of human periosteum samples taken from patients undergoing orthopaedic surgeries, stained with H&E. Six samples were collected ranging from 23 to 80 in age, harvested from multiple bone types, femur (Male, 23, Male 47, Female, 74 and Female, 80), humerus (Male, 35) and iliac crest (Male, 61).

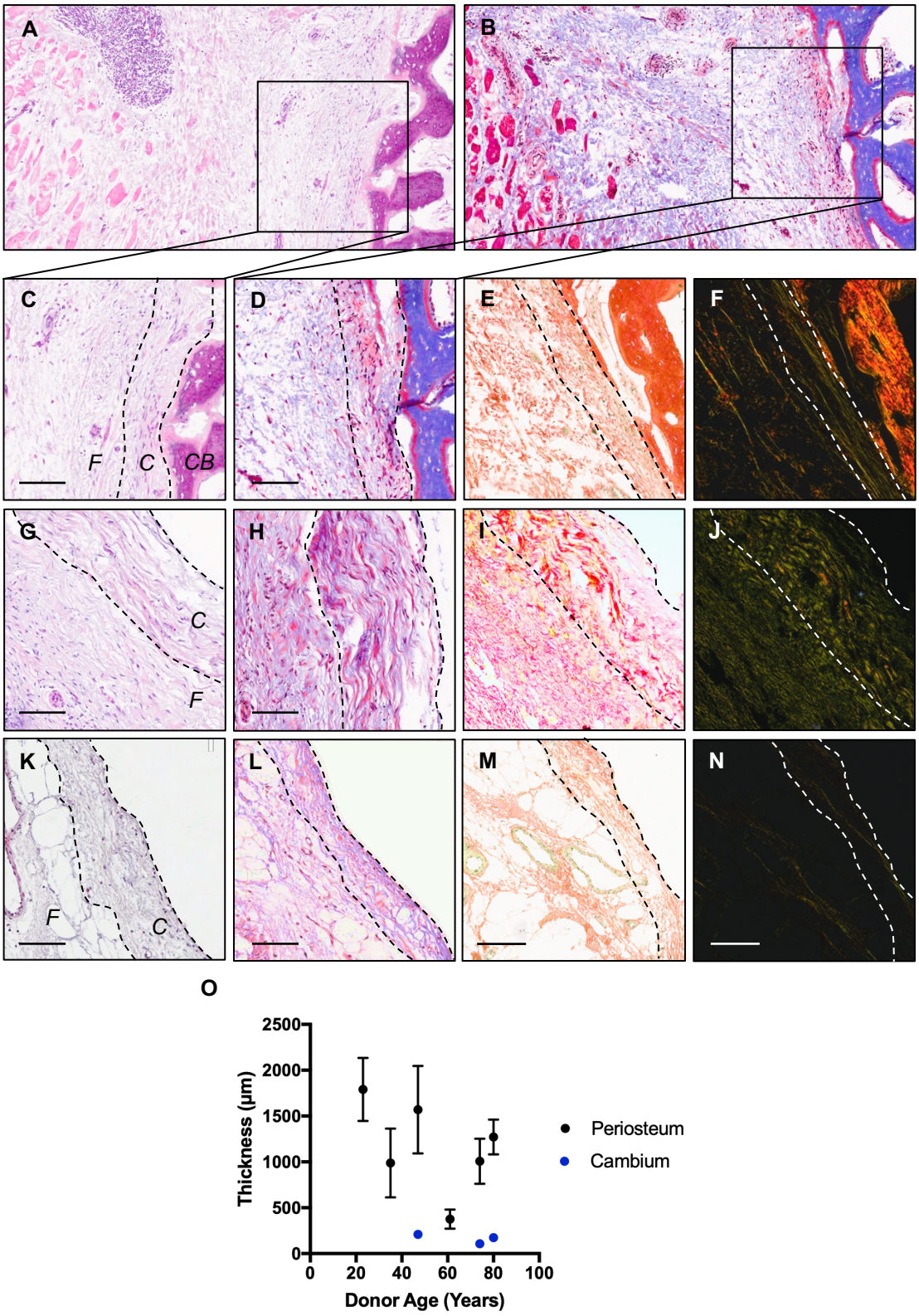

Figure 3.5: Areas of the human periosteum cambium layer. Slides were stained with H&E (A, C, G & K), Masson's Trichrome (B, D, H & L) and Picro Sirius Red (E-F, I-J and M-N), imaged under light microscopy and polarised light. **A-F)** Periosteum shown still attached onto underlying cortical bone, sample was not decalcified. Increased cellularity was seen of a thin layer in close contact with cortical bone. **G-N)** Two more samples of periosteum with potential areas of the cambium layer. **O)** Periosteal thickness was quantified

for all samples, as well as the cambium thickness when present (30 measurements taken per donor). Each row represents a different donor, row 1 & 2 – Male, 47 (femur), row 3 – Female, 80 (femur) and row 4 – Female, 74 (femur). Mean ± SEM shown. Scale bar represents 100 μm. Arrows and dotted lines, *C* = cambium, *F* = fibrous and *CB* – cortical bone.

the confirmed cambium layer sample, however, no cambium layer was seen in the remaining three samples (Figure 3.5).

The donor, Male, 47 was a periosteum sample with confirmed intact cambium layer. As can be seen, there was a thin layer next to the bone which is highly cellular (Figure 3.5A-F). After Masson's Trichrome and PSR staining, differences in collagen organisation can be seen between the bone lining cambium layer and the outer fibrous layer. The cambium layer shows higher staining for cytoplasm, appearing as yellow staining, however, under polarised light the collagen fibres appear thin. Even though differences were apparent between the fibrous and cambium layer, it did not follow the distinct differences seen with the porcine samples, where the fibrous layer was clearly a highly organised collagen structure, this difference, could be species dependent, due to trauma or age, whereby periosteum loses structure with increasing age.

All periosteum samples were measured for overall periosteum thickness as well as cambium thickness, where appropriate (Figure 3.5O). Here, a slight reduction in periosteum thickness with age was seen, where the mean thickness ranged from 377 – 1790 μm and the cambium layer was measured as 210 ± 6 μm (Male, 47), 108 ± 8 μm (Female, 74) and 174 ± 2 μm (Female, 80) (Figure 3.5O). It should be noted that two of the values were slightly lower than the others, and these samples were also the non-femur samples, taken from the humerus (Male, 35) and iliac crest (Male, 61). Also, the three cambium layer samples were all taken from the femur, but potentially at different anatomical locations along the femur. However, due to the variability seen in the porcine samples around the bone circumference and the fact that there are differences in age and location along the bone circumference, it is difficult to find strong conclusions on cambium thickness.

As previously mentioned, the other two samples that showed potential areas of cambium layer (Female, 80 and Female, 74) did not also contain the

underlying bone, thus were not able to be fully confirmed as the cambium layer. However, there were similar characteristics, with respect to differing birefringence following PSR staining compared to the surrounding tissue, (Figure 3.5J & N). The confirmed cambium layer (Male, 47) also showed there was increased birefringence within this layer and a wavy collagen structure, also differing to the surrounding tissue (Figure 3.5G-N). This differs from what was seen in the porcine samples, whereby the greatest birefringence was seen throughout the fibrous layer, rather than the cambium, this difference could be attributed to species differences as well as that porcine sample was adolescent and therefore the periosteum is still contributing to appositional growth and considered ‘active’ compared to ‘inactive’ periosteum during adulthood.

Immunohistochemistry was carried out on human periosteum samples, (Male, 23 and Male, 47 (shown), Figure 3.6) and compared to control iliac crest bone samples (Female, 39 (shown), Male, 49 and Male, 61, Figure 3.6). CD271 staining showed positivity throughout the periosteum, with the majority of staining within the fibrous layer, however there was evidence of CD271 staining within the cambium and in both cases, located surrounding blood vessels (Figure 3.6A & H). Control iliac crest bone staining of CD271 showed typical positivity within the BM, again surrounding blood vessels (Figure 3.6D). Slides were also stained with CD73, where again staining was shown located to the blood vessels for periosteum samples (Figure 3.6B). CD73 staining of the iliac crest bone was found on osteocytes within their lacunae (Figure 3.6E, black arrow), on cells lining the bone, assumed to be osteoblasts (Figure 3.6E, red arrow) and present within the BM (Figure 3.6E). There was a tendency for overstaining with CD73 at the 1:200 antibody concentration, therefore, if this was repeated again a lower concentration would be used, 1:500. Negative control, antibody diluent slides, showed an absence of staining, as to be expected (Figure 3.6C & F).

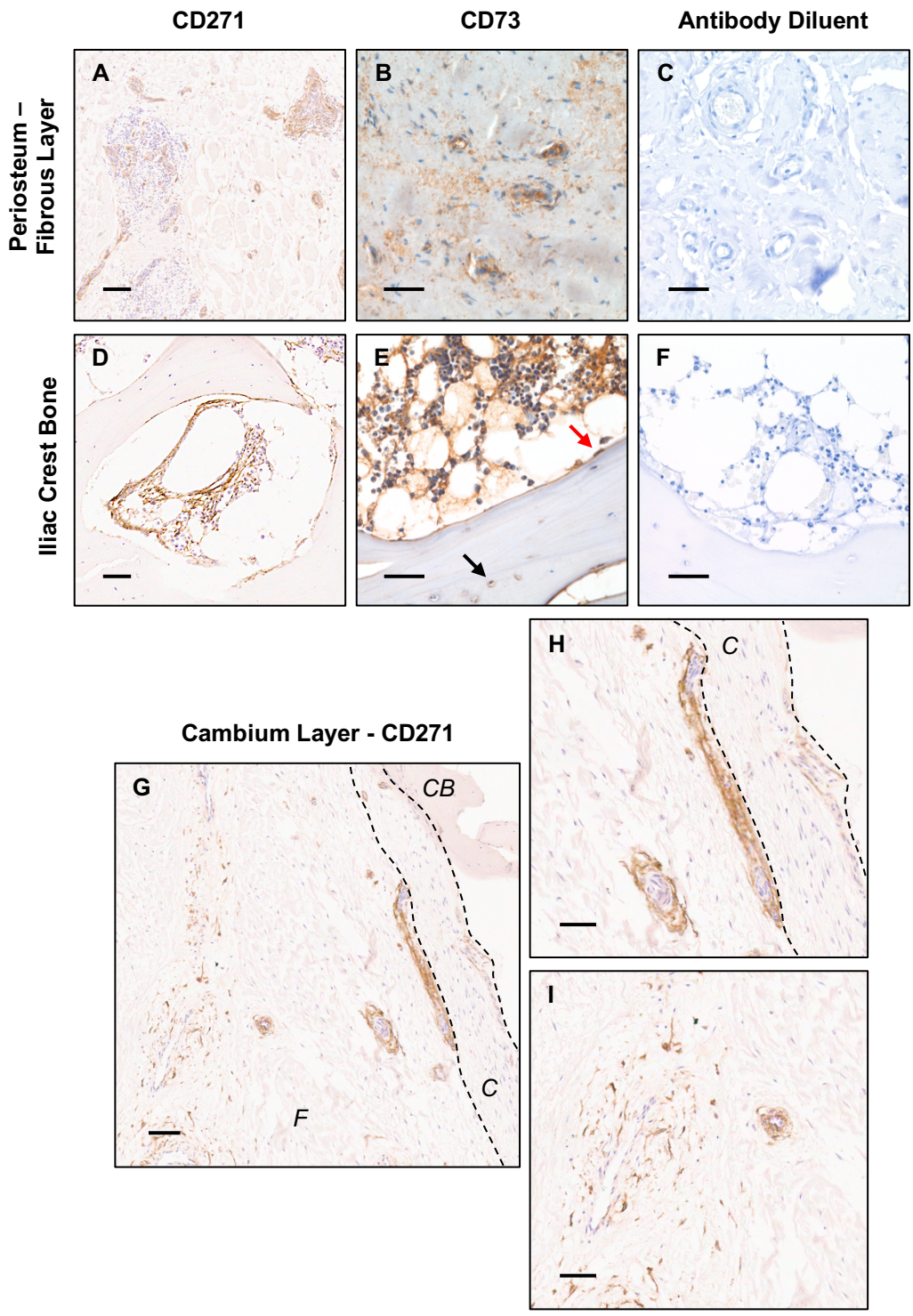

Figure 3.6: Immunohistochemistry for candidate MSC markers on periosteum and iliac crest bone. A-C) Fibrous layer of periosteum, **D-F)** iliac crest bone marrow and **G-I)** cambium layer of periosteum were stained with CD271 (A, D, H-I), CD73 (B, E) and a negative control of staining with antibody diluent (C, F). Femoral periosteum – Male, 47, iliac crest bone – Female, 39. *C* – cambium, *F* – fibrous and *CB* – cortical bone. Black arrow – osteocyte and red arrow – osteoblast. Scale bars represent 100 µm (A-F) and 50 µm (G-I).

3.3.2.2 Periosteum as a Biomaterial

As the main component of periosteum is known to be collagen (Chang & Knothe Tate 2012), the structure and organisation of collagen was assessed between samples to highlight differences (Figure 3.7). It was shown under polarised light that there is a distinct loss of birefringence with age, when looking at the fibrous layer of periosteum (Figure 3.7, right column). The youngest patient (Male, 23) shows highly organised collagen structure, with high birefringence, showing up as red or yellow under polarised light (Figure 3.7A-B), which reduces to yellow or green for donor Male, 35 (Figure 3.7C-D) and further still for donors Male, 47 and Female, 74, whereby the birefringence of the collagen is hardly visible under the sample microscopy settings (Figure 3.7E-H). It should also be noted that birefringence of the periosteum samples was not related to time since fracture (Table 3.3), even though periosteum is known to react by thickening and loosening as a response to fracture, it could have also been possible that birefringence of the samples was related to this.

The literature points to periosteum containing elastin, however, it was found that the original research in this area showed very low levels of elastin and not in every source of canine periosteum. Therefore, human samples were stained with Miller's Elastin to investigate this further. Of the six samples only two showed evidence of elastin fibres within the periosteal tissue, contained to the fibrous layer (Figure 3.8A-D). Of note both of these donors were the youngest, Male, 23 (Figure 3.8A-B) and Male, 35 (Figure 3.8C-D), however, conclusions on an age related link cannot be made due to the low number of samples tested. In addition, another two donors showed elastin staining surrounding blood vessels, in the older two donors that were tested, Male, 61 (Figure 3.8E) and Female, 80 (Figure 3.8F). These two donors showed no evidence of elastin within the periosteum. It should also be noted that an area of elastin staining of Male, 35 was in close location to a blood vessel also (Black arrow, Figure 3.8D).

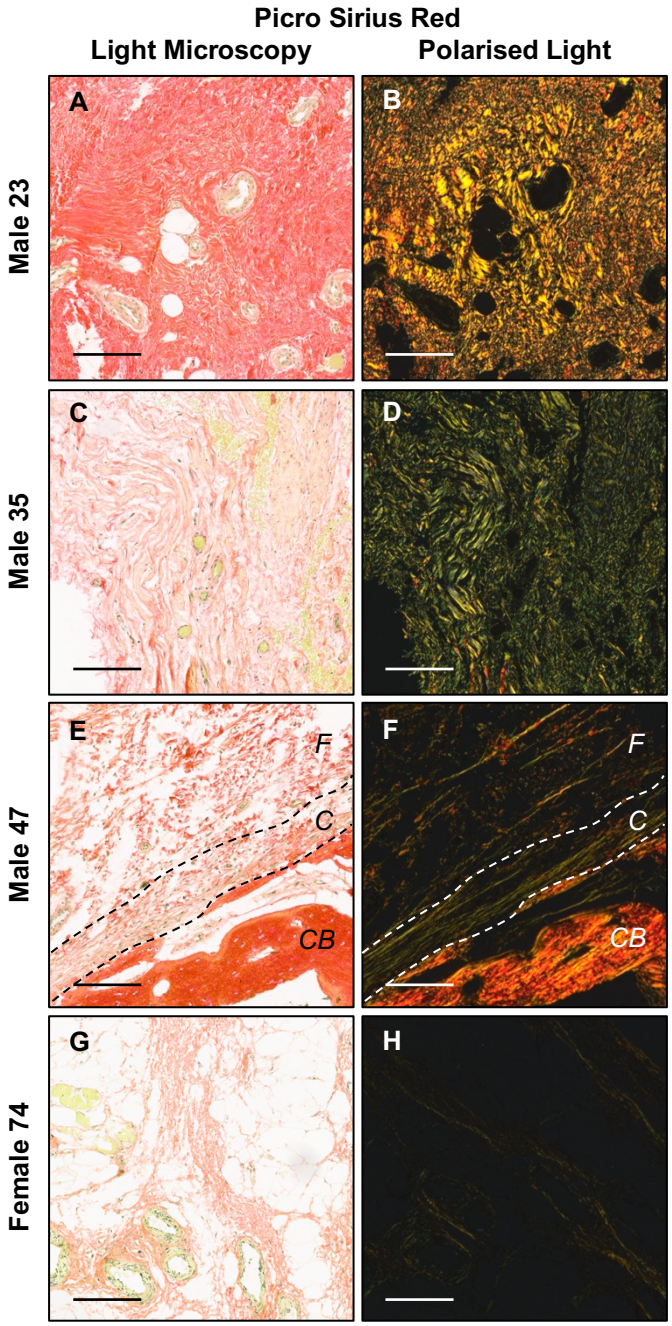

Figure 3.7: Changes in collagen staining with age of the human periosteum fibrous layer. Periosteum samples were stained with Picro Sirius Red and imaged with light microscopy (left column) and polarised light (right column). **A-H)** Changes in the birefringence of the collagen fibres could be seen with age, whereby highly organized collagen shows as red or yellow under polarised light and thin fibres or unorganized collagen is represented by green. Row 1 – Male, 23 (femur), row 2 – Male, 35 (humerus), row 3 – Male, 47 (femur) and row 4 –Female, 74 (femur). All polarised images taken under the same microscope settings to show changes between samples. Scale bar represents 100 µm. Annotations, *F* – fibrous layer, *C* – cambium layer and *CB* – cortical bone.

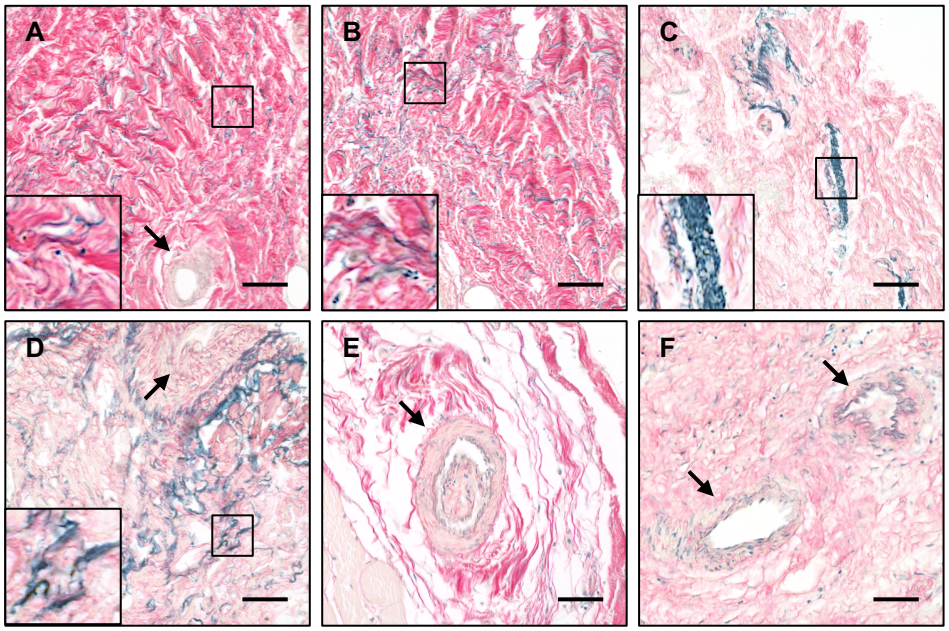

Figure 3.8: Elastin fibres within human periosteum. All human periosteum samples were stained with Miller's Elastin. A-D) Evidence of elastin fibres within the fibrous layer of periosteum was found in two donors, Male, 23 (femur) (A-B) and Male, 35 (humerus) (C-D), whereby the insert shows more detail of the elastin fibres. **E-F)** Elastin staining shown around blood vessels in two donors, Male, 61 (iliac crest) (E) and Female, 80 (femur) (F). Black arrow – blood vessel. Scale bar represents 50 µm.

Periosteum is known to be highly vascular and as the tissue that will form the basis of the development of a barrier membrane for CSBD repair, blood vessels can be thought of as 'pores' within a material, and thus were quantified. The blood vessels found throughout the periosteum were imaged and the diameter and lumen area were quantified (Figure 3.9). The majority of blood vessels could be identified in cross section, where a lumen could be seen, either empty or filled with erythrocytes (Figure 3.9B), were surrounded by a thin dense layer of smooth muscle with nuclei surrounding the lumen. Under Masson's Trichrome and PSR, this layer of smooth muscle was confirmed through pink (Masson's Trichrome) and yellow (PSR) staining (images not shown). Blood vessel diameter was found to be consistent between samples (Figure 3.9G), where the mean diameter ranged from 19.14 – 26.96 µm. There was no significant difference between the six donors measured (Kruskal-Wallis multiple comparisons test, $P<0.05$), apart from between the youngest donor (Male, 23) and the eldest donor (Female, 80), where the youngest donor blood vessel diameter was significantly smaller at 19.14 ± 0.63 µm, compared to 26.96 ± 2.78 µm ($P=0.02$).

However, the main differences between donors could be seen when the density of blood vessels was normalised to the surface area of the sample. Here, a trend in reduction of the number of blood vessels per mm^2 with age was seen, apart from one sample (Male, 47) which at 7.9 blood vessels per mm^2 had one of the lowest blood vessel densities (Figure 3.9H). However, Male, 47 was also the sample containing the confirmed cambium layer, thus the addition of this to the surface area of the periosteum could be the cause of the lower blood vessel density. After linear regression of donor age vs blood vessel per mm^2 was carried out the data showed a r^2 value of 0.68, showing reasonable correlation.

Porcine and human periosteum samples were compared for blood vessel diameter and density, it was found that porcine blood vessels were significantly smaller (Mann Whitney test, $P<0.0001$) at 6.8 ± 0.3 μm compared to 20.9 ± 0.5 μm for human samples (Figure 3.9I). In addition, porcine periosteum had a significantly lower density of blood vessels (Mann Whitney test, $P=0.02$) compared to human periosteum at 2.8 vs 14.7 blood vessels per mm^2 (Figure 3.9J).

To conclude, changes in birefringence could be seen with age for the human samples and porcine samples were shown to be more birefringent than the majority of the human samples, whereby the youngest donor (Male, 23) was the most similar in collagen fibril organisation. Human periosteum samples were shown to be significantly more vascular with blood vessels with larger diameters in comparison to porcine periosteum.

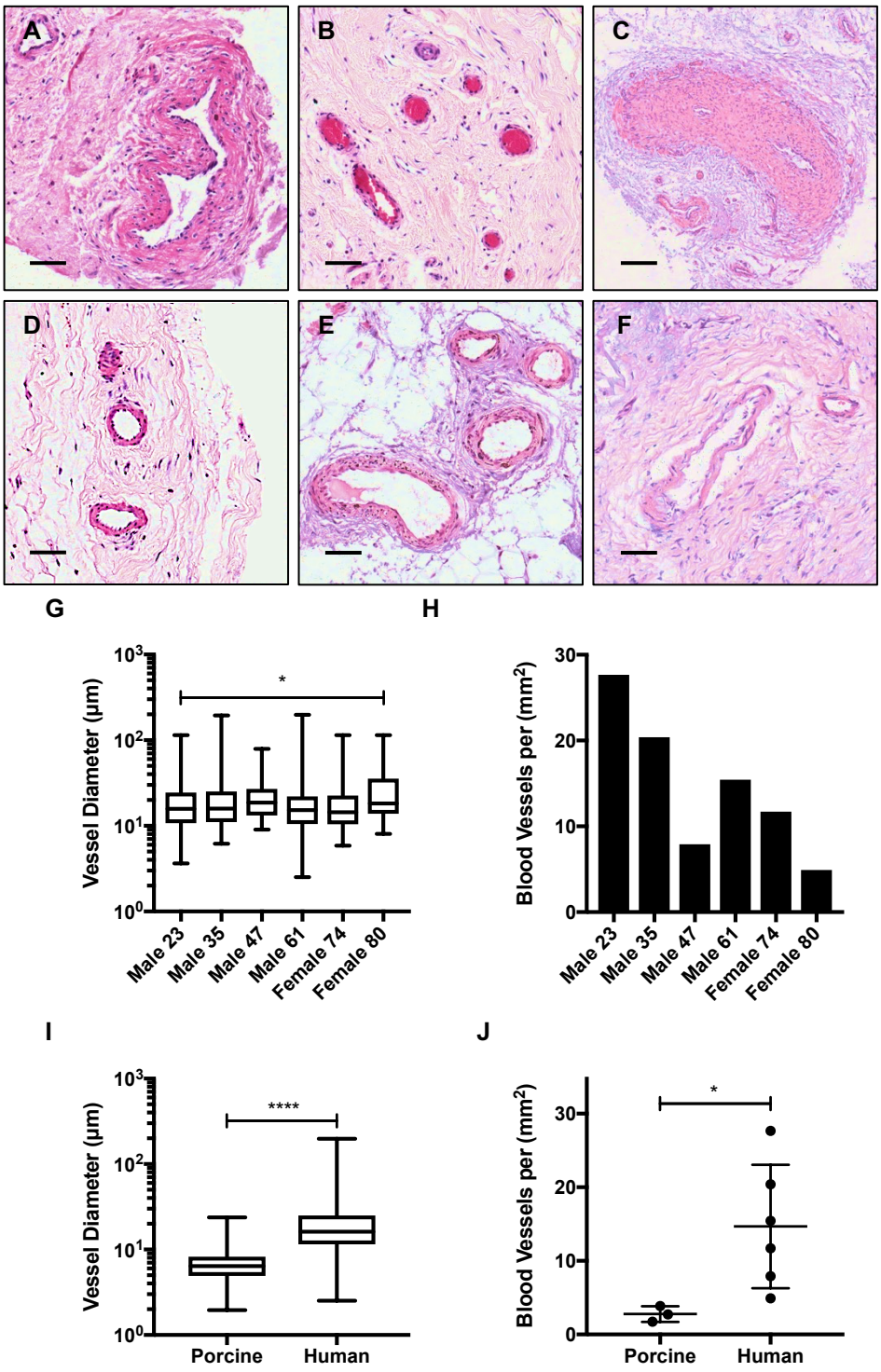

Figure 3.9: Vascularity of human periosteum in comparison to porcine periosteum. A-F) Examples of blood vessels from human periosteum, stained with haematoxylin and eosin. **G)** Blood vessel diameter was quantified for all human periosteum samples. **H)** The density of blood vessels per mm^2 was calculated, taking the surface area of the tissue measured. Comparisons were made between the porcine and human periosteum samples for, **I)** blood vessel diameter and **J)** blood vessel density. A) Male, 23 (femur), B) Male, 35 (humerus), C) Male, 47 (femur), D) Male, 61 (iliac crest), E) Female, 74 (femur), F) Female, 80 (femur). Scale bar represents 100 µm. Statistical analysis carried out using a Kruskal Wallis Test (G) or a Mann Whitney Test (I-J), * P<0.05, ****P<0.0001.

3.3.2.3 Potential Periosteal Reactions to Fracture

As previously mentioned, the human periosteum samples were harvested from patients undergoing elective orthopaedic surgeries for metal work removal, non-union, fracture infections or CSBD repair. Therefore, these patients are on average 42 weeks (range: 0.5 – 108 weeks) post fracture. In addition, the samples were taken from within surgical site, where the surgeon can clearly access periosteum, so are therefore estimated to be within 5-10 cm from the fracture site.

Areas of inflammation were seen in three of the six periosteum samples (Figure 3.10). There was a distinct area of localised inflammation in one sample (Male, 47) (Figure 3.10A-B), whereby a high density of nuclei were either found around blood vessels (Figure 3.10B) or in a clearly defined area

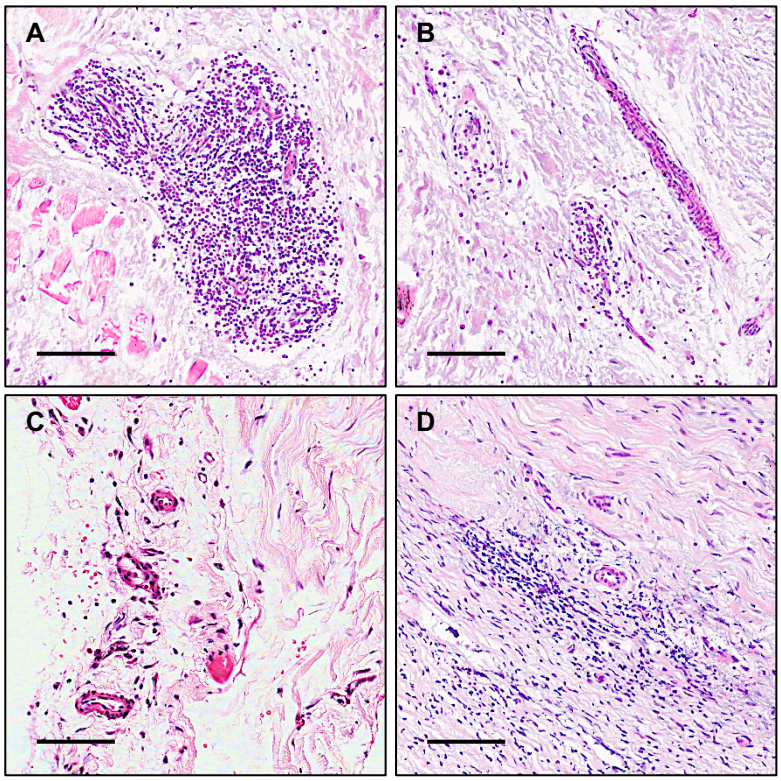

Figure 3.10: Areas of inflammation found in human periosteum. Images stained with haematoxylin and eosin. **A)** A distinct area of localised inflammation, surrounding small blood vessels. **B-C)** A more disperse area of inflammation seen, also surrounding blood vessels within two different donors. **D)** A consistent level of inflammatory cells seen to be dispersed throughout the periosteum sample, not localised to surrounding blood vessels. A-B) Male, 47 (femur), C) Male, 61 (iliac crest) and D) Female, 80 (femur). Scale bar represents 100 μm.

surrounding an area of blood vessels (Figure 3.10A). Under Masson's Trichrome and PSR straining, these cells were identified as lymphocytes or macrophages (opposed to erythrocytes cells due to their purple and black staining), respectively rather than the red or yellow respective staining expected by erythrocytes. The sample, Male, 61, showed low levels of inflammation surrounding a few blood vessels (Figure 3.10C), while another sample, Female, 80, showed widespread inflammation or high cellularity throughout the whole surface area of the sample (Figure 3.10D).

One sample, harvested from the iliac crest, contained the neighbouring skeletal muscle as well as periosteum, gave a clear cross-sectional view of skeletal muscle (Male, 61, Figure 3.11A-D). Distinct individual muscle fibres could be seen in cross section, characterised by dense cytoplasm with nuclei surrounding the edge of the fibre (Figure 3.11A-B). When stained with PSR the muscle fibres stained yellow (light microscopy) (Figure 3.11C), while the periosteum stained red (presence of collagen) and under polarised light, there was an absence of birefringence, typical for skeletal muscle (Figure 3.11D).

Four of the six periosteum samples showed areas within the periosteum that appeared similar to the skeletal muscle shown by the sample Male, 61 (Figure 3.11I-T), these samples were, Male, 23 (Figure 3.11E-H), Female – 74 (Figure 3.11I-L), Male, 47 (Figure 3.11M-P) and Male, 35 (Figure 3.11Q-T). All of these areas stained in a similar fashion to skeletal muscle, pink (H&E and Masson's Trichrome) and yellow or absence of birefringence (PSR under light microscopy and polarised light). These areas, often circular, but not arranged in an organised manner as with Male, 61, were seen throughout the fibrous layer of the periosteum, anatomically closest to skeletal muscle. This can be confirmed with Male, 47, where the periosteum was attached to cortical bone, the 'muscle-like' areas were seen on the opposite side of the sample to the bone, anatomically next to muscle (Figure 3.3).

Under higher magnification, further information of the 'muscle-like' areas could be seen (Figure 3.12), whereby in certain planes striation could be seen within these areas (Figure 3.12E). In addition, it was more apparent that there were nuclei lining the 'muscle-like' fibre as seen with the skeletal muscle sample

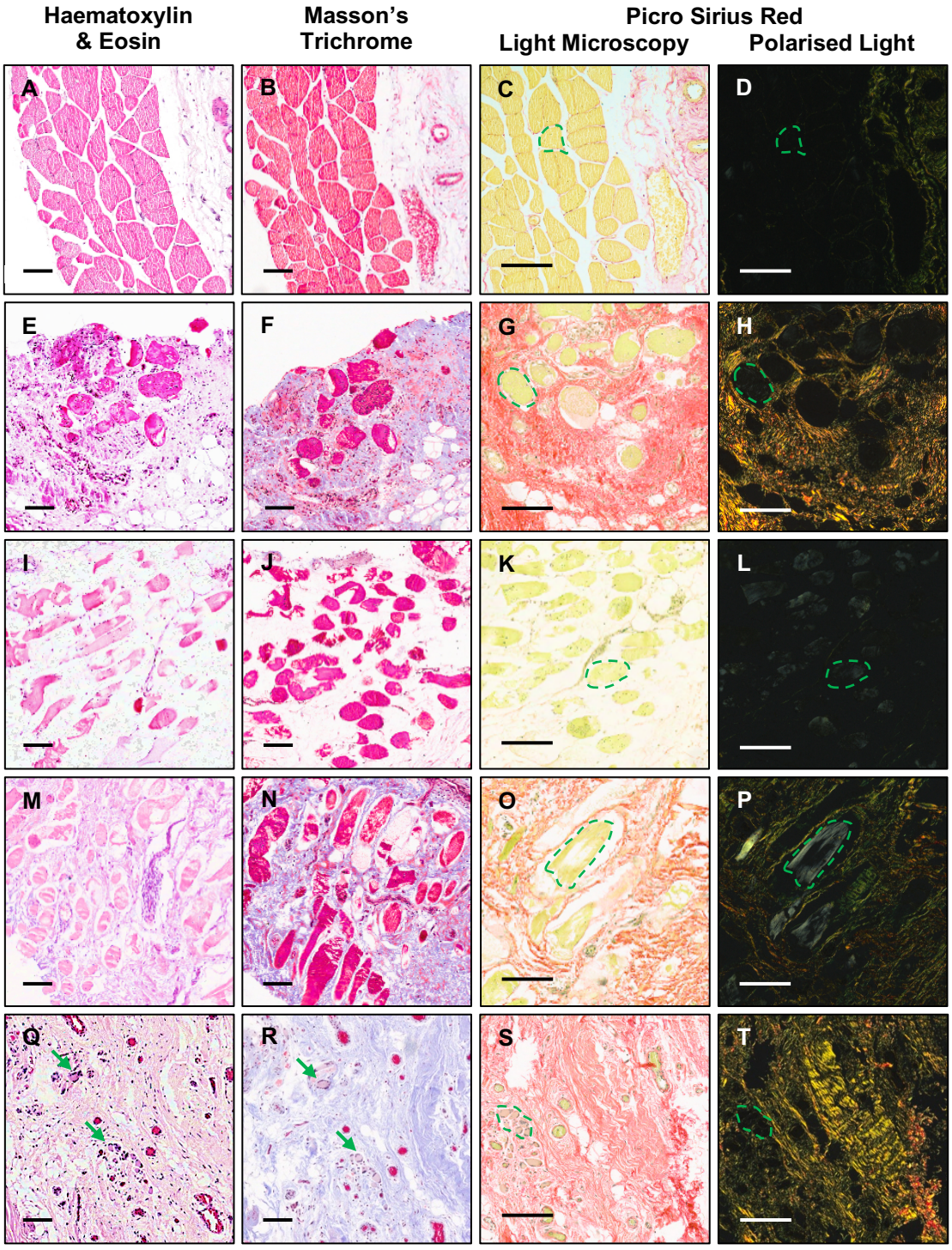

Figure 3.11: Skeletal muscle and 'muscle-like' areas on human periosteum. Slides were stained with haematoxylin and eosin (A, E, I, M, Q), Masson's Trichrome (B, F, J, N, R) and Picro Sirius Red (imaged under light microscopy and polarised light) (C-D, G-H, K-L, O-P, S-T). **A-D)** Periosteum shown next to a sample of skeletal muscle, cut through a cross section of the fibres, whereby skeletal muscle stains red/purple with Masson's Trichrome (B) and yellow with an absence of birefringence under polarised light (C-D). **E-T)** Areas of muscle-like formation within periosteum samples of four individual donors. As with skeletal muscle, the muscle-like areas stained red/purple with

Masson's Trichrome (F, J, N, R) and yellow with an absence of birefringence under polarised light (G-H, K-L, O-P, S-T). Each row represents a different donor, row 1 – Male, 61 (iliac crest), row 2 – Male, 23 (femur), row 3 – Female, 74 (femur), row 4 – Male, 47 (femur) and row 5 – Male, 35 (humerus). Scale bar represents 100 µm. Green arrows and circular dashed area highlighting 'muscle like' areas.

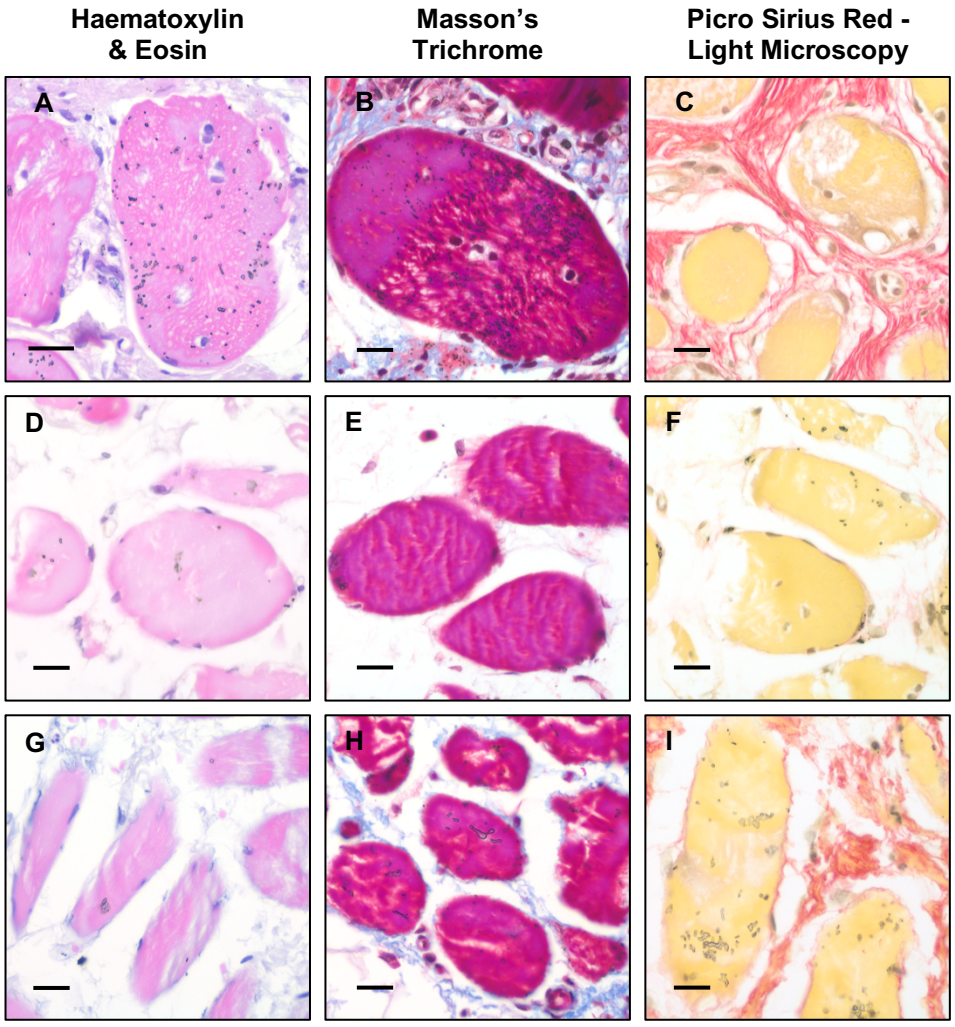

Figure 3.12: 'Muscle-like' areas on human periosteum at high magnification. Slides were stained with haematoxylin and eosin, Masson's Trichrome and Picro Sirius Red. **A-I)** High magnification images show the similarity of these 'muscle-like' areas to skeletal muscle, with evidence of nuclei around the edge. Donors shown were Male, 23 (femur) (A-C), Female, 74 (femur) (D-F), Male, 47 (femur) (G-I). Scale bars represent 20 µm.

(Figure 3.11A-D). This brings more confirmation that these areas could be forming primitive muscle.

Another common feature found within the periosteum samples, were areas in three samples that appeared ‘tendon-like’ (Figure 3.13). Male, 35 had an area where the periosteum became very aligned, as seen by high PSR staining and high collagen birefringence, whereby under polarised light the collagen appeared red suggestive of high collagen organisation and increased thickness of fibres (Figure 3.13C-D). The nuclei within this area of Male, 35 were elongated, along with clear collagen alignment this suggests of an area of a ‘tendon-like’ structure (Figure 3.13A-B).

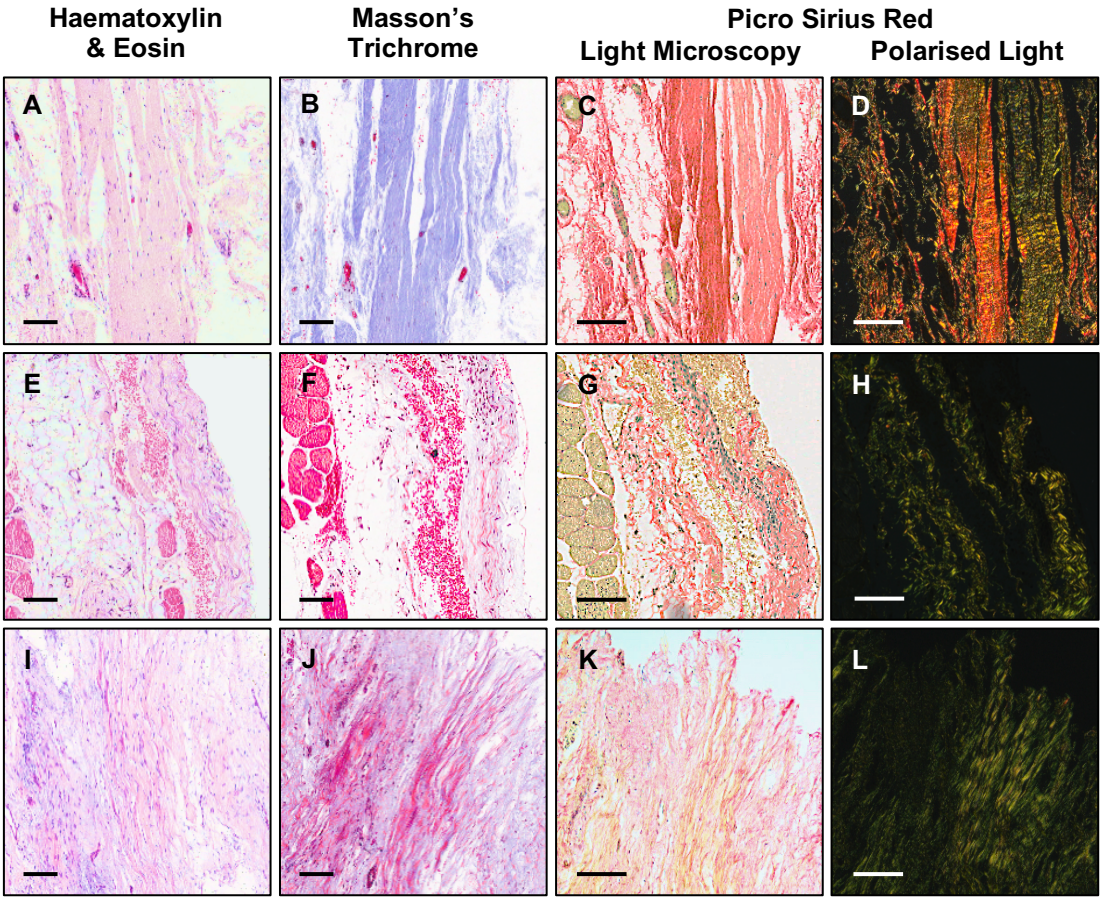

Figure 3.13: Areas of ‘tendon-like’ tissue on human periosteum samples. Slides were stained with haematoxylin and eosin (A, E & I), Masson’s Trichrome (B, F & J) and Picro Sirius Red, imaged under light and polarised microscopy (C-D, G-H & K-L). **A-L**) Areas of fibre alignment shown in three periosteum samples, with elongated nuclei as seen with tendon histology and increased collagen alignment within these areas also under polarised light. Each row represents a different donor, row 1 - Male, 35 (humerus), row 2 – Male, 61 (iliac crest) and row 3 – Female, 80 (femur). Scale bar represents 100 µm.

The other two samples, Male, 61 and Female, 80, had areas that were distinct to the rest of the periosteum, where the structure became wavy (Figure 3.13E-L). For sample, Female, 80 in particular there was evidence of high amounts of cytoplasm within the ‘wavy’ area seen with pink and yellow staining with Masson’s Trichrome and PSR, respectively (Figure 3.13I-K). However, this area was also quite birefringent under polarised light, suggestive of collagen organisation and alignment (Figure 3.13L).

Under higher magnification, more detail could be seen with respect to the elongation of nuclei found within the ‘tendon-like’ areas (Figure 3.14), this usually occurs due to the high alignment of collagen fibres within tendons, making elongated nuclei a classic identification feature. Each of the samples were from differing bones, humerus (Male, 35), iliac crest (Male, 61) and femur (Female, 80), therefore conclusions cannot be made about the potential origins of this tissue.

To conclude, there is evidence of potential ‘reactions’ to fracture within the tissue of human periosteum. This includes areas of widespread and localised inflammation as well as features with hallmarks consistent of skeletal muscle and tendon. It cannot be concluded at this point whether or not these features are found within ‘normal’ or non-activated periosteum, as samples of this nature were not tested. However, the porcine periosteum control tissue showed none of these features.

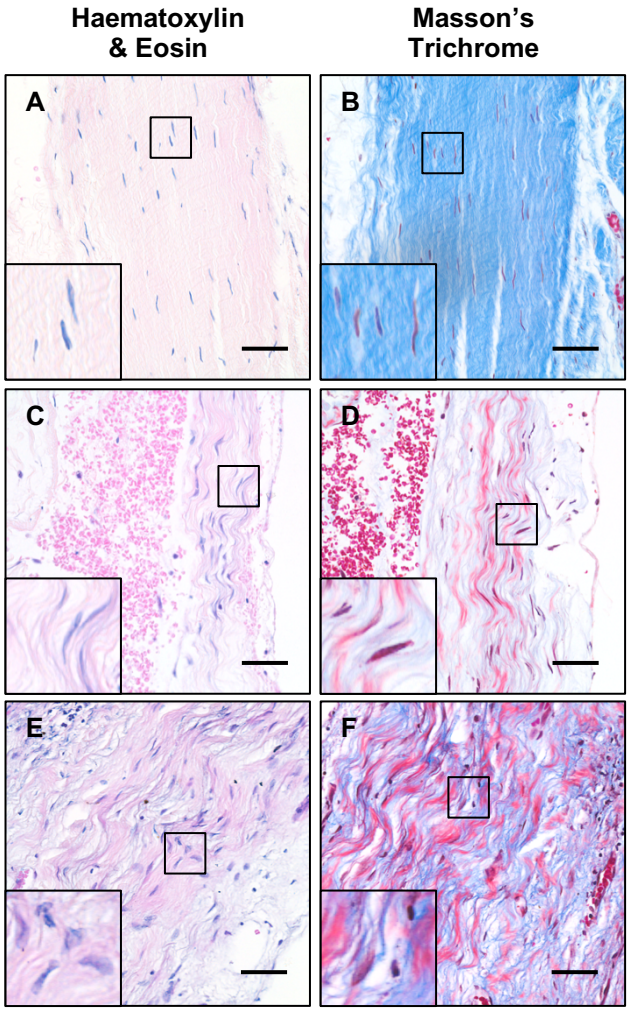

Figure 3.14: Higher magnification of 'tendon-like' areas on human periosteum samples. Slides were stained with haematoxylin and eosin (A, C & E) and Masson's Trichrome (B, D & F) and imaged at higher magnification. **A-F)** Fibre alignment can be seen in more detail, with evidence of elongated nuclei (inserts). Samples represented are, Male, 35 (humerus) (A-B), Male, 61 (iliac crest) (C-D) and Female, 80 (femur) (E-F). Scale bar represents 50 µm.

3.4 Discussion

To ascertain whether samples of clinically relevant human periosteum could have the potential to be utilised in the treatment of CSBD, the architecture and location of MSCs within human periosteum were investigated. In addition, the design process of a barrier membrane biomaterial for CSBD repair will be informed by the architecture of porcine and human periosteum.

Periosteum, especially from human sources is an under-researched area. Here, periosteum was harvested from patients undergoing orthopaedic surgery from close to the fracture site and therefore is considered to be 'clinically relevant' to what a surgeon could realistically obtain to use during surgery. The periosteum was removed from the underlying bone as resected samples using a scalpel, differing from many of the human samples found in the literature which are obtained from cadavers or amputated limbs and are thus still attached to the underlying cortical bone (Allen, Hock & Burr 2004; Allen & Burr 2005; Moore, Milz & Knothe Tate 2014). As a result, these samples were compared to *in situ*, porcine femoral periosteum samples, harvested intact to the bone, in order to obtain further information with respect to tissue architecture of periosteum attached to the bone in comparison to resected tissue.

Porcine periosteum showed two distinct layers with respect to cellularity between the cambium and fibrous layer, the former being visually highly cellularised independent of the thickness of the periosteum at a given point around the circumference of the femoral cross-section. This was to be expected due to the relative age of the porcine samples, coming from the food chain the age of the sample would have been approximately 4 months old. It is known that 'young' periosteum is highly active and thick due to its involvement in appositional bone growth (Frey et al. 2013).

In addition, 'young' periosteum is known to show distinct cambium and fibrous layers, and that this distinction between the layers is lost with age (Bisseret et al. 2015). Thus, the lack of either removing the cambium layer of adult human periosteum samples or being able to distinguish between the two layers from the human samples collected in this study was therefore unsurprising.

However, it was shown that when the cambium layer was able to be identified, it was consistently thin (approximately 164 μm), and the overall thickness was variable. As the literature surrounding the histology of human periosteum is sparse and varied in its approach, with respect to the age of samples, number of samples and 'status' of the sample either *in situ* to the underlying bone or as a resected sample, comparisons are hard to make.

The results in this study compare well to a previous publication from our group, Cuthbert et al. (2013), who measured the thickness of resected human periosteum layers, with similar values for both layers. Other papers have reported thinner cambium and fibrous layer thicknesses ranging from 23–62 μm and 52-78 μm, respectively (Allen, Hock & Burr 2004; Allen & Burr 2005; Frey et al. 2013; Moore, Milz & Knothe Tate 2014; Roberts et al. 2015). Both layers were thinner than that of this study, however, all but one of these studies exclusively looked at samples within the age range of 68-99, thus thin periosteum was to be expected. In addition, in this study samples were taken from close to a fracture site, and trauma is known to result in periosteum thickening (Colnot 2009). However, it is not clear how long periosteum will remain thickened and active during a non-union situation. Brownlow, Reed & Simpson (2001) studied this in a non-union model, where it was found that periosteum, particularly the fibrous layer, remained thickened 8 weeks post fracture, where there was fibrous tissue formed within the fracture gap and evidence of some new bone formation and in a control group of 'normal' fracture healing the periosteum was no longer thickened and had returned to a quiescent state. The samples within this study were taken at varying times post fracture (0.5 to 108 weeks), so apart from at 0.5 weeks (Male, 61) post fracture, all the samples were considered to be non-union by this point, so it could be argued that these would be thickened due to a dysfunction within the bone healing process.

With respect to porcine periosteum, the thickness of the cortical bone and periosteum was shown to vary widely throughout the circumference of the femoral bone, where periosteum thickness ranged from 127-2310 μm. However, periosteum and cambium layer thickness were not found to correlate with cortical thickness, but cambium and periosteum thickness

showed high correlation. Suggestive that the thickness of cortical bone does not influence nor is influenced by periosteal thickness. There were distinct areas throughout the cross section where periosteum thickness declined sharply, which appear to be at areas of fascia or the junctions between different muscle groups. Here, there is an area where the muscle is not close to or in contact with periosteum, but an area of connective tissue with fascioperiosteal blood vessels running through it (Simpson 1985).

The high correlation between the thickness of the cambium and fibrous layers of periosteum could also be seen in the literature, whereby the cambium was found to make up 41-55% (Table 3.1) of rat periosteum thickness with good agreement (Fan, Crawford & Xiao 2008; Fan et al. 2010; Henrich et al. 2016). In addition, with human samples there was also good agreement whereby the cambium layer made up 23-50% of periosteum thickness (Allen, Hock & Burr 2004; Allen & Burr 2005; Cuthbert et al. 2013; Moore, Milz & Knothe Tate 2014), both species examples are similar to that of the porcine, at 41% cambium layer of periosteum thickness. The fact that both adult human and young rat cambium layers make up similar percentages of periosteum thickness again corroborates the link between the two layers.

Collagen is naturally birefringent, partially due to co-alignment of molecules within type I collagen (Junqueira, Bignolas & Brentani 1979). The organisation of collagen within tissues can be assessed by using PSR staining to enhance birefringence under polarised light, where larger collagen fibres appear red or yellow/orange whereas thinner fibres appear green (Junqueira, Bignolas & Brentani 1979). Distinct differences between the two periosteal layers was not limited to cellularity for the porcine samples, changes in collagen were seen also. Here, increased organisation or thickness of the collagen fibrils was seen within the fibrous layer, compared to the cambium layer, which is in alignment with previous literature (K. Chen et al. 2015). This was also seen in the samples of human periosteum with intact cambium. For the first time it has been shown that the collagen content of human periosteum appears to become less structured or made up of thinner collagen fibres with age, as birefringence was seen to be lost, when imaged under the same conditions. Future work to increase the number of samples and age range would enhance

this data. As previously mentioned, trauma results in an activation of periosteum (Evans et al. 2013), which causes changes including thickening, a loosening of fibres resulting in changes to fluid flow, which would be responsible for changes to the collagen structure. However, the birefringence seen did not appear to correlate with time since injury.

As previously mentioned, most periosteum literature states that elastin is found within the tissue, however, the original literature outlining this found very low levels of elastin within canine palate periosteum, but not in skull periosteum (Squier, Ghoneim & Kremenak 1990), which has been perpetuated throughout the literature as true for all sources of periosteum. Human periosteum samples showed elastin staining mainly located surrounding blood vessels, with two samples showing small areas of elastin fibres throughout the periosteum. Thus, from this elastin fibres can be found within human periosteum, however at low levels, tending to be in younger donors and elastin is not found in every donor.

The vascularity of periosteum was assessed as a potential measure of porosity of the native tissue to inform the future biomaterial design process. The mean blood vessel diameter in human samples was 22 μm, with a density of 5-28 per mm^2, dependent on age, where there was a trend in a reduction to blood vessel density. It is well described that vascularity of periosteum is thought to reduce with age (Bisseret et al. 2015), therefore it was surprising to find that porcine periosteum had significantly smaller diameter blood vessels, at a lower density than human periosteum. However, further investigation throughout the length of porcine femoral samples would need to be carried to see if it was just this particular cross section showed low vascularity or if this is repeatable throughout the femur length. This is important when looking into the anatomical location of blood vessels throughout the periosteum of a particular bone. Simpson (1985) mapped out the periosteal vascular network of various bones from goats. Here, it was found that the periosteal network of the femur was made up of a series of longitudinal blood vessels with circular rings running in cross section down the shaft of the femur (Simpson 1985). Therefore, it could be likely that the cross section of femur investigated in this study could have been between the

circular vessels and therefore missed a lot of the porcine vascular network. In addition, Herring and Ochareon, (2016) investigated the porcine zygomatic arch (cheek bone of the skull), however quantification of vessel diameter was not carried out, rather a description of an extensive vascular network. So, even though there is high vascularity within the zygomatic arch, this could be a particularly vascular area of periosteum and thus cannot be compared to the femoral results of this study.

The increased size and density of blood vessels found in human samples could be attributed to the fact these samples were taken post trauma, so the periosteum would have 'reactivated' as a response to aid in the fracture healing response. All samples, bar one were greater than 17 weeks post injury, leaving enough time for angiogenesis and increased vascularisation to have occurred (Marsell & Einhorn 2011). However, as literature surrounding the vascularity of human periosteum is sparse, the only comparable literature comes from Cuthbert et al. (2013), who reported CD31 staining for blood vessels, however, the size and density of said vessels was not carried out. Therefore, even though this is an unique insight into the vascularisation of periosteum post trauma, ideally these samples would be compared to periosteum that has not responded to trauma, like cadaveric tissue.

It is well known that unregulated inflammation can result in delayed fracture healing, where dysregulated inflammation results in increased bone resorption and suppression of bone formation (Loi et al. 2016). Inflammation, either localised to a certain area or widespread and dispersed, was found in half of the human periosteal samples. These samples were also harvested the least amount of time post trauma (0.5, 17 and 19 weeks) compared to the other samples where inflammation was not seen (49, 57 and 108 weeks). Therefore, inflammation can be seen within periosteum taken close to the fracture site (approximately 5-10 cm) for up to 19 weeks post trauma from patients with no known bone infection. However, it is unknown whether this is a sign of bone healing dysfunction or a normal response of periosteum post trauma. Comparison to adult human periosteum, further away from the fracture site or from contralateral non injured limbs would be needed to investigate this further.

A candidate marker for MSCs (CD271) was used to stain for the presence of MSCs throughout the human periosteum samples. Literature points to the cambium layer being an important layer with respect to MSC location (Evans et al. 2013). However, CD271 staining was shown to be mainly surrounding the blood vessels within the fibrous layer of the periosteum. Suggestive that although CD271 staining was found in the cambium layer, removal of said layer is not essential for the isolation of MSCs from periosteum samples, which will be investigated further in Chapter 4. This finding is in agreement with Cuthbert et al., (2013), whereby CD271 staining was found to be localised to blood vessels, however, this study did not specify which periosteal layer these blood vessels were located in. Interestingly, Stro-1 was found within both the cambium and fibrous layer of juvenile rat periosteum at similar levels, which was reduced significantly in both layers for mature and aged rats (Fan, Crawford & Xiao 2008), corroborating the notion that MSCs may not be contained to the cambium layer.

Most of the human periosteum samples showed areas embedded within the tissue that appeared ‘muscle-like’ when compared to a sample with clearly identifiable skeletal muscle running alongside the periosteum. It should be noted that similar areas were not visualised on the porcine samples. Skeletal muscle is known to appear pink under Masson’s Trichrome staining and yellow under PSR staining and has an absence of birefringence under polarised light. In addition, it is easily identified due to sarcomeres having a striated appearance and cell nuclei are typically found close to the endomysium that surrounds the edge of an individual muscle fibre (Yin, Price & Rudnicki 2013). The ‘muscle’ like areas shared the staining pattern of skeletal muscle and under high magnification typical muscle striations could be imaged, suggestive that these areas could be a form of primitive muscle.

Communication between the bone fracture site and surrounding musculature is known to be important to bone healing. Muscle derived cells can be located within an open fracture callus, contributing to the healing process, when periosteum has been compromised (Liu et al. 2011). As previously discussed, periosteum ‘loosens’ in response to trauma, allowing for increased bidirectional fluid flow through the tissue, thus increasing communication

between the musculature and the fracture site (Evans et al. 2013). Therefore, it could be postulated that growth factors or cells from the muscle could migrate into periosteum causing primitive muscle formation.

Similar to this, there were other areas within the periosteum that appeared ‘tendon-like’. Like skeletal muscle, tendons have distinct hallmarks histologically, made mostly of highly aligned collagen fibres with nuclei flattened between the fibres, which were seen in each of these areas. One of the samples (Male, 61) was harvested from the iliac crest, therefore there is a chance that this sample could have been at the junction of periosteum and a tendon. However, the other two samples were taken from the mid shaft femur and humerus so it is therefore unlikely that these samples would contain tendon. It is likely that these areas are a result of periosteum loosening as previously discussed, however, these areas were particularly birefringent under polarised light, suggestive of an organised collagen structure, different to that of surrounding periosteum. Both the ‘muscle-like’ and ‘tendon-like’ like areas have not been described before within the literature. Further work would need to be carried out to ascertain whether these are reactions to fracture and trauma or could be a sign of bone healing dysfunction.

When reflecting on the limitations of the study, the porcine periosteum results are limited to the fact that only one cross sectional area was quantified in the mid shaft femur. It would be preferable to have looked at multiple areas along the length of the diaphysis of the femur to elude to changes in periosteum along the length of the bone. As resected samples, the human sections were hard to accurately orientate within the histology blocks to be sure of what plane the slides are cut through. As covered previously periosteum is kept under tension by Sharpey’s Fibres *in situ* (Evans, Chang & Knothe Tate 2013; Evans et al. 2013) therefore, the resected samples will have been subject to shrinkage in comparison to the porcine samples. Thus, the ‘clinically relevant’ resected samples, although ideal as they give a realistic picture on what could be harvested during surgery are limited as they may not give a ‘true’ picture of periosteum *in situ*, compared to a cadaveric sample where imaging of periosteum still attached to the bone could take place. Ideally more human samples would have been used for the work in this chapter, however, as the

samples were rare and also needed for cellular work in Chapter 4, the decision was taken to prioritise the cellular work over histology.

3.5 Conclusions

The samples of human periosteum investigated within this chapter will also be used in Chapter 4, here these samples will be collagenase digested to release MSCs to be cultured and compared to donor matched BM MSCs. Consequently, the knowledge that the cambium layer is often not removed during the harvesting process of 'clinically relevant' samples of periosteum is important when assessing and comparing the cells released from these samples. However, the periosteum samples taken have shown to be particularly vascular, especially in comparison to porcine counterparts, and the presence of CD271+ cells surrounding blood vessels has been shown, exposing the fact that MSCs are not confined to the 'cambium' region and can be found throughout the fibrous region also.

In addition, the assessment of the architecture of porcine and human periosteum will inform the design process of the barrier membrane to be manufactured in Chapter 5. Here, it was seen that within young, growing porcine samples periosteum has two distinct layers, however, in human samples either the distinction between the two layers is lost in adulthood or the cambium layer is not always removed during the harvesting process. Of particular interest was the variability of porcine periosteal thickness around the circumference of the femur, thus potentially removing the need to 'aim' for a certain thickness of biomaterial to match the native periosteum. It was confirmed that the majority of periosteum is made up of collagen, of varying organisation, seemingly becoming less organised with age and potentially containing small areas of elastin.

Chapter 4: Comparison of Periosteum and Bone Marrow Derived Mesenchymal Stem Cells

Histological evaluation of human and porcine samples of periosteum was carried out in Chapter 3. The human samples were collected using a scalpel, from within the surgical opening, thus close to the fracture site (within approximately 5-10 cm). It was found that the cellular cambium layer of the periosteum was often absent from the collected periosteum samples. However, CD271 and CD73 staining for resident candidate MSCs was localised around blood vessels throughout the periosteum in the cambium layer (when seen) and the outer fibrous layer. This chapter will investigate the characteristics of MSCs derived from human periosteum – similar in nature to the histological samples and iliac crest BM, the current gold standard.

4.1 Introduction

As previously discussed in Chapter 1, MSCs influence long bone fracture repair by migrating out of surrounding tissues such as the BM, periosteum and endosteum following trauma or fracture (Colnot 2009). Once MSCs have infiltrated the fracture haematoma, bone regeneration is facilitated through their potential to be able to differentiate into osteogenic and chondrogenic cell lineages needed for intramembranous and endochondral ossification (Phillips 2005). However, autologous treatments during surgical repair of fractures remain confined to the utilisation of BMA (aspirated from the iliac crest) (Nauth et al. 2015; Shao, Zhang & Yang 2015) and more recently the use of RIA waste (Cuthbert et al. 2015).

In preparation for fixation of a long bone with an intermedullary nail, the BM is reamed (using RIA) to provide a channel for the nail to follow. The irrigated waste (RIA waste) is known to contain MSCs, thus has been proposed as a replacement for using BM MSCs (Uppal et al. 2013; Cuthbert et al. 2015). However, due to a current lack of equipment or technique to ultilise this during surgery the RIA waste is still disposed of rather than ultilised in orthopaedic surgery.

MSCs isolated from BM are well researched in the literature and are known to be osteogenic and have a proven use in surgery (Nauth et al. 2015). Here, an enriched source of MSCs, BMAC, centrifuged during surgery can be combined with commercial 'bone filler' scaffolds or autograft as a supply of MSCs to a defect during CSBD repair (Jäger et al. 2011). However, MSCs are a rare cell population in BMA, ranging from 0.001-0.01% of total NCCs, which varies due to donor age, aspiration technique and the volume aspirated (Muschler, Boehm & Easley 1997; Hernigou et al. 2005; Cuthbert et al. 2012).

Human BM MSCs have been compared to adipose tissue derived MSCs (AT MSC) and umbilical cord blood MSCs (UCB MSC), whereby proliferation of BM MSCs plateaued by passage 11-12, similar to AT MSCs. However, they showed higher levels of senescence compared to UCB MSC and AT MSC, which was seen by passage 6 (Jin Jin et al. 2013), suggestive of their susceptibility to senescence. In addition to this, a recent study showed that the onset of senescence during *in vitro* culture of BM MSCs is dependent on donor age (Churchman et al. 2017).

Clearly, there are advantages (easy to access and liquid form which is easily combined with scaffolds) and pitfalls (rare cell subset of BMA and numbers are affected by aspiration technique) to the use of BM MSC and the potential of other sources of MSCs should be investigated. In particular, periosteum is known react to fracture by thickening, increasing cell proliferation and then migrating into the fracture haematoma, differentiating into osteoblasts and chondrocytes, needed for bone regeneration (Wang, Zhang & Bikle 2017). The importance of periosteum involvement is particularly stark when periosteum is stripped from the bone ends of a fracture site, whereby union rates and bone strength are seen to reduce (Ozaki et al. 2000; Utvåg, Grundnes & Reikeraos 1996; Mercurio et al. 2012). Despite this, the utilisation of periosteum, as a known critical tissue source for uneventful fracture healing, for surgical repair CSBD has not been exploited, unlike BMA.

Periosteum can be harvested from within the surgical opening, near to the fracture site or as a by-product of debridement, thus mitigating the need for a second surgical site that is needed for both BMA and adipose tissue utilisation. As previously discussed and shown during Chapter 3, the cambium layer of

periosteum is tightly attached to the underlying bone by Sharpey's fibres, thus removal of periosteum with the cambium layer attached can be difficult (Eyre-Brook 1984; Brownlow et al. 2000). Therefore, the use of 'clinically relevant' samples of periosteum for bone fracture repair needs to be investigated, referring to samples harvested using a scalpel that may or may not contain the cambium layer.

4.1.1 Human Periosteum Derived MSCs

The activation of periosteum and BM MSCs following trauma is known to be important to the success of fracture healing (Dimitriou et al. 2011; Mercurio et al. 2012), however, BM MSCs also have an important function homing and maintaining the haematopoietic compartment of BM stroma. Due to its location on the outer surface of bone, it could be logical to think that periosteum MSCs would not have this function. Sacchetti et al. (2007) investigated this through implanting periosteum, trabecular bone and BM cells subcutaneously into immunocompromised nude mice, *in vivo*. As expected BM cells formed heterotopic bone and BM stoma, however, although periosteum and trabecular bone cells formed heterotopic bone, neither formed BM stroma. This is indicative of the potential functional differences between periosteum and BM MSCs.

There are few direct comparisons between BM and periosteum derived MSCs, with even fewer using donor matched samples, therefore an appraisal of the current literature was carried out. De Bari et al. (2006) showed cells derived from human tibial periosteum to be clonogenic regardless of donor age, for up to 30 PDs and were able to be grown as clonal lines. These cells adhered to the ISCT MSC phenotype as well as tri-lineage differentiation *in vitro* and *in vivo*, whereby new bone formation was seen to be predominantly of human origin (De Bari, Dell'Accio, Vanlauwe, Eyckmans, Ilyas M Khan, et al. 2006). Follow up investigations comparing to synovial membrane derived MSCs was carried out, whereby periosteum MSC induced significantly greater osteogenesis *in vitro* and *in vivo*, seen through a higher percentage of bone area (De Bari et al. 2008).

Human tibial periosteum MSC colony formation dropped with passage, and differentiation genetic markers were also shown to change over time in tissue culture (non-clonal) (Ball et al. 2011). Sox9 (chondrogenic marker) was lost with passage, RUNX2 (osteogenic marker) levels remained the same, while collagen 1 and ALP (osteogenic markers) were increased and then plateaued, these cells were also shown to form mineralised tissue (Ball et al. 2011).

Eyckmans, Lin & Chen (2012) compared non donor matched human tibial derived MSCs to BM MSCs to assess the effect of cell spreading and cell density on differentiation capacity. Periosteum MSCs were shown to proliferate faster and were smaller than BM MSCs. During *in vitro* differentiation at differing cell densities, both MSC types were positively influenced by high cell density or micro-mass during adipogenesis and chondrogenesis, respectively (Eyckmans, Lin & Chen 2012).

The influence on osteogenesis appeared more complicated, ALP levels were increased and then reduced by 2 weeks for BM cultures, irrespective of cell density, however, mineralisation was influenced and increased with high seeding density. Whereas, periosteum cultures showed low ALP levels with a slight increase by 2 weeks, suggestive that periosteum derived cells take time to induce osteogenesis, regardless of seeding density (Eyckmans, Lin & Chen 2012). Cell shape was constrained, keeping a round, un-spread shape and compared to cells that were able to spread out. MSCs that were constrained showed higher chondrogenic and adipogenic differentiation, however, periosteum cells were less affected by shape constraints than BM MSCs (Eyckmans, Lin & Chen 2012). It could be possible that during osteogenesis cell spreading could be optimal at different stages as cells able to spread out had increased ALP expression, whereas constrained cells showed high RUNX2 expression (Eyckmans, Lin & Chen 2012).

Chen et al. (2011) compared donor matched human tibial periosteum and tibial BM MSCs, showing a similar MSC phenotype. Visually increased periosteal *in vitro* mineralisation was seen with significantly higher mature bone formation and blood vessel count when periosteum MSCs were implanted on bone scaffolds *in vivo*.

Previous work in our group involved comparison of donor matched human periosteum MSCs with cells extracted from induced membrane, a tissue that forms around bone cement placed in a debrided bone defect, as part of the 'Masquelet technique', thought to be an induced-periosteum (Masquelet & Begue 2010). Here, periosteum derived MSCs showed significantly lower levels of cells per gram of tissue, CD45+ cells (lymphocytes), CD271+CD45- (MSCs) and CD146+CD45- (pericytes), but similar levels of MSC quantification at 0.2% and *in vitro* tri lineage differentiation (Cuthbert et al. 2013).

There is a lack of literature surrounding the colony forming potential and MSC percentage of periosteal cells immediately post digest, which could be important to know, especially when looking to compare MSC sources. Cuthbert et al. (2013) carried out CFU-F assays of periosteum samples, in comparison to induced membrane samples, which showed similar MSC percentages. However, this was from thawed digest samples (fresh digest samples frozen and then thawed in the future for CFU-F assay), therefore the results could be underestimated or overestimated dependent on whether the MSCs are more or less resilient to cryopreservation than the other cell types in the fresh digest. In summary, the majority of research has been carried out on human periosteum MSCs harvested from the tibia and direct comparisons have been made with MSCs derived from tibial BM, opposed to the iliac crest to be used in this study as the current gold standard MSC source for orthopaedic surgery.

4.1.2 Synergistic Action of Bone Marrow and Periosteum MSCs

It is well known that cells are mobilised from the periosteum and BM upon injury and that when either tissue is compromised via periosteal stripping or BM reaming, respectively, bone regeneration is compromised (Dimitriou et al. 2011; Mercurio et al. 2012). Therefore, it would be reasonable to hypothesise that the presence of both cell types may result in a positive synergistic effect on bone regeneration. The current literature surrounding co-culture effects on bone regeneration focused on the co-culture of BM MSCs with endothelial progenitor cells (Thébaud et al. 2012; Khojasteh et al. 2016; Chen et al. 2019),

monocytes (Nicolaidou et al. 2012) or osteoclasts (Sinclair & Burg 2011). Here it was shown that endothelial progenitors can induce osteoblastic differentiation of MSCs *in vitro* (Thébaud et al. 2012; Chen et al. 2019) and increase bone regeneration *in vivo*, shown in a bone defect model (canine mandible) when in co-culture (Khojasteh et al. 2017). In addition, monocytes (Nicolaidou et al. 2012) and osteoclasts (Sinclair & Burg 2011) where shown to induce MSC differentiation into osteoblasts.

Investigations into the co-culture of different types of MSCs was carried out by Kim, Park & Im (2014), whereby improved *in vitro* osteogenesis and angiogenesis through indirect and direct co-culture of BM MSC and AT MSC was shown, with an optimal ratio of 2:1 (BM MSC:AT MSC), indicating a synergistic effect of the two MSC types. This was carried forward *in vivo*, differing ratios of cells were seeded onto poly(lactic-co-glycolic acid) (PLGA) scaffolds for a 5 week subcutaneous implantation model or seeded on a HA/β-TCP scaffold to be implanted into a 10 week calvarial defect nude mouse model. In both incidence MSC co-culture was seen to be similar to or improved osteogenic differentiation in comparison to BM MSC or AT MSC on their own. This study was limited by the fact that BM MSC numbers were kept the same with differing numbers of AT MSCs during co-culture, therefore in comparison to either MSC source on its own more MSCs were present. Therefore, differences seen in co-culture could be due to the increased numbers of MSC, rather than the effect of co-culture.

Chen et al. (2012) investigated co-culture using cells derived from human BM and periosteum taken from the tibia of young patients (22-30 years old) undergoing amputations. Through *in vitro* monolayer co-culture of BM and periosteum (P) MSCs (BM:P) at the ratios of 2:1, 1:1 and 1:2 it was found that co-culture showed significantly increased mineralisation and ALP activity in comparison to BM or periosteum MSC culture on its own. β-TCP scaffolds were loaded each of the cell ratios and underwent osteogenic differentiation for 3 weeks prior to subcutaneous implantation into an *in vivo* nude mouse model. After 8 weeks *in vivo* significant increases in neovascularisation was seen for all of the BM:P ratios in comparison to BM MSCs only and the 1:1 and 1:2 ratios in comparison to periosteum MSCs only (Chen et al. 2012). This

work was followed up by Chen et al. (2015), again significant increases in mineralisation during *in vitro* 3D osteogenic differentiation experiments (cell cultures loaded onto β-TCP scaffolds), was seen with ratio cultures. MSCs were pre-differentiated for 3 weeks in osteogenic media and then loaded onto β-TCP scaffolds. These constructs were implanted into an *in vivo* rabbit femoral condylar CSBD model for 4 and 12 weeks, which showed increased neovascularisation and significantly increased in all of the ratio culture groups (2:1, 1:1 and 1:2 – BM:P) (D. Chen et al. 2015).

This opens up the possibility of whether both types of MSCs, accessible to the operating surgeon can be synergistically utilised during bone fracture repair. Therefore, this chapter will also aim to investigate the synergistic effect of periosteum and BM MSCs in co-culture, as well as individually when using iliac crest BM, instead of tibial BM.

4.1.3 Chapter Aims and Objectives

The aim of this chapter is to investigate the proliferative and differentiation capacity of periosteum derived MSCs in comparison to donor matched BM MSCs, in order to explore periosteum as an alternate source of MSCs to BM to facilitate CSBD repair.

4.1.3.1 Objectives

The objectives of this work were to:

1. Quantify the percentage MSC content and colony area from CFU-F assays of donor matched periosteum and BM cultures to quantify MSC content.
2. Grow donor matched periosteum and BM cultures in long term 2D tissue culture to compare PD proliferation rates.
3. Generate an MSC phenotype profile for donor matched periosteum and BM cultures using flow cytometry.
4. Investigate donor matched periosteum and BM cultures' trilineage differentiation capacity in 2D culture conditions.
5. Investigate the effects of co-culture of periosteum and BM cultures during osteogenesis.

4.2 Specific Materials and Methodology

Donor matched BMA and periosteum samples were harvested (Section 2.1) and MSCs were isolated and grown in tissue culture in order to compare growth rates, MSC phenotype and differentiation capacity. Table 4.1 details the donors that consented to participate in this study and the specific experiments each donor was allocated to within this Chapter.

4.2.1 MSC Isolation from Bone Marrow and Periosteum

NCCs were isolated from donor matched BMA and periosteal tissue as per Section 2.2 and cell suspensions were counted (Section 2.3.1). Uncultured NCCs that were not carried forwards into CFU-F assays or tissue culture (Section 4.2.2 and Section 4.2.3) were frozen at -80°C and then transferred to liquid nitrogen tanks for long term storage (Section 2.3.3).

Table 4.1: Patient sample details and division into Chapter 4 experiments. M – male, F – female, Y – donor allocated to experiment

Gender & Age (Years)	CFU-F	Growth Kinetics	ISCT Panel	New Markers	Osteo	Chondro	Adipo	RT-PCR	CellTrace™ CFSE
M, 17	Y	Y	Y	-	Y	Y	Y	Y	Y
M, 23	Y	Y	Y	Y	Y	Y	-	-	-
M, 35	Y	Y	Y	Y	Y	Y	Y	-	-
M, 44	Y	Y	-	-	Y	-	Y	Y	-
F, 49	Y	Y	Y	-	Y	Y	Y	Y	-
M, 49	Y	Y	-	-	-	-	-	-	-
M, 55	Y	Y	Y	Y	Y	-	Y	-	-
M, 58	Y	-	-	-	-	-	-	-	-
M, 59	Y	-	-	-	-	-	-	-	-
M, 61	-	Y	Y	Y	Y	Y	Y	-	-
F, 74	Y	Y	Y	Y	-	-	-	-	-

4.2.2 Colony Forming Unit–Fibroblast Assay

CFU-F Assays were used to enumerate MSCs and performed on all BM samples. Prior to RBC lysis (Section 2.2), 200 µL or 80 µL of BMA were plated onto duplicate 100 mm or 60 mm diameter tissue culture dishes, respectively, with 15 mL or 5 mL StemMACS media (Miltenyi Biotec). Two dish sizes were used in an attempt to miniaturise the assay to conserve the periosteum and BM samples as well as the media. The dishes were incubated at 37°C, 5% CO_2. After 48 hours, non-adherent cells were removed with one wash of PBS and fresh StemMACS media was added (15 mL (100 mm diameter) or 5 mL (60 mm diameter)). Half media changes were carried out twice a week for 14 days after initial seeding.

Where periosteum digest yielded adequate cell numbers (Section 2.2), CFU-F assays were also performed. A known number of NCCs (between 5 x 10^3 to 5 x 10^4) were seeded onto 60 mm diameter tissue culture dishes containing 5 mL StemMACS media and half media changes were carried out twice a week for 14 days. The number of NCCs seeded for periosteum samples was dependent on how many NCCs were yielded. As with BM, the dishes were incubated at 37°C, 5% CO_2. On day 14 cells were washed with PBS, fixed using 3.75% formaldehyde for 15 mins and stained with methylene blue for 30 mins and then washed using tap water. Plates were scanned and converted to Tiff images. Colonies were counted – using the 'cell counter' option on ImageJ – from each dish and the mean was taken, each colony was considered to derive from a single MSC.

In order to quantify colony size, CFU-F dish images were calibrated (10 pixel/mm), using the known diameter of the dishes (60 mm or 100 mm). This allowed for individual colonies to be circled and measured to give mean colony surface area (mm^2). Frequency distribution histograms were produced from this data and Gaussian distribution was fitted. To quantify the spread of data (colony surface area) 'full width at half maximum' (FWHM) calculations were carried out using the Gaussian distribution standard deviation outputs as per Equation 4.1. FWHM is an established method to quantify the spread of an X-Ray Diffraction peak, which can be applied to the frequency distribution peaks (Pat et al. 2016).

Equation 4.1: Calculation of 'full width at half maximum' from Gaussian distribution outputs.

Full width at half maximum = 2.355 x standard deviation of the Gaussian distribution curve

4.2.2.1 Calculation of MSC Percentage in Bone Marrow and Periosteum

The number or percentage of MSCs in total NCC count for periosteum could be calculated from the known number of NCCs plated for the CFU-F assay (Equation 4.2). In order to allow for direct comparisons between BM and periosteal dishes colony numbers for BM were first converted to colonies per mL of BM, as per Equation 4.3, based on the volume of BMA that was plated for the CFU-F assay, where 200 µL BMA was plated for the 100 mm dish and 80 µL BMA for the 60 mm dish. Next, total NCC count was divided by the total volume of BMA to give the number of NCCs per mL of BMA (Equation 4.4) and therefore, as with the periosteum samples, the percentage of MSCs in NCC count could be calculated to allow for comparison (Equation 4.5).

Equation 4.2: Calculation of periosteum MSC percentage from CFU-F assays

Percentage of MSCs in NCC Count (Periosteum) = Number of CFU-F colonies / Number of NCCs plated onto CFU-F dish

Equation 4.3: Calculation of the number of CFU-F colonies in 1 mL of BMA dependent on CFU-F dish diameter.

Colonies per mL BMA (100 mm) = Number of Colonies x 5

Colonies per mL BMA (60 mm) = Number of Colonies x 12.5

Equation 4.4: Calculation of the number of NCCs in 1 mL of BMA.

NCC per mL BMA = Total NCC count / Total BMA volume (mL)

Equation 4.5: Calculation of bone marrow MSC percentage of NCCs from CFU-F Assays using Equation 4.3 and Equation 4.4.

Percentage of MSCs in NCCs (BM) = Colonies per mL BMA / Number of NCCs per mL BMA

4.2.3 Cell Growth Assessment in 2D Tissue Culture

In order to compare growth rates (calculated through PDs) of periosteum and BM derived adherent cultures, matched samples were assessed in 2D tissue culture. For periosteal samples, 1.5 x 10^5 NCCs were seeded into 25 cm^2 tissue culture flasks (5 x 10^4 NCCs per cm^2) and for BM samples 5 x 10^6 NCCs were seeded into 25 cm^2 tissue culture flasks (2 x 10^5 NCCs per cm^2) (unless stated otherwise). Seeding density was based on previous knowledge in the group on MSC percentages in BMA and periosteum. For both cell types 5 mL of StemMACS media was added and flasks were incubated at 37°C, 5% CO_2. After 48 hours, non-adherent cells were removed from BM flasks with one wash of PBS and fresh StemMACS media was added. Half media changes were carried out twice a week until 60-80% cell confluence was seen.

At this point flasks were trypsinised (Section 2.3.2) and counted (Section 2.3.1). Cells were reseeded into new 25 cm^2 flasks at densities of 1.25 x 10^5 for periosteum (Eyckmans, Lin & Chen 2012) and 2.5 x 10^5 for BM (Fossett & Khan 2012), this was repeated until at least passage 6 was reached. If the trypsinised cell count of a sample was found to not increase over two passages, senescence was assumed and the sample was not grown further. At each passage, excess cells that were not carried forward to the next passage were frozen (Section 2.3.3) for future experiments.

4.2.4 Calculation of MSC Population Doublings

For BM samples, the estimated number of MSCs seeded into tissue culture (Section 4.2.3), taken from BM NCCs was calculated as follows. Using the calculations from Section 4.2.2.1, Equation 4.3 was used to calculate ‘colonies per mL of BMA’ and Equation 4.3 calculated ‘NCCs per mL of BMA’, therefore these two outcomes were used to calculate the number of NCCs per CFU-F colonies for BM samples (Equation 4.6). From this, the number of colonies or MSCs seeded into the initial tissue culture was quantified from the known number of NCCs seeded (5 x 10^6 NCCs).

For periosteal samples, the number of colonies per number of NCCs seeded for CFU-F assay was used to approximate how many colonies were in the 1.5 x 10^5 NCCs initially seeded in culture.

Cumulative MSC PDs for periosteum and BM derived cultures were calculated as previously described by Churchman et al. (2012). Briefly, PDs accrued for the period up to the first confluence were calculated using Equation 4.7; for the first passage onwards, PD was calculated as per Equation 4.8. Cumulative PDs were then plotted against days in culture to calculate cultures' growth rates in days per PD.

Equation 4.6: Calculation of the number of NCCs per CFU-F colonies from bone marrow samples.

Number of NCCs per CFU-F Colony = NCCs per mL of BMA / Colonies per mL of BMA

Equation 4.7: Calculation of population doubling up to passage 0 (P0).

Population Doubling (<P0) = $\log_2$ (cell count at first trypsinisation/ CFU-F colonies seeded on day 0)

Equation 4.8: Calculation of population doubling from passage 0 (P0) onwards.

Population Doubling (>P0) = $\log_2$ (cell count at trypsinisation/cells seeded)

4.2.5 Flow Cytometry of Bone Marrow and Periosteal Cultures

Flow cytometry of donor matched BM and periosteal cultures was carried out to assess the 'MSC phenotype' of the cells in culture. Antibodies and their isotype (IgG (immunoglobulin G) antibodies) controls were chosen in line with the ISCT approved panel for MSC phenotyping (Table 4.2, full detail of clones used in Appendix 3.1) (Dominici et al. 2006). MSC phenotype can change with exposure to *in vitro* culture conditions (Álvarez-Viejo, Menéndez-Menéndez & Otero-Hernández 2015), therefore it was important to assess cultures at the same *in vitro* age. Using the previously calculated PDs for periosteal and BM cultures, passages of cells frozen at approximately 14 PDs were selected for flow cytometry analysis.

Table 4.2: Details of antibody cocktails used for flow cytometry phenotyping of MSCs.
* Antibody levels quantified using Attune cytometer system

	Antibody	Fluorochrome	Volume (µL)
Tube 1	CD34	APC	10.0
	CD105	FITC	10.0
	CD73	PE	5.0
	CD90	PECy7	2.5
Tube 2	IgG1	APC	5.0
	IgG1	FITC	5.0
	IgG1	PE	5.0
	IgG1	PECy7	2.5
Tube 3	SUSD2	APC	10.0
	CD14	FITC	5.0
	CD19	PE	10.0
	CD45	PECy7	2.5
Tube 4	CD271	APC	10.0
	IgG2a	FITC	5.0
	MSCA-1	PE	10.0
	IgG1	PECy7	2.5
Extra Tubes	CD146	PE	5.0
	CD105	PE	5.0
	HLA-DR*	VioGreen	2.0

Firstly, frozen cells were thawed and recovered in tissue culture, grown in StemMACS media (Section 2.3.4). After a week cells were trypsinised (Section 2.3.2) and counted (Section 2.3.1). For cell staining, cells were centrifuged again and re-suspended in blocking buffer (see Appendix 1.2) for 15 mins at RT and then split into fluorescence-activated cell sorting (FACS) tubes and incubated with different antibody cocktails (Table 4.2) for 30 minutes on ice. 500 µL of FACS buffer (see Appendix 1.1) was added to each tube and centrifuged at 400 g for 5 mins. FACS tubes were then re-suspended in 500 µL 4',6-diamidino-2-phenylindole (DAPI) buffer (see Appendix 1.2) ready to be analysed. DAPI was used as a stain for dead cells.

Cell suspensions were analysed using an LSRII flow cytometer (BD Pharmingen) equipped with four solid state lasers. The laser named Coherent Sapphire™ (Blue, 20 mV at 488 nm excitation) was used for the following fluorochromes, Fluorescein isothiocyanate (FITC), R-phycoerythrin (PE) and (PE/Cyanine7) PECy7. The Lightwave Xcyte™ laser (UV, 20 mV at 355 nm excitation) was used for DAPI and the HeNe laser (Red, 18 mV at 633 nm excitation) was used for Allophycocyanin (APC). The Coherent vioFlame™

PLUS laser (Violet, 25 mV at 405 nm excitation) was not utilised. Spectral compensation was set up with the first sample using single stained control tubes for each fluorophore (SUSD2 – APC, CD105 – FITC, CD73 – PE and CD90 – PECy7). Isotype controls (see Appendix 3.1) were used for each sample to ensure correct gating positioning for each cell population and a minimum of 10,000 events were collected. FACS DIVA software was used to analyse marker expression data; gates were set at 2% of corresponding isotype controls allowing for percentage expression of each marker to be calculated. Overlay plots of each marker with the corresponding isotype control was created.

Half way through the project the LSRII was taken out of commission, therefore a new system was set up, using the Attune 2 Laser system (Applied Biosystems). The Attune system includes a violet laser (405 nm), which excited VioGreen (520 nm emission) and a blue laser (488 nm), which was used to excite FITC and PerCP-Vio (675 nm). As with the LSRII single stain antibody controls were set up and the last three samples were used to quantify HLA-DR expression. Samples were stained as before, using volumes of antibodies found in Appendix 3.2, however samples were resuspended in FACS Buffer opposed to DAPI buffer. Gating strategies were set up and ran as with LSRII, using Attune Cytometric Software (Invitrogen), however live cells were taken based on forward and side scatter rather than DAPI staining.

4.2.6 MSC Differentiation Assays

The trilineage differentiation capacity of BM and periosteum derived cultures was assessed during osteogenic, adipogenic and chondrogenic conditions. Frozen cell stocks of passage 1-3 of matched BM and periosteum-derived cultures were thawed and recovered in tissue culture until confluent, then trypsinised and counted (see Section 2.3.1, Section 2.3.2 and Section 2.3.4). For three donors, an extra well was set up for each donor in the trilineage conditions to be used for RNA extraction (see Section 4.2.3).

4.2.6.1 Osteogenic Differentiation Assay

For the osteogenic assays, 1 x 10^4 cells per well were seeded (number of wells used per assay stated below) into 12 well flat bottom plates with 2 mL of OsteoDiff Media (supplemented with 1% PS, Miltenyi Biotec), or with 3 x 10^4 cells per well in a 6 well flat bottom plate with 3 mL of OsteoDiff Media. Cultures were grown for two or three weeks with bi weekly half media changes and incubated at 37°C, 5% CO_2. Three end-point assays were set up to measure the osteogenic capacity of MSCs.

After two weeks of culture, cells were stained (6 or 12 well plate in duplicate) using Fast Blue to stain for and visualise ALP activity, a marker of early osteogenesis (Aubin 2001). For this, the differentiation media was gently removed from the wells and cells washed twice using PBS. Cells were fixed using citrate fixative (see Appendix 1.2) for 30 seconds, washed twice with distilled water (dH_2O) and then stained with Fast Blue (see Appendix 1.2) for 30 mins in the dark at RT. The wells were then washed twice with dH_2O and left to dry.

When handling the osteogenic assays, care was taken to pipette gently in order to not disturb the cells in the well, cells become less adherent to tissue culture plastic during osteogenic differentiation, when calcium deposits are being produced. After 3 weeks of culture, cells were stained (6 or 12 well plate in duplicate) with Alizarin Red, to visualise calcium deposits following differentiation (Gregory et al. 2004). Media was gently removed and wells were washed in PBS. Cells were fixed in pre chilled (stored in -20°C freezer prior to use) 70% EtOH for 1 h and washed five times with dH_2O. Wells were stained with Alizarin Red (40 mM Alizarin red in dH_2O, pH 4.1, see Appendix 1.2) for 10 mins at RT, followed by five times of washing with dH_2O and left to dry. Post-staining, wells were imaged using bright field microscopy using a microscope (GX-L5200B). Magnifications of x10 were used. Images were captured using an Infinity 1 camera and processed using Infinity Image acquisition software, this allowed for focusing and scale bars to be imposed on images.

In addition, at 3 weeks of culture the calcium content of the wells (12 well plate in triplicate) as quantified using a Calcium assay (Sentinel Diagnostics). Media

was gently removed from the wells and washed twice in PBS (Ca^{2+} free). After this, a known volume (250-500 µL) of 0.5 M hydrochloric acid (HCl) was added to the wells (dependent on how mineralised the sample was when visualised using light microscopy) to hydrolyse the cells. After 10 mins, cells were scraped from the well and the solution was transferred to an Eppendorf tube, Ca^{2+} was extracted through continuous mixing using a tube spinner (VWR) for 4 h, at 4°C. After this samples were stored at -20°C until the Calcium assay was carried out.

Calcium content was quantified using a Calcium Liquid Assay (Sentinel Diagnostics), where samples were thawed and then centrifuged (6000 g, 5 mins) to remove cell debris from solution that could interfere with the assay. The supernatant, containing calcium was then directly plated (4 µL) in triplicate into a flat bottomed 96 well plate. In addition, a calcium standard curve was also set up by serial dilution in 0.5 M HCl from 100 mg/µL to 0 mg/µL and also plated in triplicate (4 µL). The calcium liquid was prepared as per manufacturer instructions at a ratio of 5:2 for Reagent 1: Reagent 2, 200 µL was added to each well. Colour change was seen based on calcium concentration of each sample and the absorbance was measured using a plate reader at 570 nm within 30 mins.

Extra wells were set up for three of the donors to measure DNA content and to be lysed for RNA extraction (See Section 4.2.7.2). To quantify the DNA content of a well, cells were washed with PBS and lysed in 200 µL of 0.1% Triton-X 100 and frozen at -20°C. DNA content was quantified using a PicoGreen Assay (Thermo Scientific) alongside a DNA standard curve, carried out following manufacturer's instructions. Ca^{2+} content was then normalised to DNA content.

4.2.6.2 Adipogenic Differentiation Assay

Adipogenesis assays were carried out in flat bottomed 24 well plates, with 5 x 10^4 cells were per well with 1 mL of AdipoDiff Media (supplemented with 1% PS, Miltenyi Biotec) or in a flat bottom 48 well plate with 4 x 10^4 cells per well with 0.5 mL of AdipoDiff media. Plates were incubated at 37°C, 5% CO_2 and

half media changes were carried out biweekly. Two end point assays to assess fat droplet formation after 3 weeks were set up.

The first assay used Oil Red to stain the cells (Aldridge et al. 2013), on day 21 media was removed and wells were rinsed twice with PBS and then fixed for 10 mins using 3.75% formaldehyde at RT. Formaldehyde was removed and the wells were washed with PBS. Oil red stock (0.5% Oil red in isopropanol, see Appendix 1.2) was diluted prior to use in dH_2O (ratio of 3:2) and filtered using 0.45 µm followed by 0.2 µm filters to remove debris. Oil red staining solution was added to the wells for 10 mins, removed and washed in PBS. Samples were kept in fresh PBS, wells were imaged using bright field microscopy using a microscope (GX-L5200B). Magnifications of x10 were used. Images were captured using an Infinity 1 camera and processed using Infinity Image acquisition software, this allowed for focusing and scale bars to be imposed on images.

The second assay used Nile Red and DAPI (nuclei stain), to be able to quantify the fat deposition as well as the cell density (Aldridge et al. 2013). After 3 weeks media was removed and the wells were washed twice in PBS. The cells were fixed in 3.75% formaldehyde for 30 mins at RT. The formaldehyde was removed and the wells were washed twice with PBS and 200 µL of PBS was added back to the wells. At this point the plate was read on a fluorescent plate reader (Berthold) for DAPI (355/460 nm) and Nile Red (485/535 nm) to establish the background reading.

After removal of the PBS, 200 µL of a Nile Red and DAPI solution (1 µg/mL in 0.2% Saponin, in PBS, see Appendix 1.1) was added to the wells and incubated for 15 mins at RT in the dark. Three PBS washes followed to remove excess dye and 200 µL of PBS was added to each well. The plate was then read again on a plate reader for DAPI and Nile Red as above. The absorbance readouts were exported onto Excel spreadsheets, the background absorbance was subtracted from ‘stained’ absorbance for both quantification of DAPI and Nile Red levels. In addition, Nile Red levels were normalised to DAPI levels (Nile Red:DAPI ratio).

4.2.6.3 Chondrogenic Differentiation Assays

Chondrogenic assays were carried out in sterile 1.5 mL screw cap Eppendorf tubes, where 2.5 x 10^5 cells were added to each tube and centrifuged (800 g, 5 mins). The supernatant media was removed and the cell pellet was resuspended in 0.5 mL of ChondroDIFF media (supplemented with 1% PS, Miltenyi Biotec). The tubes were centrifuged (800 g, 5 mins) to create a cell pellet, this pellet was left, the cap was loosened to allow for gaseous exchange and placed in an incubator at 37°C, 5% CO_2 for 3 weeks. Half media changes were made three times a week.

After 3 weeks, pellets had formed, these were removed and photographed for macro images. A pellet was then snap frozen in optimal cutting temperature (OCT) compound, using liquid nitrogen for histological purposes and stored at -20°C. Frozen pellets were cut using a cryostat (Leica Biosystems) and allowed to dry onto histology slides. This was followed up by staining for GAG content using toluidine blue. Slides were fixed for 2 mins with methanol (pre chilled to -20°C) and then stained with toluidine blue (1% toluidine blue in 50% isopropanol, diluted with dH_2O, pre warmed to 37°C) for 30 mins at 37°C. Slides were decolourised for a few seconds in isopropanol, dehydrated in xylene (3 rounds, 5 mins) and covered with a cover slip using DPX and imaged using light microscopy.

In addition, three pellets were digested in 100 µL of papain digest buffer (see Appendix 1.2) in a water bath, at 65°C overnight. The sulphated GAG content of the digested pellet was then quantified using a sulphated GAG assay kit (Blyscan). A GAG standard (0-5 µg) was set up in Eppendorf's alongside test samples, 1 mL of Blyscan dye reagent was added to each tube, and placed on a mechanical shaker for 30 mins, RT. Tubes were centrifuged (13,400 g, 10 mins) to form a GAG-dye complex at the bottom of the tube, the supernatant was removed. Dissociation reagent (0.5 mL) was added to the tubes and vortexed to release the bound dye into solution, followed by another centrifuge step (13,400 g, 5 mins). 200 µL of each sample was transferred to a 96 flat well plate in duplicate for the standards and test samples and read using a plate reader at 656 nm.

4.2.7 Quantitative Reverse Transcription-PCR

As further confirmation of the trilineage differentiation assays (Section 4.2.6), RNA was taken from three matched BM and periosteum samples at day 0 (samples grown in StemMACS media, prior to differentiation) as well as at day 21 from each of the trilineage differentiation assays. The gene expression markers indicated for osteogenesis (RUNX2 and Bone gamma-carboxyglutamate (gla) protein (Osteocalcin) (BGLAP)), adipogenesis (fatty acid binding protein 4 (FABP4) and peroxisome proliferator-activated receptor-gamma (PPAR-γ)) and chondrogenesis (Collagen, type 2, alpha 1 (COL2A1) and Sox9) were used to assess how gene expression of these transcripts' changes following differentiation induction for each MSC type.

4.2.7.1 Preparation of RNA Lysates

Following the setup of differentiation assays (Section 4.2.6), excess cells were centrifuged (650 g, 5 min). The supernatant was removed, and the cell pellet was re-suspended in sterile PBS and transferred into autoclaved 1.5 mL Eppendorf tubes to be centrifuged again (650 g, 5 min), and the supernatant was removed. The cell pellet (containing at least 1 x 10^5 cells) was lysed in 200 µL RNA lysis buffer (1:100 β-Mercaptoethanol with RL buffer, Norgen) for each sample and transferred to -80°C for storage until RNA extraction.

As previously described (see in Sections 4.2.6.1, 4.2.6.2 and 4.2.6.3), an extra well (osteogenesis and adipogenesis) or tube (chondrogenesis) was set up per differentiation assay. At day 21 differentiation media was removed from the well or tube, and a sterile PBS wash was carried out to remove excess media. After this 200 µL of RNA lysis buffer was added to the wells or tubes to lyse the cell monolayer (osteogenesis and adipogenesis) and cell pellet (chondrogenesis). The RNA lysate was then transferred into autoclaved 1.5 mL Eppendorf tubes and frozen at -80°C until RNA extraction was carried out.

4.2.7.2 RNA Extraction

RNA extraction was carried out using a Single Cell RNA Purification Kit (Norgen), as per manufacturers guidance. RNA lysates were removed from -80°C and thawed on ice. Each lysate sample was made up to 600 µL in

volume by adding 400 µL of EtOH, the entire lysate volume was added to a 'Single cell RNA Spin Column', sat inside a collection tube. The column was centrifuged (15,700 g, 1 min - the standard speed and time that was carried through for the rest of RNA extraction), and the flow through was discarded. At this point the RNA is bound to the column. The column was washed by adding 400 µL of Wash Solution A to the column and centrifuging, the flow through was discarded.

To elute the RNA, the column was transferred to a 1.7 mL Elution tube (provided with the kit and RNA free), 15 µL of Elution Solution A was added to the column, care was taken to ensure the solution went on the column and the column was centrifuged. This released the RNA from the column into Elution Solution A. The RNA concentration of each sample was measured using a NanoDrop Spectrophotometer. Elution Solution A was used to zero the equipment and 2 µL of the 15 µL of RNA was added to the stage. Measurements were taken at 230 nm, 260 nm and 280 nm and the 260/280 and 260/230 ratios were calculated as well as the RNA concentration in ng/µL (calculated by the NanoDrop software). A 260/280 ratio of ~1.8 is a good measure of pure DNA and ~2.0 is a good measure of pure RNA, whereas a low ratio suggests contamination with protein or phenol that absorb at 280 nm. A 260/230 ratio of 2.0-2.2 is another estimate of nucleic acid purity, where a low ratio suggests contaminants that absorb at 230 nm (EDTA, carbohydrates or phenol). After calculating RNA concentration, purified RNA samples were stored at -80°C.

4.2.7.3 cDNA Synthesis – Reverse Transcription

RNA samples were thawed and kept on ice. Using the RNA concentrations of each sample, measured in Section 4.2.7.4, the volume needed for 100 ng of RNA was calculated, and diluted with Nuclease Free Water, to make a 10 µL of solution, into a reaction tube (e.g. RNA concentration of 44 ng/µL, 2.27 µL of RNA was mixed with 7.73 µL of Nuclease Free Water, to give 10 µL containing 100 ng of RNA).

A reverse transcription master mix was made up per sample as shown in Table 4.3, and 10 µL of the master mix was transferred to each reaction tube.

Tube caps were added to the reaction tubes and the samples were put in a Thermal Cycler (Applied Biosystems), with a pre-set step cycle (Table 4.4), samples of cDNA were then kept at -20°C for storage.

Table 4.3: Master mix components for reverse transcription

Component	Reverse Transcription Mix (µL)
10x RT Buffer	2.0
25x dNTP Mix	0.8
10x RT Random Primers	2.0
Multiscribe Reverse Transcriptase	1.0
RNase Inhibitor	1.0
Nuclease Free Water	3.2
Total Volume Per Reaction (µL)	**10.0**

Table 4.4: Thermocycler programme for reverse transcription

	Step 1	Step 2	Step 3	Step 4
Temperature (°C)	25	37	85	4
Time (min)	10	120	5	Until transferred to -20°C

4.2.7.4 TaqMan Assays for Real Time-PCR

Each sample was loaded onto a 384 well plate, kept on ice, in duplicate for each of the 6 TaqMan Probes (see Appendix 4.1) tested and also in duplicate for the housekeeping gene, hypoxanthine phosphoribosyltransferase 1 (HPRT1) (a total of 14 wells per sample). Each well consisted of 0.5 µL of TaqMan gene expression assay (Thermo Fisher) (see list of primers in Appendix 4.1), 5 µL TaqMan Universal Master Mix and 4.5 µL of cDNA (diluted in nuclease free water when needed). The plates were sealed with a cover (MicroAmp™ Optical Adhesive Film), centrifuged to eliminate air bubbles and ensure the contents were mixed at the bottom of each well. The real time-PCR (RT-PCR) reaction was run with the conditions set out in Table 4.5 using a QuantStudio™ 7 Flex Real-Time PCR System and SDS software, which recorded the fluorescence in real time. Data was normalised to the reference housekeeping gene HPRT1 to exclude variations of potentially different levels of mRNA in the reaction. Analysis was carried out using the $2^{-\Delta(Ct)}$ method, to calculate normalised gene expression (Churchman et al. 2012). Whereby, Ct refers to ‘cycle threshold’, the number of cycles required for the fluorescence

signal to reach threshold detection. Δ(Ct) refers to change in Ct of test gene compared to HPRT1.

Table 4.5: Real Time-PCR Thermocycler conditions

	Step 1	Step 2	Step 3 (40 x amplification cycles)	Step 4
Temperature (°C)	50	95	95	60
Time (min)	2	10	10 sec	1

4.2.8 CellTrace™ CFSE Fluorescent Cell Tagging

Adherent cell cultures of periosteum MSCs were stained with CellTrace™ CFSE (5(6)-Carboxyfluorescein N-hydroxysuccinimidyl ester) Cell Proliferation Kits (Invitrogen) (referred to as CFSE). CFSE is a non-fluorescent 'pro-dye' that can cross cell membranes, once intracellular, acetate groups are cleaved by intracellular esterase's, resulting in carboxyfluorescein (that now fluoresces green), which is membrane impermeant. Succinimidyl ester groups react with intracellular free amines, resulting in covalently bonded dye-protein conjugates that act as a fluorescent label that can be quantified. CFSE was diluted to a stock concentration of 5 mM through adding 18 µL of DMSO to a vial of CellTrace™ reagent and mixing well. The stock concentration CellTrace™/DMSO solution was further diluted in 10 mL (2.5 µm), 20 mL (5 µm) or 40 mL (10 µm) pre warmed (37°C) protein free DMEM (FCS free).

A flask of adherent cultures of periosteum MSCs, previously thawed (Section 2.3.4), counted (Section 2.3.1) and seeded into tissue culture flasks 4 days prior had media removed and washed with PBS to remove trace presence of FCS that would inactivate CFSE, 5 mL of the loading solution (at either 2.5 µm, 5 µm or 10 µm) was added to the flask and incubated for 20 mins at 37°C, 5% CO_2, protected from UV. The loading solution was removed from the flask and the cells were washed twice with DMEM media with 10% FCS and replaced with pre warmed StemMACS media and incubated at 37°C, 5% CO_2 for 20 mins, to allow for acetate hydrolysis (described above) to take place.

Flasks were imaged immediately post staining, 1 days and 4 days post staining using a CKX41 Microscope (Olympus) with a fluorescent bulb attachment to view the cells under brightfield and fluorescent light. Separate flasks of CFSE stained (concentrations 2.5 µm, 5 µm and 10 µm) and non-stained periosteal cells were trypsinised (Section 2.3.2) and counted (Section 2.3.1). At each concentration, two conditions were created, 'stained only' and 'stained and unstained', whereby stained cells and unstained cells were added together at a 1:1 ratio and 2 x 10^5 cells were taken for flow cytometry analysis and the rest returned to tissue culture for later time points.

4.2.8.1 Flow Cytometry of CellTrace™ CFSE

The different experimental conditions were further stained with antibodies for CD73 and CD45 (lymphocyte common antigen) (as per Section 4.2.5 and Table 4.2) as a positive and negative MSC marker, respectively, as per Section 4.25). Briefly, cells were transferred to FACS tubes and centrifuged (400 g, 5 mins), re-suspended in blocking buffer (15 mins, RT) and then incubated with the antibodies (30 mins, on ice). FACS buffer was added and the cell suspension was centrifuged again (400 g, 5 mins) and re-suspended in 500 µL of DAPI buffer to be analysed using an LSR II flow cytometer (BD Pharmingen). Isotype controls had been previously set up (Section 4.2.5) and CFSE with excitation and emission peaks of 492 nm and 517 nm was equivalent to FITC, therefore the cytometer settings were carried forward from previous experiments. A minimum of 10,000 events were collected, and FACS DIVA software was used for analysis.

4.2.9 Statistical Analysis

Where possible statistical analysis was carried out using paired, non-parametric tests (Wilcoxon matched-pairs signed rank test) to compare donor matched periosteum and BM samples, where $P<0.05$ was considered significant. Data was presented mean ± standard error of the mean (SEM).

4.3 Results

Donor matched samples of human periosteum and iliac crest BMA were harvested from patients undergoing orthopaedic surgery. MSCs were isolated from both tissue sources using collagenase digest and RBC lysis, respectively. Following CFU-F assays, NCCs were grown alongside in 2D tissue culture to compare growth kinetics, MSC flow cytometry phenotype, as well as trilineage differentiation capacity for osteogenesis, chondrogenesis and adipogenesis. In addition to this, the presence of a candidate marker for periosteum MSCs, fluorescent cell tagging of MSCs and the effect of co-culture of periosteum and BM MSCs on osteogenesis was investigated.

4.3.1 MSC Colony Formation and Growth Characterisation

CFU-F assays are the standard for quantification of the number of MSCs in various tissue types (Sakaguchi et al. 2005). However, there is little CFU-F data on periosteum, especially compared to donor matched BM, thus insight into the growth kinetics of periosteum derived cells from digest to the first passage is needed. Here, for the first time the colony forming potential of cells released from freshly digested human periosteum samples in comparison to donor matched BMA was carried out.

Donor matched iliac crest BMA and periosteum samples (n=10) were collected and CFU-F assays were carried out to quantify colony formation as a measure of MSC frequency (Figure 4.1A). Each colony (of greater than 50 cells) was counted and taken to represent the presence of a singular MSC, the frequency of MSCs in the NCC count was calculated (see Section 4.2.2) in order for comparisons of BM and periosteum CFU-Fs to be carried out.

BM CFU-F showed that $7.9 \times 10^{-4} \pm 2.2 \times 10^{-4}$% (or 1 in $2.0 \times 10^{4} \pm 3.9 \times 10^{3}$ NCCs) of NCCs seeded formed colonies and therefore taken as the percentage of cells within BM that are MSCs, however, this was significantly different (Wilcoxon test, n=10, P=0.004), by a 4 log fold margin, to 2.0 ± 0.6% (or 1 in 43 ± 32 NCCs) MSC frequency for periosteum (Figure 4.1B). In order to further analyse the differences between colony formation, donor matched CFU-F dishes were scanned (Figure 4.1A) and colony surface area was

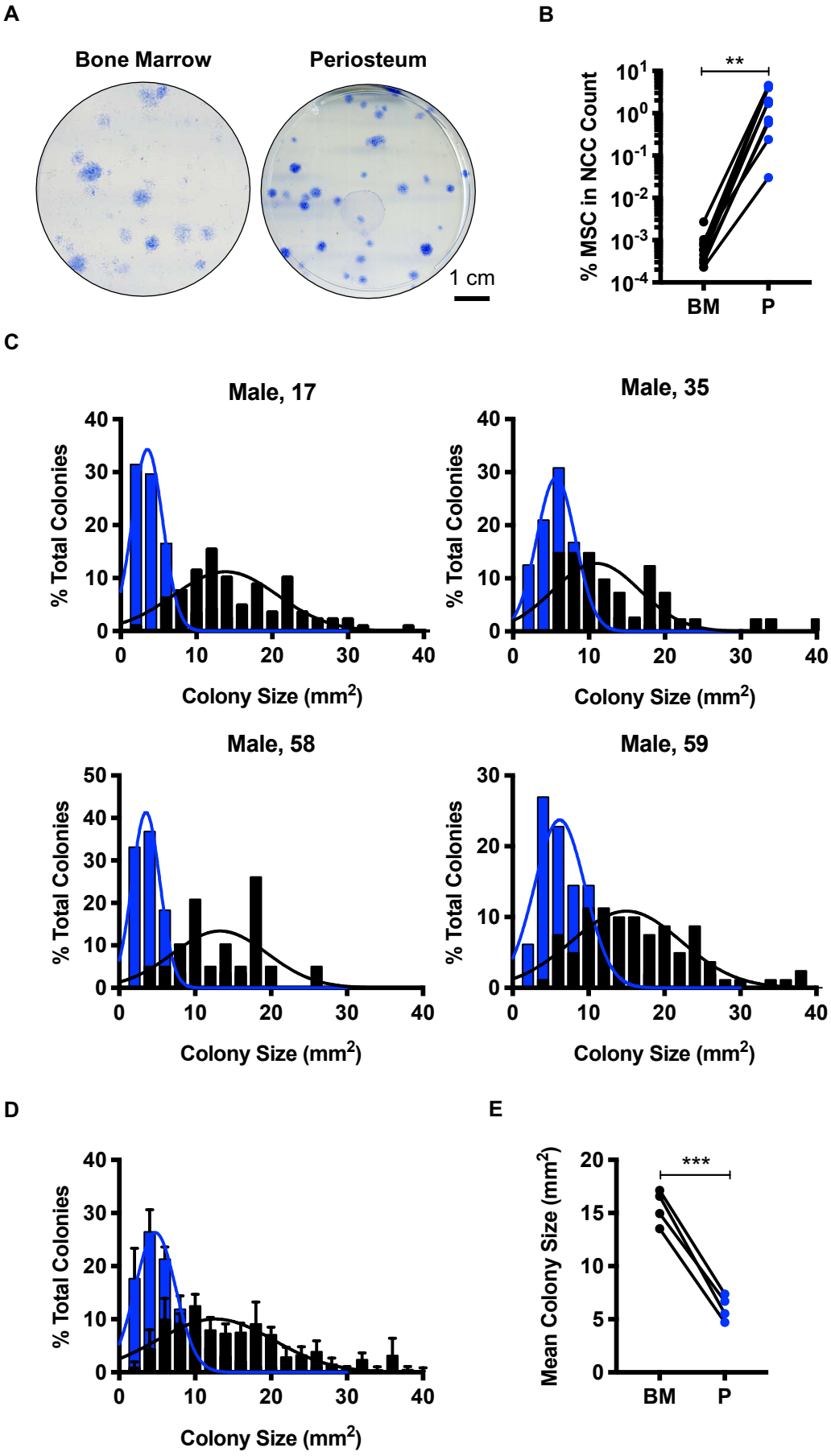

Figure 4.1: Quantification of colony number and size in donor matched periosteum and bone marrow samples. A) Representative CFU-F plate stained with methylene blue. **B)** Percentage MSC (defined as a single colony)

in nucleated cell count. **C)** Colony surface area of 4 donor matched samples was quantified and frequency distribution plotted. **D)** Pooled colony size (n=4). **E)** Mean colony size for each donor was shown (n=4). Black – bone marrow (BM), blue – periosteum. Gaussian distribution shown on graphs C-D. Statistical tests carried out using Wilcoxon test (B) ** P=0.004 or a paired Students t-test (E) *** P=0.0006.

quantified from dishes with more than 20 colonies (n=4). When comparing colonies from individual donors (Figure 4.2C) as well as pooling the four donors together (Figure 4.1D), periosteum colonies where shown to be more homogenous and smaller compared to BM colonies, which were more heterogeneous and larger. Periosteum colonies ranged from 2.0-29.6 mm^2, with a mean colony size of 6.1 ± 0.6 mm^2, compared to BM colonies which ranged from 2.1-54.3 mm^2, with a significantly higher mean colony size of 15.5 ± 0.8 mm^2 (paired Students t-test, n=4, P=0.0006) (Figure 4.1E). This shows that BM has a subset of larger colonies over the size of 30 mm^2, accounting for 6.4 ± 2.2% of all BM colonies, that were not seen in periosteum colonies.

Colony surface area was normally distributed (Figure 4.1C-D) and as a measure of the spread of distribution, FWHM was calculated (Section 4.2.2). BM colonies had a distribution spread of 15.32 ± 0.79 mm^2 which was significantly higher than the periosteum colonies at 5.73 ± 0.79 mm^2 (paired Students t-test, P=0.001). Thus, confirming the homogenous nature of periosteum colonies compared to BM. Taken together this showed that MSCs in periosteum were significantly more frequent, which formed colonies that were more homogenous in size, in comparison to BM.

4.3.2 Growth Kinetics

Long term *in vitro* culture was carried out to test whether the aforementioned differences affected MSC proliferation in the long term. There is a lack of quantification of MSCs present in periosteum cultures; the current literature typically refers to growth kinetics starting from the first passage onwards (Eyckmans, Lin & Chen 2012). Therefore, comparison of the growth kinetics from day 0 (day of digestion) of donor matched BM and periosteum cultures was investigated. Donor matched cultures were grown in tissue culture until passage 4. Two growth patterns could be seen for both tissue sources, the first from day 0 (when the sample was initially seeded) to P0 (<P0) and then

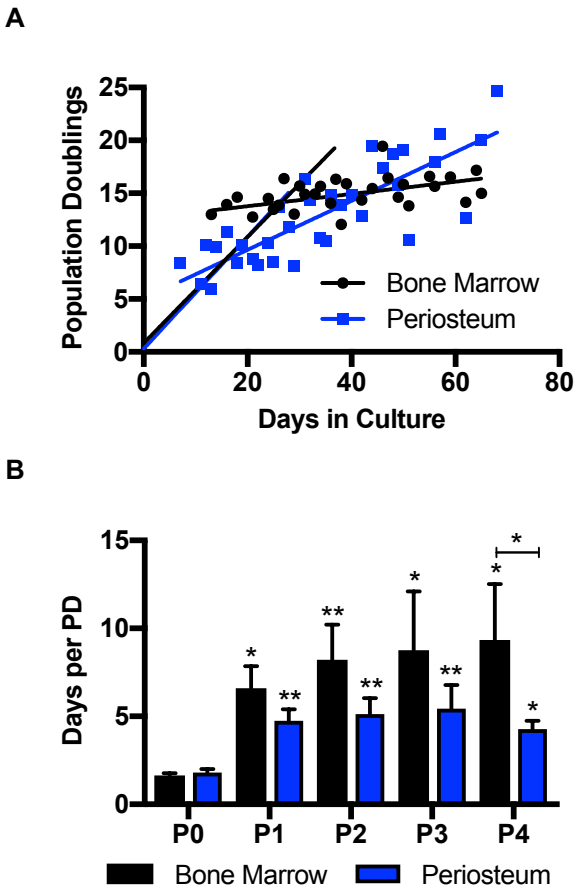

Figure 4.2: Growth kinetics of donor matched periosteum and bone marrow derived cells in 2D tissue culture conditions. A) Pooled cumulative population doublings (PD) against days in culture for nine donors. **B)** days per PD for each passage (P0-P4), showing two distinct growth rates from day zero in culture to the first passage and first passage to passage four. Kruskal-Wallis test for comparison of P0 to P1-P4, * P<0.02, ** P<0.001. Wilcoxon test between bone marrow and periosteum at each passage, * P<0.05.

from P0 onwards (>P0) (Figure 4.2). Time (days) per PD for <P0 was not significant (Mann-Whitney U test, P>0.05) between BM (1.64 ± 0.13 days per PD) and periosteum cultures (1.80 ± 0.21 days per PD) (Figure 4.2A-B). Linear regression was carried out to quantify the slope of the <P0 growth line, which again were similar at 0.50 (BM) and 0.53 (periosteum), with good correlation shown through r^2 values of 0.87 and 0.91 respectively. However, as BM cultures were starting from a lower number of MSCs compared to periosteum (Figure 4.1B), a significantly higher number of PDs were seen at P0 in BM cultures, compared to periosteum cultures (BM – 13.26 ± 0.46 PDs at P0, Periosteum – 8.46 ± 1.1 PDs at P0, P=0.02 – Wilcoxon test). Again, linear regression was carried out, whereby the slope of the >P0 growth lines

were 0.06 (BM) and 0.23 (periosteum), with r^2 value of 0.19 and 0.62 respectively, showing that although periosteum showed consistency and correlation between time in culture and PDs, BM samples did not past P0. This gives a previously unknown insight into the early growth of MSCs in tissue culture, where it is important to note that periosteum cultures are likely to be 'younger', with lower *in vitro* ageing than their BM counterparts at the same passage.

After the first passage (P1-P4) the rate of PD was seen to significantly slow in both culture types (Figure 4.2B), where in comparison to P0, days per PD was seen to be significantly increased at P1, P2, P3 and P4 (Kruskal-Wallis test, $P<0.01$). However, there were no significant differences seen between BM and periosteum cultures until P4, where it became significant as days per PD increased two fold, from 4.28 ± 0.47 days for periosteum to 9.34 ± 3.17 days for BM (Wilcoxon test, $P<0.05$).

Here it has been shown that PDs up to P0 are similar between the two MSC sources, however, proliferation rates drop off significantly following passage for BM sources, whereas periosteum proliferation continues, this could be related to the smaller number of MSCs BM cultures start from.

4.3.3 MSC Flow Cytometry Phenotyping

In vitro cultures were started from a mixed population of NCCs, of which only a small percentage were initially MSCs (Figure 4.1), therefore the ISCT MSC phenotype (Dominici et al. 2006) was tested on BM and periosteum cultures of a similar PD (approximately 14 PD, passages 2-4). The expression level for CD73 (ecto-5'-nucleotidase), CD90 (Thy1) and CD105 (Endoglin) was >94% and below 2.5% for CD14 (monocyte differentiation antigen), CD19 (B-lymphocyte antigen), CD34 (haematopoietic progenitor cell antigen), CD45 (lymphocyte common antigen, hematopoietic cell marker) and HLA-DR (human leukocyte antigen-DR isotype) (Figure 4.3).

The original conjugate for CD105 was FITC (see Table 4.2 and Appendix 3), which showed low expression, after increasing the volume of antibody used from 5 to 20 µL and seeing little improvement on the percentage expression for both cell culture types a PE conjugate was used instead. In addition, where

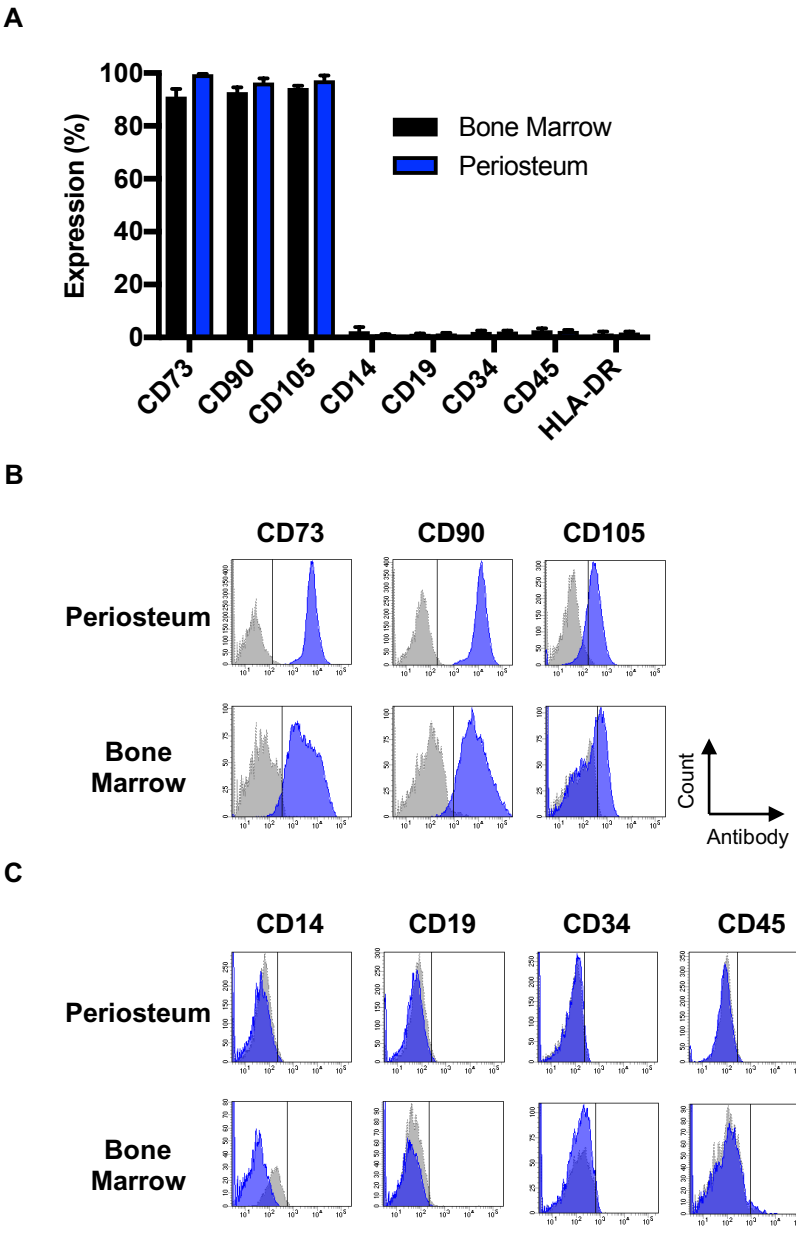

Figure 4.3: Cell surface marker phenotype of donor matched periosteum and bone marrow MSCs. A) Percentage expression of positive MSC markers CD73, CD90 and CD105 and negative MSC markers CD14, CD19, CD34, CD45 and HLA-DR, **B-C)** representative flow cytometry histograms of positive (B) and negative markers (C). Data presented as mean ± SEM.

needed BM cultures were tested again at a later passage due to small amounts of contamination (data not shown) with haematopoietic lineage cells, particularly CD34+ cells (haematopoietic progenitors), CD45+ cells (lymphocytes) or CD14+ cells (monocytes), still present by P2 or P3. It is clear that there is contamination in early BM cultures with haematopoietic cell lineages, that is not seen in periosteum cultures. However, it is unknown

whether this could enhance colony formation during CFU-F assays. The cells in periosteum and BM cultures will now be referred to as MSCs, due proof of colony formation, tissue culture adherence and a known 'MSC phenotype'.

4.3.4 Trilineage Differentiation Capacity

Differentiation assays were not only carried out to prove the tri-lineage nature of periosteum and BM MSCs, but also to ascertain whether there are any differences in differentiation potential of the two MSC sources. Of particular importance are the osteogenic and chondrogenic potential, through the direct need for CSBD repair of formation of osteoblasts and chondrocytes. Tri-lineage differentiation assays were carried out on donor matched BM and periosteum MSCs, from cultures of passages 2-4.

4.3.4.1 Osteogenesis

Osteogenic assays were carried out for two weeks and the cells were fixed and stained with Fast Blue for ALP activity, visually similar staining for ALP could be seen. However, there was noticeably more proliferation by periosteum MSCs compared to donor matched BM MSC for each donor, seen as much higher cellular density within each well (Figure 4.4A). Increased proliferation was also seen after three weeks, when cultures were stained for Alizarin Red to show calcium deposition.

Calcium content was quantified at three weeks and was found to be 68.8 ± 24.52 µg/mL (range 8.2-182.9 µg/mL) for periosteum MSCs, which was slightly higher than in BM MSCs, at 44.0 ± 16.9 µg/mL (range 7.5-126.6 µg/mL) (Figure 4.4B), differences seen were not significant (Wilcoxon test, n=7, P=0.08). However, on an individual donor basis, significance (Wilcoxon test, $P<0.05$) was seen with three donors, Male, 17 (P=0.0007), Male, 44 (P=0.009) and Male, 61 (P=009) (Figure 4.4C). There was variation in the trends seen between donors where 5 out of the 7 donors (Male, 17, Male, 23, Male, 35, Male, 44 and Male, 55) showed increased calcium deposition by periosteal MSCs, while 2 showed reduced calcium deposition (Female, 49 and Male, 61). Suggestive of large donor variation that does not appear correlate with donor age, as linear regression analysis showed low r^2 values of 0.17

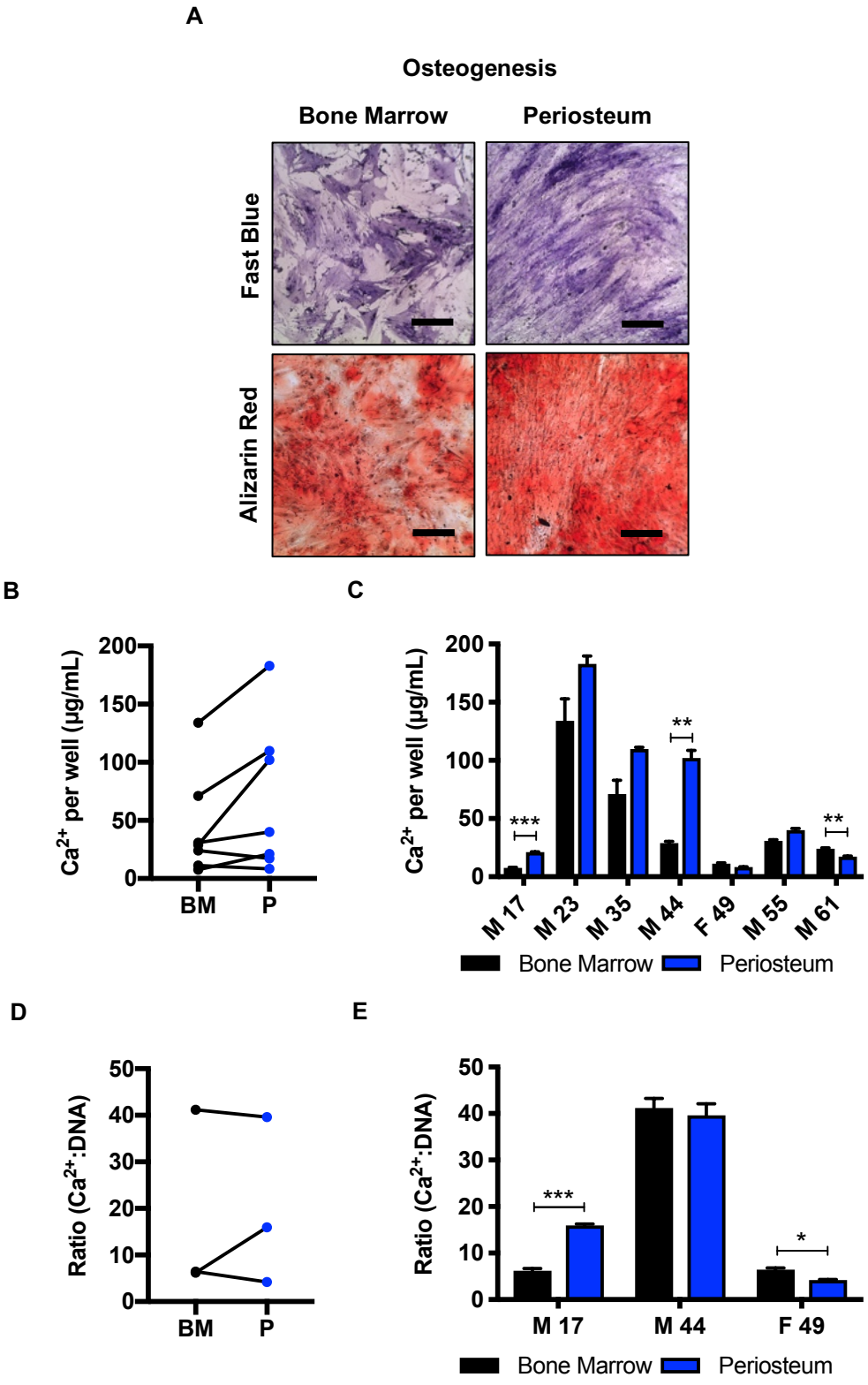

Figure 4.4: Comparison of donor matched periosteum and bone marrow MSC osteogenic differentiation potential. A) Light microscopy images for alkaline phosphatase (fast blue) and Ca^{2+} deposition (alizarin red). **B)** Pooled donor matched bone marrow (BM) and periosteum Ca^{2+} content per well (n=7). **C)** Individual matched donors of BM and periosteum MSC Ca^{2+} content per well (n=7). **D)** Ca^{2+} content per well was normalised to DNA content, quantified using the PicoGreen Assay. Pooled donor matched BM and

periosteum Ca^{2+} content:DNA ratio (n=3). **E)** Individual matched BM and periosteum Ca^{2+} content:DNA ratio (n=3). Black - BM, blue – periosteum (P). Wilcoxon test, * P<0.05, ** P<0.01, *** P<0.001. Data presented as mean ± SEM. Scale bars represent 500 μm.

(BM) and 0.22 (periosteum), related to the low mineralisation of Male, 17.

As proliferation rates were visually different between the two culture types, the effect of the number of cells within the well, taken as DNA content, was assessed. For three donors an extra well was added, whereby a PicoGreen DNA assay was carried out to quantify DNA content. BM cultures lower levels of DNA compared to periosteum cultures, at 1.23 ± 0.31 ng per well and 1.96 ± 0.36 ng per well, respectively, however differences were not significant (Wilcoxon test, n=3, P=0.25). Calcium content was normalised to DNA levels and when pooled (Figure 4.4D), differences were not significant (Wilcoxon test, n=3, P<0.05). However, significant (Wilcoxon test, n=3, P<0.05) differences were still seen between two of the three tested cultures, Male, 17 (P=0.001) and Male, 44 (0.03) (Figure 4.4E). Of note the MSCs derived from Male, 44 showed a significant increase of 76.21 μg/mL (Ca^{2+} per well) from BM to periosteum cultures (Figure 4.4C), however, when normalised to DNA content, the differences in Ca^{2+} production per cell was not significant (P=0.7).

This again highlighted the donor variability of these samples, as well as the fact that the proliferation rates can have an impact on mineralisation on a donor by donor basis. In addition, no significant differences were seen when individuals were pooled, due to the variation in mineralisation seen between donors (Figure 4.4B & D). There was also a trend in a reduction of Ca^{2+} production with age, however, due to the low Ca^{2+} production by Male, 17, a strong conclusion cannot be made on this.

4.3.4.2 Chondrogenesis

After three weeks in chondrogenic conditions, pellets of similar sizes were seen to form in periosteum and BM pellet cultures and staining for GAG (toluidine blue) was confirmed in both MSC pellet types (Figure 4.5A). Upon quantification of pellet GAG content, no significant differences (Wilcoxon test, n=5, P=0.99) were seen between periosteum and BM pellets, when different donors were pooled (Figure 4.5B), where GAG production was 5.34 ± 0.89 μg

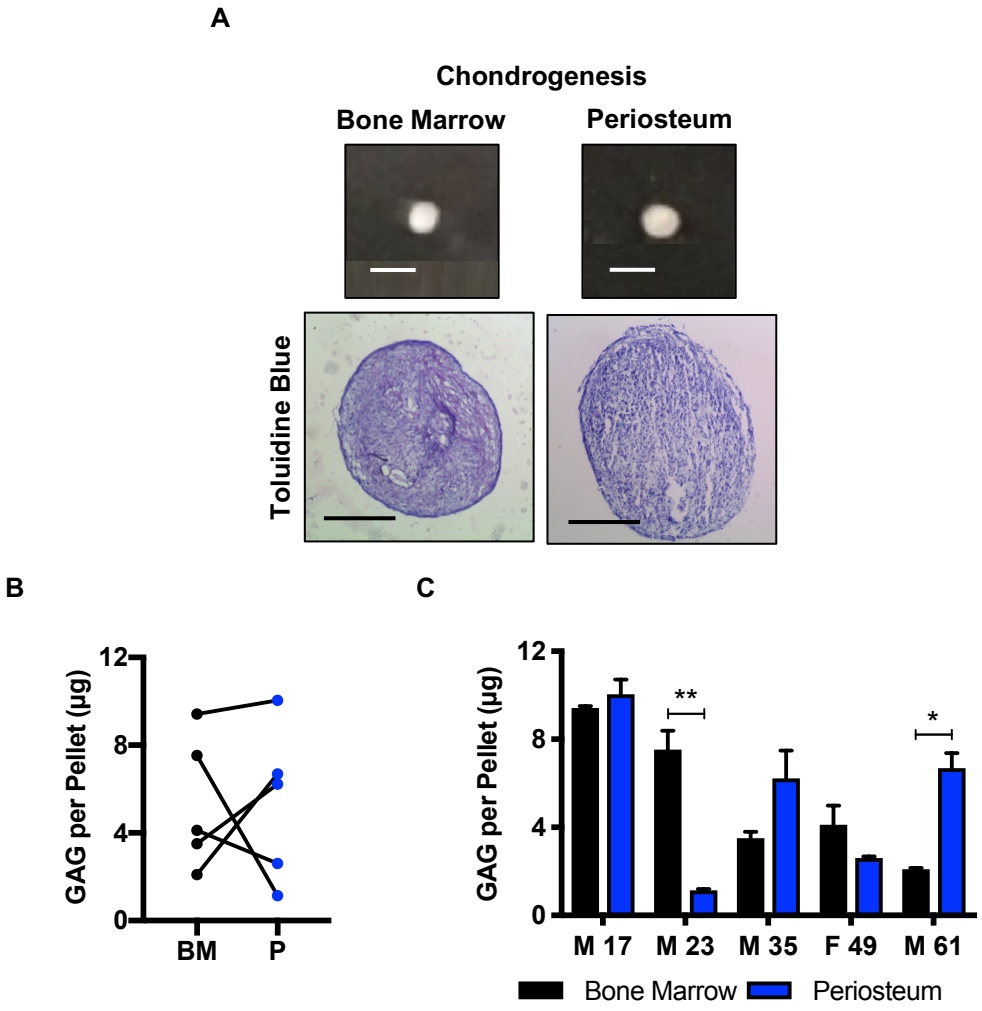

Figure 4.5: Comparison of donor matched periosteum and bone marrow MSC chondrogenic differentiation potential. A) Macro image of pellets formed and light microscopy images of chondrogenic staining for glycosaminoglycans (GAG) (toluidine blue). **B)** Pooled donor matched bone marrow (BM) and periosteum GAG content (n=5). **C)** Individual matched donors for GAG content of pellets (n=5). Black - BM, blue – periosteum (P). Wilcoxon test, * P<0.05, ** P<0.002. Data presented as mean ± SEM. Scale bars represent 2 mm (macro images) and 500 µm (toluidine blue).

and 5.68 ± 0.81 µg per pellet, respectively. As with the osteogenic assays, when individual donors were assessed wide variation in GAG production was shown. There was a trend for age to negatively affect GAG production for BM MSCs, whereby linear regression showed a high correlation of $r^2 = 0.77$ that was not seen by periosteum MSCs ($r^2 = 0.02$) (Figure 4.5C). Periosteum MSC GAG content ranged from 1.14-10.05 µg per pellet and BM MSC ranged from 2.10-9.42 µg per pellet. Of the five donors tested, three had higher periosteum MSC GAG content (Male, 17, Male, 35 and Male, 61), and two had lower GAG content (Male, 23 and Female, 49). However, only two donors were shown to

be significantly different from each other (Wilcoxon test, n=3, P<0.05), Male, 23 (P=0.002) and Male, 61 (P=0.01).

4.3.4.3 Adipogenesis

Adipogenic assays were carried out for three weeks, there was noticeably greater fat deposition in BM cultures compared to periosteum MSC cultures (Figure 4.6A) (n=6). Upon quantification this was confirmed with a significant increase in Nile Red:DAPI ratio for BM cultures in comparison to periosteum cultures (Wilcoxon test, n=3, P=0.02) (Figure 4.6B). In addition, when looking at donors individually, each BM culture displayed significantly higher Nile Red:DAPI ratios (Wilcoxon test, n=3, P<0.05).

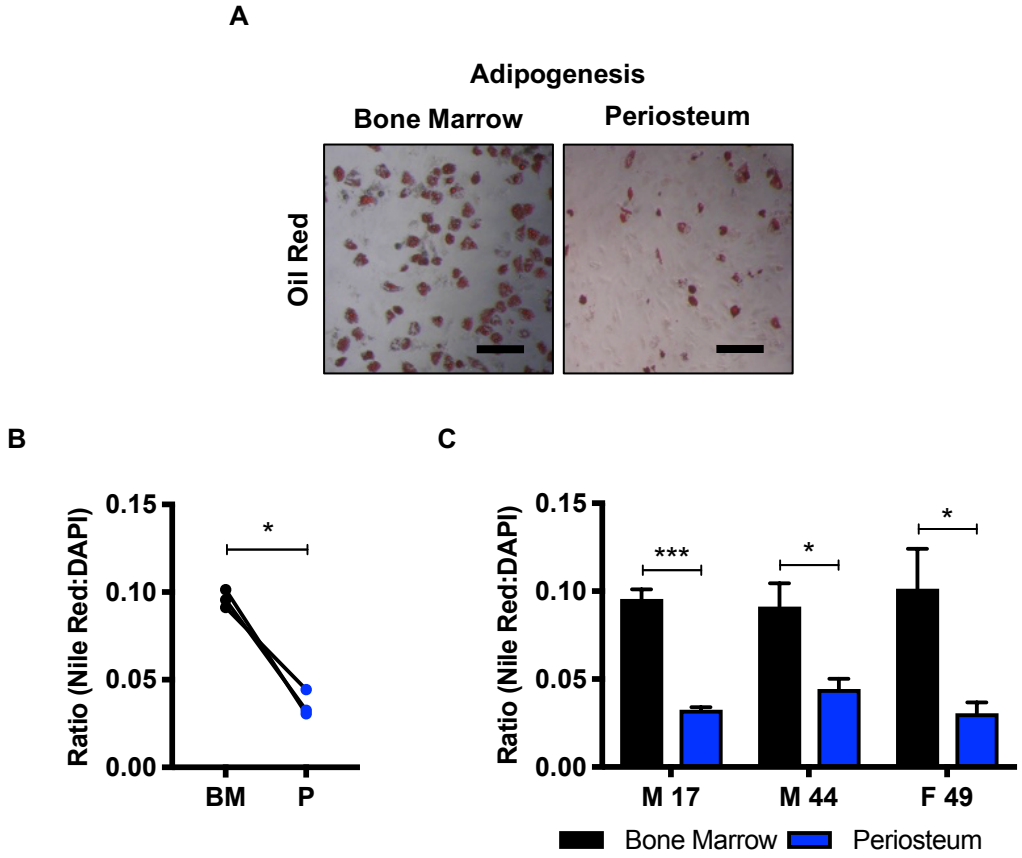

Figure 4.6: Comparison of donor matched periosteum and bone marrow MSC adipogenic differentiation potential. A) Light microscopy images of adipogenic staining for fat droplet formation (oil red). **B)** Pooled donor matched bone marrow (BM) and periosteum Nile Red:DAPI ratio (n=3). **C)** Individual matched donors for Nile red staining, DAPI staining and Nile Red:DAPI ratio (n=3). Black – BM, blue – periosteum (P). Wilcoxon test, * P<0.05, ** P<0.003, *** P<0.003. Scale bars represent 500 µm.

4.3.4.4 Gene Transcript Expression Following Differentiation Induction

RT-PCR was carried out on MSC cultures from 'day 0', grown in StemMACS media, in comparison to cultures after 21 days in osteogenic, chondrogenic or adipogenic differentiation media for donor matched BM and periosteum MSCs (n=3) (Figure 4.7).

On day 21, following osteogenic induction, increases in BGLAP, a common marker for osteogenic differentiation (Nakamura et al. 2009) were seen in both periosteum and BM cultures (n=3). In contrast, RUNX2, a marker for early osteogenesis (Komori 2010), levels for both culture types were shown to be reduced from day 0 to day 21 (Figure 4.7A). Markers for chondrogenesis,

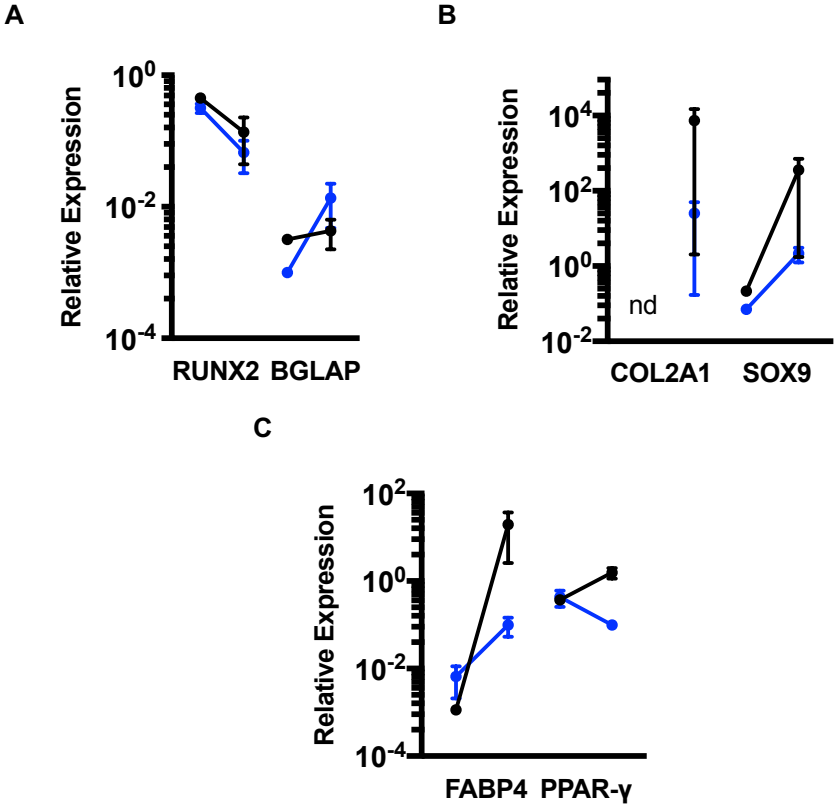

Figure 4.7: Comparison of trilineage differentiation gene transcripts prior to and post 3 weeks of differentiation induction for donor matched periosteum and bone marrow MSCs. A) Gene transcripts used after 3 weeks of osteogenic induction were RUNX2 - Runt-related transcription factor 2 and BGLAP – bone gamma-carboxyglutamate (gla) protein, **B)** chondrogenic induction, COL2A1 – Collagen type 2 alpha 1 and SOX9 – SRY (sex determining region Y)-box 9 and **C)** adipogenic induction, FABP4 – fatty acid binding protein 4 and PPAR-γ – peroxisome proliferator-activated receptor-gamma. Black – bone marrow, blue – periosteum, nd – not detected. For each gene the left marker represents day 0 expression and the right, day 21. Data presented as mean ± SEM.

COL2A1 and SOX9 were increased in both periosteum and BM cultures, following 21 days of chondrogenic induction, where in both cases BM was higher than periosteum cultures (Figure 4.7B). As expected, COL2A1 was undetectable at day 0 in both MSC culture types. FABP4 was seen to increase in both culture types after 21 days of adipogenic differentiation induction (Figure 4.7C). Again, BM MSCs showed a greater induction of FABP4 expression. However, differences in the trend were seen with PPAR-γ expression, where it was increased in BM cultures, but reduced in periosteum cultures.

To summarise, no differences in osteogenic and chondrogenic differentiation capacity were seen between donor matched periosteum and BM MSCs, however reductions in chondrogenic potential was seen to correlate with age in BM MSCs, but not periosteum MSCs. In addition, periosteum MSCs showed a reduced adipogenic potential, compared to BM MSCs, which in part could be related to the down regulation of PPAR-γ expression.

4.3.5 Candidate Surface Markers to Distinguish Between Periosteum and Bone Marrow MSCs

Distinct differences in colony formation, proliferation *in vitro* and adipogenic differentiation have been shown between periosteum and BM MSCs, there is potential that these differences could be reflected in cell marker expression. Therefore, four additional markers were assessed for potential differential expression between BM and periosteal MSCs to explore the potential of a new specific marker for periosteal MSCs. The markers chosen were SUSD2 (Sushi domain containing 2), CD146, MSCA-1 (mesenchymal stromal cell antigen-1) and CD271 (Álvarez-Viejo, Menéndez-Menéndez & Otero-Hernández 2015; Sivasubramaniyan et al. 2013; Bühring et al. 2009; Battula et al. 2009) and were tested on MSC cultures of P2-4, at approximately 14 PDs.

Recently, it was shown that SUSD2 and MSCA-1 were location specific and expressed higher in BM MSCs in comparison to RIA and femoral head MSCs, therefore the hypothesis was that these markers would be absent on periosteal MSCs (Cuthbert et al. 2015). However, SUSD2 showed relatively high expression at 55.28 ± 13.8% and 77.4 ± 10.5% for BM and periosteal

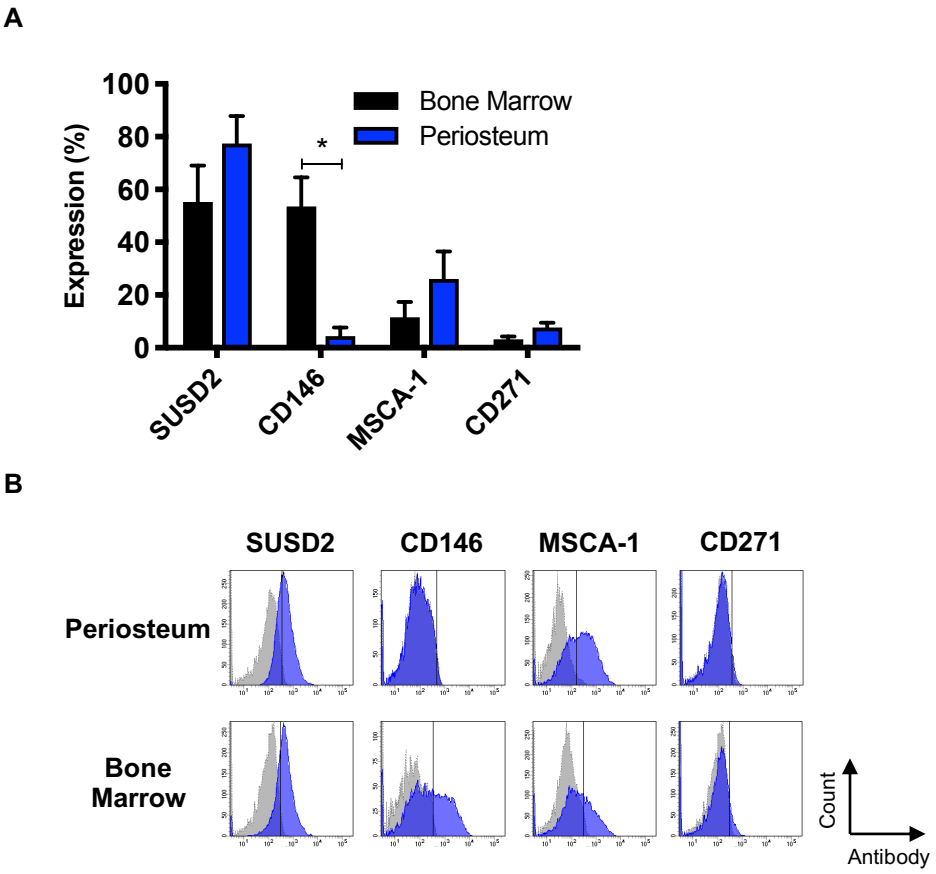

Figure 4.8: Candidate markers for periosteum and bone marrow MSCs. A) Percentage expression of candidate MSC markers SUSD2, CD146, MSCA-1 and CD271, using donor matched bone marrow and periosteum MSC cultures (n=5). **B)** Representative flow cytometry histograms. Wilcoxon test carried out (P<0.05), * P<0.05. Data presented as mean ± SEM.

MSC cultures. MSCA-1 showed low expression for BM MSC cultures at 11.6 ± 5.8% and slightly higher expression with more variation between donors for periosteum MSC cultures at 26.1 ± 10.4% (Figure 4.8).

CD146 is a marker for a subset of BM MSCs surrounding blood vessels (Tormin et al. 2011). Expression on BM MSCs was seen to be variable, at 53.6 ± 11.0%, whereas, for periosteum cultures percentage expression was low, at 4.4 ± 3.3% (Figure 4.8), this was found to be significant (Wilcoxon test, n=4, P=0.01) CD271 is an MSC marker, the expression of which is known to be lost in culture for BM MSCs, it was used to see whether this was the case for periosteal MSCs also (Álvarez-Viejo, Menéndez-Menéndez & Otero-Hernández 2015). CD271 expression on both BM and periosteum MSC cultures was seen to be low, with mean expression at 3.2 ± 1.1% and 7.7 ± 1.8%, respectively (Figure 4.8).

4.3.6 The Effects of Co-Culture of Periosteum and Bone Marrow MSCs on Osteogenesis

The attempt to find a differential marker for periosteal MSCs was unsuccessful, Although CD146 was confirmed to be differentially expressed on periosteum and BM MSC, it was not expressed on 100% of BM MSCs (Figure 4.8). Therefore, the use of the CellTrace^{TM} CFSE Cell Proliferation Kit (referred to as CFSE) was investigated as a tool to fluorescently 'tag' a subset of cells in order to be able to differentiate between BM and periosteum MSCs during co-culture conditions.

Adherent cultures of periosteum MSCs were stained with CFSE and imaged under light and fluorescent microscopy. Clear staining of all adherent cells was achieved (Figure 4.9A-B). However, when imaged again 1 day post staining, the media itself appeared fluorescent, preventing imaging of the adherent cells (Figure 4.9C-D). After washing with PBS and imaging again it was apparent that there was a loss of CFSE staining of the adherent MSCs, with only faint fluorescence being seen (Figure 4.9E-F). When repeated at 4 days post staining, the media appeared slightly fluorescent (Figure 4.9G-H) and after washing with PBS, there was a complete visual loss of CFSE staining for any of the cells (Figure 4.9I-J). At each stage the MSCs remained adhered to the tissue culture flasks, with low amounts of debris, suggestive that CFSE was not toxic to the cells.

To confirm this loss of CFSE from the periosteum MSCs, flow cytometry was carried out at two time points, immediately and 4 days post staining. Three different CFSE staining concentrations were used, 2.5 μM, 5 μM and 10 μM and a mixture of stained and unstained MSCs (ratio 1:1) were compared to a 'stained only' population. Flow cytometry gates for CFSE positivity as well as CD73 and CD45 positivity were set using an unstained population (shown as the vertical line on the histograms, Figure 4.10).

With increasing concentration of CFSE, the 'stained only' population showed increasing positivity through shifting of the histogram peak, showing that each concentration used resulted in positive staining of the MSCs (Figure 4.10A). The mixed population of 'stained and unstained' MSCs showed a double peak

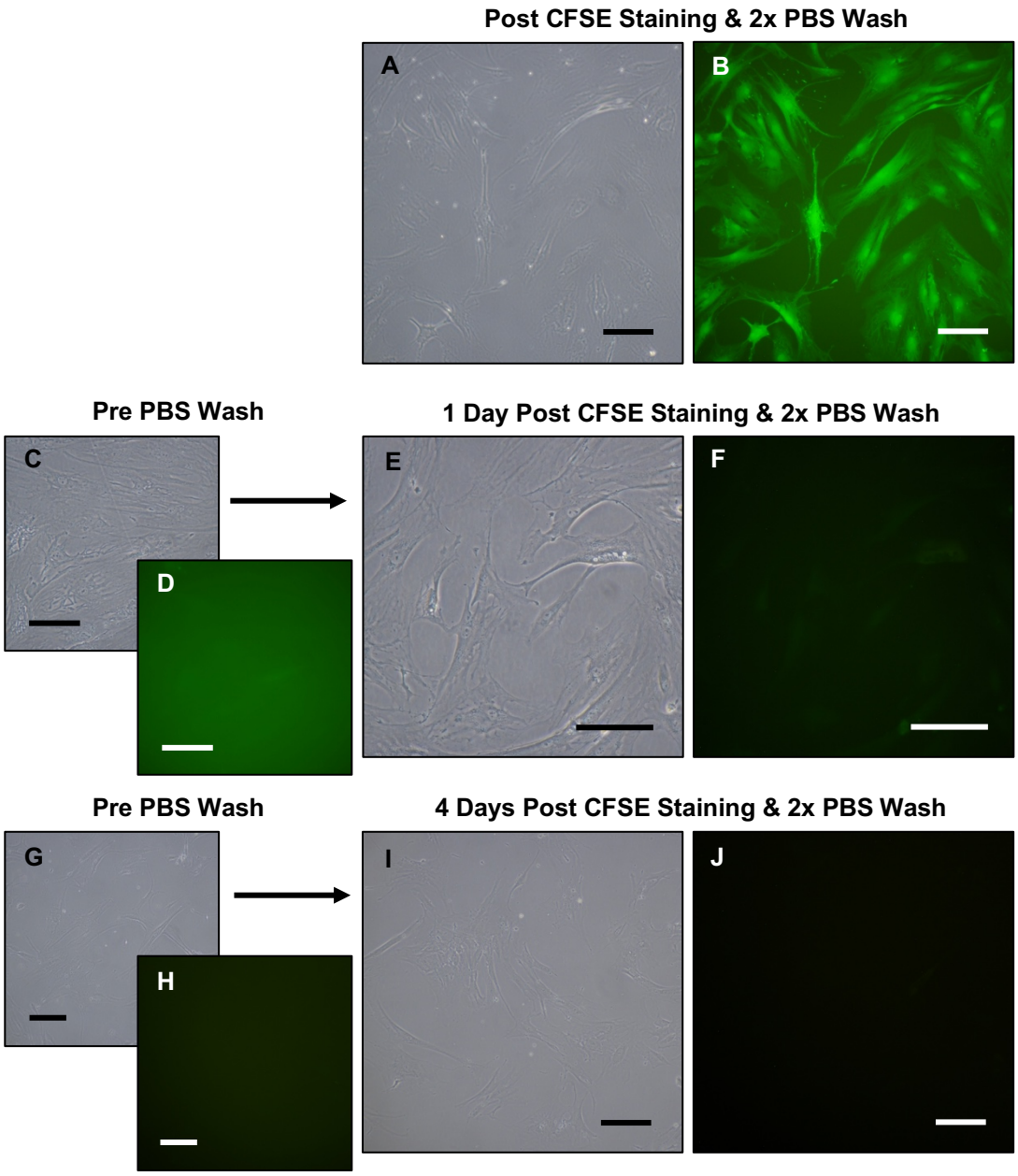

Figure 4.9: Imaging of CFSE stained periosteum MSCs under light microscopy. A-B) Post CFSE staining with 2x PBS wash showing good staining of all adherent cells. **C-F)** 1 day post CFSE staining, pre and post PBS wash, showing release of CFSE into media and an almost complete loss of CFSE staining of the adherent cells. **G-J)** 4 days post CFSE staining, pre and post PBS wash, showing a smaller release of CFSE into the media and complete loss of CFSE staining of the adherent cells. Light microscopy - A, C, E, G & I, Fluorescent microscopy – B, D, F, H & J. Scale bars all represent 100 µm, A-B & G-J x10 magnification, C-F x20 magnification.

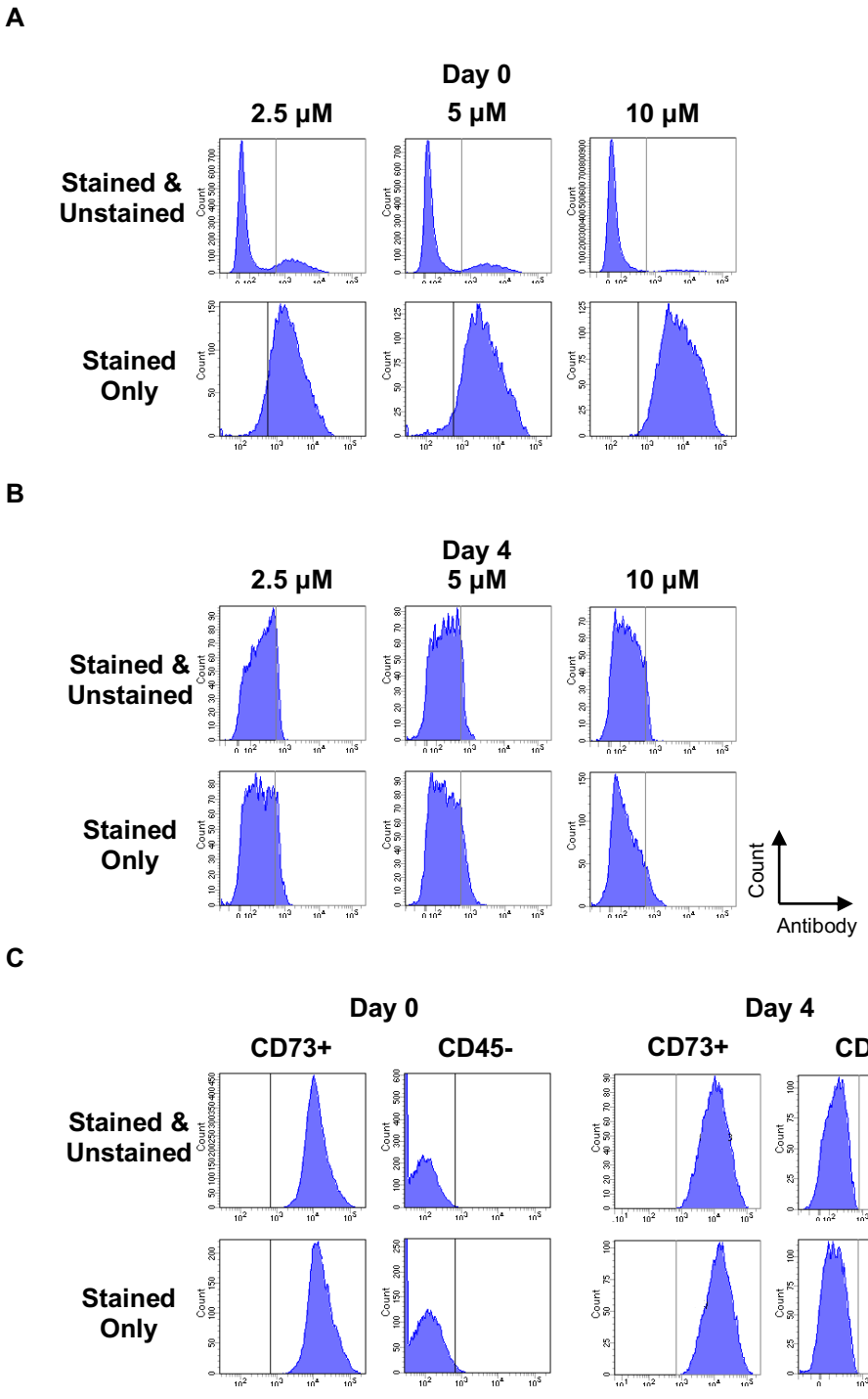

Figure 4.10: Flow cytometry confirmation of CFSE staining loss of periosteum MSCs over time. Adherent MSC cultures were stained at three different concentrations, 2.5 µM, 5 µM and 10 µM and were either mixed with unstained MSCs for flow cytometry analysis or kept as 'stained only'. **A)** CFSE positivity immediately post staining (day 0), for each concentration of CFSE and the mixed population of stained and unstained MSCs or the stained only MSCs. **B)** CFSE staining at day 4. **C)** Confirmation of retainment of the MSC phenotype with CFSE staining, cells were CD73+CD45- at day 0 and day 4. Positivity was taken as the histogram peak being to the right of line.

of negative and positively stained MSCs (Figure 4.10A). By day 4, as with the microscopy, both experimental conditions were found to be negative for CFSE staining, confirming loss of CFSE from the stained MSCs (Figure 4.10B). Samples were also stained with CD73 and CD45 (as in Section 4.3.3), at all CFSE staining concentrations and time points MSCs were found to be CD73+/CD45- indicative of the MSC phenotype.

Following unsuccessful attempts to establish a new technique to fluorescently differentiate between BM and periosteum MSCs when in co-culture, it was decided to carry out unlabeled co-culture cultures of BM and periosteum MSCs during osteogenesis, at a 1:1 ratio (BM to periosteum) for four donors, in comparison to BM and periosteum cultures on their own (Figure 4.11). ALP staining was carried out at 14 days, showing the presence of ALP at differing levels for each culture condition, whereby periosteum MSCs showed higher levels of staining than BM MSC cultures and co-cultures (Figure 4.11A). Following 21 days of osteogenic induction, Ca^{2+} deposition was quantified, showing no significant difference between BM MSC culture, co-culture (1:1) and periosteum MSC cultures when pooled (n=4) (Figure 4.11B). However, when separated into individual donors, differences could be seen (Figure 4.11C). For each donor, BM was seen to be significantly different to periosteum (Male, 17 $P<0.0001$, Male, 23 $P=0.0002$, Male, 44 $P=0.004$ and Female, 49 $P=0.0001$, Kruskal Wallis test) (Figure 4.11C). Three of the donors showed significant differences between BM and co-culture, Male, 17 ($P<0.05$) and Male, 44 ($P=0.0002$) showed significantly higher Ca^{2+} deposition in co-culture, however, Female, 49 ($P=0.006$) showed lower Ca^{2+} deposition.

Unlike in the work of Chen et al. (2012) and D. Chen et al. (2015), that showed a synergistic enhancement of mineralisation in co-culture, it has been shown using the samples in this Chapter that co-culture results in an improvement in mineralisation above that of BM MSCs alone, but not above periosteum MSC levels.

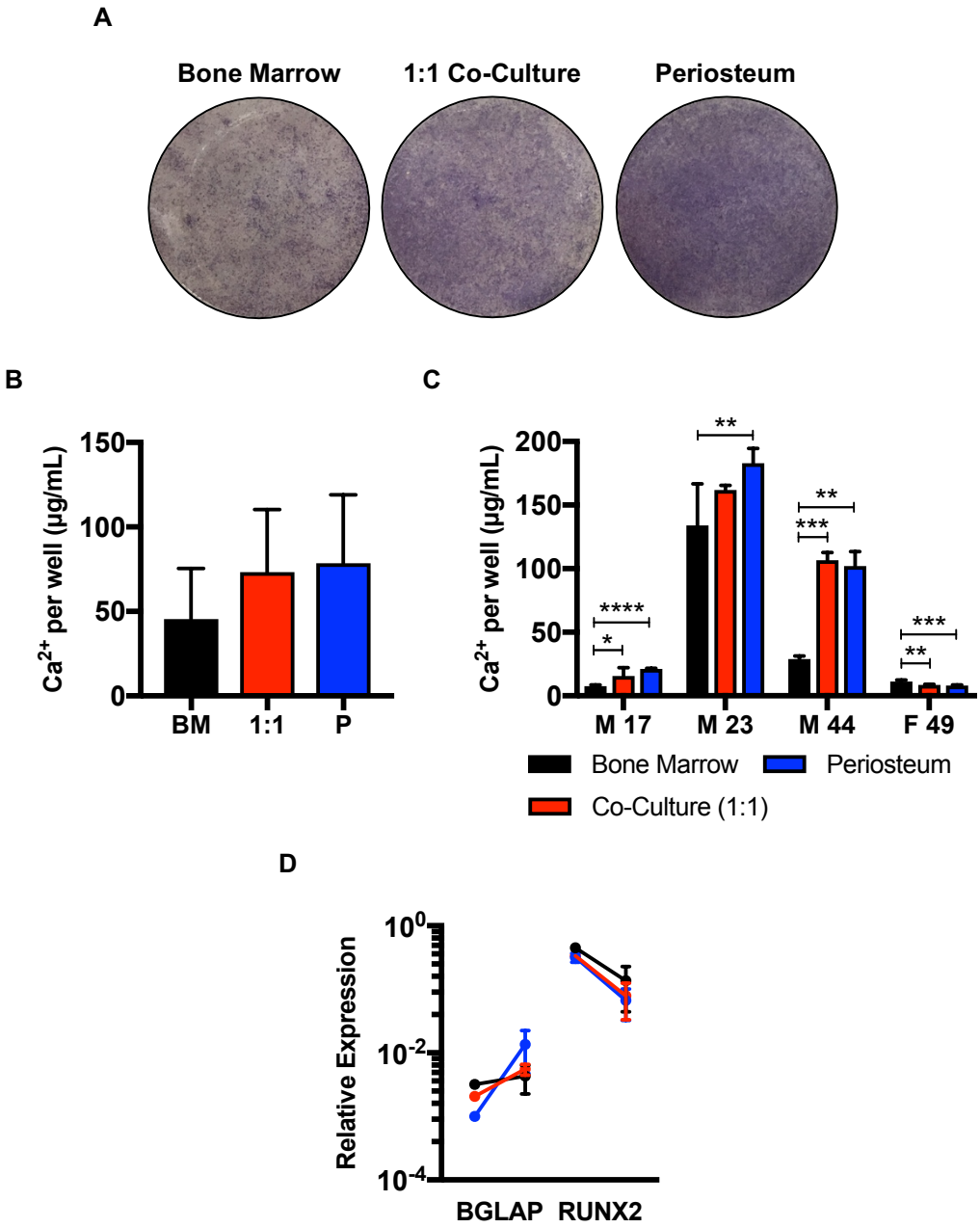

Figure 4.11: Investigation into the effect of co-culture on osteogenic differentiation of periosteum and bone marrow MSCs at a ratio of 1:1, using donor matched MSC cultures. A) Light microscopy images of staining for alkaline phosphatase (fast blue) at 14 days. **B)** Pooled donor matched bone marrow (BM), periosteum and co-culture Ca^{2+} content per well (n=4). **C)** Individual matched donors of BM, periosteum and co-culture MSC Ca^{2+} content per well. **D)** Comparison of osteogenic differentiation gene transcripts prior to and after 3 weeks of differentiation induction for donor matched BM, periosteum and 1:1 co-culture MSC cultures (n=3). Gene transcripts shown for osteogenic induction BGLAP bone gamma-carboxyglutamate (gla) protein (also known as osteocalcin) and RUNX2 – runt-related transcription factor 2 at day 0 (left) and day 21 (right). Black – BM, red – co-culture (1:1) and blue – periosteum. Kruskal Wallis test (B) or one-way ANOVA, with a Tukey's multiple comparisons test (C), * $P<0.05$, ** $P<0.01$, *** $P<0.001$, **** $P<0.0001$. Data presented as mean ± SEM.

4.4 Discussion

This Chapter set out to assess the potential for periosteal derived MSCs as a source of bone regenerating cells for CSBD repair. In the literature, periosteum and BM MSCs have been investigated for their regenerative capacities through their ability to be grown in tissue culture and the potential to differentiate into osteogenic and chondrogenic cell lineages, needed for CSBD repair. However, direct comparisons of MSCs derived from human periosteum and BM have been lacking, especially when donor matched. In addition, the literature surrounding donor matched assessments used tibial BM, opposed to iliac crest BMA, as in this study, which is a 'clinically relevant' supply of MSCs, currently used in clinic.

4.4.1 Quantification of MSC Frequency and Colony Formation

Periosteum and BM MSCs were harvested using well established methods from the literature, by collagenase digest (periosteum) and ammonium chloride aided RBC lysis (BM) (Cuthbert et al. 2012; Cuthbert et al. 2013). CFU-F assays were carried out from 'fresh digest' for both tissue types, where previously only thawed digest stocks of periosteum samples have been carried out (Cuthbert et al. 2013). MSC numbers were found to be significantly higher in periosteum compared to BM (4 log fold higher), when looking at percentage MSC occurrence in NCCs. As previously mentioned, MSCs in the BM are found at low levels, typically 0.001 – 0.01% of total NCCs (Bernardo, Locatelli & Fibbe 2009), showing that the BM samples harvested in this study have been at the low end of the spectrum with respect to percentage MSC at 0.0008% (range 0.0002-0.003%).

As 10 donors were assessed using CFU-F, with an age range of 17-74, this cannot be specifically attributed to the known decrease in MSCs found in BM with age (Stolzing et al. 2008). Whereas it is more likely to be due to the collection methods, where some BM samples were taken from a 60 mL aspiration, which is more likely to be diluted in peripheral blood (Muschler, Boehm & Easley 1997; Hernigou et al. 2005; Churchman et al. 2012), thus reducing MSC percentage in the sample. In stark contrast, MSCs from periosteum were found at 2.0% in total NCCs, ranging from 0.03-4.54%.

Sakaguchi et al. (2005) compared the percentage of MSC in different types of human mesenchymal tissues, which found donor matched periosteum and BM to have 0.4% and 0.002% MSC in total NCCs respectively, from freshly harvested samples. In addition, Cuthbert et al. (2013) reported an MSC frequency of 0.5% from periosteum samples, however, this study used collagenase digested periosteal samples that were previously frozen. Therefore, even though this Chapter found MSC frequency to be approximately 10 fold higher than other papers (fresh and frozen samples), this is a good indication of MSC frequency in periosteum from clinically relevant samples.

Periosteum MSCs formed significantly smaller colonies following CFU-F assays (mean 6.1 mm^2 compared to 15.5 mm^2), with a smaller spread of colonies as well as the absence of a subset of larger colonies >30 mm^2 present in BM cultures. This provided a previously unknown insight into the colonies formed from periosteal tissue and how they differ to that of BM. As, of yet it is unknown whether this is an advantage for bone repair, however, clearly periosteum provides a richer source of MSCs in comparison to BM per cell count from a very small tissue sample (approximately 0.1 g).

Future work would aim to compare the colony formation of assays plated as BMA (as in this chapter) to lysed BM, in order to ascertain whether the presence of platelets and growth factors within BMA during the first two days of the CFU-F assay during cell attachment has an effect on colony number, size or density. In addition, even though colony diameter was quantified, colony ‘density’ was not investigated, therefore information on the number of cells within each colony from BM and periosteum would further answer questions on initial *in vitro* growth of MSCs. To investigate this, four CFU-F plates could be set up, allowing for two to be fixed and stained for colony quantification and the other could be trypsinised and the cell number could be counted, allowing for correlations to be made with the number of colonies formed as well as the surface area of colonies.

Flow cytometry can be used to enumerate the number of MSC in a sample by staining for CD271 and using counting beads (El-Jawhari et al. 2017; Cuthbert et al. 2012), which could give a more accurate assessment of the percentage

of MSC in periosteum. However, the number of NCCs harvested from periosteum varied from 1 x 10^5 - 1 x 10^6, low in comparison to BM (1 x 10^7 – 1 x 10^8), thus making it difficult to have enough NCCs to perform flow cytometry as well as growing MSC in tissue culture for future experiments. Therefore, a separate study would need to be set up in order to investigate this, whereby CFU-F assays would be carried out alongside CD271 enumeration, using flow cytometry. Perivascular localisation of CD271 staining on periosteum was shown in Chapter 3 and work carried out by Alexander et al. (2009) to show higher CD271 expression in mineralised jaw periosteum cells, suggestive of the potential of CD271 being a reliable periosteal MSC marker. With developing technologies this will become more feasible, the use of the Attune Flow Cytometer allows for sample recovery from the machine and therefore lower amounts of sample waste.

It should be noted that only two of the donors used in this chapter were female, gender balance would ideally have been achieved. However, the attainment of periosteum samples is more difficult than BMA, which is taken as a routine part of the surgical procedure for this subset of non-union patients. From anecdotal evidence it would appear that the majority of patients that we could obtain samples from were male. Female patients were rarer and more likely to be elderly, so were often ineligible for donation, making the attainment of female samples harder for this study. The donor age in this study ranged from 17-74, with a mean of 46.4 years.

4.4.2 Growth Kinetics

When donor matched periosteum and BM MSCs were grown in tissue culture it was found that growth rates up to P0 were seen to be comparable between the two tissue types. However, the number of PDs required to reach P0 was significantly higher for BM cultures, most likely due to the higher number of MSCs being seeded in periosteum cultures. Stark differences were seen after P0 for both tissue types, whereby from P1 onwards days per PD increased significantly in comparison to P0 and by P4 BM cultures were dividing at a significantly slower rate than matched periosteum samples. This represents the first time growth rates of donor matched periosteum and BM MSC have

been quantified in long term tissue culture starting from ‘fresh digest’. As CFU-F data for periosteum samples are rarely carried out, probably due to the low number of NCCs that are harvested, growth rates are usually taken from P0 onwards unlike this study which works out PD from ‘day zero’.

With non-donor matched BM and periosteum cultures, Eyckmans, Lin & Chen (2012) showed that periosteal cultures yielded higher numbers of cells over 14 days in culture, equating to approximately (estimated from graphs and methods) 4.1 days per PD compared to 5.0 days per PD for BM cultures, similar to this study. However, this was carried out over a singular passage, compared to over 4 passages in this study, showing a more robust and longitudinal insight into periosteal MSC growth kinetics.

The PD of BM cultures plateaued from after P0 (1.64 (P0) to 9.34 days per PD at P4), compared to periosteum cultures which increased from 1.80 (P0) to 4.48 (P4) days per PD, achieving doubling in approximately half the time as BM by P4. There could be several reasons for this, as previously discussed, there were low levels of BM in the collected BMA samples, as a result, low numbers of MSCs were seeded into tissue culture, especially compared to periosteal cultures. Therefore, BM cultures have derived from a much lower number of original MSCs and have a higher *in vitro* age by the time P0 is reached in comparison to periosteum cultures (13.3 PD compared to 8.5 PD).

An area that has not been investigated is senescence levels found within both types of MSC cultures, it was found that BM cultures tended to stop proliferating by passage 4, whereby, at the following passage no increase in cell number was seen, which was attributed to, but not confirmed to senescence. Future work, would quantify senescence levels within MSC cultures, β-galactosidase assays are a well-established method for measuring senescence that could be used to investigate this (Bellotti et al. 2016).

4.4.3 MSC Phenotype

Flow cytometry was used to assess the MSC phenotype of donor matched periosteum and BM cultures as well as to investigate the potential for a marker to differentiate between the two tissue sources of MSCs. Due to the previously shown differences in PD at P0, it was decided to match, as closely as possible,

the number of PDs that had occurred at the point of carrying out flow cytometry. Expression of the positive MSC markers was >94% for periosteum cultures with consistently low expression of the negative markers, in line with the ISCT minimal requirements for MSC phenotypes, confirming the cultures as MSCs (Dominici et al. 2006). Following optimisation of CD105 staining, BM MSCs also adhered to the minimum criteria.

To remove haematopoietic cell contamination (CD34 and CD45) of BM cultures, samples needed to be passaged at least three times before a 'pure' MSC culture was seen. This pitfall of BM samples was not seen with periosteum, which produces a 'pure' MSC culture from a much earlier passage, again showing another advantage of the tissue.

So far there has been no report of a systematic comparison of the surface marker expression of donor matched human periosteum and BM derived MSCs using flow cytometry. However, this has been carried out using equine tissue, where periosteal derived cells were able to adhere to plastic, had trilineage differentiation and the presence of CD90 in combination with the absence of CD34 and CD45 (Radtke et al. 2013). As found in the work of this Chapter, periosteum derived cells were found to proliferate significantly faster than matched BM MSCs (Radtke et al. 2013).

Human proximal tibia periosteal MSCs, have been compared to donor matched synovium MSCs, obtained during knee surgery. Here, periosteum samples from P4-6 showed expression levels of greater than 90% for CD73, approximately 55% for CD105 and >5% for CD45 (De Bari et al. 2008), in line with the results from this study. The complete ISCT panel, as set out by (Dominici et al. 2006), was not carried out in this study. In another study, P3 proximal tibia periosteal MSCs were found to be positive for CD73, CD90 and CD105 (>77%) and negative for CD34 and CD45 (<5%) (Sampaio de Mara et al. 2011), however, this was not compared to MSCs of differing tissue origin.

4.4.4 Trilineage Differentiation Capacity

As with growth kinetics, the literature has lacked investigation into the comparison of differentiation capacity of donor matched periosteum and BM MSC samples. It should be noted that all donors assessed showed

osteogenic, chondrogenic and adipogenic differentiation potential, albeit to varying degrees for both periosteum and BM samples. The proven trilineage potential of both periosteum and BM cultures in combination with tissue culture plastic adherence and flow cytometry 'MSC phenotype' means that both cell types can be confirmed as MSCs, as per the ISCT criteria (Dominici et al. 2006).

Mouse models have shown that MSCs of periosteum origin are found in high levels within a fracture callus, alongside those of BM origin, suggestive that both cell types contribute to fracture healing (Knight & Hankenson 2013). Therefore, when assessing periosteum as a candidate for use in orthopaedic surgery to aid in fracture healing it is important to assess periosteal osteogenic and chondrogenic capacity, relating to the importance of this for intramembranous and endochondral ossification, respectively.

Osteogenic assays carried out showed significant differences between periosteum and BM cultures. However, apparent donor variation was seen in not only the level of Ca^{2+} deposition, but also within donor matched samples for whether BM or periosteum showed increased Ca^{2+} deposition. With an age range of 17-61, there was a trend in reduction of Ca^{2+} deposition with age, however, low correlation was seen for both tissue sources of the cultures, due to the low Ca^{2+} deposition quantified from the youngest donor (Male, 17). Despite this, age related osteogenic potential reduction of MSCs has been covered previously in the literature (Ippolito et al. 1999). The DNA content of osteogenic cultures was quantified to assess whether proliferative cultures with increased cell numbers produced increased Ca^{2+} levels. DNA content was significantly lower in BM cultures compared to periosteum, however, when Ca^{2+} content was normalised only one of the donors (Male, 44) showed that the BM cultures produced higher amounts of Ca^{2+} per cell compared to periosteum. Gene transcripts for osteogenic markers, BGLAP and RUNX2 were shown to be increased and decreased respectively, following osteogenic induction for both periosteum and BM cultures.

Recently, the co-culture of MSCs of periosteum and BM origin onto a bone scaffold was investigated *in vitro* and *in vivo*. A ratio of MSCs at 1:2 (BM:P) was shown to result in optimal mineralisation, calcium deposition, ALP activity

as well as increased mRNA expression of osteogenic markers, during *in vitro* 3D experiments and a rabbit femoral condyle CSBD *in vivo* model (Chen et al. 2011; D. Chen et al. 2015). However, the studies pre-induced osteogenic differentiation of the MSCs for three weeks using osteogenic media, leaving the question of whether co-culture improves the osteogenic capacity when MSCs have not been pre differentiated. In addition, the attachment, migration through bone scaffolds and proliferation of the two types of MSCs through porous bone scaffolds was not quantified. Both antibody marker expression and CellTrace^{TM} CFSE cell tagging were unsuccessful attempts at being able to distinguish between the two MSC types. Therefore, the synergistic effect of the two MSC types in 2D co-culture on osteogenesis, as found by the aforementioned articles was verified using our 'clinically relevant' MSC sources. Co-culture (1:1) of periosteum and BM MSCs did not show increased mineralisation capacity or osteogenic gene transcripts for any of the donors above 'periosteal only' cultures, therefore 3D co-culture work was not pursued due to time constraints on the project. However, it should be noted that co-culture had the potential to improve osteogenic potential above 'BM only' cultures, thus adding value to the fact that periosteum could be used in conjunction with BM.

As with osteogenesis, there was donor variation seen in GAG production following chondrogenic induction, with periosteum pellets producing increased and decreased GAG levels in comparison to donor matched BM pellets. DNA levels within the pellets were not tested, therefore it is unknown whether differences in donors were due to proliferation within the pellet during the differentiation assay. However, as 2.5 x 10^5 cells were needed per pellet, with 5 replicates, 1.25 x 10^6 cells were needed per donor, which for the BM cultures, with lower proliferation rates was difficult to achieve. BM cultures, more so than periosteal cultures, showed reduced GAG content with age, however, with 5 donors this is not a reliable conclusion. SOX9 levels were shown to be upregulated following chondrogenic induction, in addition COL2A1 was not detected at day 0, but was shown at day 21. Eyckmans, Lin & Chen (2012) did not compare day 0 values, but showed increased COL2A1 and SOX9 levels with increased cell density. Periosteal cultures were shown to have higher levels COL2A1 than BM cultures, but similar SOX9 levels

(Eyckmans, Lin & Chen 2012), however, it should be noted that COL2A1 expression had large variation in the samples tested in this chapter.

The clearest differences between the two MSC subtypes was seen following adipogenic differentiation, for all donors, BM MSC cultures were shown to be highly adipogenic in comparison with their periosteum MSC culture counterparts, which showed visual signs of fat droplet formation, but at a much lower occurrence. In addition, BM MSCs were more proliferative in adipogenic media than periosteum MSCs. The adipogenic potential of periosteum MSCs has been previously shown to be influenced by seeding density during tissue culture, where 5 x 10^3 per cm^2 (as used in this study) was shown to have the lowest adipogenic potential whereas MSCs grown at 8.5 x 10^3 per cm^4 showed significantly increased Oil Red staining (Eyckmans, Lin & Chen 2012). Gene transcript data showed FABP4 to be increased upon differentiation induction, however, to a lower level than BM counterparts, whereas PPAR-γ was shown to reduce upon differentiation induction. Eyckmans, Lin & Chen (2012) showed reduced PPAR-γ and lipoprotein lipase expression of periosteal cultures in comparison to non-donor matched BM culture, however, did not compare to ‘day 0’ values, therefore not yielding information on the pre-differentiation levels of the gene transcripts. However, Stich et al. (2017) showed increased FAPB4 and PPAR-γ expression following adipogenic induction of periosteum MSCs, but of the 12 donors tested for FABP4 three showed no increase from ‘day 0’ or in comparison to non-induced cultures.

Stich et al. (2017) created clones from various mastoid periosteal donors and showed donor variation with respect to trilineage differentiation capacity, whereby 100% of clones had osteogenic capacity and 94% were chondrogenic, however, only 53% of the clones were considered to be adipogenic. Therefore, if the assumption that half of the cells in periosteal cultures fail to be driven down the adipogenic lineage is taken, then this can provide a potential explanation as to why the mixed population, opposed to clonal, of periosteal cultures showed lower adipogenic potential.

In summary, all donor matched periosteum and BM cultures had trilineage differentiation capacity, however, at varying levels that could be associated with age, but not confirmed. With respect to periosteum samples, other factors

could be at play, histological analysis in Chapter 3 showed it is possible that periosteum samples are variable not only with respect to cambium layer content but also the presence of skeletal muscle. Adipogenesis was shown to consistently be significantly lower in periosteum samples. This could be attributed to the fact that *in vivo* periosteum is not involved in adipogenesis, unlike BMA whereby fat is an essential part of the microenvironment of BM (Rosen et al. 2012). Additionally linking to the aforementioned work of Sacchetti et al. (2007) that showed periosteal cells did not form heterotopic BM stroma *in vivo*. Importantly, PPAR-γ was downregulated in periosteum following adipogenic induction, this molecule is known to be critical to initiating the cascade for adipocyte differentiation (Rosen et al. 2012). Future work into the specifics of how PPAR-γ is downregulated and whether this also applies to CCAAT/enhancer-binding protein beta (Cebpβ), another important initiator of adipogenesis is needed.

4.4.5 Candidate Marker Expression and Fluorescent Cell Tagging

The expression of CD271, SUSD2, MSCA-1 and CD146 was not differentially expressed to allow for these markers to be used to distinguish between periosteum and BM MSCs using flow cytometry. Direct expression analysis using flow cytometry of donor matched periosteum and BM MSCs has not been carried out before on these markers. Most analysis of SUSD2 and MSCA-1 expression on periosteum MSCs was carried out on fresh, uncultured samples.

CD271 is a marker used to isolate BM MSCs from primary tissue, but expression is lost in culture (Martinez et al. 2007), as confirmed in this study. CD271 expression has been shown on uncultured periosteum MSCs as well as histologically, localised to surrounding blood vessels (Cuthbert et al. 2013), also confirmed in Chapter 3. Here, it was shown that cultured periosteum MSC also lack CD271 expression.

MSCA-1 expression, known to be tissue non-specific alkaline phosphatase (Sobiesiak et al. 2010), varied depending on the mineralisation potential of the jaw periosteal MSCs measured (Alexander et al. 2010). It was found that MSCA-1 was expressed higher on ‘mineralising’ cells in comparison to ‘non-

mineralising' cells (Alexander et al. 2010). Cranial periosteal MSCs showed 33% MSCA-1 expression, again linking MSCA-1 with osteogenic progenitors found within periosteum (Alexander et al. 2015). It would be interesting to test MSCA-1 expression on fresh periosteum MSCs to see if MSCA-1 is lost in culture as with CD271, or if MSCA-1 expression is specifically linked to mineralisation as suggested by the aforementioned studies.

SUSD2, a type 1 integral membrane protein, has not been tested on uncultured or cultured periosteum MSCs previously, but is known to be positive on uncultured BM MSCs (Cuthbert et al. 2015). Additionally, SUSD2 and MSCA-1 have been described to enrich for CFU-F and tri-lineage differentiation potential for MSCs derived from BM (Lv et al. 2014). Lv et al. (2014) demonstrated maintained SUSD2 positive expression in culture for BM MSCs, but a lack of MSCA-1 expression. In contrast, this Chapter showed large variation in SUSD2 expression on BM MSC, but periosteum culture levels were higher.

Cultured periosteum was negative for CD146 expression, whereas 0.02% of all cells isolated from BM are CD271+/CD45-/CD146+, shown to differentiate a perivascular BM MSC population from endosteal BM MSCs (Tormin et al. 2011). Cultured BM MSC expression for CD146 was variable, therefore, even though CD146 was consistently negative in periosteal cultures, due to the variability of its expression in BM cultures it could not be used consistently as a marker to differentiate between the two. A recent study developed an immortalised human cranial periosteal cell line, whereby the proportion of cells expressing CD146 increased from 15% in primary cells to 72% upon immortalisation, in agreement with this study that CD146 expression in periosteal cells is low (Alexander et al. 2015; Umrath et al. 2018).

Due to the lack of success in identifying a marker that would differentiate between periosteum and BM MSCs, a 'cell tagging' approach was taken. CellTrace™ CFSE, a fluorescent probe used to label and track the proliferation of immune cells (Noort et al. 2011) was used to fluorescently tag MSC cultures. However, even though CFSE was shown to initially tag MSCs, a rapid loss of the dye from the MSCs could be seen after one day, released into the culture media. This was followed by a complete loss of CFSE

detection by day 4, the loss of fluorescence could not be attributed to serial dilution of CFSE due to cell division as proliferation rates are known to be approximately 4 days per PD. Therefore, another mechanism must be at play, whereby the MSCs have quickly recycled the probe out of the cytoplasm and into the culture media.

A recent paper utilised CFSE through staining MSCs that were subsequently seeded onto bone scaffolds for 4 days and then digested from the scaffolds and CFSE levels were quantified again to assess cell proliferation in 3D conditions (El-Jawhari et al. 2016). Conversely, Weir et al. (2008) reported findings similar to that of this Chapter, whereby the CFSE signal of MSCs was shown to be lost rapidly within 5-8 days at a range of staining concentrations. Although, time limitations of this project did not allow for this avenue to be pursued any further, future work would use another probe, CellTracker™ CM-DiI (Invitrogen) for MSC tracking. Weir et al. (2008) found that unlike CFSE, CM-DiI stained MSCs were significantly detectable from unstained controls using flow cytometry for 4 weeks, whereby they found 4 μm to be the optimal dye concentration as >6 μm resulted in impaired cell division.

4.5 Conclusion

The samples obtained for this study were realistic to what can be harvested during an orthopaedic operation. Despite the suboptimal nature of the periosteum samples (absence of cambium layer), the MSCs still outperformed their matched BM counterparts with respect to percentage of MSCs within total NCC count, growth kinetics and equal purity of MSC phenotype in tissue culture. MSCs were found at higher frequency in periosteum, compared to donor matched BM MSCs, where periosteum MSCs formed smaller and homogenous colonies in comparison to BM MSCs which were larger and heterogenous. Periosteal MSCs were more proliferative after the first passage than donor matched BM MSCs. Periosteum MSCs have a lower adipogenic potential, but similar osteogenic and chondrogenic potential, where large donor variation was seen in both MSC types. Co-culture of periosteum and BM MSCs did not enhance osteogenesis, but improved BM levels on an individual donor basis.

Chapter 5: Manufacture of Free Surface Electrospun Barrier Membranes

5.1 Introduction

In order to investigate the feasibility of the 'hybrid graft' treatment strategy for surgical intervention of CSBD, a barrier membrane to wrap around and contain the defect site was realised. As previously discussed in Chapter 1, the manufacture of this membrane was pursued in order to fulfil specific functional and clinical requirements, e.g. ensuring that not only a barrier membrane was produced, but that it met the needs of the end user, orthopaedic surgeons.

5.1.1 Barrier Membrane Product Specification

A product specification was set out in order to guide and inform the development of a barrier membrane that complies with a medical device translation pathway for future use in orthopaedics (Figure 5.1). The barrier membrane should enable prevention of soft tissue invasion into the defect site, which can hinder fracture healing (Ogiso et al. 1991). In addition, the barrier membrane should act as a containment device, preventing the loss of grafting material, i.e. MSCs, autologous or commercial bone grafting material and growth factors from the defect site, allowing for an optimal biological environment for osteogenesis to be maintained.

As the barrier membrane will be wrapped around the outer layer of bone, it will come into contact with the periosteum, therefore it should support periosteal regrowth, an important component for bone healing (Dwek 2010). The membrane will therefore be designed to support periosteum MSC (characterised in Chapter 4) growth and migration along the material (covered in Chapter 6). The periosteum will also form the basis of the architecture of the barrier membrane, whereby investigations throughout Chapter 3 inform the design and manufacture of the barrier membrane.

Finally, by pursuing a clinically led approach an orthopaedic product will be realised where the need for ease of handling for surgeons, scalable manufacture and biocompatibility will be taken into consideration throughout

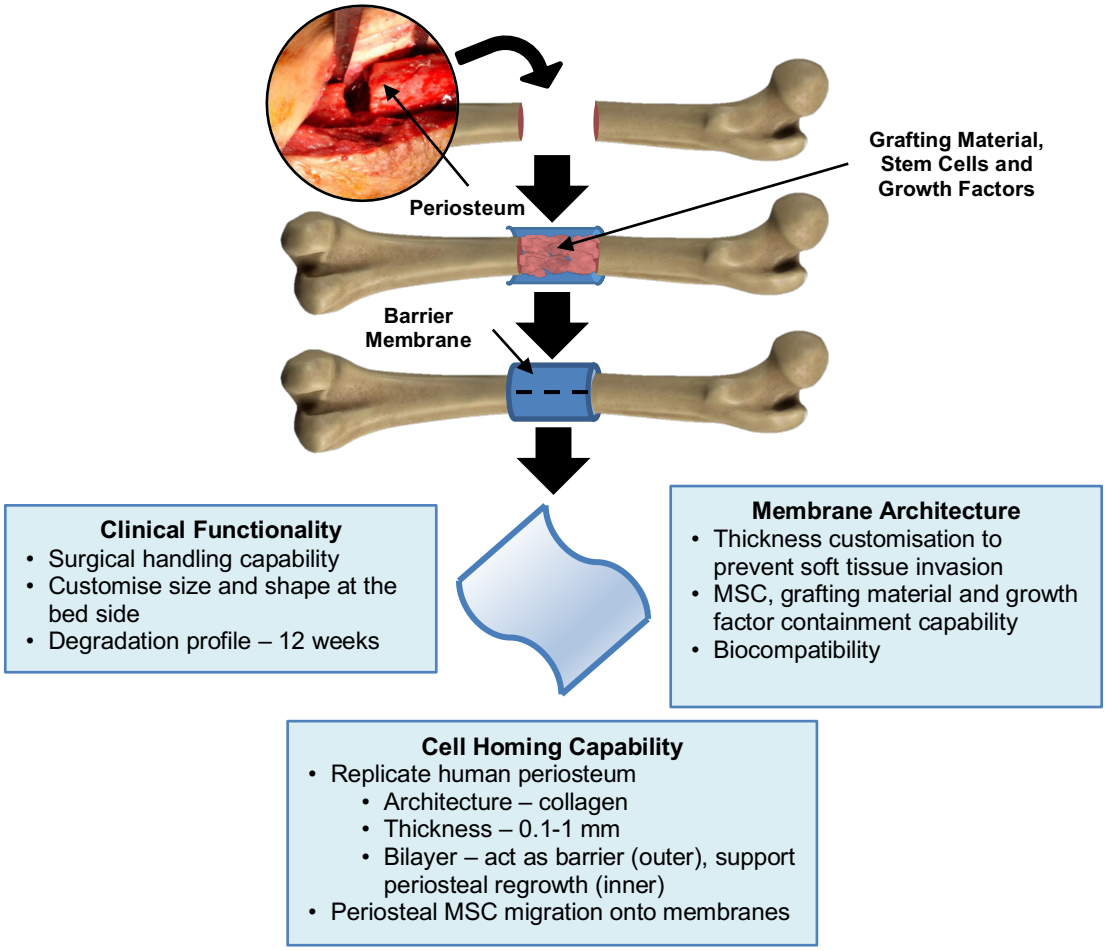

Figure 5.1: Barrier membrane product specification for hybrid graft surgical treatment strategy for critical size bone defects. *Insert:* photograph of tibial bone defect, taken during surgery, with the patient's consent and ethical approval (see Appendix 5).

the development process. In addition, a known and controllable membrane degradation profile of 12 weeks *in vivo* will be pertinent to prevent a second surgery for membrane removal. This is an important distinction to be made as this subset of patients are likely to undergo many surgeries, thus reducing the number of surgeries this technique will need is imperative. This would allow the membrane to be resorbed over time, whilst allowing for cell homing, attachment and proliferation.

5.1.2 Mimicking Periosteal Architecture

Through the histological investigation of human and porcine periosteum (Chapter 3) it was shown that periosteum thickness was 1167 ± 204 μm (range, 377–1790 μm), in humans. Likewise, porcine samples showed that

periosteum thickness around the circumference of the femur was variable and dependent on anatomical location, with a mean of 524 ± 505 μm (range, 127–2310 μm). Collagen is the main ECM component that makes up the periosteum and induced membrane (Dwek 2010; Sivakumar et al. 2016), this was confirmed histologically as collagen appeared to make up the majority of the structure of periosteum. However, the protein organisation of the collagen appeared to degrade with age. Whereby, younger patients were found to have highly organised collagen fibrils, but in older patients the collagen was seen to be less organised and sparser. It was found that there was a high coverage of blood vessels throughout the periosteum (3 (Porcine) and 15 (Human) blood vessels per mm^2), with varying diameter size (7 μm (Porcine) and 21 μm (Human)). When the cambium layer of periosteum was visualised, it was seen that the collagen fibres aligned along the bone axis, which was confirmed in porcine samples. Staining with a candidate MSCs marker (CD271) was found throughout the periosteum, not just within the cambium layer, mainly located surrounding blood vessels.

5.1.3 Material Basis to the Barrier Membrane

Collagen was chosen as the building block of the barrier membrane due to its abundance within periosteum. Manufacturing a barrier membrane based on collagen harnesses the biodegradability of collagen, which is dependent on the degree to which collagen molecules are cross linked (Meyer, Baltzer & Schwikal 2010), which gives certain advantages over stable polymer implants. Collagen is also biocompatible and can be purified *ex vivo* in order to present minimal antigenicity (Lynn, Yannas & Bonfield 2004). As a biological material, collagen also allows for cell attachment, proliferation and differentiation (Lee, Singla & Lee 2001). Type I collagen in particular is known to be important for the regulation of an osteoblastic phenotype that aids bone regeneration (Shi, Kirk & Kahn 1996). Thus, an in-house developed technique for isolation of type I collagen from rat tail tendons will be utilised (Arafat et al. 2015) to afford inexpensive use of collagen, with the long term plan of switching to a medical grade (GMP), purified collagen source if the membrane were to be developed further for clinical use. Recently, the chemical and dichroic characteristics of type I rat tail collagen have been confirmed to be comparable to the ones of

medical grade bovine atelocollagen (Tronci et al. 2016), promising for its employability in the translation pathway of the membrane prototype.

It is important to know the contents of this source of collagen, as a non-purified material. Tendons are made up of collagen, whereby approximations of dry weight collagen content range from 70% (collagen type I) (Voleti, Buckley & Soslowsky 2012) to 86% collagen (type not defined) (Lin, Cardenas & Soslowsky 2004). Collagen type III levels change during growth within tendons, whereby in the immature tendon collagen type I and type III are co-distributed throughout tendon fascicles (Birk & Mayne 1997). However, but collagen type III expression is lost over time, while the endotendineum (connective tissue separating fascicles) increases its expression (Birk & Mayne 1997; Kurose et al. 2006; Franchi et al. 2007). The collagen within tendons is embedded in ECM, thus also contains proteoglycans (decorin and fibromodulin), glycoproteins, GAGs, elastin, fibroblasts and tenocytes (Voleti, Buckley & Soslowsky 2012; Craig et al. 1989; Lin, Cardenas & Soslowsky 2004; Franchi et al. 2007).

Free surface electrospinning will be the nonwovens manufacturing process used in this Chapter. As previously discussed (Section 1.3.2.1) its virtues come due to its potential for commercial upscale of manufacture and its relative under representation in the literature in comparison to needle-based electrospinning.

It is known that collagen can be produced in membrane-sheet form via needle based electrospinning. However, it has been shown that when collagen is electrospun on its own and not crosslinked it is unable to be peeled away from the collection fabric (typically foil for needle based electrospinning) (Chakrapani et al. 2012), thus not suitable for development into a material that can be handled. Different studies have crosslinked collagen or gelatin, prior to or post electrospinning in order to improve tensile properties. Ribeiro et al. (2014) found a reduction in the Young's modulus upon crosslinking, whereas, in contrast Agheb et al. (2017) found an increase in Young's modulus with crosslinking, combined with an increased stress at break value also, showing the complexity of crosslinking of a collagen based material and the result to tensile properties.

An alternative approach to improve the mechanical strength and handling properties of electrospun collagen, whilst maintaining the cell homing capabilities could be to introduce a biodegradable polymer alongside collagen in the electrospinning solution. PCL is a bioresorbable polymer that has been used extensively for tissue engineering purposes (Woodruff & Hutmacher 2010). An additional reason for the combination of collagen with a polymer is to fulfil the requirement that the barrier membrane is intact for up to 12 weeks *in vivo*. Collagen based materials are likely to degrade faster than 12 weeks, thus introducing a PCL phase to the barrier membrane will allow for collagen to degrade and the PCL component of the material to be intact for up to 12 weeks.

5.1.3.1 Collagen and PCL Electrospinning

Collagen (and its denatured counterpart gelatin) has been electrospun with PCL previously, however, only using needle based electrospinning systems. Ren et al. (2017) produced PCL/gelatin needle electrospun constructs; however due to phase separation of the blended electrospinning polymer solution (prepared in 2,2,2-Trifluoroethanol), the addition of acetic acid (0.2% v/v (volume to volume)) was required to homogenise the mixture. Nonwoven gelatin-PCL materials were realised with increasing gelatin content (up to 30% gelatin at 10% w/v (weight to volume)) and crosslinking with Genipin (2% in EtOH, 24 hours). The introduction of gelatin improved the wettability of the membrane with respect to the PCL controls, whilst crosslinking of gelatin improved the tensile properties of the electrospun hybrid samples. Another study developed an 80:20 (20% w/v) collagen:PCL membrane impregnated in Heprasil™ hydrogel, which proved to support human umbilical vein endothelial cells (HUVECs) and IMR90 fibroblast growth, in addition to allowing for the incorporation of VEGF and PDGF as beneficial to induce *in vivo* vascularisation (Ekaputra et al. 2011). Gelatin and PCL (50:50 at 10% w/v)) were electrospun directly onto a commercial polyurethane material (Tegaserm™) for wound healing applications, whereby human dermal fibroblast cells were shown to effectively populate the membrane (Chong et al. 2007). Another study investigated the formation of electrospun poly(L-lactic acid) (PLLA) coated with collagen followed by freeze drying and crosslinking

(Cai et al. 2010). The resulting 2 mm thick bilayer membrane supported BM-MSC growth and differentiation *in vitro* and aided repair of a 15 mm length large tibial bone defect *in vivo*.

All these reports indicate that collagen or gelatin can be electrospun with PCL via needle based electrospinning, using a variety of solvent systems, whilst collagen-coated needle-electrospun PCL membranes have also been reported (Cai et al. 2010). Both types of membranes showed evidence of cell adhesion *in vitro,* in addition to *in vivo* bone regeneration (Ekaputra et al. 2011). Therefore, it was hypothesised that free-surface electrospinning could offer a novel yet scalable manufacturing route to generate a collagen-PCL blended barrier membrane prototype. With a microstructure that could be tuned to enable MSC containment and soft tissue barrier functionalities, aiming at an application for CSBD repair.

5.1.4 Chapter Aims and Objectives

This chapter aims to report the manufacturing and material characterisation of collagen-PCL and PCL control electrospun membranes realised via free surface electrospinning and engineered for the application of CSBD repair.

5.1.4.1 Objectives

The objectives of this work were to:

1. Accomplish free surface electrospinning of collagen-PCL membranes (with varied collagen-PCL weight ratios) and PCL membrane controls.
2. Characterise resulting membranes with regards to dimensions and microstructure (including fibre diameter and pore size distribution), tensile properties and wettability (via water contact angle measurements).
3. Assess membrane collagen content in the freshly-synthesised and saline-incubated samples using circular dichroism (CD) and histological staining.

5.2 Specific Materials and Methodology

The manufacture of the free surface electrospun membranes and the material characterisation during the optimisation study (Section 5.3.1) were carried out in partnership with Katrina Moisley (PhD Student, University of Leeds). Material characterisation of the free surface electrospun membranes in Section 5.3.2 and Section 5.3.3 was carried out independently.

5.2.1 Materials

Poly (ε-caprolactone) (PCL) (M_n: 80,000 g mol^{-1}) was purchased from Sigma and 1,1,1,3,3,3-Hexafluoro-2-propanol (HFIP) was purchased from Flurochem. Type I collagen was isolated from rat tail tendons, as previously described (Tronci, Russell & Wood 2013). Frozen rat tails were acquired from an animal house, University of Leeds. After thawing, the tails were placed into 70% (v/v) EtOH, using tweezers and forceps, the skin was removed and the tails were put into another container of 70% EtOH. Rat tails contain four tendons, each was stripped from the tail and placed in 17.4 mM acetic acid (50 tails in 2 L 17.4 mM acetic acid) at 4°C, for collagen extraction. After two days, the solution was centrifuged (Ultra Centrifuge, Beckman) at 48,300 g for 1 h. As the collagen remains in solution, the supernatant was frozen at -80°C and freeze dried (Alpha 2-4 LD Plus, Christ Martin). Freeze dried collagen was stored at 4°C until use.

5.2.2 Free Surface Electrospinning

Solutions with different ratios of collagen to PCL were prepared in HFIP. Solutions were made with 6% (w/v) overall polymer concentration, with increasing collagen:PCL weight ratio (50:50, 60:40, 70:30 and 80:20 (see Appendix 1.1 for w/v solutions)) under stirring for 24 h. Control solutions with 3% (w/v) PCL in HFIP were used, as 6% (w/v) PCL solutions in HFIP were too viscous to allow for free surface electrospinning. Hereafter, solutions will be described using the following nomenclature, S6%-CP50:50, S6%-CP60:40, S6%-CP70:30, S6%-CP80:20 (e.g. solution 6% (w/v), collagen:PCL at 50:50 ratio) , S3%-PCL (solution 3% (w/v), PCL).

A needleless electrospinning system was used (NanoSpider Lab-200, Elmarco), where a low volume spike electrode (surface area of 0.78 cm^2) was used to generate electrospun membranes. During an optimisation study using S6%-CP50:50, the effect of distance from the spike electrode to the static grounded collector was investigated by selecting either a 120 mm or 155 mm electrode-to-collector distance, whilst the electrostatic voltage was also varied, ranging in multiples of 10 kV from 20 kV to 60 kV. Approximately 5 mL of electrospinning solution was used to create membranes with an approximate size of 314 cm^2 where fibres were collected on to, and peeled away from, a polypropylene (PP) thermally bonded spunbond fabric (Elmarco).

Following the process optimisation study using S6%-CP50:50 (Section 5.2.3), thicker membrane samples were then produced by using an electrospinning solution volume of 10 mL. At this point an increase in collagen:PCL weight ratio was investigated, using S6%-CP50:50, S6%-CP60:40, S6%-CP70:30 and S6%-CP80:20 where electrospun membranes were manufactured and compared to S3%-PCL, a PCL membrane control. For consistency, all solutions were electrospun at a spinning distance of 155 mm and 40 kV. When in membrane form differing samples will be described as follows – M6%-CP50:50, M6%-CP60:40, M6%-CP70:30, M6%-CP80:20 (e.g. membrane 6% (w/v), collagen:PCL at 50:50 ratio) and M3%-PCL (membrane 3% (w/v), PCL).

5.2.3 Material Characterisation

All membranes were analysed and compared for their material characteristics. Fibre size analysis was carried out using SEM imaging, pore size distribution was measured using capillary flow porometry and the tensile strength properties were measured using tensile testing. Water contact angle measurements (Section 5.2.8) and CD (Section 5.2.9) were not carried out on the optimisation study membranes. The electrospun membranes were peeled from the PP backing fabric and cut to the size needed for each test, detailed in Table 5.1.

Table 5.1: Details of sample sizes needed for each free surface electrospun membrane characterisation test.

Material Characterisation Test	Described in Section	Details of Membrane Sample Size Needed for Test
SEM	5.2.4	10 x 10 mm
Sample Thickness	5.2.5	40 x 40 mm
Porometry	5.2.6	30 mm (circle diameter)
Tensile Testing	5.2.7	15 x 30 mm
Water Contact Angle	5.2.8	15 x 50 mm
Circular Dichroism	5.2.9	20 x 20 mm
Collagen Assay	5.2.10.2	20 x 20 mm

5.2.4 Scanning Electron Microscopy

Scanning Electron Microscopy (SEM) has been used to characterise the free surface electrospun membranes. Dry membranes (10 x 10 mm) were sputter-coated with gold at 40 mA for 30 seconds in an argon atmosphere (Agar Auto Sputter Coater) and imaged under vacuum using an SEM (Hitachi, S-3400N) (see Section 2.4.1). Fibre morphology and diameter (at least n=20 measurements taken per image, three images taken) was assessed. Unless stated otherwise, samples were analysed under vacuum with an accelerating voltage of 20 kV, a working distance of 5 mm was used. Elemental analysis of electrospun samples was carried out using Energy Dispersive X-Ray (EDX) spectroscopy (129 eV Bruker), using backscatter mode, with a 30 min scan, measuring for Nitrogen, Carbon and Oxygen. Images were captured using Hitachi SEM software over 80 seconds at a pixel rate of 2560 x 1920. Scale bars and magnification were automatically superimposed onto images.

5.2.5 Sample Thickness Measurements

Samples were measured in triplicate for their thickness using a ProGage thickness tester (Thwing-Albert Instrument Company). All samples were measured under 0.5 kilo pascals (kPa) of pressure and thickness was measured using a digital gauge. The sample thicknesses measured here were

used for when setting up porometry tests (see section 5.2.6) and for conversion of force to stress for tensile testing (see section 5.2.7).

5.2.6 Porometry

Pore size distribution was assessed using capillary flow porometry. Circular samples (diameter – 30 mm), thickness ~ 100 µm) were wetted using a wetting fluid (surface tension – 15.6 mN/m, Galpore^{TM}). Using a 25 mm sample holder (effective diameter of 19.5 mm), pore sizes were estimated using a porometer (Porolux 100FM). The wetting fluid absorbed by the sample was displaced by the application of a pressurised gas to the sample. Quantification of gas flow at a given pressure allowed for a 'wet curve' (Blue curve – Figure 5.2) to be produced. At this point the wetting fluid has been removed from the sample and a second measurement was taken of the flow of pressurised gas through the sample, thus creating a 'dry curve' (Black curve – Figure 5.2).

Pressure was plotted against flow rate, where key parameters were measured. First bubble point (largest pore), which is the first pore measured. The mean flow pore diameter – pore size measured at 50% of the total gas

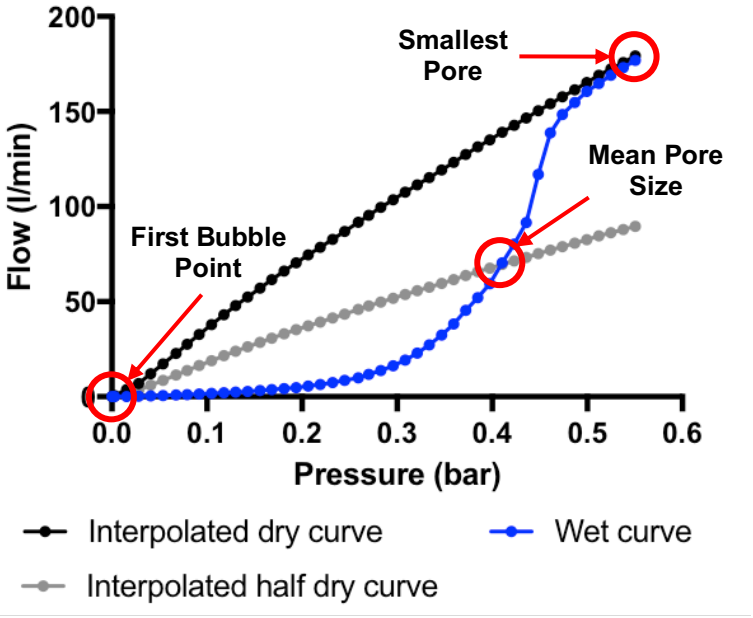

Figure 5.2: Example porometry plot. Two measurements are taken through a sample being tested using capillary flow porometry. The sample is wetted with Galpore and gas flow is measured through the sample (Blue – wet curve, a second measurement is taken through the now dry sample (Black – interpolated dry curve), the values measured were halved (Grey – interpolated dry curve.

flow, which is taken as the ‘mean’ pore size - calculated when the ‘interpolated half dry curve’ meets the ‘wet curve’ (Figure 5.2). Finally, the smallest pore, measured when the ‘interpolated dry curve’ intersects with the ‘wet curve’.

5.2.7 Tensile Testing

The tensile characteristics of the electrospun membranes were determined via tensile testing, whereby the M6%-CP50:50 ‘optimisation’ membranes (Section 5.3.1.3) were tested using a Zwick Machine with a 10 N load cell and the ‘prototype’ membranes (Section 5.3.2.4) using a Titan, with a 100 N load cell.

Samples of electrospun membranes were cut into rectangular strips (15 mm x 30 mm) and tested with a gauge length of 20 mm and a crosshead speed of 20 mm/min until breakpoint (F_{max}), with 5 replicates for each sample composition being taken. The specimen pre-load was 1 cN (centinewton) (Zwick), there was no pretension set for the samples testing using the Titan, data was re-zeroed post acquisition. Data output was as extension (%) and force (N). Extension (%) was converted to Strain (ε) (mm/mm) using Equation 5.1 and force (N) was converted to Stress (σ) (Pa, pascals) using Equation 5.3.

Equation 5.1: Conversion of extension (mm) to strain (mm/mm).

Strain (mm/mm) = (Extended length (mm) – Original Length (mm)) / Original Length (mm)

Equation 5.2: Conversion of force (N) to stress (Pa).

Stress (Pa) = Force (N) / Cross Sectional Area of Sample (m^2)

5.2.8 Water Contact Angle Measurements

Water contact angle measurements were carried out on the electrospun ‘barrier membrane’ samples (M6%-CP50:50, M6%-CP60:40, M6%-CP70:30, M6%-CP80:20 and M3%-PCL control) as well as on corresponding pore-free films (S6%-CP50:50-F, S6%-CP60:40-F, S6%-CP70:30-F, S6%-CP80:20-F

and S3%-PCL-F). In addition, a collagen only film was cast (S3%-C-F), in order to compare to the collagen containing films. To make the films, 5 mL of the electrospinning solution was cast onto a glass slide, HFIP was allowed to evaporate. For each of the electrospun membranes, a 15 x 50 mm sample was adhered to glass slides using double sided tape.

A contact angle goniometer (CAM 200, KSV Instruments, Ltd) was used, whereby a micro-syringe with an automatic dispenser would issue a droplet of ultra-pure water onto the material surface. The water contact angle of a droplet was measured twice a second over 15 seconds by a CCD fire wire camera. Water contact angle measurements were calculated from the images automatically, samples were tested in triplicate and the mean contact angle was taken.

5.2.9 Circular Dichroism

CD was carried out by CD facilities at the Faculty of Biological Sciences, University of Leeds. Solutions (200 µL) at approximately 0.3 mg/mL protein content were loaded into 10 mm path-length cuvettes and samples run using an AAP Chirascan CD Spectropolarimeter, where a 'far UV' spectral region from 190-260 nm was tested at 20°C. Blank cuvettes of 17.4 mM acetic acid or HFIP were tested, to remove background from the test samples. The test samples (at approximately 0.3 mg/mL) are detailed below.

Electrospinning Solutions (pre electrospinning)

- PCL in HFIP
- Collagen in Acetic Acid
- Collagen in HFIP
- S6%-CP70:30 in HFIP

Electrospun Membrane Fibres Dissolved in Solution (post electrospinning)

- M6%-CP70:30-Fibre dissolved in HFIP
- M6%-CP70:30-Fibre dissolved in Acetic Acid

Post-acquisition the 'blank' data was taken away from the 'test' samples and then used to calculate the mean residue ellipticity at wavelength (λ) (Equation 5.3). Whereby, mean residue weight (MRW) was taken as 110 ± 5 Da, θ_λ – wavelength, d – pathlength (1 cm) and c – concentration (0.003 g/mL).

Equation 5.3: The mean residue ellipticity at wavelength (λ).

$$[\theta]_{mrw,\lambda} \text{ (deg cm}^2 \text{ dmol}^{-1}) = \text{MRW} \times \theta_\lambda / 10 \times d \times c$$

5.2.10 Functional Testing of Membrane

Further functional testing of the barrier membranes was carried out, at this point the M6%-CP70:30 prototype was taken forward as a candidate membrane and was compared to M3%-PCL, to ascertain the effect of collagen on membrane function. Here, the collagen content and stability within the M6%-CP70:30 prototypes was investigated further.

5.2.10.1 Imaging of Collagen on Electrospun Membranes

PSR is used in histology to stain collagen fibres in tissues (Junqueira, Bignolas & Brentani 1979), this stain was therefore used to confirm the presence of collagen within the electrospun samples. Samples of M6%-CP70:30 and M3%-PCL were cut to 20 x 20 mm, and were stained with 1 mL of PSR for 1 h. Unbound dye was removed using two washes of PBS followed by one wash of acidified water (0.5M Glacial Acetic Acid in dH_2O). Samples were photographed for macro images followed by imaging using light microscopy (Zeiss).

5.2.10.2 Stability of Collagen within Electrospun Membranes

The stability of collagen within the electrospun M6%-CP70:30 prototypes in culture conditions was assessed for up to three weeks. Dry membranes were cut into 20 x 20 mm pieces and weighed. Three replicates were taken for each time point with the mean sample weight was 1.2 mg. Test samples were sterilised under UV light in a class II fume hood for 1 h. Samples of M6%-CP70:30, in triplicate for each time point, were placed in 6 well plates with 2

mL of sterile PBS + 1% PS and incubated at 37°C. Time points were taken at day 0 (just post-manufacture), day 1, day 4, day 7, day 14 and day 21.

At each time point free surface electrospun membrane samples were washed with 1 mL PBS and stained in 1 mL of PSR for 1 h. The stain was removed and membranes were washed twice with 1 mL PBS, followed by one wash of acidified water (0.5 M Glacial Acetic Acid in dH_2O) to remove all unbound dye. Bound PSR dye on the samples was released in 1 mL of 0.1 M sodium hydroxide, samples were placed on a mechanical shaker for 4 h to allow for maximum dye release (Ferreira et al. 2016).

100 µL of the 1 mL PSR releasate was plated in triplicate onto a flat bottom 96 well plate and absorbance was measured using a plate reader (Berthold) at 540 nm. Absorbance values were compared to a standard curve of known collagen concentrations, as described below.

5.2.11 Statistical Analysis

Statistical analysis was carried out on using one-way ANOVA, with a Tukey's multiple comparisons post hoc test, where the data was parametric (D'Agostino & Pearson normality test carried out prior to statistical analysis). Where data was nonparametric a Kruskal-Wallis test was carried out. Statistical significance was taken as $P<0.05$ and unless stated otherwise data has been plotted as mean ± standard deviation.

5.3 Results

5.3.1 Free Surface Electrospinning Optimisation Study

In order to establish reproducible process-structure relationships, an optimisation study was carried out with free surface electrospinning of a collagen-PCL solution. Electrospun membranes were manufactured where the spinning solvent (solvent used to dissolve spinning substrates in), spinning distance (distance from the spike electrode to the collection material) and spinning voltage (voltage (kV) applied to the spike electrode) were altered to obtain optimal electrospinning.

Optimal electrospinning was judged based on the speed at which the solvent would evaporate from the spike electrode, visual confirmation of fibre 'spinning' followed by visual inspection for 'spitting', whereby if the solvent does not evaporate before the electrospinning jet hits the collection fabric the solvent dissolves previously laid down material. Acetone was first used as a solvent system; however, this was found to evaporate too quickly from the spike electrode. This evaluation was carried out on the Elmarco Nanospider Lab-200, whereby the spinning solution is an open bath, and is therefore not contained, meaning volatile solvents are liable to evaporation. As acetone was found to evaporate too quickly, HFIP was evaluated and this reduced the evaporation rate as HFIP is known to have a higher flash point of 93°C, in comparison to acetone (-18°C).

A spinning solution, containing rat tail collagen and PCL, dissolved in HFIP – S6%-CP50:50 – was therefore used to test the parameters of spinning distance and voltage. For the optimisation study, a small spike electrode was used in order to reduce material waste. Thus, spinning distances were tested at the minimum distance of 120 mm and maximum of 155 mm. At the 120 mm spinning distance the solution was found to spin from approximately 16 kV onwards and therefore was tested at 10 kV intervals from 20 kV to 60 kV. By increasing the spinning distance to 155 mm, the solution only started to spin at 40 kV, so was tested at 40, 50 and 60 kV.

5.3.1.1 Membrane Microstructure

Samples were visualised using SEM, whereby fibres appeared to be randomly orientated and non-aligned in all formulations investigated (Figure 5.3A-B & F-G). Fibre diameter was quantified from SEM images, where the fibre

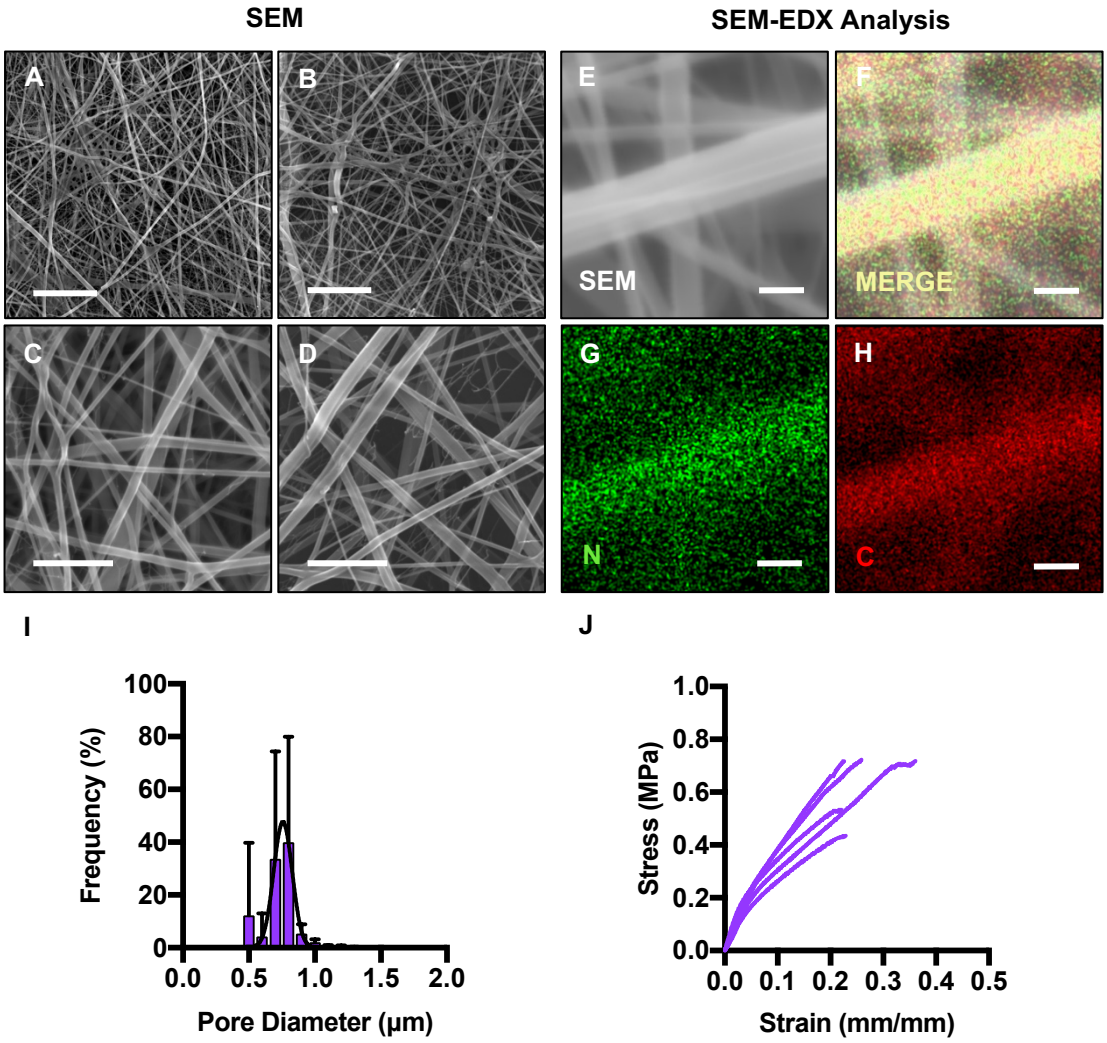

Figure 5.3: Free surface electrospinning optimisation study. A-D) Electrospun optimisation membranes (M6%-CP50:50) were imaged using SEM, two compositions were shown as representative – 155 mm, 30 kV (A,C) and 155 mm, 60 kV (B,D). **E-H)** The presence of collagen within the membranes was confirmed using energy dispersive X-ray (EDX) spectroscopy. A representative SEM image (E) was used to show elemental mapping overlay of nitrogen and carbon (F). Nitrogen only (G) and carbon only (H) mapping were also shown to form over distinct fibres. I) Pore size quantification (n=5) was carried out using gas flow porometry, pore size distribution was plotted and showed normal distribution (Gaussian). J) Tensile testing to failure was carried out (n=5), allowing for a stress-strain curve to be plotted. Scale bars represent 10 µm (A-B, x1000), 2.5 µm (C-D, x 10000) and 500 nm (E-H).

diameter was in the range of 236-401 nm (Table 5.2). At this point, influence of spinning voltage or distance could not be discerned on the resultant dimensions and the structure of the as-spun materials as fibre diameter was seen to be similar despite changes to spinning distance and voltage. However, a trend of increasing fibre diameter with increased spinning voltage was observed, however this was not significant (one-way ANOVA, $P>0.05$). Although the use of a higher voltage resulted in faster spinning times, it also increased the likelihood defects in the collected fibre web, due to droplets of unevaporated solvent reaching the collector, and dissolving proximal fibres. Herein, this is referred to as 'solvent damage' and was particularly apparent at the lower spinning distance of 120 mm.

To confirm that both collagen and PCL were spinning together with minimal phase separation during fibre formation, EDX analysis on SEM images was carried out, whereby the overlay of nitrogen (taken as the presence of collagen) and carbon (for Collagen and PCL) for individual fibres was taken as a confirmation of the blended collagen-PCL fibres (Figure 5.3C-D & G-H).

Table 5.2: Mean fibre diameter of the optimisation electrospun membranes. Mean ± standard deviation (SD) shown.

Composition	Distance (mm)	Voltage (kV)	Mean Fibre Diameter ± SD (nm)	Fibre Diameter Range (nm)
M6%-CP50:50	120	20	292 ± 138	65 - 603
		30	280 ± 117	28 - 553
		40	366 ± 184	140 - 893
		50	356 ± 148	160 - 747
		60	362 ± 162	116 - 683
	155	40	236 ± 84	101 - 373
		50	322 ± 198	63 - 959
		60	401 ± 257	99 - 1280

5.3.1.2 Pore Size Analysis

Samples of the M6%-CP50:50 were taken to analyse pore size distribution using capillary flow porometry. Here, samples (n=5) were wetted with a fluid of known surface tension (15.6 mN/m, Galpore, Porometer) and pressurised gas was pushed through a sample. Three key parameters were measured using this process, where the smallest pore was measured to be 0.63 ± 0.08 µm, which was seen to be significantly different to the mean pore size which was 0.77 ± 0.10 µm (paired t-test, P=0.0007). The first bubble point, or largest pore was measured at 17.61 ± 4.81 µm, however accounted for only about 0.00021% of all pores so would be unlikely to influence the overall porosity.

Pore size distribution was analysed, showing normal distribution (Gaussian) (Figure 5.3I), whereby 96 ± 1% of all pore diameter's were found within the range of 0-1 µm and 4 ± 1% of all pores were found to be between 1-2 µm and 0.06 ± 0.02% of all pores were greater than 2 µm.

5.3.1.3 Tensile Testing

Tensile testing was carried out on M6%-CP50:50 (Figure 5.3J), whereby σ at F_{max} was measured at 0.62 ± 0.13 mega pascals (MPa) and ε at F_{max} was 0.26 ± 0.06 mm/mm. The elastic modulus was taken between 0.02 to 0.06 mm/mm and calculated to be 3.57 ± 0.90 MPa.

5.3.2 Generation of Barrier Membranes

Membranes with increased thickness were made by increasing the electrospinning solution volume from 5 to 10 mL. This made the membranes easier to remove from the collection fabric as well as easier to handle by increasing the thickness of the material from approximately 50 µm to 100 µm (data not shown) (Figure 5.4A-B-macro image). This section details the manufacture and characterisation of blended collagen and PCL (6% w/v) based membranes (M6%-CP50:50, M6%-CP60:40, M6%-CP70:30 and M6%-CP80:20) in comparison to M3%-PCL, to show the effect collagen has on material characteristics. The differing concentrations used were optimised during preliminary work, whereby PCL at 6% w/v was too viscous to be electrospun. In addition, a 100% collagen solution (6% w/v) was tested,

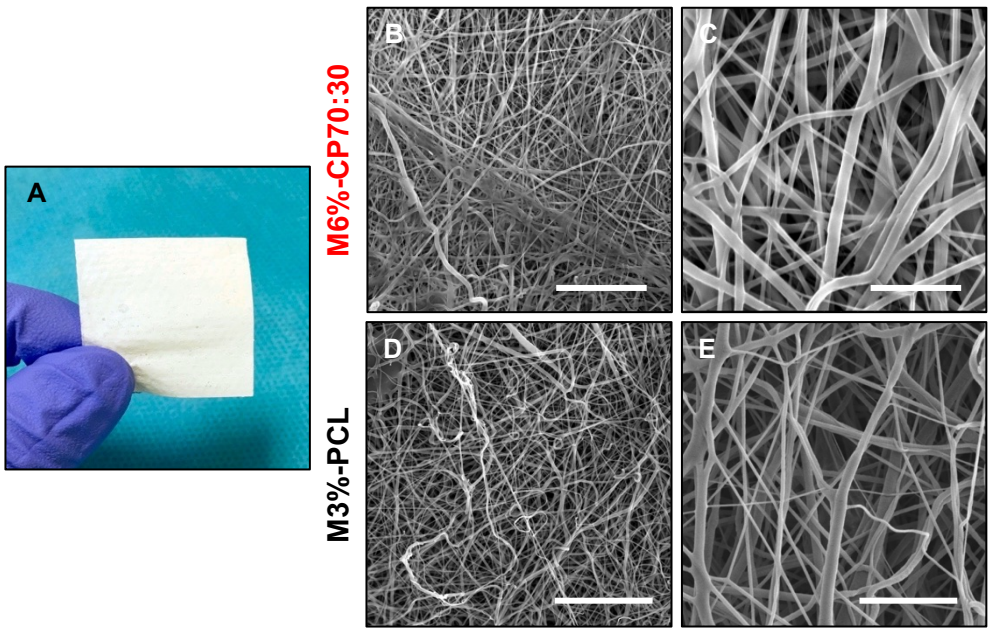

Figure 5.4: Material characterisation of free surface electrospun membranes. A) Macro image of the produced membranes (20 x 20 mm sample). **B-E)** SEM imaging showed free surface electrospun membranes produced randomly aligned fibres. SEM images at increasing magnification of M6%-CP70:30 and M3%-PCL. Magnification and scale bars, x1000, 25 µm (B&D), x5000, 5 µm (C&E).

however, it did not form an adequate web to be peeled from the backing fabric, thus was not carried forward to characterisation. Each of the solutions were subjected to the same electrospinning conditions, to maintain consistency, whereby an electrical field of 30 kV was applied to a spike electrode which had a spinning distance of 155 mm, from spike to grounding collector.

5.3.2.1 Barrier Membrane Microstructure

As with the membranes generated in the optimisation study, randomly aligned nonwoven fibres were imaged under SEM (Figure 5.4). All of the collagen-PCL membranes (M6%-CP70:30 taken as representative images, Figure 5.4B-C) were found to look similar to M3%-PCL (Figure 5.4D-E). Fibre size diameter was measured from these SEM images, where three images were taken and n=20 measurements were taken from each image, for all compositions (Table 5.3).

Even distribution of nano-fibre diameter was seen for all membrane compositions (Table 5.3). Fibre diameter was seen to be 354 ± 174 nm (116-788 range) for M3%-PCL which was not significantly different (Kruskal-Wallis

test, P<0.05) to the collagen-based membranes, with fibre diameters of 278 ± 126 nm (M6%-CP50:50), 414 ± 175 nm (M6%-CP60:40), 319 ± 108 nm (M6%-CP70:30) and 272 ± 101 nm (M6%-CP80:20). It should be noted that M6%-CP60:40 was found to have significantly higher mean fibre diameter in comparison to M6%-CP50:50 and M6%-CP80:20 (P<0.0001).

Table 5.3: Mean fibre diameter of the free surface electrospun membranes. Mean ± standard deviation (SD) shown. **** P<0.0001 against M6%-CP60:40, Kruskal Wallis test, Tukey's multiple comparisons post hoc test.

Membrane Composition	Mean Fibre Diameter ± SD (nm)	Fibre Diameter Range (nm)
M3%-PCL	354 ± 174	116 – 788
M6%-CP50:50****	278 ± 126	119 – 607
M6%-CP60:40	414 ± 175	116 – 754
M6%-CP70:30	319 ± 108	140 – 549
M6%-CP80:20****	272 ± 101	112 – 701

5.3.2.2 Pore Size Analysis

An interconnected network of fibres was seen using SEM (Figure 5.4), producing a porous web structure. Quantification of membrane pore size (in triplicate) was carried out using gas flow porometry. It was shown that the addition of collagen to the membranes (M6%-CP50:50, M6%-CP60:40, M6%-CP70:30 and M6%-CP80:20 compositions) caused a reduction in pore size (Figure 5.5A-B).

The smallest measured pore size significantly (one-way ANOVA, P<0.001) reduced from 1.01 ± 0.13 µm (M3%-PCL) to 0.26 ± 0.03 µm, 0.49 ± 0.08 µm, 0.27 ± 0.05 µm and 0.43 ± 0.21 µm for the M6%-CP50:50, M6%-CP60:40, M6%-CP70:30 and M6%-CP80:20 compositions, respectively (Figure 5.5E).

This was also true for mean pore size, which significantly reduced from 1.37 ± 0.06 µm (M3%-PCL) to 0.48 ± 0.05 µm, 0.65 ± 0.11 µm, 0.41 ± 0.01 µm and 0.61 ± 0.08 µm for the M6%-CP50:50, M6%-CP60:40, M6%-CP70:30 and M6%-CP80:20 compositions, respectively (one-way ANOVA, P<0.0001)) (Figure 5.5D). The first bubble point or largest pore size also reduced from 34.98 ± 0.09 µm (M3%-PCL) to 19.24 ± 0.02 µm, 5.43 ± 4.18 µm, 11.64 ± 8.48

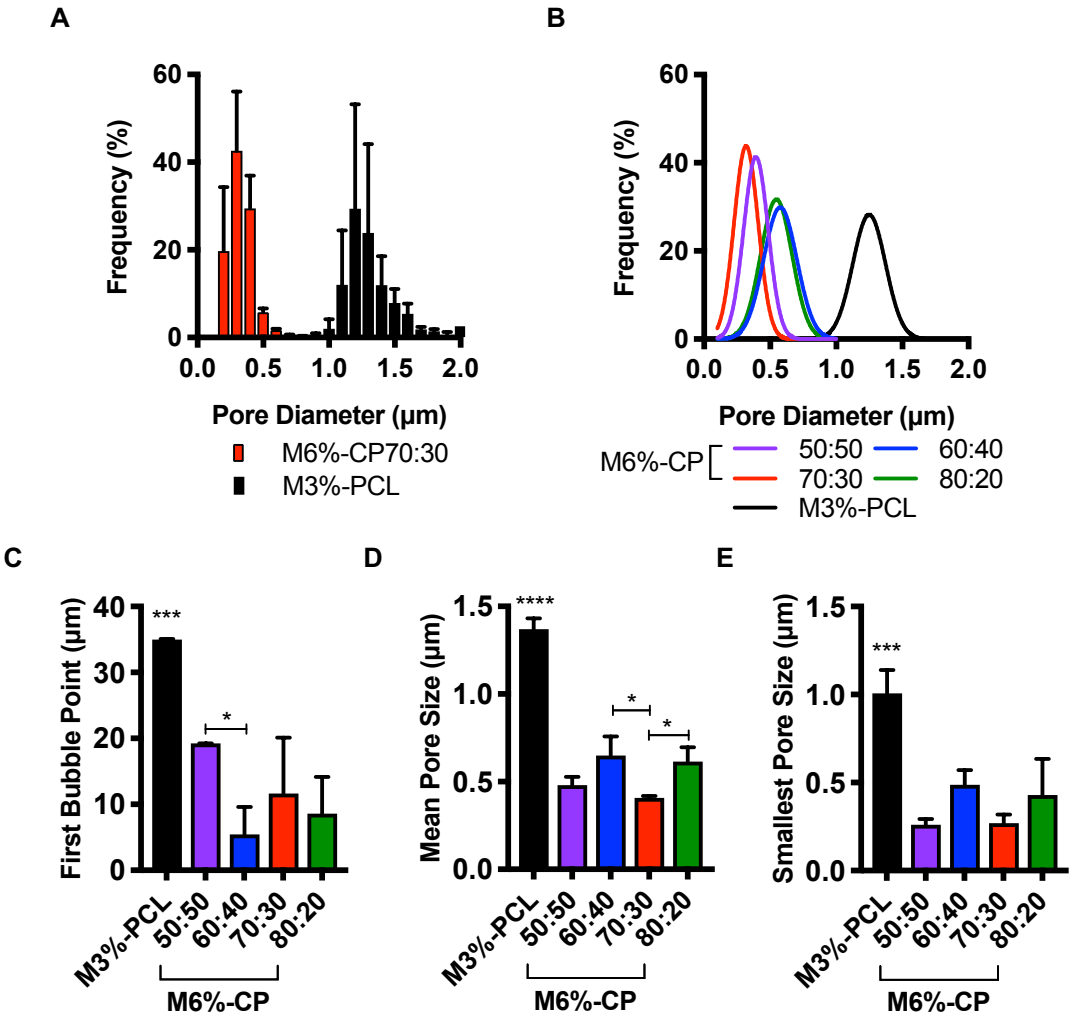

Figure 5.5: Pore size analysis of free surface electrospun membranes. Gas flow porometry was used to measure the pore sizes of the membranes of the M3%-PCL and the M6%-CP50:50, M6%-CP60:40, M6%-CP70:30 and M6%-CP80:20 compositions. A) Pore sizes distribution shown as frequency distribution, comparison of M3%-PCL and M6%-CP70:30. **B)** Gaussian distribution shown for all samples. **C)** First bubble point or the largest measured pore was quantified (first pore to be measured). **D)** Mean pore size, at the mean flow point (intersection of the wet curve and interpolated half dry curve, Figure 5.2). **E)** Smallest measured pore size (intersection of wet curve and dry curve, Figure 5.2). Data was collected in triplicate and plotted as mean ± standard deviation. One-way ANOVA with Tukey's multiple comparisons post hoc test was carried out ($P<0.05$). Stars above M3%-PCL bar shows significance compared all of the collagen containing compositions, *** ($P<0.001$), **** ($P<0.0001$). Line with * ($P<0.05$) shows significance between collagen containing samples.

μm and 8.61 ± 5.54 μm (one-way ANOVA, P<0.001) (Figure 5.5C). Pore size frequency distribution was shown to be normally distributed in all cases, with minimal amounts (0.27 ± 0.14%, 2.95 ± 1.08%, 0.05 ± 0.01%, 1.51 ± 0.52%) of pore sizes above 1 μm for all the collagen-PCL compositions. However, in comparison 99.36 ± 0.41% pores were above 1 μm for M3%-PCL, with only 2.61 ± 0.03% of this measuring above 2 μm in diameter. Knowing that almost all pore sizes consistently sit below 2 μm (M3%-PCL) or 1 μm (M6%-CP50:50, M6%-CP60:40, M6%-CP70:30 and M6%-CP80:20 compositions) and based on the fact that MSCs (the chosen cell type to create a barrier for) and fibroblasts have a diameter of 12-21 μm (Jones et al. 2002; Walker et al. 2010; Siegel et al. 2013), this provides evidence to justify that a 'barrier' membrane has been created.

5.3.2.3 Water Contact Angle Measurements

In order to assess the hydrophobicity of the produced electrospun membranes and assess the effect of the collagen phase, water contact angle measurements were taken. Samples of each membrane were mounted on glass slides and a droplet of ultra-pure water was dropped onto the membrane (n=3). An image of the droplet on the membrane was taken twice a second and the contact angle of the droplet with the membrane was calculated (Figure 5.6C-D) and plotted over 15 seconds. This process was then repeated for equivalent pore free 'films' of each of the membrane compositions, including a PCL-free collagen control (S3%-C-Film) in order to show the effect of fibre formation of each of the membrane compositions.

The 'films' displayed water contact angle measurements with minimal variations over time for most of the samples investigated (Figure 5.A & C). However, S6%-CP60:40-Film saw a reduction in angle measured over 15 seconds from 114 ± 1° to 82 ± 4°, which was greater than the other films (Figure 5.A & C). All of the collagen-PCL containing films had an initial water contact angle of between 110-114°, whereby the S6%-C-Film started at a lower angle of 92 ± 4° and S3%-PCL-Film at a higher angle of 125 ± 1°.

When each of the electrospun membranes were tested, not only were the initial water contact angles measured smaller than the corresponding film for

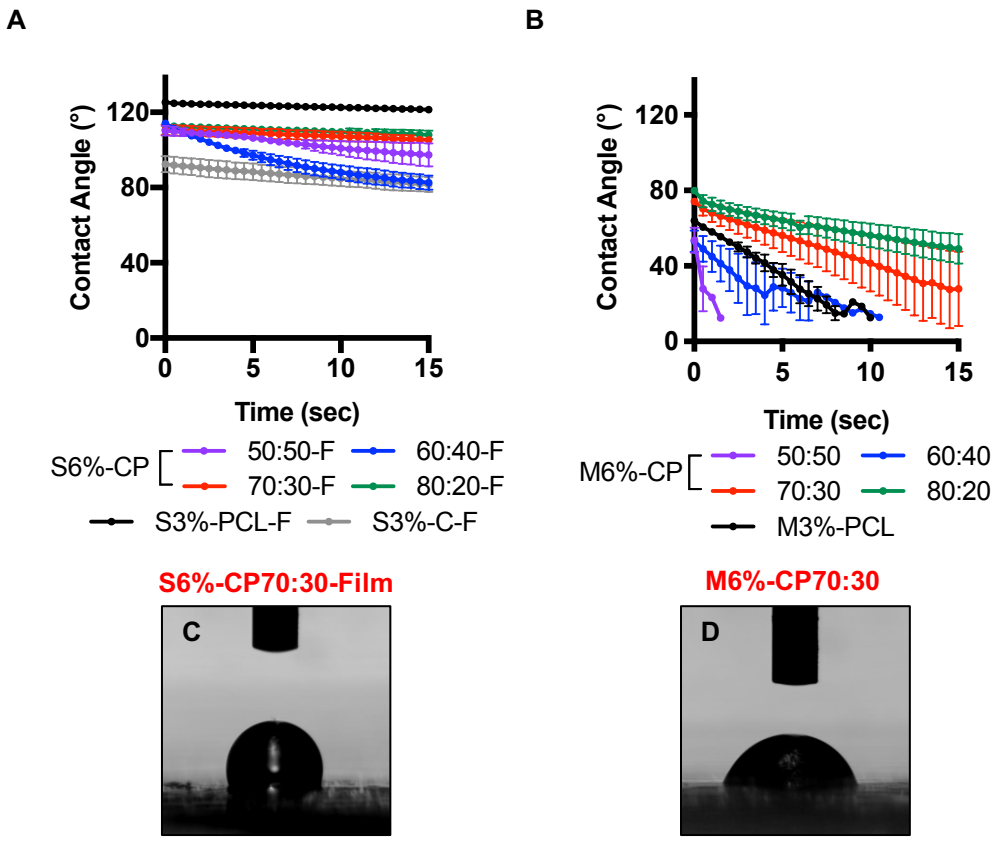

Figure 5.6: Water contact angle measurements of the free surface electrospun membranes in comparison to cast films. A) Water contact angle measurements were taken to assess the hydrophobicity of cast films, of the solutions used for electrospinning, to compare to, **B)** the free surface electrospun membranes using goniometry, where contact angle measurements of ultra-pure water were measured over time (15 seconds), in triplicate. **C)** Exemplar image of the water contact angle of S6%-CP70:30-Film and **D)** M6%-CP70:30. F – film.

each membrane but the angle measured showed a marked reduction over 15 seconds (Figure 5.B & D), most likely due to the porous nature of the web.

Initial recorded water contact angle for the tested free surface electrospun membranes was lower than that of respective films, measured at 54-80°, the water contact angle for M3%-PCL was found to sit in the middle of this data set at 64 ± 1°, a reduction of 61° in comparison to the S3%-PCL-Film. Over 15 seconds a reduction in water contact angle was seen for all free surface electrospun membranes, only two of the membranes maintained a visible water droplet for 15 seconds, whereby the final angle measured was 29 ± 20° (M6%-CP70:30) and 49 ± 8° (M6%-CP80:20) (Figure 5.B). The remaining three membranes absorbed the water droplet quicker than this, whereby the

last detectable water contact angle (in triplicate) was at 8 secs (15 ± 4°, M3%-PCL), 6.5 secs (21 ± 10°, M6%-CP60:40) and 0.5 secs (28 ± 12°, M6%-CP50:50). This shows that changing each electrospinning composition into a fibre form through free surface electrospinning results in a reduction of initial water contact angle and the further reduction of said angle over 15 seconds.

5.3.2.4 Tensile Testing

Tensile testing was carried out (n=5) on all collagen-PCL compositions in comparison to M3%-PCL (Figure 5.7A-F). These experiments were carried out without pretension, so the data was re-zeroed post acquisition (Section 5.2.7). From the force-extension graphs force at break (F_{max}) and extension at F_{max} were quantified. In addition, the elastic modulus of the material, taken as the gradient of the force-extension curve between 2-6 % extension was also calculated.

The F_{max} values were seen to reduce with the introduction of collagen to the membrane. However, significant reductions compared to the rest of the membranes was only seen at 80% collagen content (M6%-CP80:20) (one-way ANOVA, Tukey's post hoc, $P<0.05$), where F_{max} was 0.88 ± 0.22 N (Figure 5.7G). M3%-PCL displayed the highest stress at break value of 1.97 ± 0.40 N, but as previously described, was not significantly different to the other collagen-PCL membranes.

The most striking differences between the electrospun membranes was seen in the extension at F_{max} values, which was 69.5 ± 4.7 % for M3%-PCL, significantly decreasing for all collagen-PCL membranes (one-way ANOVA, Tukey's post hoc, $P<0.0001$) to 26.7 ± 3.4 % (M6%-CP50:50), 30.0 ± 2.8 % (M6%-CP60:40), 19.2 ± 3.7 % (M6%-CP70:30) and 12.4 ± 2.2 % (M6%-CP80:20) (Figure 5.7H). Within the collagen-PCL membranes the M6%-CP80:20 composition exhibited a significantly lower values ($P<0.05$) (Figure 5.7D&H) in comparison to all other collagen-PCL membranes. The tensile strain of M6%-CP70:30 composition was significantly lower ($P<0.02$) than that of M6%-CP50:50 and M6%-CP60:40, whilst, no significant difference was seen between M6%-CP50:50 and M6%-CP60:40 (Figure 5.7H).

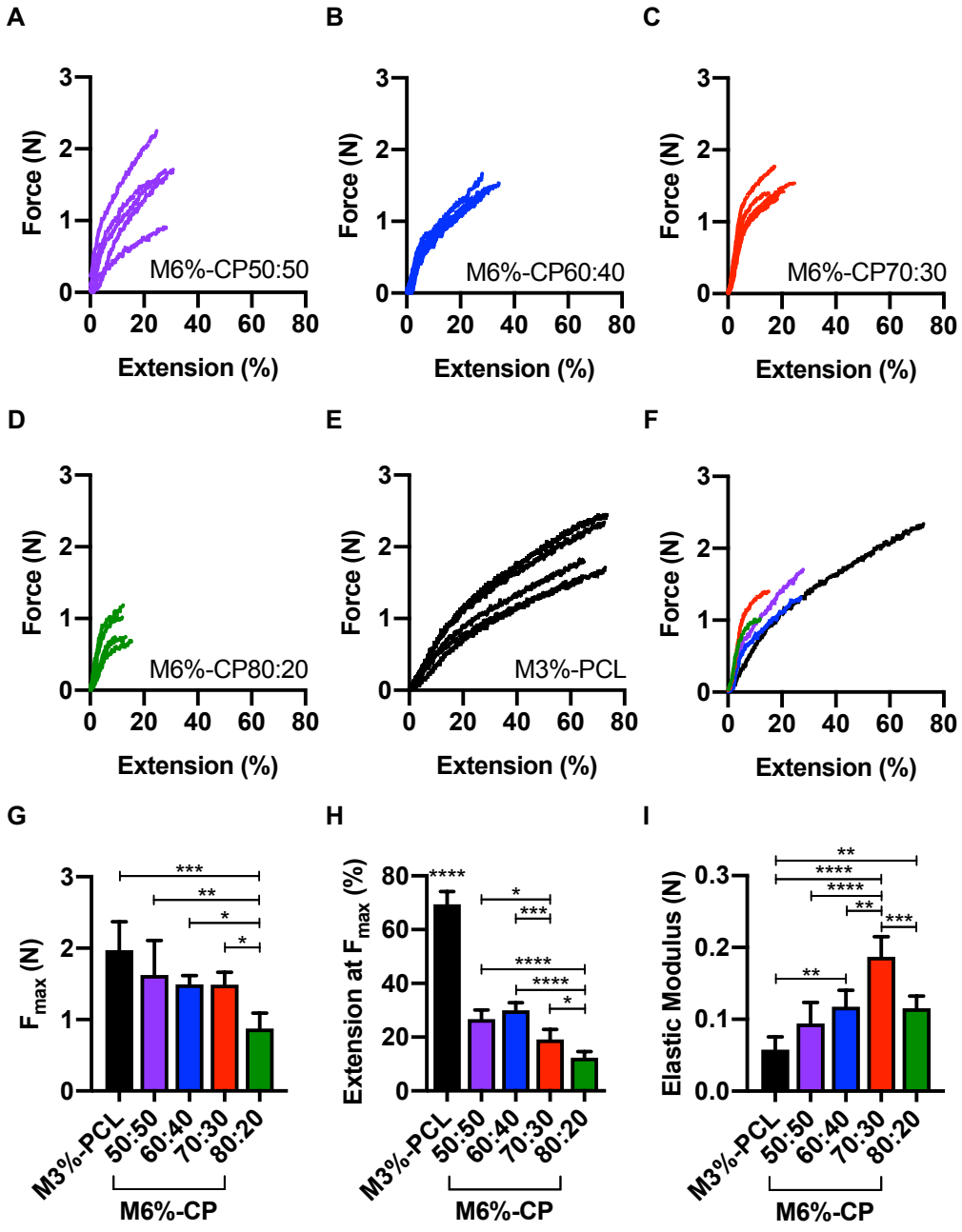

Figure 5.7: Tensile testing of free surface electrospun membranes. Samples were loaded under constant strain until break point, where a force-extension curve was plotted. **A)** M6%-CP50:50, **B)** M6%-CP60:40, **C)** M6%-CP70:30, **D)** M6%-CP80:20 and **E)** the M3%-PCL membrane. **F)** Curve for each membrane plotted together. **G)** Force (Newtons) measured at break (F_{max}). **H)** Extension (%) measured at F_{max} and **I)** elastic modulus – linear regression of the gradient of the tensile testing curve measured between 2-6 % extension. One-way ANOVA carried out with Tukey's multiple comparisons post hoc test ($P<0.05$). Stars above M3%-PCL (H) shows significance compared to all other membranes. Line with stars shows significance between membranes, * ($P<0.05$), ** ($P<0.01$), *** ($P<0.001$) and *** ($P<0.0001$).

The linear elastic region for each composition was quantified, as previously described (Figure 5.7I). M3%-PCL was found to have a significantly lower elastic modulus than all of the collagen-PCL membranes, apart from M6%-CP50:50 (one-way ANOVA, Tukey's post hoc, $P<0.05$), at 0.06 ± 0.02 N. In addition, the elastic modulus for M6%-CP70:30 was found to be significantly higher ($P<0.001$) than all other membranes at, 0.18 ± 0.03 N. However, the remaining collagen-PCL membranes were not significant from each other (0.09 ± 0.03 N (M6%-CP50:50), 0.12 ± 0.02 N (M6%-CP60:40) and 0.12 ± 0.02 N (M6%-CP80:20)) (Figure 5.7I).

To conclude, it was decided to take forward the M6%-CP70:30 membrane out of all of the developed range of free surface electrospun collagen-PCL membranes for future experiments in comparison to M3%-PCL, as a PCL control to ascertain the effect of collagen on membrane function. As the M6%-CP70:30 membrane contained the highest levels of collagen that still maintained tensile strength, unlike M6%-CP80:20 that had significantly ($P<0.05$) lower F_{max} and extension at F_{max} values.

5.3.3 Assessment of Barrier Membrane Collagen Content

Further to developing a range of collagen-PCL barrier membranes in comparison to the M3%-PCL control, the collagen content in the M6%-CP70:30 collagen-PCL barrier membrane was assessed.

5.3.3.1 Circular Dichroism

After initial confirmation of collagen content within the collagen-PCL free surface electrospun membranes using SEM-EDX (Figure 5.3), the effect of the solvent (HFIP) and electrospinning to the helical structure of the collagen within the membranes was assessed using CD. CD was reported as ellipticity (θ) at a given wavelength (nm), which is related to measured absorbance (See Section 5.2.9, Equation 5.3).

In-house rat tail collagen was isolated in acetic acid, so that collagen in the form of triple helix could be extracted. The acid-extracted collagen product was re-solubilised in either 17.4 mM acetic acid or HFIP to assess the effect of solvent and electrospinning on the helical structure of the collagen.

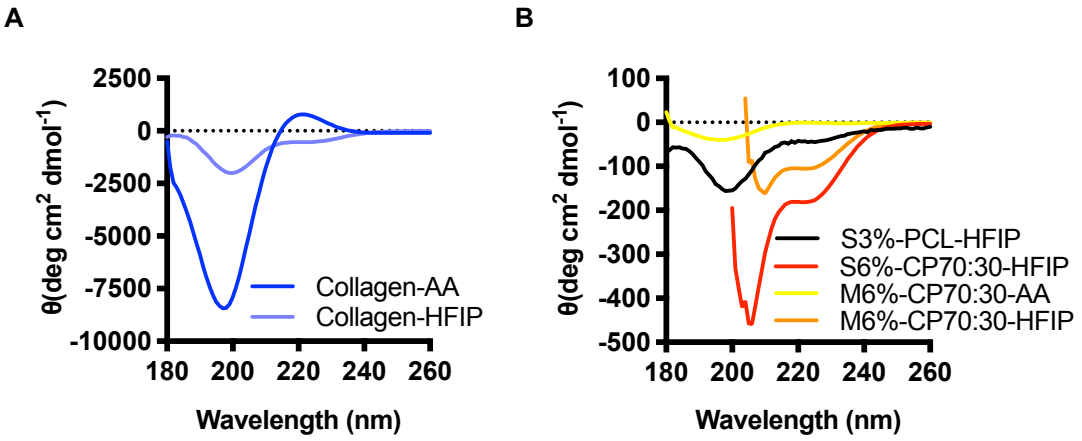

Figure 5.8: Assessment of helical structure of collagen before and after free surface electrospinning. A) Circular dichroism (CD) was carried out on in-house extracted rat tail collagen solutions prepared in either acetic acid (AA) (17.4 mM) or HFIP. **B)** CD was also carried out on the S6%-CP70:30 electrospinning solution (in HFIP), the solutions obtained via incubation of M6%-CP70:30 in either HFIP or AA and S3%-PCL in HFIP.

The CD spectrum of the collagen solution in acetic acid (Figure 5.8A) showed typical peaks at around 220 nm (positive peak) and 197 nm (negative peak) of collagen (Tronci, Russell & Wood 2013; Arafat et al. 2015). On the other hand, the solution of collagen in HFIP did not reveal a noticeable peak at 220 nm, whilst detectable intensity was measured at 190 nm. These results therefore suggest that solubilisation of collagen with HFIP is associated with partial denaturation of the triple helix collagen conformation (Figure 5.8.A).

In order to assess the effect of electrospinning (40 kV used) and fibre formation on the collagen organisation, samples of M6%-CP70:30 were solubilised in acetic acid or HFIP and compared to a sample of S6%-CP70:30 spinning solution (solvent system – HFIP) (Figure 5.8B). A reduction in the positive and negative peak were seen from the S6%-CP70:30 electrospinning solution (red, Figure 5.8B) and then resolubilised in HFIP membrane, M6%-CP70:30-HFIP (orange, Figure 5.8B). Electrospun collagen, was also solubilised out of free surface electrospun membrane, M6%-CP70:30, leaving behind the PCL in order to evaluate the helical structure of electrospun collagen without interference from the PCL signal, seen when S6%-CP70:30-HFIP and M6%-CP70:30-HFIP were tested (red and orange, Figure 5.B). As can be seen (Figure 5.B), the alterations to the original CD spectrum of collagen were observed in the case of the electrospun samples (RPN ~0.02),

suggesting that the denaturation of the collagen was also partially associated with the application of electrostatic voltage during fibre spinning.

5.3.3.2 Membrane Collagen Content and Release Profile in PBS

Collagen content of the membranes was confirmed visually by staining a collagen containing membrane (M6%-CP70:30) with PSR dye (Figure 5.9A-B). The collagen-free PCL membrane was also stained as a control and showed no staining, confirming the PSR dye does not bind to PCL, only collagen (Figure 5.9C-D). The collagen content of M6%-CP70:30 over time was next assessed. Samples were kept in PBS in tissue culture conditions for up to 3 weeks, at each time point samples were stained for PSR and the dye was released from the membrane and quantified spectrophotometrically. Unlike the PCL control, which showed no PSR staining, a significant immediate release of collagen was observed after 24 hours *in vitro* ($P<0.0001$), whereby approximately 50% of the original dye was lost (Figure 5.9E). The remaining content of collagen did not significantly vary up to day 7. At day 14, another 25% loss (seen in absorbance) of the original collagen content was measured, so that about 25 wt.% collagen could still be found in the membrane following 21 days *in vitro* (Figure 5.E).

It has been shown that the helical structure of the collagen within the M6%-CP70:30 has been partially degraded following being subjected to 40 kV during the free surface electrospinning process as well as through exposure to HFIP. In addition, this partially degraded collagen is also release from the membrane over a period of three weeks, with 50% of the collagen being released in the first 24 hours.

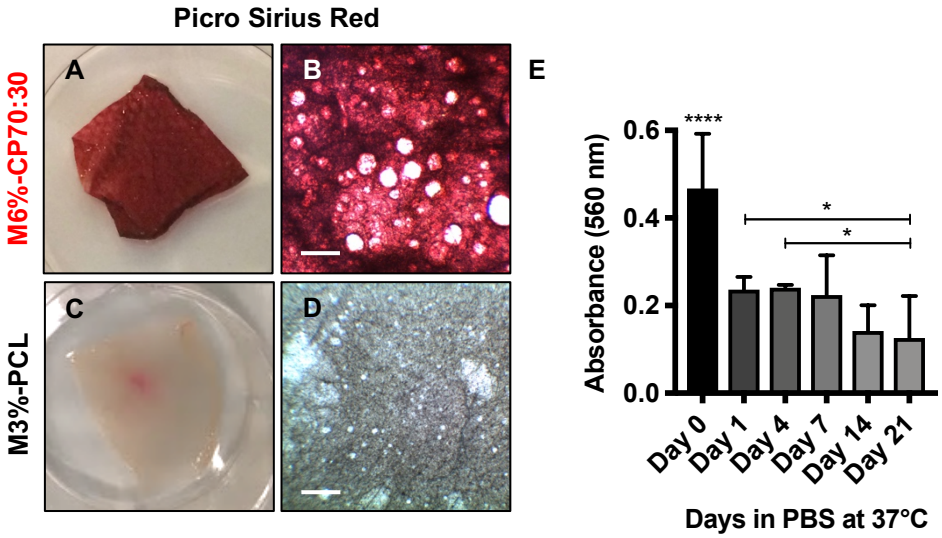

Figure 5.9: Collagen stability of M6%-CP70:30 in PBS. A&C) Digital macrographs of PSR-stained and acidified water-washed samples of M6%-CP70:30 and M3%-PCL membranes. **B&D)** Light microscopy images of PSR stained fibres of M6%-CP70:30 and M3%-PCL. **E)** Collagen content within the electrospun membranes was assessed over time when placed in PBS at 37°C for up to 21 days. Collagen content on the membrane was quantified via PSR dyeing and UV-Vis spectrophotometry. One-way ANOVA was carried out with Tukey's multiple comparisons post hoc test ($P<0.05$). **** ($P<0.0001$) above the day 0 bar denotes significance against the rest of the time points. Samples shown in A,B are 20 x 20 mm. Line with * shows significance between time points, * ($P<0.05$). Scale bar represents 200 µm (B,D).

5.4 Discussion

Free surface electrospinning was investigated as a one-step strategy to generate a set of prototype membranes equipped with soft tissue barrier and MSC containment functionalities. A series of collagen-PCL free surface electrospun membranes were developed with increasing levels of collagen and compared to a PCL membrane control. The rationale for inclusion of collagen was to provide bioactive function, whilst PCL would maintain the long-term, coherent barrier function. Membrane characterisation was carried out at molecular, microarchitectural and macroscopic scale, aiming to develop reliable process-structure relationships and achieve collagen-based prototypes with surgical manipulation capability. The material characteristics of said membranes were evaluated to assess the tensile strength and collagen content of the membranes at the time of manufacture and over time *in vitro*.

5.4.1 Comparison of Prototype Membranes

The optimisation membrane (Section 5.3.1) and the barrier membranes (Section 5.3.2) differ with respect to how much solution volume was employed during free surface electrospinning (i.e. 5 compared to 10 mL). The increase in spinning volume resulted in the formation of membranes with increased handling capabilities as well as increased fibre deposition area (seen visually). Fibre diameter was found to be similar in M6%-CP50:50 membranes electrospun with varied volume of electrospinning solution, whilst the mean pore size was found to slightly reduce from 0.77 μm to 0.48 μm, suggesting that the increase in numerical fibre deposition led to greater pore occlusion. Most notably σ at F_{max} increased from 0.62 MPa to 1.4 MPa, therefore showing that increasing the number of fibres laid down resulted in an increase in fibre network (web) strength. However, Young's modulus, a measure of material stiffness (Schneider & Schultrich 1998), increased from 3.57 to 5.64 MPa, showing that the resistance to extension at low load also increased.

5.4.2 Comparison of Collagen Containing and PCL Membranes

For the first time, collagen-PCL containing fibres were free surface electrospun up to 80% collagen (M6%-CP80:20) to produce 'barrier'

membranes. Previous studies have used needle-electrospinning, rather than commercially scalable free surface electrospinning, to produce membranes of up to 80% collagen or 50-70% gelatin or combined with a hydrogel (Ekaputra et al. 2011; Chong et al. 2007; Ren et al. 2017).

The combination of a mean fibre diameter in the range of 272 – 414 nm and >95% of all pores being of 0-1 μm in diameter for the collagen-PCL membranes and 1-2 μm for M3%-PCL membranes is consistent with a 'barrier' membrane being produced, MSCs and fibroblasts are highly unlikely to penetrate due to size exclusion. The cell size of MSCs and fibroblasts are approximately 12 μm in diameter for uncultured BM MSCs and 21 μm for cultured BM MSCs (Jones et al. 2002; Walker et al. 2010; Siegel et al. 2013), so the aforementioned pore sizes can be expected to prevent migration thus acting as an effective containment device of MSCs to the bone defect site.

Polysulfone (PSU) based electrospun membranes with a mean fibre diameter of 92 nm have been were shown to have a more consistent fibre diameter, similar to reported in the present study, although the variation reported herein was slightly higher (Wang et al. 2011). Upon cell seeding, BM MSCs stayed on the surface of the fibre webs rather than infiltrating, confirming barrier performance (Wang et al. 2011). Pore size has been reported to be larger in PCL needle electrospun membranes, whereby mean pore size ranged from 5-22 μm, dependent on the geometry of the spinning collector material (Vaquette & Cooper-White 2011). It was found with increased pore size of 0-50 μm, opposed to only 1-2 μm (as in this study), cell penetration depth-wise into the scaffolds was approximately 250 μm (Vaquette & Cooper-White 2011). This further supports the effective barrier function that can be expected the membranes produced in this study, preventing cell penetration. This assertion is investigated in further depth in Chapter 6.

Upon comparing films of each of the materials to testing the materials as fibre, the water contact angles were reduced for all membranes, including M3%-PCL. Suggestive that even though PCL is known to be a hydrophobic polymer (Woodruff & Hutmacher 2010), in the electrospun nonwoven fibre-web form, wettability improves. Chakrapani et al., (2012) showed similar results, with water contact angle of an electrospun PCL membrane reducing from 128° to

44°, although starting with a higher water contact angle than that of this study a reduction was angle was seen, in agreement with this study. In addition, the introduction of collagen to the electrospun membranes resulted in a reduction in water contact angle, for not only the films, but the membranes, suggestive that collagen reduces the hydrophobicity of the membranes. Previous studies have also found this, whereby similar electrospun membranes showed initial water contact angles to the collagen-PCL electrospun membranes of 37-63° (Chakrapani et al. 2012; Gong et al. 2019; Ren et al. 2017).

Tensile testing of the collagen-PCL membranes in comparison to M3%-PCL showed a significant reduction in extension at break, upon the introduction of collagen, which has been shown in similar studies, however, Chakrapani et al., (2012) showed no change with the introduction of collagen. Reductions in force at break with all collagen-PCL membranes in comparison to M3%-PCL membranes were seen. However, this was only significant for M6%-CP80:20, which was significantly weaker than all the other membranes. Due to this it was decided that M6%-CP70:30 should be taken forward as the candidate collagen-PCL membrane to test in comparison to M3%-PCL, as the highest collagen content membrane, with the best mechanical strength properties.

The elastic modulus and therefore stiffness of the membranes was shown to significantly increase with the introduction of membranes with over 60% collagen, however, M6%-CP70:30 was shown to be significantly stiffer than all other membranes. Ke et al. (2017) developed a Gelatin-PCL needle based electrospun membranes at 50:50 and 70:30 ratios in comparison to PCL control membranes, equivalent to that of this study. Similar trends were seen whereby the PCL control membrane had a lower Young's modulus but higher strength and strain at break compared to the collagen containing membranes. However, peak strength was 30 MPa (PCL) and 15 MPa (50:50 and 70:30), which, even though higher than this study, is still comparable.

Another similar study, using needle electrospinning to co-spin collagen with PCL produced 50:50 and 75:25 membranes with a similar fibre diameter of 130 nm (Chakrapani et al. 2012). The tensile properties were comparable to that of this study at 1.2 MPa and 0.84 MPa, respectively, with a break point extension of 56% and 54% (Chakrapani et al. 2012). Both of the

aforementioned studies confirm that a drop in tensile strength is seen with the introduction of or increase in collagen content of the membranes.

To draw all of the membrane characterisation data together, it has been shown that fibre diameter is similar between M3%-PCL and the collagen-PCL membranes. However, pore size is reduced in the collagen-PCL membranes compared to M3%-PCL, suggestive of a higher density of fibres and material in the collagen-PCL membranes. Therefore, tensile testing data was not converted into stress-strain curves as the samples were not weighed (thickness was measured) prior to testing so density could not be ascertained.

5.4.3 Assessment of Membrane Collagen Content

Collagen is insoluble in nature and must be dissolved in order to carry out electrospinning. Acetic acid can be used to solubilise collagen, however cannot be electrospun without the presence of a second polymer (Chakrapani et al. 2012). Thus, to successfully spin collagen, fluoroalcohol solvents such as HFIP are normally used. However, it has been shown that the process of electrospinning as well as HFIP can denature collagen (Zeugolis et al. 2008). This was confirmed during this study where it was shown that solubilising collagen into HFIP caused a certain level of denaturation of the collagen, which was increased upon electrospinning. Therefore, it is important to consider that the collagen content of M6%-CP70:30 is likely to have high levels of gelatin, rather than collagen.

Collagen or gelatin, referred to ‘collagen product’ from herein, content of the produced collagen-PCL membranes was confirmed during the optimisation study using SEM-EDX to map nitrogen localisation on the electrospun fibres. However, this was discontinued due to the subjective nature of elemental mapping for organics. Following on from this a histological stain for collagen – PSR which binds to basic groups with the collagen molecule (Junqueira, Bignolas & Brentani 1979), was utilised to visualise an even distribution of collagen throughout the electrospun barrier membranes. Quantification of collagen using an adapted protocol from Ferreira et al. (2016) the M6%-CP70:30 barrier membrane showed a loss of 75% of the original collagen content over three weeks, which was to be expected due to the lack of

crosslinking of the collagen and PCL. Future work (Chapter 6) will show if this loss of collagen from the membrane, especially as 50% is lost in the first 24 hours, has an effect on cellular attachment and proliferation.

The loss of ‘collagen product’ from the barrier membrane within the first 24 hours in PBS can be explained in terms of its denaturation into gelatin, i.e. the water soluble degradation product of intact helical collagen (Veis, Anesey & Cohen 1961). Future work could involve adopting other forms of fibrous membrane production, that do not necessitate processing collagen with HFIP or exposing the material to high voltage, liable to disrupt the helical structure. Preliminary work (not shown in this thesis) has been carried out using free surface electrospinning of a methacrylated form of PCL, which when subsequently coated in methacrylated helical collagen UV crosslinked, produces a PCL membrane covalently bonded to undenatured collagen. This not only produces a material that contains intact collagen, but it is also crosslinked to the underlying structural polymer, thus giving potential to reduce the collagen loss when incubated in saline.

As this material was developed with its future use in mind, a product specification was produced (Figure 5.1). The produced membranes are easy to handle, customisable in size, degradable and biocompatible. Early assessment on pore size suggests that the membrane can contain grafting materials whilst preventing cell migration, whilst mimicking human periosteum by containing collagen and being of similar thickness. Limitations to the study include the aforementioned lack of crosslinking of the collagen, which results in early loss of collagen from the material, as well as the partial denaturation of the helical collagen source into gelatin, however, at this point it is unknown whether this is a negative or not. In addition, viscosity measurements of the electrospinning solutions were not carried out, due to lack of remaining collagen and time constraints. Ideally this would be carried out in future work to allow for easy replication of membranes in the future.

5.5 Conclusions

Two free surface electrospun barrier membranes have been developed of known porosity and tensile strength. Mechanical integrity was lost at M6%-CP80:20, therefore the candidate membrane was M6%-CP70:30. The collagen-PCL membranes have slightly smaller pores than M3%-PCL, however, both are indicative of a barrier to cellular infiltration. Collagen content improved the wettability of the membranes in comparison to M3%-PCL. However, the collagen present was mostly denatured upon contact with HFIP and electrospinning, thus should be considered as mostly gelatin. In addition, a large amount of ‘collagen product’ (collagen or gelatin) is lost over 3 weeks, but the majority occurs after 24 hours. Note however, that whilst the ‘collagen product’ is lost from the membrane over time, PCL remains intact such that barrier function is not compromised.

Chapter 6: Tracking MSC Migration and MSC Proliferation onto Electrospun Barrier Membranes

6.1 Introduction

Throughout this thesis, the architecture of periosteum (Chapter 3) and two sources of MSCs (BM and periosteum) (Chapter 4) were assessed. Based on the architecture of periosteum and orthopaedic surgeons need, free surface electrospun membranes were manufactured (Chapter 5), made from PCL (M3%-PCL) or a blend of collagen and PCL (M6%-CP70:30). These membranes were characterised for material properties and collagen content.

This work was carried out to ascertain whether samples of periosteum harvested during surgery and the MSCs digested from this tissue were a viable source of cells that could improve bone regeneration in the clinical setting of CSBD repair. The free surface electrospun membranes were developed to be a barrier to cell migration from the outer skeletal musculature (Ogiso et al. 1991) as well as to contain MSCs and grafting material to the defect site during the early stages of bone regeneration. In addition, the membrane will provide support for periosteum regeneration, through facilitating cell adhesion, proliferation and migration onto the material.

6.1.1 Cellular Attachment onto Electrospun Membranes

As the main function of the free surface electrospun membranes (produced in Chapter 5), is to support periosteum regrowth during CSBD repair, the ability of said membranes to promote cellular attachment is paramount. The following section investigates the current literature surrounding MSC and osteoblast growth onto membranes, mainly focusing on those that are electrospun in nature as comparisons to the work carried out in this thesis.

6.1.1.1 MSC Attachment onto Electrospun Membranes

Human BM MSCs were grown onto PSU electrospun membranes, whereby the BM MSCs were shown to attach and proliferate onto the membranes, with minimal dead cells (Wang et al. 2011). Upon osteogenic induction, ALP

activity and Ca^{2+} deposition was shown to be significantly higher on the PSU membranes compared to tissue culture plastic (Wang et al. 2011), displaying the membrane's potential to provide a surface to allow for osteogenesis of human BM MSCs. In another study, electrospun PCL-Gelatin membranes were functionalised with SDF-1 (Ji et al. 2013), a chemokine known to be important to MSC homing and localisation in the BM (Honczarenko et al. 2005). Functionalisation showed a 5-7 fold increase in cell migration (transwell migration assay) compared to PCL-Gelatin control membranes *in vitro* and upon *in vivo* assessment (rat cranial defect), functionalised scaffolds resulted in 6 fold higher bone formation after 8 weeks, compared to the PCL-Gelatin control scaffold (Ji et al. 2013).

Phipps et al. (2011) demonstrated BM MSC attachment and proliferation onto electrospun PCL-collagen-HA membranes, which was increased compared to PCL control membranes after 1 day in culture. Interestingly, by day 7 in culture the human green fluorescent protein (GFP)-labelled MSCs showed cellular alignment onto the PCL-collagen-HA membrane, which was not seen on the PCL control membranes (Phipps et al. 2011). This potential for MSCs to align could be particularly important when attempting to produce new periosteum. Cells lining bone within the cambium layer of periosteum have been shown to be aligned longitudinally along the bone (Foolen et al. 2008; Shi et al. 2014). The process of developing a biomaterial that would guide MSC alignment was investigated by Shi et al. (2014). Here, cast PLGA nanosheets were produced with regular aligned 'grooves', shown to replicate native grooves within periosteum. Following fibronectin surface treatment, human AT MSCs were shown to align along the grooves within the nanosheets, whereas no alignment was seen with 'flat' nanosheets with no grooves (Shi et al. 2014).

It should be noted that most MSCs used in these studies have been of BM origin, however, with the aim to replicate or support periosteum, the interaction between material and periosteum derived cells is of importance. However, in Filion & Song (2013) rat MSCs derived from periosteum (femur and tibia) and BM (femur and tibia marrow cavity) were grown onto electrospun membranes, made from cellulose and sulphated cellulose. In standard culture conditions initial MSC attachment was higher for the sulphated membranes but no

differences were seen between MSC type. Upon osteogenic induction of periosteum MSCs, the sulphated membranes also resulted in higher Ca^{2+} staining, however, comparisons to BM counterparts were not made (Filion & Song 2013).

6.1.1.2 Osteoblast Cell Line Attachment

Osteoblasts, the mature cell type that MSCs differentiate into following osteogenic induction, have been targeted as another cell type used to investigate cellular interactions with biomaterials for bone repair. Stachewicz et al. (2015) grew osteoblast cell lines from rats (UMR106) and mice (MC3T3-E1) onto aligned and randomly aligned electrospun PLGA fibres. It was shown that with alignment of fibres, a homogenous distribution of osteoblasts was seen, which were more elongated, with fibre direction influencing cell growth as well as preventing cellular penetration into the membrane (Stachewicz et al. 2015).

Another study produced electrospun membranes similar to those in Chapter 5, both the PCL and Collagen-PCL membranes showed good adhesion for mouse osteoblasts and increased Ca^{2+} deposition in comparison to osteoblasts grown on tissue culture plastic following osteogenic induction (Ren et al. 2017). A recent study looked at crosslinked PCL-Gelatin electrospun membranes that were co-spun with antibacterial drugs (Gong et al. 2019). Mouse osteoblasts were shown to attach and proliferate onto the PCL-Gelatin membrane as well as the drug loaded membrane, however, the drug loaded membrane showed favourable *in vitro* proliferation and *in vivo* bone formation, during rabbit forelimb CSBD repair (Gong et al. 2019).

To conclude, the current literature points to successful MSC attachment onto electrospun membranes of various polymer types and combinations with collagen or gelatin. BM MSCs were shown to align onto randomly fibre orientated membranes in one case due to the presence of collagen within the PCL-Collagen membrane, whereas AT MSCs showed cellular alignment as a result of precast grooves in the membrane, as alignment was not seen when the aligned grooves were not present. This could be due to seeding densities, differences in cellular attachment based on polymer type (PCL-Collagen vs

PLGA) or due to the MSC source. However, when periosteum and BM MSCs were compared, minimal differences were shown. Osteoblast cell lines also attach and proliferate onto electrospun membranes, with differences in morphology shown to be driven by the underlying fibre orientation. Thus, there is good basis that the free surface electrospun membranes produced in Chapter 5 will support MSC attachment and proliferation.

6.1.2 Live Cell Imaging of MSC Migration and Proliferation

As a result of quantifying colony formation from periosteum and BM derived cells, during Chapter 4, it was found that periosteum derived cells formed small, homogenous colonies, whereas BM derived cells formed larger, heterogenous colonies. This gave insight into not only the increased percentage of MSCs in periosteum samples compared to BM samples, but also that in the first two weeks following harvest the MSCs behave differently dependent on their source. Therefore, further investigation into how colonies develop over the two weeks with respect to cell morphology, migration and proliferation behaviours is needed to fully understand the differences in the two MSC types *in vitro*. This information could also have the potential to inform how MSCs are likely to migrate and colonise biomaterials, such as the free surface electrospun membranes produced in Chapter 5.

The current standard is to carry out CFU-F assays for two weeks, as in Chapter 4. However, this only gives a ‘snapshot’ of MSC morphology and colony formation and a method to calculate the percentage of MSCs within a chosen tissue. Therefore, the development of a method whereby MSCs can be tracked or imaged over time would provide insightful information on MSC behaviour. Such capabilities can be carried out using microscopes with motorised stages, whereby certain coordinates can be imaged at different time points allowing for certain cells to be imaged.

However, such techniques require constant equipment access, where equipment time can become expensive. Also, meaningful quantification from collected images would be time consuming and laborious. New technologies are being produced in order to circumvent such disadvantages, for example phase holographic imaging has been developed to provide time lapse imaging

that does not require fluorescent labelling (as with confocal microscopy) or fixation of samples. Thus, cells can be imaged via time lapse and cell dynamics can be quantified using specialised software with respect to cell morphology, migration and movement as well as tracking of cell proliferation.

Phase holographic imaging is an emerging technology, therefore only three articles exist using holographic imaging with MSCs, showing the potential for novel results. Kawase et al. (2016) imaged irradiated AT MSCs, BM MSCs and alveolar (jaw) periosteal cells and quantified changes in cell area, thickness and volume over 4 days. All cell types showed that cell surface area was maintained, however, cell thickness was significantly reduced by day 4 (Kawase et al. 2016). In contrast, Petecchia, Viti, et al. (2017) studied human BM MSCs underdoing osteogenic and adipogenic differentiation, in addition the effect of 'trans-differentiation', whereby the differentiation media (osteogenic or adipogenic) was switched at two weeks to the other for another two weeks. Here, diffraction of the microscope laser caused by lipid droplets during adipogenesis is particularly stark when using holographic imaging, allowing for easy identification of adipocytes (Petecchia, Viti, et al. 2017). Another paper from the same group investigated the growth and osteogenic differentiation of human BM MSCs onto glass or a titanium oxide (TiO_2) coating using holographic imaging (Petecchia, Usai, et al. 2017). It was shown that BM MSCs grown in culture media on a TiO_2 surface are larger (perimeter), thicker and more irregular (deviation from circle shape) compared to glass, suggestive of favourable cell adhesion due to increased cell spreading. Following osteogenic induction, most parameters measured remained constant apart from cell thickness, which increased with time in culture (Petecchia, Usai, et al. 2017)

Phase holographic imaging will allow for time lapse imaging of MSCs and quantifiable comparisons to be made, which could lead to underpinning the cause of the different colony formation seen in CFU-F assays. In addition, this also allows for comparisons to be made between MSCs grown onto tissue culture plastic as well as onto the free surface electrospun membranes. The current literature surrounding MSCs and holographic imaging is small, thus allowing for an opportunity to produce novel results.

6.1.3 Literature Surrounding the 'Barrier Function' of Membranes

A key characteristic of the developed free surface electrospun membranes was for the membranes to function as a 'barrier' during CSBD repair. Here, the membrane will be used to wrap around the defect size, containing bone graft and MSC material to the defect site, whilst acting to prevent soft tissue invasion into the defect site or invasion of surrounding skeletal muscle, which could impede bone regeneration. Tarchala et al. (2018) investigated this theory *in vivo*, CSBD were created in rabbit forelimbs and surgically repaired using the Masquelet technique (addition of PMMA to defect, which causes induced membrane to form around the PMMA), in comparison to the use of a 'barrier' PTFE membrane (either porous or non-porous) wrapped around the defect site, filled with allograft. It was shown that the use of a physical barrier (porous or non-porous) to prevent soft tissue ingrowth resulted in a similar amount of produced bone volume in comparison to the Masquelet technique (Tarchala et al. 2018)

Currently, the research surrounding the development of a 'barrier' membrane has proven this function through quantification of pore sizes and porosity and an assumption of cell size with respect to this. Chapter 5 investigated this through showing that most of the pores were below 1.4 µm (M3%-PCL) or 0.4 µm (M6%-CP70:30) in diameter, much smaller than the assumed MSC cell size of 12 µm. The following section aims to describe how the current literature quantifies or experimentally tests the barrier function of materials.

Wang et al. (2011) developed an electrospun 'barrier' membrane to support guided bone regeneration, utilising a material that was 'thin and porous for good nutrients transit'. However, *in vitro* examination was not carried out to prove that this membrane could function as barrier or allow nutrients through the material. Similarly, Ma et al. (2014) did not test the *in vitro* barrier function of a crosslinked chitosan membrane, however, during an *in vivo* study it was suggested that the 'dense' layer of the membrane acted as a physical barrier. However, it should be noted that the permeability of the membrane to fluorescent bovine-serum albumin (BSA), as a model nutrient, was measured showing that BSA could move through the membrane (Ma et al. 2014).

The most robust *in vitro* assessments of membrane barrier function were carried out by Ekaputra et al. (2011), Vaquette & Cooper-White (2011) and Phipps et al. (2012). Cell penetration into electrospun PCL-Collagen-hyaluronic acid membranes was assessed through histological staining and confocal imaging of cross sections (taken using a cryo-microtome) of the membranes following fibroblast and HUVEC attachment (Ekaputra et al. 2011). Here, it was shown that co-culture of fibroblast and HUVECs resulted in extensive infiltration of endothelial cells and formation of 'capillary like structures', whereas monoculture of endothelial cells saw little penetration (Ekaputra et al. 2011).

Whereas Vaquette & Cooper-White (2011) demonstrated that increasing the pore size of electrospun membranes resulted in improved cell penetration into the membrane. Quantification of pore size and porosity was carried out, followed by SEM imaging of cell adhesion (fibroblasts), whereby evidence of cells was shown underneath fibres of the membrane, suggestive of cell penetration (Vaquette & Cooper-White 2011).

In addition, confocal imaging was used to image and measure the depth of cellular nucleus infiltration into the thickness of the membrane, by imaging the depth of nuclei from the surface of the material. Here fibroblasts were shown to penetrate to a depth of 250 μm (mean pore size, 20 μm (diameter)). This was in contrast to a penetration of 30 μm of membranes with a mean pore size of 5 μm (diameter) (Vaquette & Cooper-White 2011), more similar to that of the free surface electrospun membranes produced in Chapter 5.

Previously mentioned research by Phipps et al. (2011) was developed further to show that increasing the pore size of an electrospun membrane (PCL-Collagen-HA) would result in increased cell infiltration (Phipps et al. 2012). Here, *in vitro* confocal imaging of MSC seeded membranes showed increased cell infiltration from 6 μm to 46 μm with increased pore sizes and an *ex vivo* mouse organ culture model showed a similar trend of 20 μm increasing to 63 μm distance of mouse calvarial cell invasion (Phipps et al. 2012).

The current literature either tends to make assumptions about the 'barrier' function of membranes based on fibre diameter and pore size or uses confocal imaging through taking 'z' stack images through the depth of a construct as a

measure of cell penetration into materials. However, all of these studies have shown cellular penetration into the materials, but not whether cells can migrate through the whole material onto the other side of the material. In addition, the materials are thicker than those produced in Chapter 5, at approximately 200-300 μm thickness, opposed to approximately 100 μm, which could cause problems with being able to clearly image cell penetration into the electrospun membranes. Also, these studies have not shown the effect of a nutrient's gradient, and the effect that this may have on cell migration, as it is known that if serum starved, cells will migrate towards 'nutrients', or an area of serum containing media. This has the potential to be relevant *in vivo* if there is a stimulus (cytokine or growth factor) or nutrient's gradient that could trigger cell migration into or out of a CSBD site. Therefore, this Chapter will endeavour to functionally assess the free surface electrospun membrane's ability to block cell migration.

6.1.4 Chapter Aims and Objectives

The aim of this chapter is to investigate changes in cell morphology, migration and proliferation patterns of periosteum and BM MSCs *in vitro*. In addition, to robustly test the cellular interactions of MSCs (periosteum and BM) with M3%-PCL and M6%-CP70:30 over time *in vitro* and functionally testing the membrane's ability to block cell migration.

6.1.4.1 Objectives

The objectives of this work were to:

1. Investigate periosteum and BM MSC's morphological characteristics and migratory profiles using phase Holographic imaging.
2. Assess cell attachment and proliferation of periosteum and BM MSCs onto M3%-PCL and M6%-CP70:30.
3. Develop an assay to functionally test cell migration through the free surface electrospun membranes in order to test their barrier function.

6.2 Specific Materials and Methodology

The migratory and topographic differences between periosteum and BM MSCs during early *in vitro* culture was investigated using Holographic live cell imaging. Chapter 5 detailed the development and characterisation of collagen containing free surface electrospun membranes, made from collagen and PCL at varying ratios as well as a PCL control membrane. The M6%-CP70:30 prototype membrane was chosen as the candidate membrane and therefore taken forward for further testing, alongside the PCL control membrane, M3%-PCL. These membranes were further assessed in cell culture with periosteal and BM MSCs (isolated and characterised in Chapter 4) to assess cell attachment and proliferation capacity as well as functionally testing the membranes' barrier capacity to cell migration.

6.2.1 HoloMonitor Cell Tracking of Periosteum and Bone Marrow MSCs

To assess the migratory capacity of periosteum and BM MSCs, non-passaged (denoted as NP) and P0 cells were seeded onto cell culture plates and imaged using Holographic live cell imaging to track and quantify MSC movement and proliferation. P0 vials of donor matched (Male, 17, as seen in Chapter 4) BM and periosteum MSCs were thawed (Section 2.3.4), counted (Section 2.3.1) and seeded in duplicate onto a Lumox® multiwell 24 well, cell culture plate (Sarstedt) at three cell densities – 100, 250 and 500 cells per well. In addition, non-donor matched, freshly digested and non-passaged (NP) frozen vials of periosteum NCCs (matched to P0 cultures, Male, 17) and BM NCCs were also thawed, counted and seeded in duplicate at 2.5×10^3 and 2.5×10^4 cells per well (periosteum) and 2×10^6 cells per well (BM).

The cultures were grown for 3 days at 37°C, 5% CO_2 in StemMACS media. On day 3, following a half media change, the media was topped up to 2 mL per well and the plate lid was replaced with PHI HoloLids™ (PHI, Phase Holographic Imaging) imaging covers (sterilised in 70% EtOH for 10 mins). Care was taken to prevent an air bubble forming between the HoloLid™ and the media. The plate was placed onto the xy motorised stage of a HoloMonitor M4 Microscope, set up inside an incubator. Using the Hstudio software three

coordinates in each well were manually focused and set to automatically image every hour for 6 days. A media change was carried out every 48 hours.

6.2.1.1 Post Processing of Images Collected

Using the Hstudio software a 'mask' was applied to the images, where a threshold was set to distinguish from the bottom of the well and the cells. This allowed for cell identification and an outline to be automatically drawn around each cell, and then applied to subsequent images. Using the cell tracking tab, cells were assigned a number and the software automatically could track each cell over a period of time – this was checked manually and cell divisions were recorded also. An example of this process can be seen in Figure 6.1.

The Hstudio outputs for tracking cell movement that were chosen to investigate are shown below.

- Migration – displacement from the start point coordinates an individual cell was tracked from (μm)
- Motility – cumulative distance travelled (μm)
- Migration directness – migration divided by motility at a certain time point (ratio from 0-1)
- Motility speed – cumulative distance travelled divided by time (μm/h)

In addition, other cell morphological outputs were investigated, shown below

- Confluency – percentage cell coverage of the image taken (500 μm^2)
- Cell surface area – (μm^2)
- Cell volume – optical volume, takes the cell surface area and multiplies by the measured optical thickness (phase shift of the light) (μm^3)
- Cell perimeter – the circumference of the cell (μm)
- Cell eccentricity – measurement of how elongated a cell is, how much the cell deviated from being a circle (0 – perfect circle, 1 – maximum eccentricity)

All outputs were exported from the Hstudio software into Excel files and then plotted using Prism.

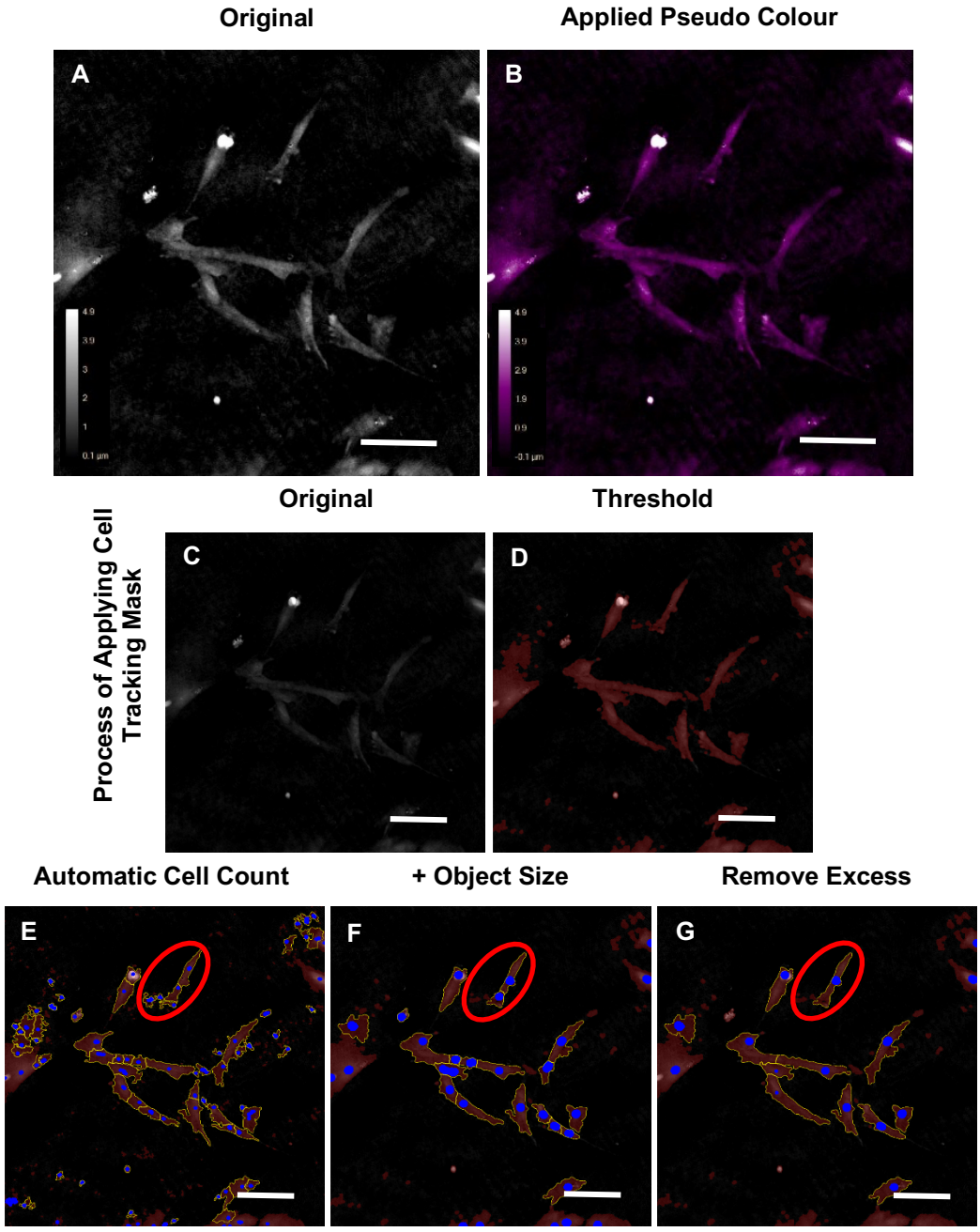

Figure 6.1: Detail of post processing of HoloMonitor images, through applying pseudo colour and thresholding for cell tracking. A) Example of an original image. **B)** Example image with pseudo colour representing cell thickness applied. The process of applying appropriate 'mask' to identify individual cells for future cell tracking. **C)** Original image, **D)** with applied threshold (red cover) to identify cells from surface of the tissue culture plate. **E)** Automatic cell count applied (object size – 20, Back ground threshold – 128), area in red circle identified 5 cells. **F)** Increased object size to 40, area in red circle identified 2 cells. **G)** Manual removal of excess cell identification, area in red circle correctly identifies 1 cell. Scale bars represent 100 µm (A-B) and 50 µm (C-G).

6.2.2 MSC Attachment onto M6%-CP70:30 and M3%-PCL

To investigate periosteum and BM MSC attachment and proliferation on the barrier membranes developed in Chapter 5, both MSC types were cultured with M6%-CP70:30 and M3%-PCL for up to 28 days. M6%-CP70:30 and M3%-PCL electrospun membranes were manufactured (as per Section 5.2.2), cut into 20 mm x 20 mm pieces and sterilised under UV light for 1 h in a class II fume hood.

Passage 3 periosteum and BM MSCs (Male, 17, as seen in Chapter 4) were thawed, counted and grown for a week in standard tissue culture conditions (see Section 2.3.1 and Section 2.3.4) and then trypsinised (see Section 2.3.2), counted (Section 2.3.1) and re-suspended as 10^4 cells per 200 µL (high density) or 10^3 cells per 200 µL (low density) of StemMACS media, in order to assess the effect of cell density. In triplicate, the M6%-CP70:30 and M3%-PCL membranes were placed onto non-tissue culture treated 6 well plates (CellStar, Greiner BioOne) and 100 µL of cell suspension (either 10^3 or 10^4 cells, of either periosteum or BM MSCs) was pipetted in duplicate onto the top of the individual membranes and left to attach for 4 h, at 37°C, 5% CO_2. Following attachment, 2 mL of StemMACS media was added, and half media changes were carried out biweekly.

This was set up for multiple time points, where day 4 was used to see early attachment followed by day 7, day 14, day 21 and day 28 to assess periosteal and BM MSC proliferation on the M6%-CP70:30 and M3%-PCL membranes (Table 6.1). The low cell density (10^3 cells), was only set up for three time

Table 6.1: Set up of MSC attachment onto electrospun membranes.

	M3%-PCL				M6%-CP70:30	
Days	**Periosteum MSC**		**Bone Marrow MSC**		**Periosteum MSC**	
	(10^3)	**(10^4)**	**(10^3)**	**(10^4)**	**(10^3)**	**(10^4)**
4	Y	Y	Y	Y	Y	Y
7	-	Y	-	Y	-	Y
14	Y	Y	Y	Y	Y	Y
21	-	Y	-	Y	-	Y
28	Y	Y	Y	Y	Y	Y

points, at day 4, 14 and 28. At each time point, membranes were washed in PBS, fixed in 3.75% formaldehyde overnight and imaged using confocal microscopy (Section 6.2.4).

Stains used were DAPI and Phalloidin-FITC to image cell nuclei and actin fibres to show cell morphology on the materials. The cells attached to the electrospun membranes were permeabilised with 0.1% Tween for 10 mins, followed by a PBS wash and then stained with 0.1% Phalloidin-FITC for 15 mins in the dark, followed by a PBS wash. Finally, samples were stained with 0.1% DAPI for 1 h in the dark. Excess DAPI dye was washed off with at least three PBS washes and samples were stored in PBS at 4°C in the dark until imaged (Section 6.2.4).

6.2.3 Barrier Function Assessment of M6%-CP70:30 and M3%-PCL

The barrier function of M6%-CP70:30 and M3%-PCL was assessed for the ability of human periosteal MSCs to be able to penetrate through the material using a modified Transwell migration assay (Figure 6.2). In addition, membranes were laser cut to produce holes of a known size, in order to produce a positive control membrane that would not impede cell migration (Figure 6.2B). The free surface electrospun membranes were laser cut using a flatbed laser (FB700, Cad Cam Technologies), with the laser head 3 mm from the samples. It was set to take one pass over the fabric, at a velocity of 600 mm/s with 10% laser power, where the laser was programmed (ApS-Ethos control software) to make a 200 μm diameter hole every 2 mm. The actual hole size varied from this and was 500 ± 30 μm for M3%-PCL and 280 ± 15 μm for M6%-CP70:30. Samples were then cut into 1.3 cm^2 pieces, sterilised under UV light within a class II fume hood for 1 h. Laser cutting was carried out by Katrina Moisley (PhD Student, University of Leeds).

MINUSHEET® tissue carriers (Minucell) were used to create a 'modified transwell assay system' (Figure 6.2A), where the electrospun membranes were contained between a MINUSHEET® tissue carrier and a MINUSHEET® tension ring (Minuth & Denk 2012). Prior to this, the MINUSHEET® tissue carriers were sterilised (autoclaved). The MINUSHEET® tissue carrier was

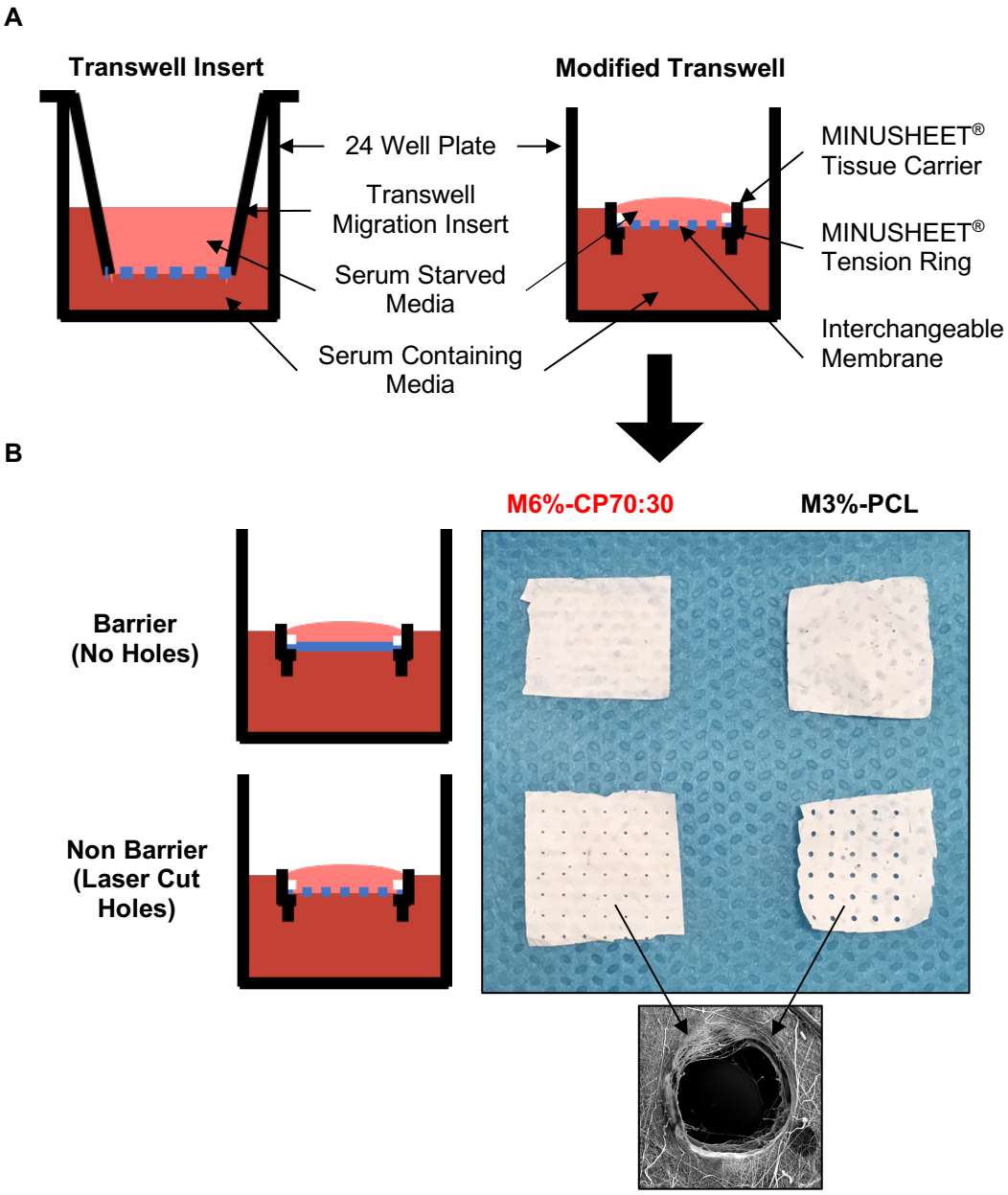

Figure 6.2: Schematic of the experimental set-up of the barrier function assay. **A)** The concept of the transwell insert migration assay was modified using MINUSHEET® technology. The MINUSHEET® Tissue Carrier and Tension Ring holds the membranes, which floats in a 24 well plate. **B)** Both membranes (M6%-CP70:30 and M3%-PCL) had laser cut holes, of approximately 280 µm or 500 µm in diameter, creating a positive membrane control that would allow for cellular migration from the top of the membrane to the bottom.

placed into a 24 well plate, 500 µL of media was added to the bottom of the well and 100 µL of cell suspension (see below) to the top of the MINUSHEET® tissue carrier (Figure 6.2A).

Human periosteum MSCs (passage 3), grown for a week as per Section 6.2.3, were serum starved overnight, through changing the StemMACS media to FCS free DMEM media. Cells were trypsinised as previously described (see Section 2.3.2), however the trypsin was neutralised using low FCS DMEM media (2% FCS, opposed to 10% FCS), cells were counted and re-suspended at 10^4 cells per 100 µL (seeding density at 5 x 10^3 cells per cm^2, inner radius of the MINUSHEET® tissue carrier was 4 mm).

The assay was set up using M6%-CP70:30 and M3%-PCL membranes (manufactured as per Chapter 5), with laser cut samples of M6%-CP70:30 and M3%-PCL as positive controls (Figure 6.1B). Three time points were set up for 24 h, day 4 and day 7. At each time point samples were washed in PBS and fixed in 3.75% formaldehyde for 24 h. Each membrane was taken out of the MINUSHEET® tissue carriers and transferred onto a histology slide, with the cell containing side of the sample facing upwards. A drop of Prolong Gold Antifade DAPI (ThermoFisher) was added on top of the sample and then covered with a coverslip and left to cure overnight. The slide was then sealed with clear nail varnish. The top and bottom of the membranes were imaged using confocal, where 3 images were taken (See Section 6.2.4.1).

6.2.4 Confocal Microscopy of 3D Structures

Section 6.2.2 and Section 6.2.3 produced cell-material constructs to be imaged using confocal microscopy to assess cellular interactions with the underlying materials. Samples were washed using PBS, followed by fixation using 3.75% formaldehyde for 24 h (previously described in Section 6.2.2 and Section 6.2.3).

It was found that the M6%-CP70:30 membranes were auto-fluorescent throughout the FITC wavelengths due to the collagen content of the membrane. Therefore, Vector® TrueVIEW™ Autofluorescence Quenching Kit (Vector Laboratory) was used to quench auto-fluorescence. The system was optimised to permeabilise the samples first and then quench the samples,

whereby solution A, B and C were mixed together at the ratio of 1:1:1 and incubated with the sample for 5 mins. The auto fluorescence of M6%-CP70:30 (Figure 6.3A-C) was reduced following the quenching process, with minimal 'flecks' of autofluorescence seen (Figure 6.3D-F, yellow arrow). M3%-PCL was not auto-fluorescent and therefore not subjected to quenching.

Following a PBS wash, M6%-CP70:30 samples were stained with Phalloidin-FITC and DAPI (Section 6.2.2) or DAPI only (samples from Section 6.2.3).

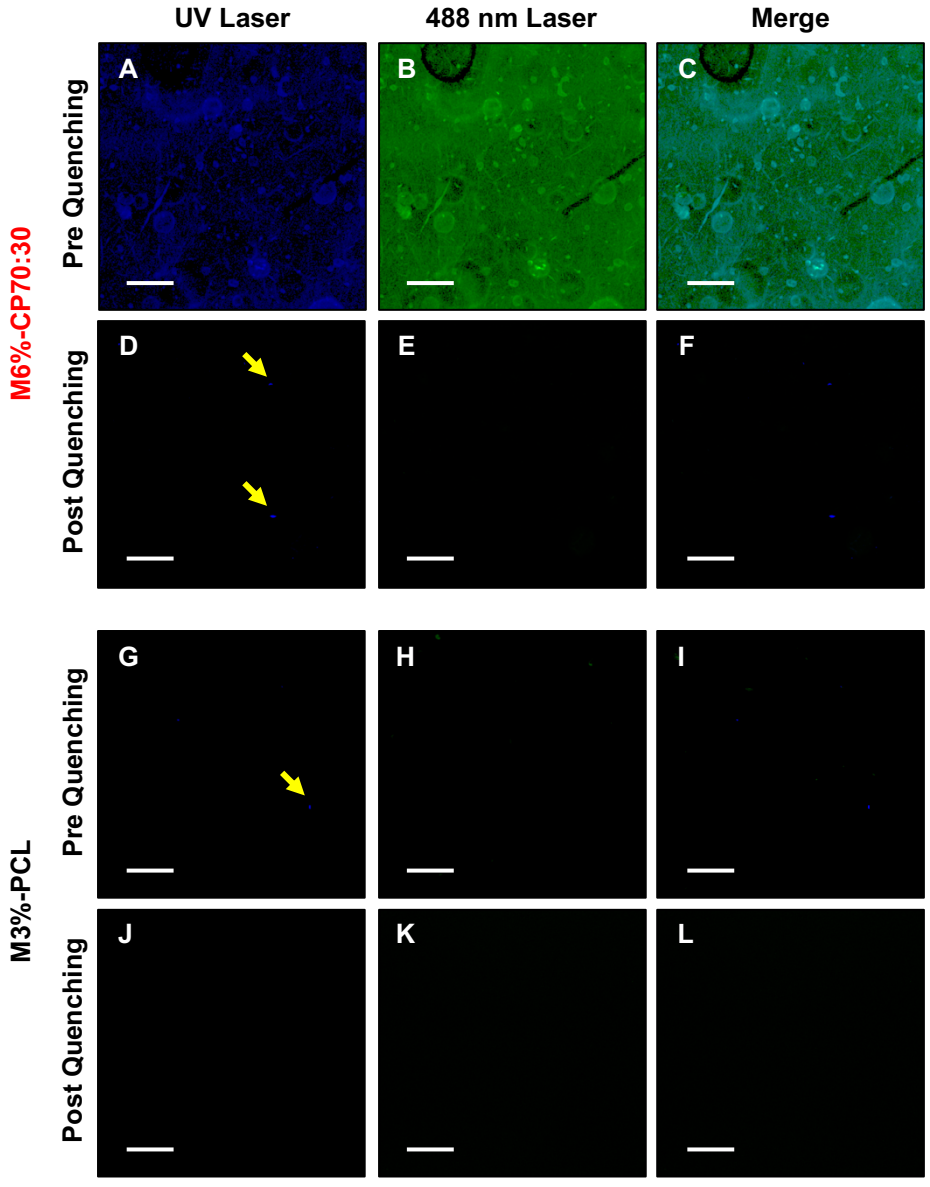

Figure 6.3: Effect of TrueView™ Quenching Kit on 'empty' free surface electrospun membranes. (A-F) M6%-CP70:30 and (G-L) M3%-PCL membranes were imaged before and after the quenching process. Auto-fluorescence was seen with the collagen containing membrane (M6%-CP70:30), which was removed in the quenching process. Yellow arrow – auto-fluorescent areas on the UV laser (corresponds with DAPI).

Samples were then mounted onto histology slides using VECTASHIELD® Vibrance™ Antifade Mounting Medium (Vector Labs) and immediately imaged using confocal microscopy to check if the sample was facing the right way up (cells facing upwards).

Fixed and stained samples from Section 6.2.2 and Section 6.2.3 were imaged using a Leica Confocal Microscope (DM6 CS). Sample orientation known prior to mounting onto histology slides and slides were imaged using x10 or x20 dry lens'. The confocal microscope was controlled by and images were collected using LAS X, Leica software. Here laser power was set to 10% for the UV and 488 nm laser, for DAPI and FITC wavelengths, respectively (samples from Section 6.2.2). Transmitted light was used to take images of the underlying membrane, in combination with DAPI (samples from Section 6.2.3). Sliced images were taken every 1.27 µm and maximum projections of the stacks were taken as representative images. DAPI and FITC were imaged separately and as a merge for Section 6.2.2, whereas Transmitted light and DAPI was imaged for Section 6.2.3.

6.2.4.1 ImageJ Post Analysis of Confocal Imaging

To assess cellular alignment during the Assessment of MSC Attachment Assay (Section 6.2.2), five images per experimental time condition were taken. The DAPI only images (showing only nuclei, not the actin filaments) were processed in ImageJ in order to be made binary so that the produced objects could be quantified. The original image was filtered to remove objects of less than 2 pixels, the image was then made binary (black and white pixels) and the objects were 'dilated' to make a smoother object to measure and then the 'fill holes' tool was applied to fill in each of the objects (Figure 6.4A). Following this, each of the 'objects' could be individually counted and measured, whereby the 'object' angle was able to be quantified, care was taken to compare back to the original image to ensure that only measurements of nuclei were taken, and when nuclei were shown to overlap (blue arrow – example measurement 45, Figure 6.4A) manual measurements were taken.

Optimisation of the process of angle measurement was carried out, two outputs were quantified, 'angle' and 'Feret angle'. 'Feret angle' was a

measurement of the angle of the ‘Feret’s diameter’ which is taken as the longest distance between two points within a selection boundary of a measured object and ‘angle’ measures the angle between the primary axis of an object and the x axis of the image. Both measurements were taken but it was shown that the ‘Feret angle’ did not measure any output angles from -5° to +5°, despite there being many nuclei that were in this region or ‘near vertical’ (Figure 6.4B). Using a ‘near vertical’ nuclei as an example, the ‘angle’ was measured at 0.4° and the ‘Feret angle’ was measured at 23.4° (Figure 6.4B), however when a manual estimate of the angle was taken, this was 4.5°, closer to the ‘angle’ measurement. Therefore, the ‘angle’ measurement was taken forward as the measurement of nuclei alignment.

Outputs were exported into Excel; frequency distribution histograms were produced and Gaussian distribution curves were fitted to the data. The spread of data was quantified by FWHM (See Section 4.2.2), using Equation 4.1 (Section 4.2.2).

6.2.5 Statistical Analysis

Statistical analysis was carried out on using one-way ANOVA, with a Tukey’s multiple comparisons post hoc test, where the data was parametric (D'Agostino & Pearson normality test carried out prior to statistical analysis). Where two data sets were being compared, unpaired t-tests were carried out. Statistical significance was taken as $P<0.05$ and data has been plotted as mean ± standard deviation.

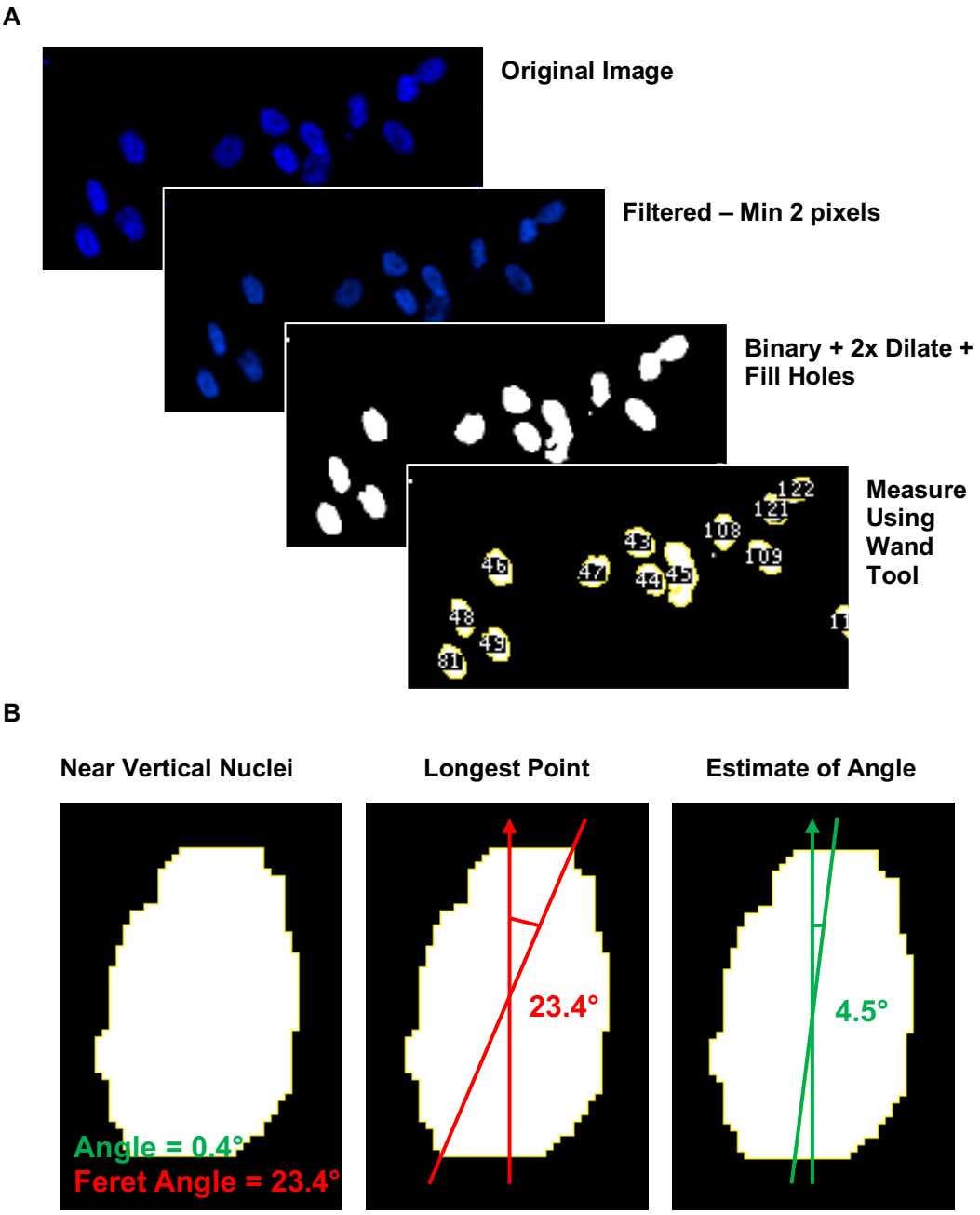

Figure 6.4: Post confocal microscopy image processing to quantify nuclei alignment using ImageJ. A) DAPI staining images were quantified in ImageJ, where images were filtered and made binary (black and white pixels) to allow identification of individual nuclei. Using the 'measure' function, individual objects were counted and quantified. **B)** To quantify nuclei alignment, optimisation of the measured angle was carried out using 'Angle' and 'Feret Angle'.

6.3 Results

6.3.1 Live Cell Tracking of Periosteum and Bone Marrow MSCs

Donor matched cell cultures (Male, 17) of thawed P0 stocks (previously grown in culture for 13 days, 6.6 PD (periosteum) and 13.0 (BM)) of periosteum and BM derived cells were plated onto a 24 well plate, alongside a non-donor matched thawed freshly digested (NP) of BM (non-matched) and donor matched periosteum (Male, 17). Cells were allowed to attach and grow for three days before imaging using a HoloMonitor microscope for six days, where an image at predetermined coordinates within a well was taken every hour.

Unfortunately, the coordinates chosen for the NP BM cultures failed to show any images of cell growth and could not be repeated as the HoloMonitor microscope was requested on demo from the company. However, P0 BM and both periosteum cultures yielded time lapse imaging that could be quantified, allowing for cell tracking and quantifiable data on cell migration, division and topographic cell characteristics to be collected.

6.3.1.1 Morphological Analysis of MSCs

Clear migration of cells and evidence of cell division was seen (Figure 6.5). To show this, a snapshot of an area within a well from P0 periosteum culture of three cells in close proximity was taken and shown every 2 hours for up to 10 hours (Figure 6.5). One of the cells (red arrow, Figure 6.5) showed cell division within this time, whereby at the 4 hour time point a clear retraction of cell processes could be seen as the cell became more spherical. At 6 hours, the cell began to flatten out again, splitting in two and by 8 hours two separate cells were visible, and cell division complete (Figure 6.5). Another cell (yellow arrow, Figure 6.5) imaged migrated away from its original position and by 10 hours this cell had also gone through a cell division. The third cell (green arrow, Figure 6.5) remained static throughout the 10 hours of imaging and had the hallmarks by 8 and 10 hours that this cell would potentially also undergo division.

There was also clear evidence that the morphology of the MSCs was particularly changeable over time, especially when focusing on one MSC (cell

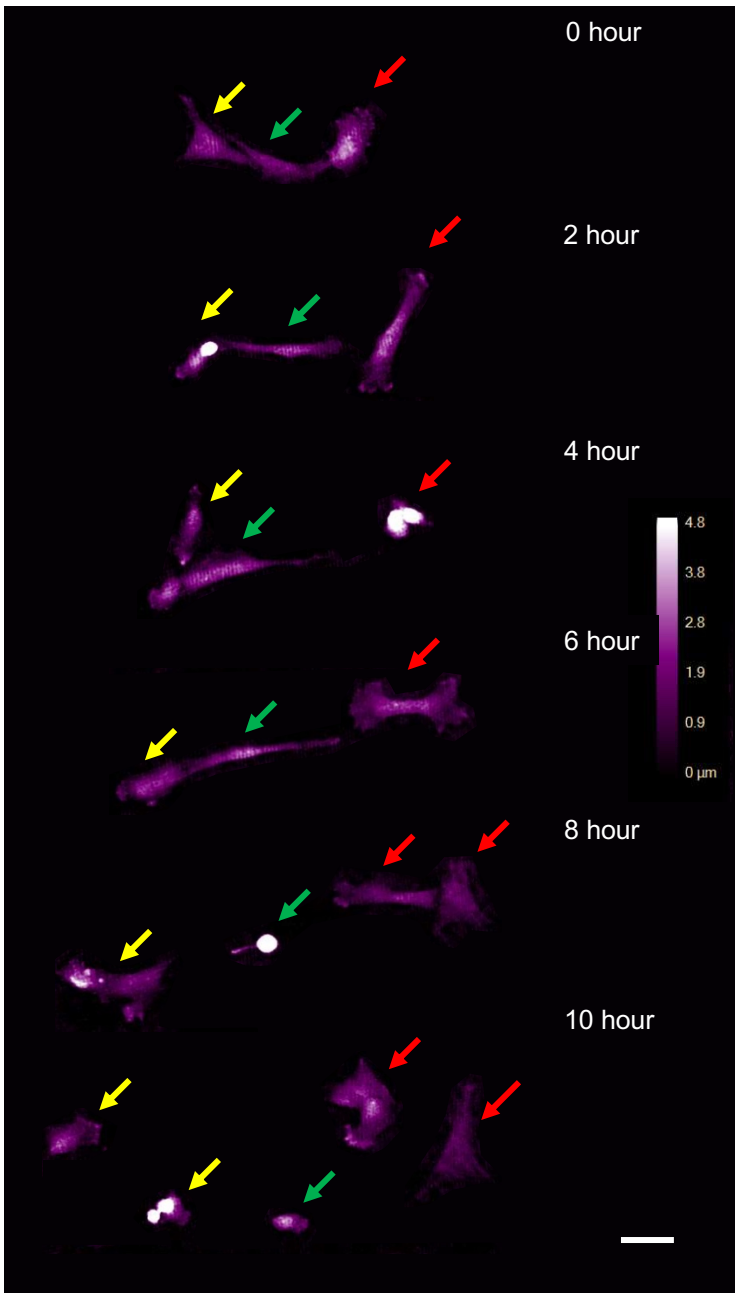

Figure 6.5: Time-lapse holographic imaging of periosteum MSCs in culture. Three cells tracked, identified by yellow, green and red arrows. Imposed pseudo colour scale (purple to white) onto the images to represent 3D thickness of the cell (0-4.8 µm). Each image represents a snapshot of the well over 10 hours, taken every 2 hours. **0 hours;** three cells close to each other, **2 hours;** with slight movement. **4 hours;** evidence of a cell (red) going into division as seen by retracting of cell processes. **6 hours;** dividing cell (red) starting to split apart into two cells, **8 hours;** fully separated (red) into two cells. **10 hours;** another cell splits into two cells (yellow), without the characteristic cell process retraction. White scale bar represents – 50 µm (2D).

A) over time (approximately 20 hours) as the cell divides into two cells (denoted as A.1 (red) and A.2 (blue)) and migrates (Figure 6.6A). At the 4 hour time point cell division was seen (blue arrow, Figure 6.6A) and two cells were visible by 5 hours, cell A.2 (blue arrow) started to migrate away and by 12 hours (green arrow, Figure 6.6A) had migrated out of the field of view. By applying a threshold on the individual images (Figure 6.1D) and assigning each cell an 'Object', the HoloMonitor software can apply a mask to the images (Figure 6.1G) allowing for each cell to be quantified individually over time. From this cell morphology was quantified (Figure 6.6B-D).

The cell perimeter of each cell was variable at 132-249 μm (Cell A), 67-266 μm (Cell A.1) and 89-186 μm (Cell A.2) (Figure 6.6B). The largest values of which were seen at 2 hours, just prior to evidence of cell division of cell A (249 μm) and at 17 hours, whereby cell A.1 (266 μm) appeared particularly elongated. Cell thickness was measured as a mean across the whole cell (bottom three lines, Figure 6.6C), as well as taken at the thickest point of the cell (top three lines) (Figure 6.6C). Here all three cells' mean thickness over 20 hours remained similar, measured at 1.6 ± 0.2 μm (cell A), 1.4 ± 0.3 μm (cell A.1) and 1.5 ± 0.3 μm (cell A.2). The thickest measured point on the cell ranged from 2.9-3.3 μm (cell A), 2.2-4.3 μm (cell A.1) and 2.3-5.0 μm (cell A.2) (Figure 6.6C). The maximum measured thickness for both cells A.1 and A.2 was found at 4 hours, the first point at which the two separate cells were imaged (Figure 6.6B). Cell surface area was also shown to be variable throughout the tracked time period, ranging from 554-1002 μm^2 (mean 743 ± 207 μm^2, cell A), 330–1395 μm^2 (mean 663 ± 298 μm^2, cell A.1) and 418–943 μm^2 (mean 564 ± 197 μm^2, cell A.2), whereby one of the lowest recorded points was measured at 4 hours (cell division) at 402 μm^2 (cell A.1) and 421 μm^2 (cell A.2).

Up until now only a few cells have been characterised, however, many more cells appear in each of the fields of view tracked. For each cell type (NP periosteum, P0 periosteum and P0 BM) three different fields of view were chosen based on the following criteria. That cell tracking was possible for >24 hours; the cells remained in focus during this time; the field of view was of a confluency throughout that still allowed for identification of individual cells.

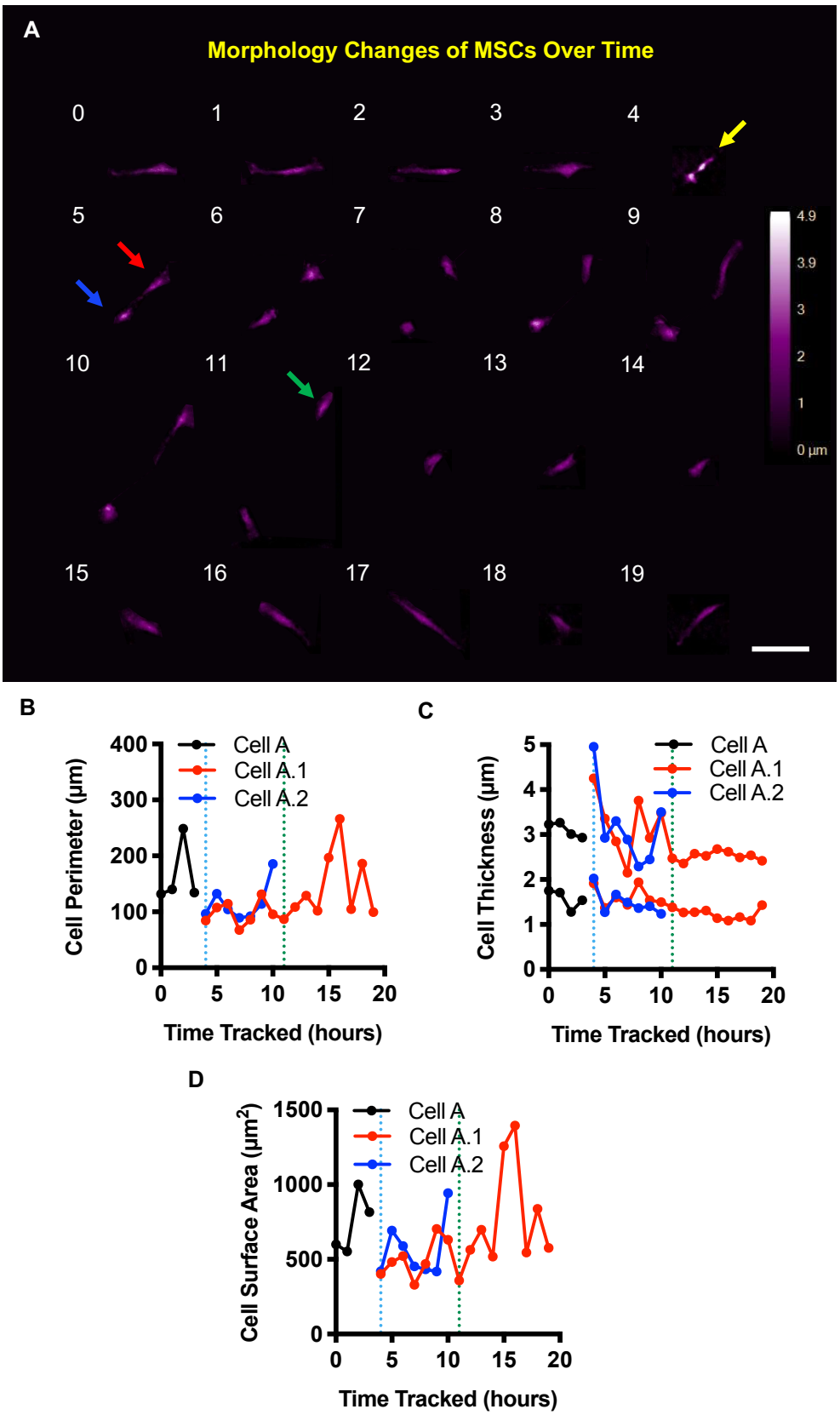

Figure 6.6: Morphology changes of MSCs over time. A) A singular cell tracked for 20 hours (image taken once an hour), showing changes in morphology and evidence of cell division taking place. Cell characteristics were quantified and changes in **B)** cell perimeter **C)** cell thickness (average – bottom three lines, maximum – top three lines) and **D)** cell surface area were

plotted against time. Yellow arrow – cell division, red arrow – cell A.1, blue arrow – cell A.2 an green arrow – cell A.2 migrating out of the field of view. Scale bar represents 100 μm.

Following quantification, it was apparent that there were three differing cell morphologies within the MSC population. 'Dividing' cells (Figure 6.7A), which had higher mean cell thickness (>2.5 μm) but a small cell surface area (<1700 μm^2), 'spindle' shaped cells (Figure 6.7C) which had a mean cell thickness of 0-2.5 μm and a cell surface area of <2500 μm^2 and finally a population of 'flat' cells (Figure 6.7B) with cell thickness of 0-2.5 μm, but a large cell surface area (>2500 μm^2).

When each cell was plotted as cell surface area vs cell thickness (mean), the majority of the cells for each cell type were 'spindle' shaped, the classical MSC morphology (NP periosteum - 90.98%, P0 periosteum – 97.35% and P0 BM – 97.88%). However, differences could be seen with percentages of 'dividing' and 'flat' cells. The most 'dividing' cells were found in NP periosteum cultures, whereby 4.05% of all the cells quantified were in the process of dividing at some point throughout being tracked, this was reduced to 2.05% (periosteum) and 2.12% (BM) for the P0 cultures. The highest proportion of 'flat' cells were also found in NP periosteum (4.97% of all cells), which again reduced in the P0 cultures to 0.60% (periosteum) and 0% (BM).

When comparisons were made between the different MSC types no significant differences in mean cell thickness and surface area were seen with the subset of 'flat' cells (Table 6.2). In contrast, significant differences were seen between all three MSC types within the 'spindle' shaped cells (one-way ANOVA, Tukey's multiple comparisons post hoc test, $P<0.0001$) of mean cell thickness and cell surface area, however, these differences were confounded due to the high number of values analysed (n=2269 (NP periosteum), n=2426 (P0 periosteum) and n=1061 (P0 BM), Table 6.2). Here, small differences in mean cell thickness were seen to be statistically significant (Table 6.2). In addition, NP periosteum cells were shown to have a larger cell surface area in comparison to P0 cells.

With respect to the 'dividing' cells, the mean thickness of P0 periosteum (6.1 ± 2.5 μm) was significantly higher (one-way ANOVA, Tukey's multiple comparisons post hoc test, $P<0.0001$) than NP periosteum (3.9 ± 1.3 μm)

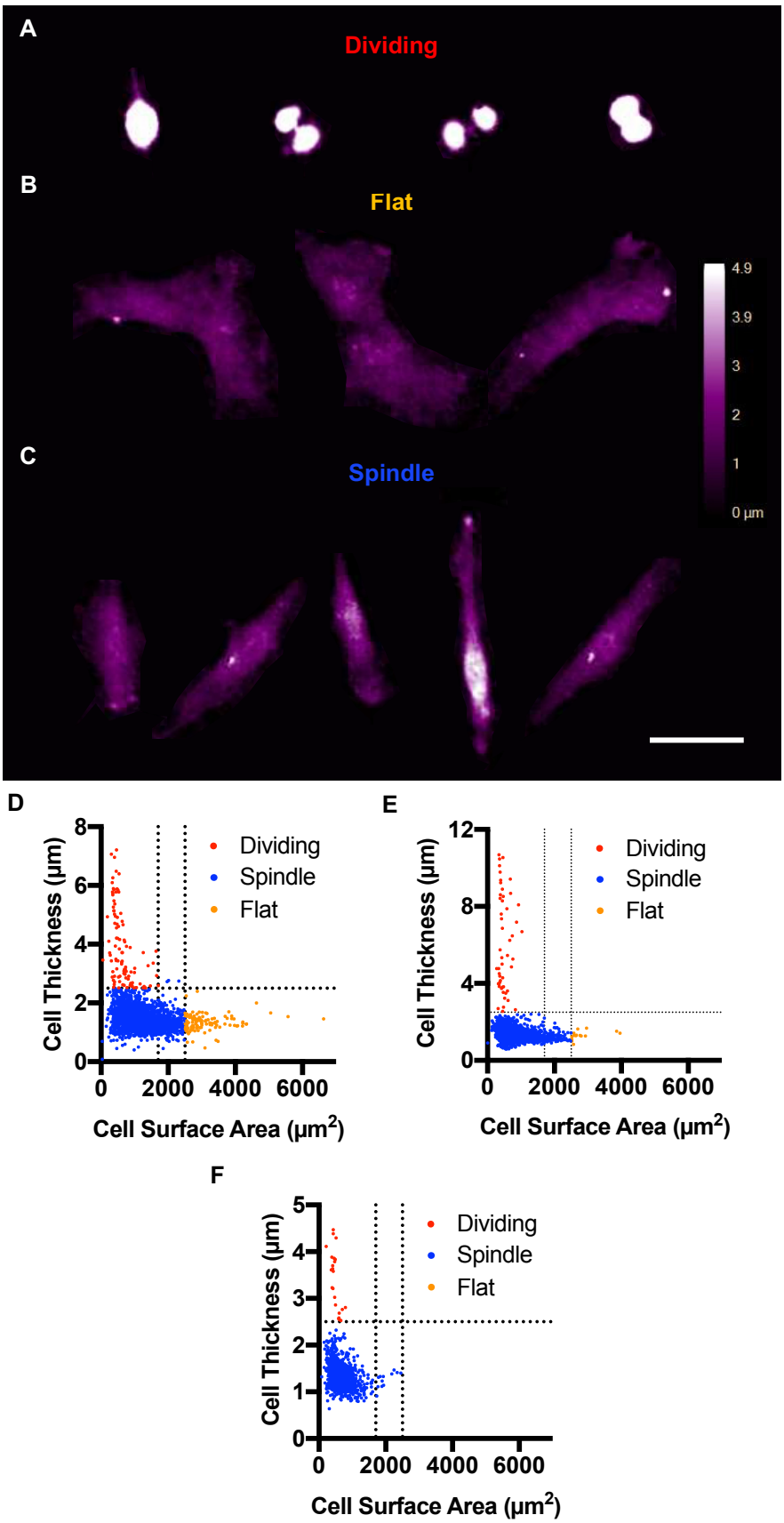

Figure 6.7: Distinct morphology types of MSCs into 'dividing', 'flat' and 'spindle' shaped. A) Four individual cells currently dividing. **B)** Two individual 'flat' cells, with an extra two 'flat' cells sitting close to each other (middle). **C)** Five individual 'spindle' shaped cells, the classical MSC phenotype. All quantified cells were plotted cell surface area vs cell thickness to show the

three different morphologies, **D)** non-passaged (NP) periosteum, **E)** passage 0 (P0) periosteum, **F)** P0 Bone marrow. Scale bar represents 50 μm. Dividing cells – red, spindle cell – blue and flat cells – orange. Separation of cell types at y=2.5 μm and x=1700 μm^2 and 2500 μm^2.

Table 6.2: Summary of cell morphology outputs from Figure 6.6. NP – non passaged, P0 – passage 0. One-way ANOVA carried out with Tukey's post hoc test, * P<0.05, ** P<0.01 and **** P<0.0001. **/* - Periosteum/Bone Marrow.

Cell Morphology Characteristic		Number of Cells Measured	Mean Cell Thickness (μm)	Cell Surface Area (μm^2)
Dividing	NP Periosteum	101	3.9 ± 1.3	650 ± 342**/*
	P0 Periosteum	51	6.1 ± 2.5****	497 ± 172
	P0 Bone Marrow	23	3.4 ± 0.6	493 ± 126
Flat	NP Periosteum	124	1.3 ± 0.3	3085 ± 657
	P0 Periosteum	15	1.3 ± 0.2	2839 ± 567
	P0 Bone Marrow	0	-	-
Spindle	NP Periosteum	2269	1.5 ± 0.3****	1187 ± 512****
	P0 Periosteum	2426	1.4 ± 0.3****	817 ± 393****
	P0 Bone Marrow	1061	1.3 ± 0.3****	668 ± 297****

and P0 BM (3.4 ± 0.6 μm). In contrast, cell surface area was significantly higher for NP periosteum cells (650 ± 342 μm^2) compared to P0 periosteum (497 ± 172 μm^2) and P0 BM (493 ± 126 μm^2) (one-way ANOVA, Tukey's multiple comparisons post hoc test, P=0.005 (P0 periosteum) and P=0.04 (P0 BM)).

This more detailed picture relating to cell size and morphology of MSCs from differing sources could prove useful with respect to predicting MSC migration through the free surface electrospun membranes developed in Chapter 5. The data suggests, even though cell size is variable within a culture, at any given point in time NP periosteum cells appear to be larger than the P0 counterparts, therefore, uncultured cells could have more difficulty migrating through a material. In addition, periosteal cells appear to be larger than their BM counterpart. Therefore, it is important to take into context the cultured nature and source of the cells when creating an ideal barrier to migration.

6.3.1.2 Tracking of MSC Migration Patterns

The migration and movement patterns of the MSC cultures were assessed next, through application of a threshold and an appropriate cell mask (Figure 6.1), cell tracking could be carried out using the HoloMonitor cell tracking software by assigning an individual cell number to each defined 'cell object'. Figure 6.1 gives an example of how this is carried out using a few cells over 5 hours. Here, different colours and cell numbers are assigned to each individual cell at time point 0 hours (Figure 6.8A), and then the software automatically tracks each cell through the time lapse images, which was checked manually to ensure accuracy (Figure 6.8B-F).

The HoloMonitor software produces quantifiable outputs for each individual cell tracked, including a map of cell movement (Figure 6.9). It was seen that some cells remained in the same area of the well, in addition to other cells that tended to move across the field of view that were migratory. Therefore,

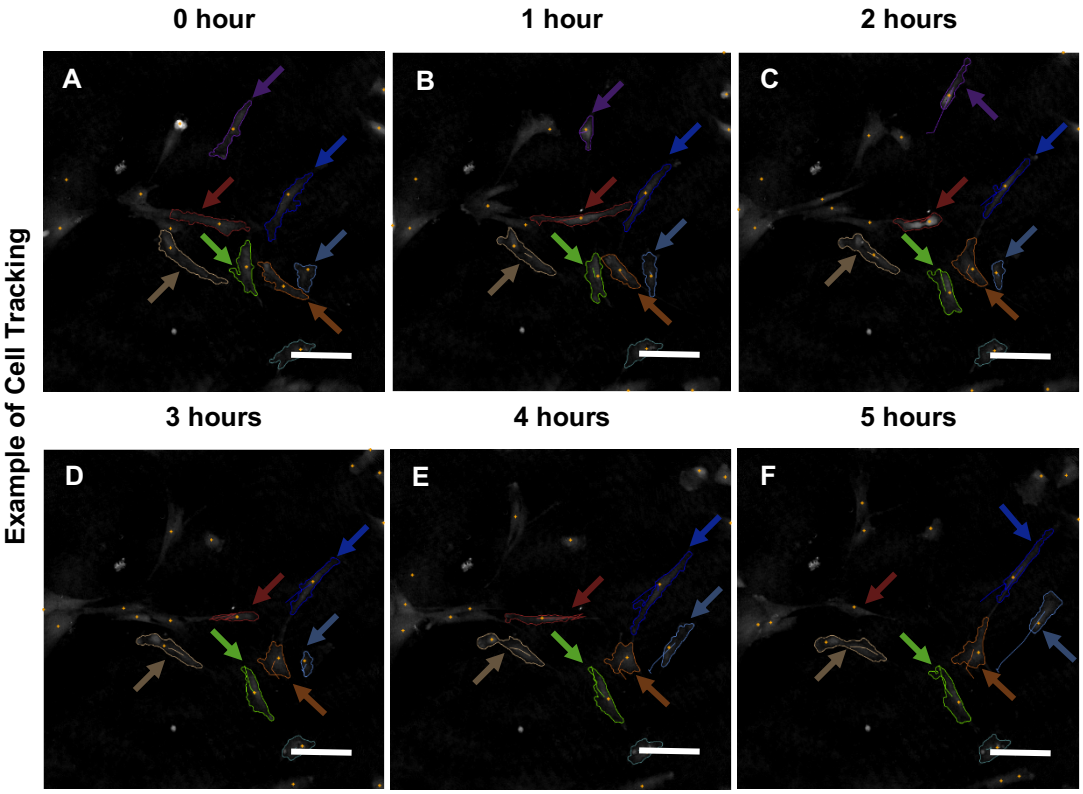

Figure 6.8: Example images of cell tracking, using HoloMonitor software. **A-F)** Cell tracking of five cells in a field of view over 5 hours. Scale bar represents 50 µm.

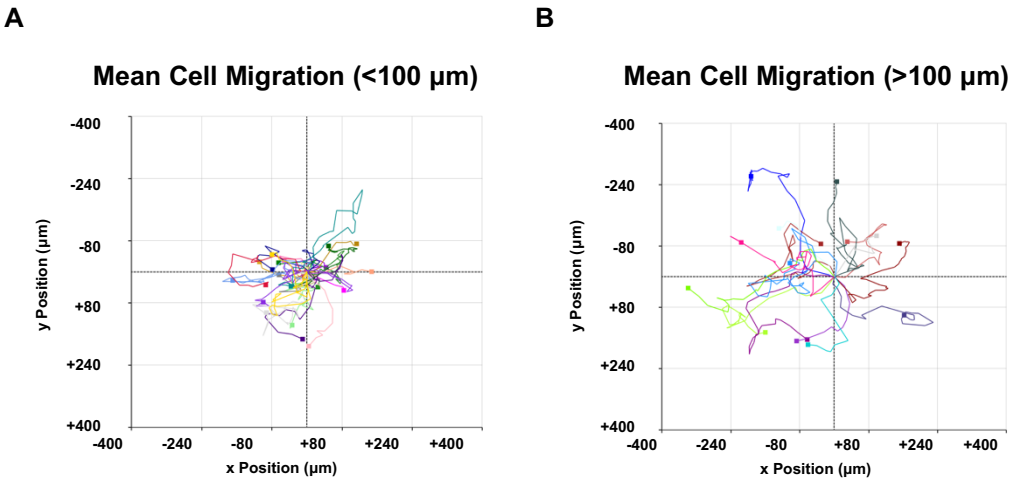

Figure 6.9: Cell migration map of individually tracked cells. Example of cells tracked from periosteum derived cells (passage 0). **A)** Migration map of cells with <100 µm mean cell migration or **B)** >100 µm mean cell migration. Each colour represents a single cells migration map (colours repeated).

Table 6.3: Summary of confluency, cell migration split and cell motility speed following cell tracking of different MSC cultures.
NP – non passaged, P0 – passage 0

MSC Culture	Confluency (% Cell Coverage)		Number of Cells Split by Cell Migration (%)		Cell Motility (µm/h)	
	0 hours	25 hours	<100 µm	>100 µm	<100 µm	>100 µm
Periosteum (NP)	4.7 ± 5.3	6.2 ± 5.9	58.5 (n=55)	41.5 (n=39)	17.7	22.4
Periosteum (P0)	5.0 ± 1.2	9.9 ± 3.3	42.2 (n=19)	57.8 (n=26)	17.5	20.4
Bone Marrow (P0)	0.9 ± 0.3	2.7 ± 0.6	62.8 (n=59)	37.2 (n=35)	22.3	32.0

analysis of the migration patterns separately to compare and contrast between the two, as well as between the three MSC types was carried out. Cell migration was quantified over time, if mean migration was <100 µm it was considered to be 'non migratory, conversely if mean migration was >100 µm, it was a 'migratory' cell (Figure 6.9). The number of cells allocated to the 'non-migratory' or 'migratory' category for each MSC culture type was summarised in Table 6.3, with a relatively even split between two of the cultures (58.5% (NP periosteum) and 62.8% (P0 BM), <100 µm), with a slight decrease in the proportion of non-migratory cells for P0 periosteum cultures 42.2%.

The cell confluency, or percentage coverage of the field of view with cells was quantified at the beginning and end time points (0 and 25 hours) (Table 6.3), it was found to be similar for both the periosteum cultures, 4.7 ± 5.3% increasing to 6.2 ± 5.9% by 25 hours (NP, periosteum) and 5.0 ± 1.2% increasing to 9.9 ± 3.3% (P0, periosteum). The fields of view quantified for P0, BM had a lower confluency at 0.9 ± 0.3% increasing to 2.7 ± 0.6% (Table 6.3), although these differences were not significant.

Cell migration quantifies the displacement of the tracked cell from the first position or coordinates an individual cell was tracked from. As a whole population each of the three MSC cultures was quantified (3 fields of view pooled) for cell migration after 5 hours of tracking and 25 hours. No differences were seen between the mean cell migration of the periosteum derived cultures (NP vs P0) at 5 hours (71.9 ± 41.7 μm (NP), 61.8 ± 38.0 μm (P0) or 25 hours (161.8 ± 109 μm (NP), 128.8 ± 71 μm (P0)) (Figure 6.10A). In contrast when comparing P0 BM and periosteum cultures, BM cultures were found to have significantly higher mean cell migration (unpaired t-test, $P<0.0001$ (5 hours), $P=0.001$ (20 hours)) at 5 hours (102.6 ± 54.6 μm (BM), 53.5 ± 32.6 μm (Periosteum)) and 20 hours (209.1 ± 129.2 μm (BM) and 123.6 ± 67.6 μm (Periosteum)) (Figure 6.10B).

Each of the MSC cultures were then split for </>100 μm mean cell migration in order to allow for comparisons to be made between the non-migratory and the migratory cells within each population (Figure 6.10C-E). Significant increases in cell migration or displacement away from the initial tracked point were seen from 5 hours onwards between the migratory and non-migratory cells for all culture types (unpaired t-test, $P<0.05$) (Figure 6.10C-E). Similar patterns were seen, where cell migration steadily increased in a linear fashion and then starts to plateau.

When comparing periosteum cultures, the linear increase in migration was seen for approximately 15 hours for both migratory cell types from NP periosteum (Figure 6.10C). However, with P0, periosteum the plateau occurs after about 15 hours for the non-migratory cells (<100 μm), the migratory cells (>100 μm) had a less defined plateau (Figure 6.10D). The P0 BM cultures saw the plateau occur earlier, at approximately 8 hours (>100 μm) and 5 hours

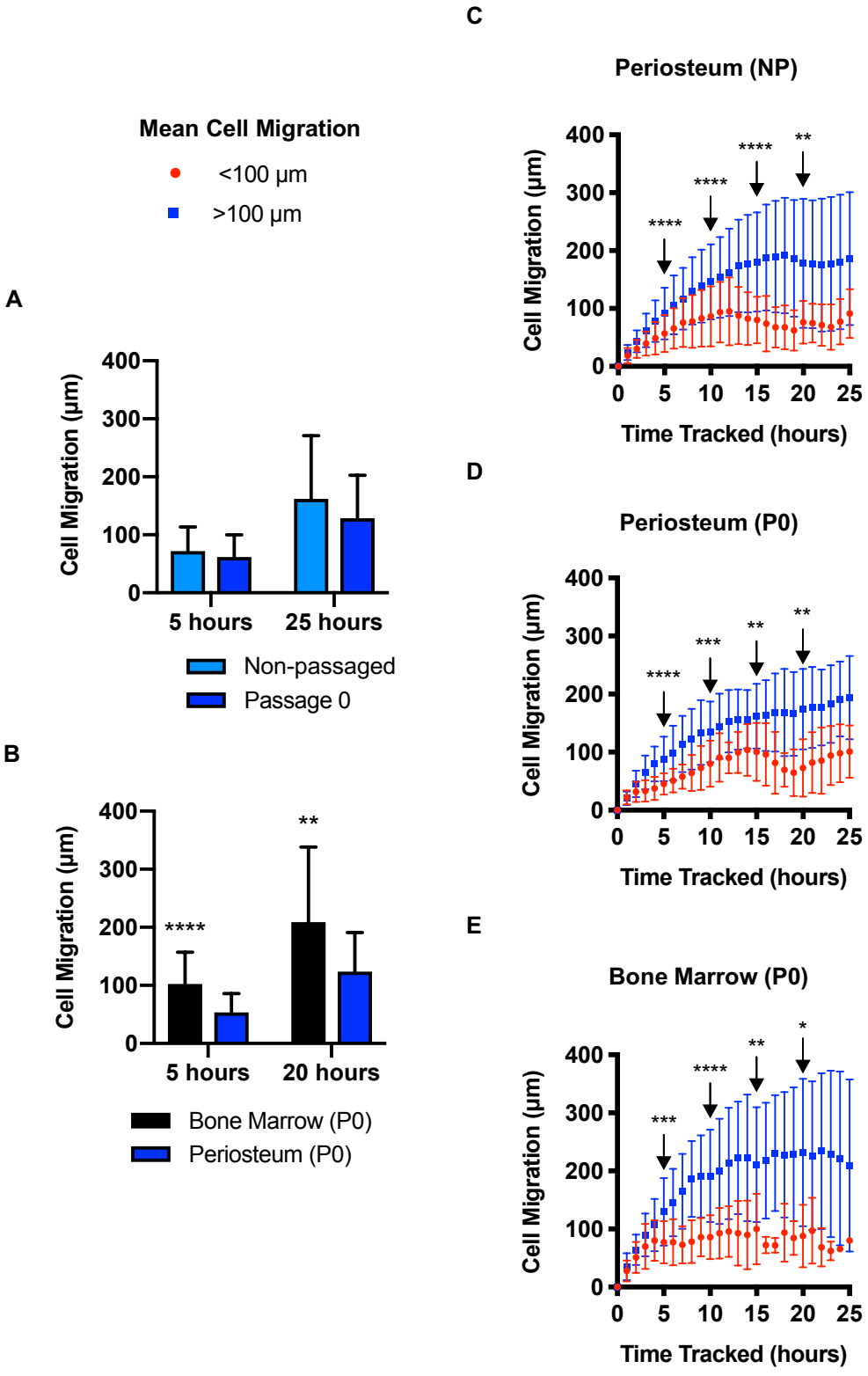

Figure 6.10: Quantified cell migration of periosteum and bone marrow cultures over time. Cell migration is a quantification of the displacement of a tracked cell from the initial tracked coordinates. **A)** Cell migration at 5 hours and 25 hours, comparing periosteum derived cultures from non-passaged (NP) and passage 0 (P0) (cultured for 14 days). **B)** Cell migration at 5 hours and 20 hours, comparing P0 cultures (cultured for 14 days) from bone marrow (BM) and periosteum. Individually tracked cells were split into </>100 µm

mean cell migration for **C)** NP periosteum, **D)** P0 periosteum and **E)** P0 BM. Unpaired t-test, P<0.05, **** P<0.0001, *** P<0.001, ** P<0.005, * P<0.05.

(<100 µm) (Figure 6.10E). As previously shown, cell migration was higher overall for the BM cultures by 5 hours, it should also be noted that linear increase of the migratory cells was not only 'faster' than the periosteum counterparts (8 hours (BM) vs 15 hours (Periosteum)), but also 'further away' from the tracked start point (approximately 190 µm (BM) vs 150 µm (Periosteum) (Figure 6.10D-E). Thus, suggestive that the speed of cell movement was greater in BM cultures.

Therefore, cell motility was assessed, which refers to the cumulative distance travelled each time point. As with cell migration, no significant differences were seen between the periosteal cultures (NP vs P0) with respect to cell motility after 5 hours (106.2 ± 42.4 µm (NP), 95.6 ± 35.0 µm (P0)) and 25 hours (518.2 ± 147.2 µm (NP), 470.9 ± 98.2 µm (P0) (Figure 6.11A). With respect to comparisons of P0 cultures, BM cultures showed significantly higher cell motility over time (Unpaired t-test, P<0.05), when compared to periosteal cultures, where at 5 hours, total cell motility (distance travelled) was 151.4 ± 53.6 µm (BM) compared to 95.6 ± 35.0 µm (Periosteum) and by 20 hours this difference had increased to 594 ± 136.0 µm (BM) and 384.2 ± 81.5 µm (Periosteum) (Figure 6.11B).

When analysing cell motility, following splitting of the tracked cells into non-migratory and migratory cells (</>100 µm mean cell migration), significant increases in cell motility or distance (rather than displacement) migrated over time was seen with the migratory cells (>100 µm), compared to the non-migratory cells (<100 µm) from 5 hours onwards (Unpaired t-test, P<0.005), irrespective of culture type (Figure 6.11C-E). Also, cell motility was found to be linear for all MSC cultures, irrespective of being non-migratory or migratory, shown through linear regression analysis with r^2 values of >0.994 for both P0 cultures (Periosteum and BM) and for NP periosteum r^2=0.73 (<100 µm) and r^2=0.81 (>100 µm).

Therefore, the speed (µm/h) at which the tracked cells migrated could be quantified from the linear regression gradient of the cell motility graphs (Figure 6.11C-E). Here, as with previous results the motility speed of the cells derived

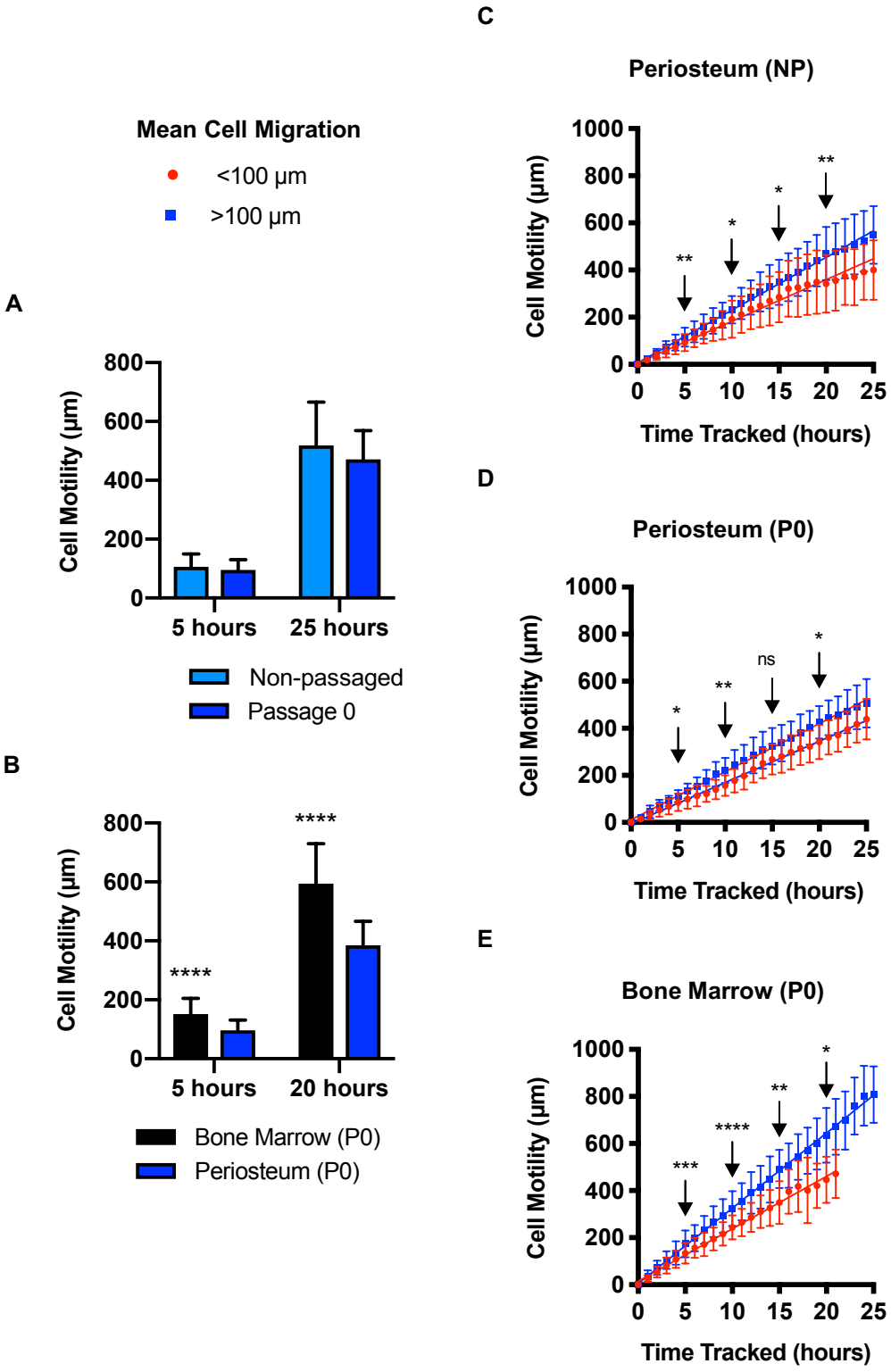

Figure 6.11: Quantified cell motility of periosteum and bone marrow cultures over time. Cell motility is a quantification of the cumulative distance travelled by a tracked cell over time. **A)** Cell motility at 5 hours and 25 hours, comparing periosteum derived cultures from non-passaged (NP) and passage 0 (P0) (cultured for 14 days). **B)** Cell motility at 5 hours and 20 hours, comparing P0 cultures (cultured for 14 days) from bone marrow (BM) and periosteum. Individually tracked cells were split into </>100 µm mean cell migration, as in Figure 6.9 and cell motility was displayed for **C)** NP

periosteum, **D)** P0 periosteum and **E)** P0 BM. Unpaired t-test, P<0.05, **** P<0.0001, *** P<0.001, ** P<0.005, * P<0.05.

from periosteum (NP vs P0) were similar for non-migratory (17.7 μm/h (NP), 17.5 μm/h (P0)) and migratory cells (22.4 μm/h (NP), 20.4 μm/h (P0)) (Table 6.3). However, it should be noted that the speed of the migratory cells was higher than that of the non-migratory cells. When comparing the P0 cultures, BM cultures were shown to migrate at either 22.3 μm/h (<100 μm) or 32.0 μm/h (>100 μm), again showing BM cultures to migrate with greater speed than periosteum cultures.

Thus far, migration and motility have been used as parameters to quantify differences in MSC migration patterns. Cell migration, a measure of displacement from the original tracked point, has merits as it allows for showing how far MSCs migrate and allows for quantification of migratory and non-migratory cells and this to be applied to other parameters. However, motility and thus cell velocity shows the speed and overall distance cells can cover, showing BM (P0) to be significantly faster and more motile than its periosteum (P0) counterparts.

Another of the parameters quantified using the HoloMonitor software is cell migration directness, a ratio of migration (displacement) to motility (distance), whereby 1 refers to a cell moving in a straight line and 0 refers to a cell moving completely randomly. This can be used to describe whether cells migrate randomly or with apparent ‘purpose’. In contrast to the previous parameters, no significant differences were seen between the MSC culture types over time (Figure 6.12A-B). For all the MSC culture types, cell migration directness reduced over time, with the non-migratory cells showing significantly reduced ratios at 5 hours and 10 hours, however, by 20 hours the differences were no longer significant (Unpaired t-test, P<0.05). Therefore, migration directness could also be influenced by confluence as this increases with time also. There was a trend for the non-migratory cells to migrate in a more random fashion in comparison to the migratory cells, which corresponds with the cell tracking maps shown in Figure 6.9. Here, the migratory cells can be seen to move away from the initial tracked coordinates, compared to the non-migratory cells which migrate within a smaller area (Figure 6.9). Therefore, migratory cells could have more ‘purpose’ to their migration, but within increased confluence

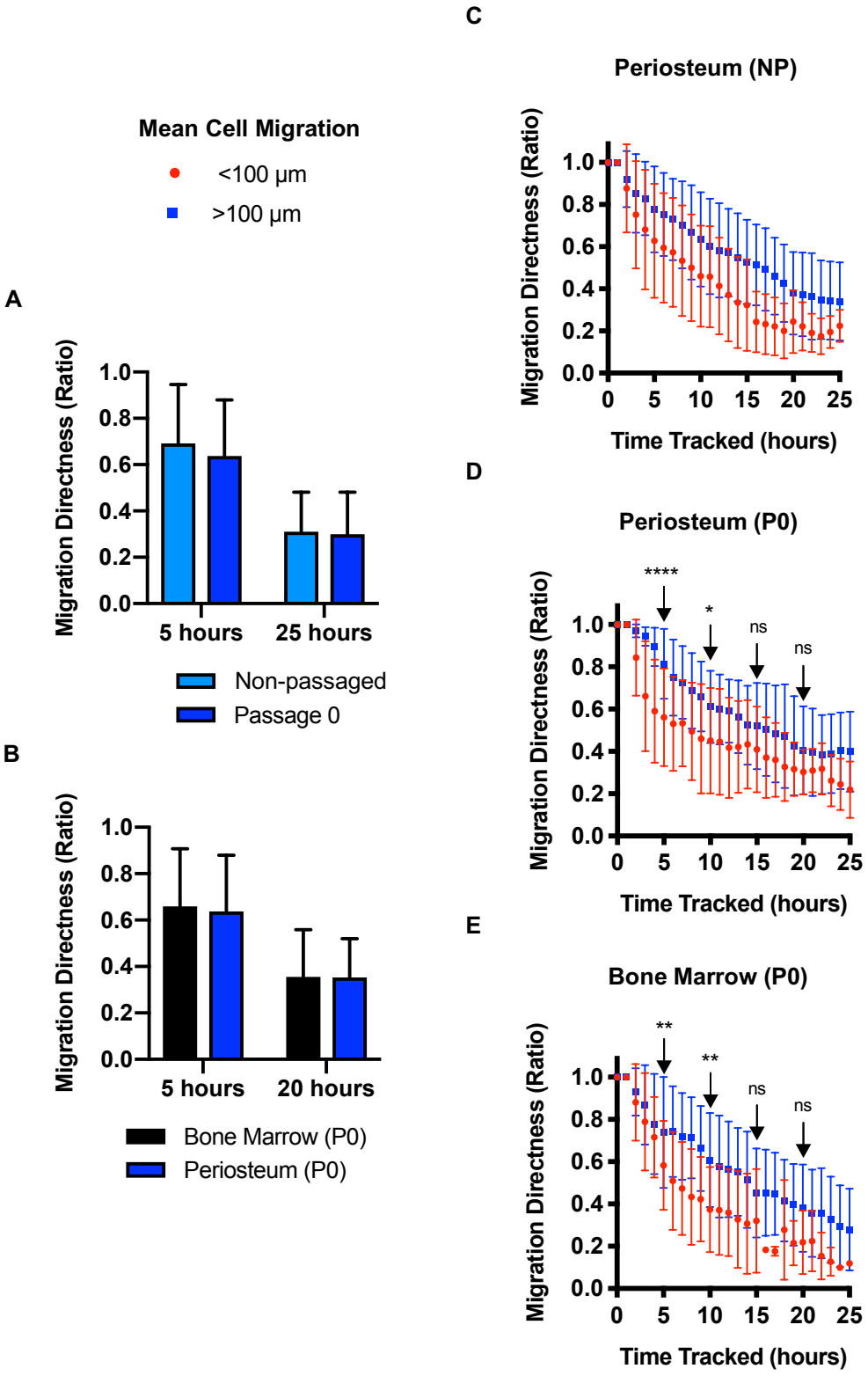

Figure 6.12: Quantified cell migration directness of periosteum and bone marrow cultures over time. Cell migration directness is a ratio of cell migration to cell motility, whereby a value of 1 shows a cell migrating in a straight line opposed to 0 which refers to a cell with completely random movements. **A)** Cell migration directness at 5 hours and 25 hours, comparing periosteum derived cultures from non-passaged (P0) and passage 0 (P0) (cultured for 14 days). **B)** Cell migration directness at 5 hours and 20 hours,

comparing P0 cultures (cultured for 14 days) from bone marrow (BM) and periosteum. Individually tracked cells were split into </>100 μm mean cell migration, as in Figure 6.9 and cell migration directness was displayed for **C)** NP periosteum, **D)** P0 periosteum and **E)** P0 BM. Unpaired t-test, P<0.05, **** P<0.0001, *** P<0.001, ** P<0.005, * P<0.05.

and with less space to migrate in they are forced to migrate more randomly with time.

To summarise, there appears to be little difference between the migration patterns and movements of cells from periosteum cultures when comparing 'NP' cells and 'P0' cells that had been grown for 14 days in culture previously. However, BM (P0) cultures were shown to have the capacity of significantly higher cell migration and therefore potential to displace away from the initial tracking coordinates when compared to periosteum (P0) cultures, in a donor matched study. In addition, cells from BM cultures were shown to cover more distance during migration at a higher speed. Although, there is potential that the migratory BM cells act as a 'burst', whereby they migrate quickly, approximately 200 μm away and then plateau. Whereas, migratory periosteum cells could tend to migrate slowly away over a longer period of time. Non-migratory cells (<100 μm) were shown to remain in the same vicinity, migrating smaller distances, slower and in a more random nature in comparison to migratory cells. This was true for all MSC culture types tested.

These findings can be potentially extrapolated onto predicting potential differences in how periosteum and BM MSCs will grow and populate onto the free surface electrospun membranes. It could be expected that BM MSCs would spread out across the membranes faster, based on the migratory subset of cells showing faster motility velocity. However, as tissue culture plastic is a completely different surface in comparison to the nano-fibre network of the free surface electrospun membranes, especially M6%-CP70:30 that contains collagen, more differences in MSC behaviour would be expected.

6.3.2 Free Surface Electrospun Membrane Cellular Attachment

A key function of the free surface electrospun membranes developed in Chapter 5 (M6%-CP70:30 and M3%-PCL) was to support periosteal regrowth during CSBD. Therefore, it was pertinent to assess the ability of said membranes to support periosteum MSC attachment, growth and proliferation *in vitro*. Samples of M6%-CP70:30 and M3%-PCL (4 cm^2 pieces) were incubated with 10^4 MSCs (suspended in 200 µL) of either periosteum or BM origin and grown in tissue culture for up to 4 weeks. Time points were taken over the course of the assay at days 4, 14 and 28 (10^3 cell density) and days 4, 7, 14, 21 and 28 (10^4 cell density). This allowed for not only the two membranes to be compared, but also assess the effect of MSC type (periosteum or BM), cell density (10^3 or 10^4 seeded cells) as well as the effect of time in culture.

At each time point membrane:MSC constructs were fixed and stained with DAPI and Phalloidin-FITC to enable confocal imaging (n=5, random areas taken in the same orientation) of the cell nuclei and actin filaments, respectively. Post imaging analysis was carried out on the DAPI only images to count the number of nuclei in the field of view (0.316 mm^2), as well as to quantify nuclei angles (See Figure 6.5) and therefore cellular alignment on the underlying material over time.

6.3.2.1 MSC Attachment onto M6%-CP70:30

Fluorescent imaging of M6%-CP70:30 was particularly difficult, the membrane was found to be auto-fluorescent throughout the majority of the available wavelengths (approximately 385-650 nm). There was high background staining throughout the wavelength range used for DAPI, although there was enough contrast to allow for nuclei imaging with high background auto-fluorescence. However, imaging of actin filaments throughout the FITC spectrum (485-650 nm) was impossible as the auto-fluorescence was too high. To combat this the wavelength range imaged were narrowed to 450-470 nm (DAPI) and 510-530 nm (FITC) in addition to incorporating the use of the TrueVIEW™ Autofluorescence Quenching Kit (Vector Laboratories), designed to quench the collagen's auto-fluorescence.

Standard use of this kit is to stain the sample first and then quench afterwards, however following optimisation for this membrane and staining regime it was found that the constructs should be permeabilised, quenched and then stained with Phalloidin-FITC and DAPI. This process was decided due to the permeabilisation process visually reversing the quenching of the samples, whereby quenched samples are stained blue, but following permeabilisation, the stain was released. In addition, quenching reduced the 'brightness' of the fluorescent staining, thus samples were stained post-quenching.

Periosteum MSCs were imaged attaching and proliferating onto M6%-CP70:30 at low and high cell densities, over a period of 4 weeks (Figure 6.13). Periosteum MSCs throughout all the time points and cell densities were shown to be spindle shaped. There was a low level of cellular attachment and proliferation at the low cell density (Figure 6.13A-B). However, proliferation was seen at the higher cell density by day 14 and day 28 (Figure 6.13E-F). Nuclei alignment was not seen at day 4 or day 14 for the low cell density, thus Gaussian distribution was not able to be plotted (Figure 6.13A-B). By day 28 Gaussian distribution was plottable, however with a particularly flat distribution, suggestive of a lack of nuclei alignment. At the higher cell density, nuclei alignment was seen to be normally distributed at all time points, whereby at day 4 the distribution was flat, but became more bell shaped at the later time points (day 14 and day 28) (Figure 6.13D-F).

It should be noted that M6%-CP70:30 showed positive DAPI staining, whereby the morphology of the specific staining sites appeared smaller than expected of a cell nucleus, particularly apparent at day 14 of the lower cell density (red arrow, Figure 6.13B). Here, small circular or elongated fragments stained with DAPI (blue) were shown in areas that did not overlap with actin filament staining (green, Phalloidin). 'Cell free' M6%-CP70:30 and M3%-PCL were imaged pre and post quenching (Figure 6.3) to show the reduction in auto-fluorescence of M6%-CP70:30 following quenching, here it was shown that small 'flecks' of auto-fluorescence under the UV laser (corresponding to DAPI) were seen, however these were noticeably smaller than those seen when the membranes were further stained with DAPI. This is suggestive that the DAPI staining not corresponding with clear Phalloidin staining, as shown

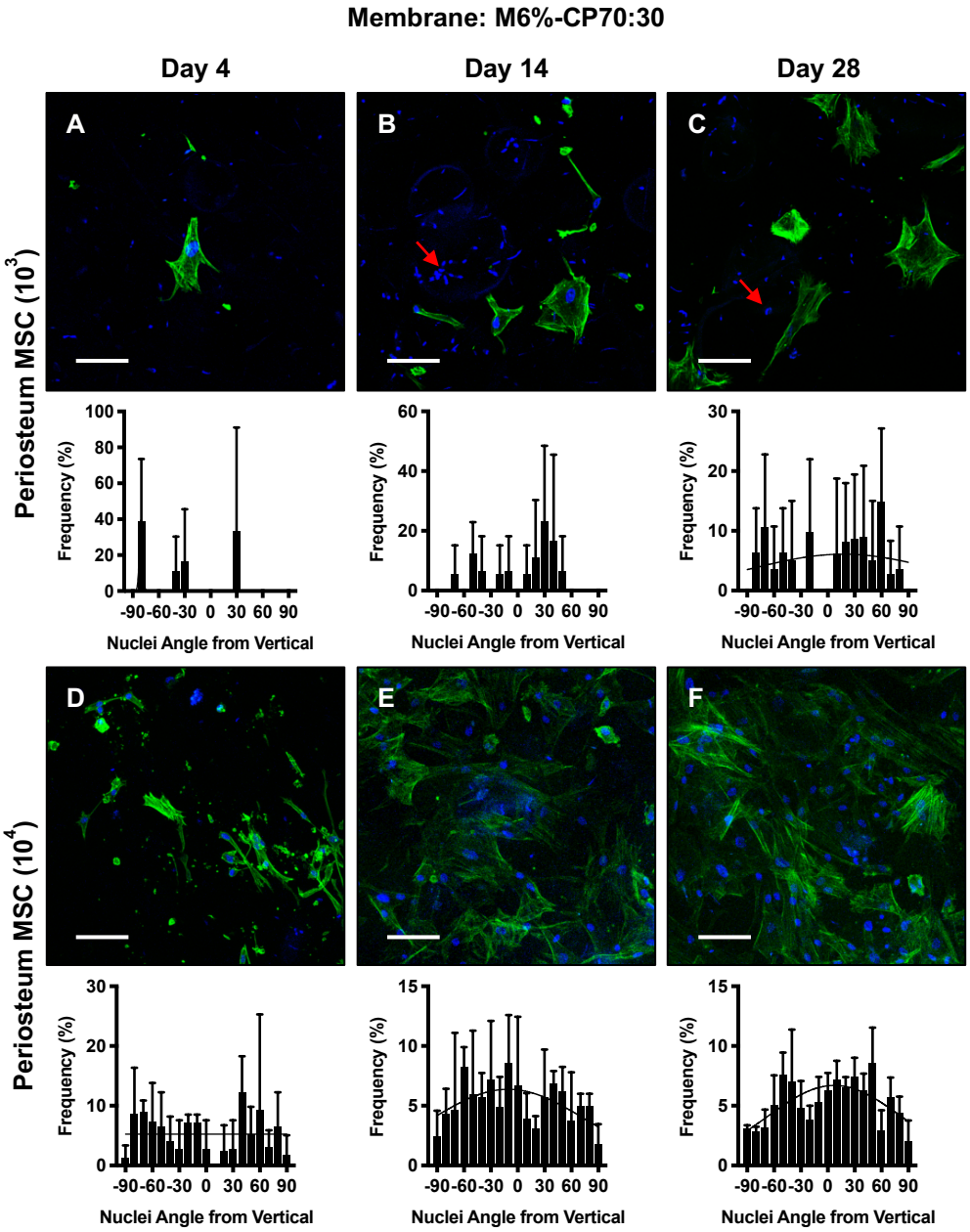

Figure 6.13: Periosteum MSC attachment and proliferation over 4 weeks, onto M6%-CP70:30 at low and high cell seeding densities. M6%-CP70:30-MSC membrane constructs were fixed, stained with DAPI (Nuclei) and Phalloidin-FITC (Actin filaments) and imaged (n=5) using confocal microscopy, representative image shown at each time point. Nuclei angle and alignment was quantified (n=5 images taken) and frequency distribution displayed (mean ± SD) below the corresponding time point. Low seeding density (10^3) of periosteum MSCs, with three time points, **A)** Day 4, **B)** Day 14 and **C)** Day 28 was compared to a higher seeding density (10^4) at **D)** Day 4, **E)** Day 14 and **F)** Day 28. Images were taken at x20 magnification, scale bar represents 100 µm. Red arrow – potential DNA fragments.

in Figure 6.13B, could not be attributed to auto-fluorescence of M6%-CP70:30. Thus, it was concluded that these fragments were 'true' DAPI staining, consistent with nuclei fragments.

The collagen source used to manufacture M6%-CP70:30 is of rat tail tendon origin, generated in-house, with the potential to contain the nuclei from cells within the tendon, which could be in fragment form following the electrospinning process and exposure to HFIP. In addition, the nuclei fragments could also be from the seeded human periosteum MSCs that failed to attach onto M6%-CP70:30, thus going into apoptosis. However, following several wash steps are carried out during the fixation and staining process, therefore it would be expected that any dead or fragmented cells would have detached from the underlying membrane. Based on this, correct nuclei morphology and co-localisation with actin staining was needed for inclusion in nuclei quantification.

6.3.2.2 MSC Attachment onto M3%-PCL

M3%-PCL posed an easier material to image using confocal microscopy, due to the absence of collagen throughout the membrane, there was not any auto-fluorescence when using Phalloidin-FITC to image actin filaments. Both periosteum and BM MSCs were shown to attach and proliferate at both cellular densities on M3%-PCL (Figure 6.14 and Figure 6.15). At the lower cell density of 10^3 seeded cells, periosteum MSCs were spindle shaped and randomly aligned at 4 days in culture (Figure 6.14A), by day 14 (Figure 6.14B) there was slight alignment, however, by day 28 there was clear normal distribution of the nuclei alignment (Figure 6.14C). With the higher cell density (10^4), periosteum MSCs were shown to align by day 7 (Figure 6.14E), with increasing alignment shown over the following time points (day 14, day 21 and day 28) (Figure 6.14F-H). The cellular alignment shown by periosteum MSCs grown at low and high cellular densities on M3%-PCL was also shown through the alignment of the actin filaments, which support the corresponding frequency distribution of nucleus angle.

To assess whether the cellular alignment seen on M3%-PCL was merely due to the nature of periosteum MSCs in culture donor matched BM MSCs were also seeded onto M3%-PCL at low (Figure 6.15A-C) and high cellular

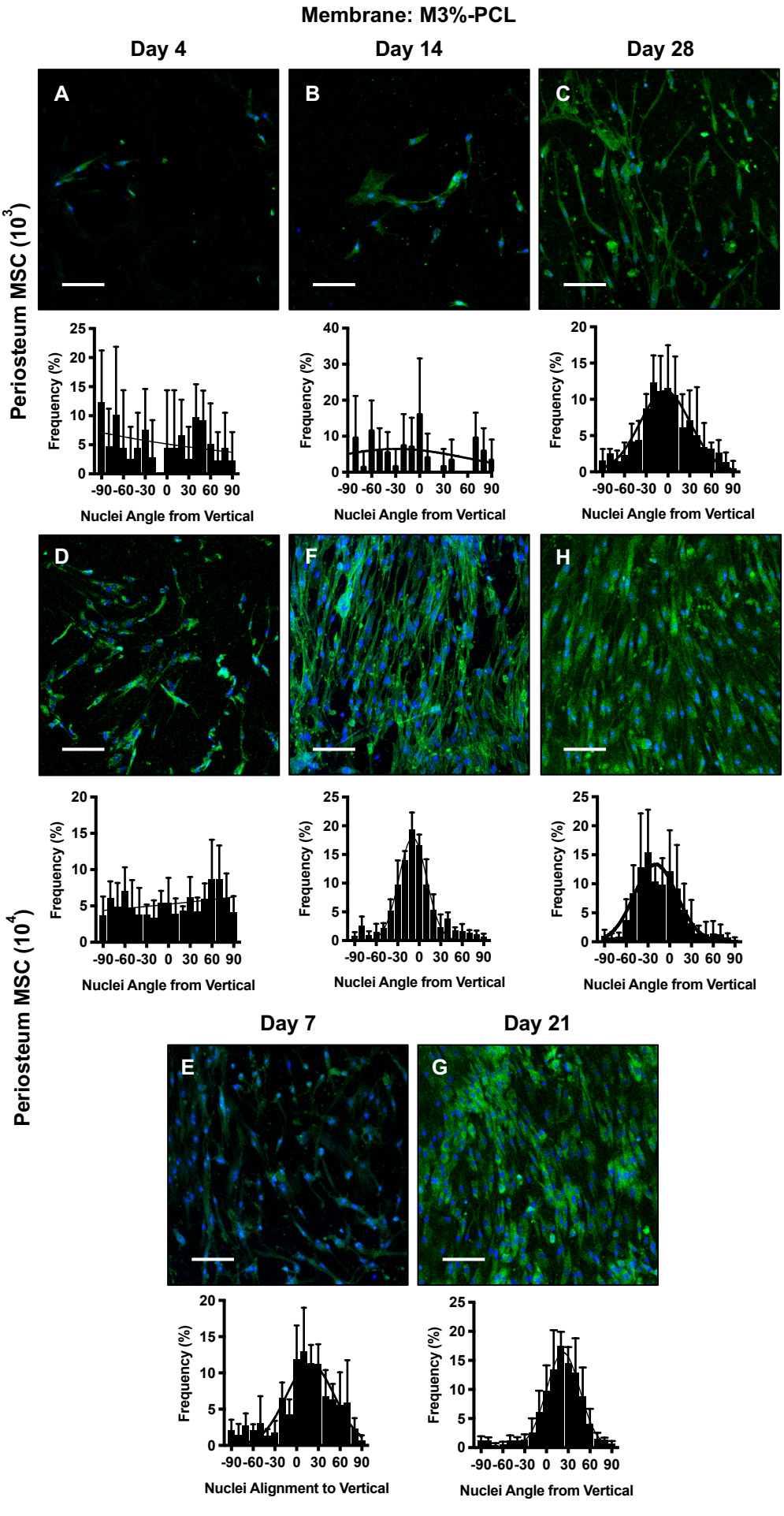
Membrane: M3%-PCL
Day 4
Day 14
Day 28
Periosteum MSC (10^3)
A
B
C
Frequency (%)
Nuclei Angle from Vertical
D
F
H
Periosteum MSC (10^4)
Day 7
Day 21
E
G
Nuclei Alignment to Vertical
-90 -60 -30 0 30 60 90

Figure 6.14: Periosteum MSC attachment and proliferation over 4 weeks, onto M3%-PCL at low and high cell seeding densities. M3%-PCL:MSC membrane constructs were fixed, stained with DAPI (Nuclei) and Phalloidin-FITC (Actin filaments) and imaged (n=5) using confocal microscopy, representative image shown at each time point. Nuclei angle and alignment were quantified (n=5 images taken) and frequency distribution displayed (mean ± SD) below the corresponding time point. Low seeding density (10^3) of periosteum MSCs, with three time points, **A)** Day 4, **B)** Day 14 and **C)** Day 28 was compared to a higher seeding density (10^4), with five time points, **D)** Day 4, **E)** Day 7, **F)** Day 14, **G)** Day 21 and **H)** Day 28. Images were taken at x20 magnification, scale bar represents 100 µm.

densities (Figure 6.15D-G). At the low cell density, as with periosteum MSCs, BM MSCs were randomly aligned at day 4 and 14 (Figure 6.15A-B). Normal distribution of nucleus angle was shown by day 28, however, the peak of the frequency distribution histogram was not pronounced, suggestive that BM MSCs were not aligning to the same extent by day 28 as periosteum MSCs had (Figure 6.15A-C). In addition, the BM MSCs were shown to be distinctly spindle shaped, with the actin filaments being visually randomly orientated. BM MSCs, at high cell density (Figure 6.15D-G) were also randomly orientated for the first three time points, day 4, 7 and 14 (Figure 6.15D-E), however, nuclei alignment was visible at day 21 and 28 (Figure 6.15G-H).

6.3.2.3 Comparison of MSC Proliferation on M6%-CP70:30 and M3%-PCL

To compare the differences in proliferation patterns of the periosteum and BM MSCs onto the free surface electrospun membranes, the number of nuclei imaged (n=5) per construct was quantified and compared (Figure 6.16A-D). There was limited cell proliferation of periosteum MSCs onto M6%-CP70:30 at the lower cell density, whereby initial attachment at day 4 was 2 ± 1 cells, increasing to 7.3 ± 1.7 cells by day 28, this increase was shown as significant (one-way ANOVA, Tukey's multiple comparisons test, $P<0.05$) (Figure 6.16A). However, with increased cellular density clear proliferation was seen, with initial cellular attachment at 19.0 ± 7.6 cells, increasing to 107.7 ± 15.5 cells by day 28 (Figure 6.16C). The number of cells present by day 28 was significantly greater than all other day points (one-way ANOVA, Tukey's multiple comparisons test, day 4 ($P<0.0001$), day 7 ($P<0.0001$), day 14 ($P=0.0003$) and day 21 ($P=0.003$)).

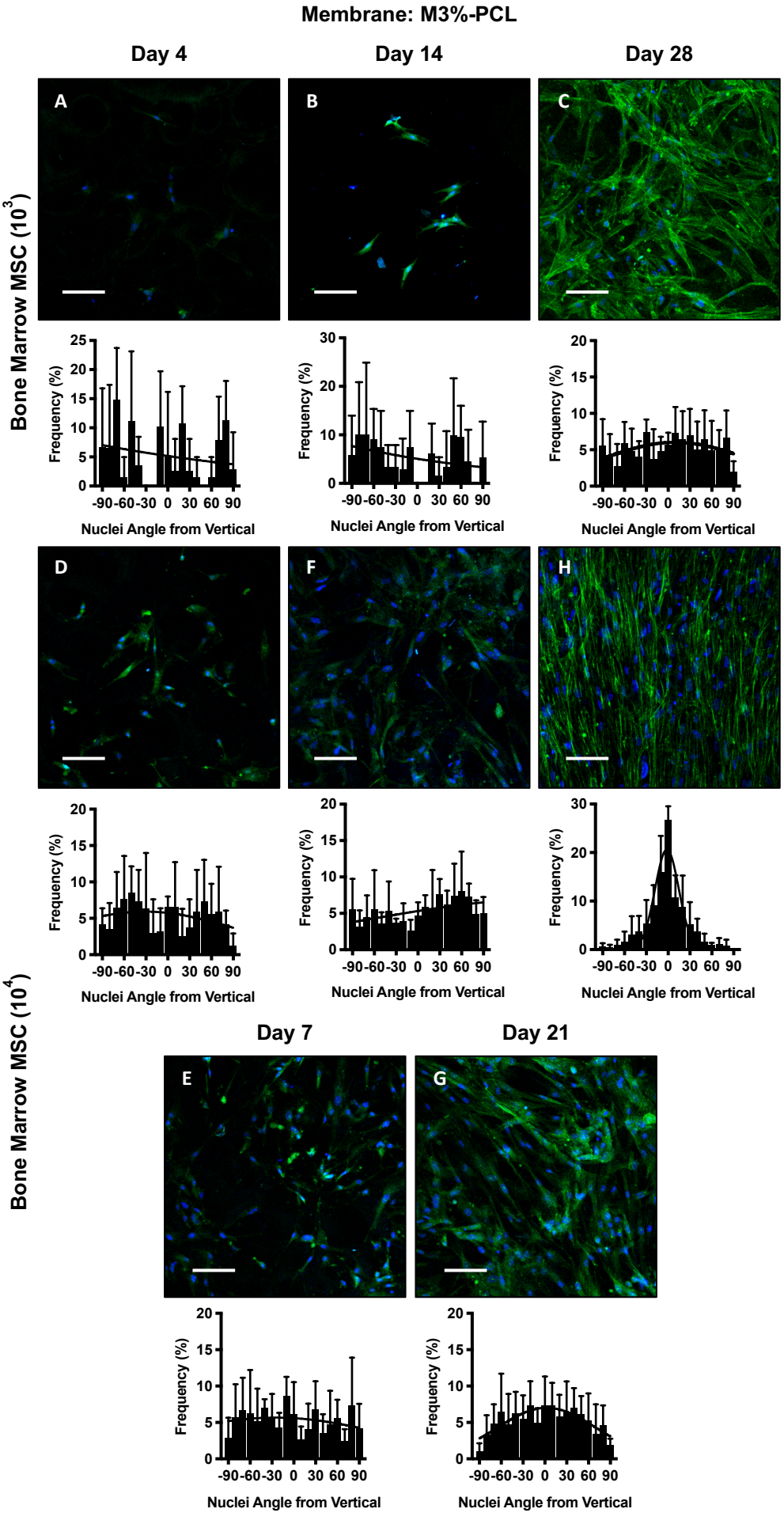
Membrane: M3%-PCL
Day 4
Day 14
Day 28
Bone Marrow MSC (10^3)
A
B
C
Frequency (%)
Nuclei Angle from Vertical
-90 -60 -30 0 30 60 90
D
F
H
Bone Marrow MSC (10^4)
Day 7
Day 21
E
G

Figure 6.15: Bone marrow MSC attachment and proliferation, over 4 weeks, onto M3%-PCL at low and high cell seeding densities. M3%-PCL:MSC membrane constructs were fixed, stained with DAPI (Nuclei) and Phalloidin-FITC (Actin filaments) and imaged (n=5) using confocal microscopy, representative image shown at each time point. Nuclei angle and alignment was quantified (n=5 images taken) and frequency distribution displayed (mean ± SD) below the corresponding time point. Low seeding density (10^3) of periosteum MSCs, with three time points, **A)** Day 4, **B)** Day 14 and **C)** Day 28 was compared to a higher seeding density (10^4), with five time points, **D)** Day 4, **E)** Day 7, **F)** Day 14, **G)** Day 21 and **H)** Day 28. Images were taken at x20 magnification, scale bar represents 100 μm.

With respect to M3%-PCL, the lower cell density showed the same number of initial MSC attachment for both MSC types (8.8 ± 1.8 – periosteum MSC, 8.8 ± 2.8 – BM MSC) (Figure 6.16B). This did not increase by day 14 (12.4 ± 2.6 – periosteum MSC, 8.4 ± 3.2 – BM MSC). However, by day 28 significant increases in nucleus counts were shown, increasing to 54.0 ± 17.4 (periosteum MSC) and 79.9 ± 9.7 (BM MSC), which was significantly increased in comparison to the day 4 and 14 values (one-way ANOVA, Tukey's multiple comparisons test, $P<0.0001$). In addition, BM MSCs nucleus count was significantly higher than periosteum MSCs at day 28 (unpaired t-test, $P=0.02$).

The higher cell density (10^4) nucleus count at day 4 was 35.8 ± 5.8 (periosteum MSC) and 31.4 ± 6.1 (BM MSC), respectively, which increased (although not significantly) to 89.0 ± 16.0 (periosteum MSC) and 58.4 ± 24.5 (BM MSC, respectively at day 7. However, the periosteum MSC value was significantly increased compared to BM MSC (unpaired t-test, $P<0.05$) (Figure 6.16D). For the remaining three time points, periosteum MSC nucleus count remained significantly increased compared to BM MSC (unpaired t-test, day 14 ($P=0.003$), day 21 ($P=0.04$), day 28 ($P=0.03$)), whereby periosteum MSC increased from 135.3 ± 19.3 (day 14) to 176.6 ± 41.2 (day 21) to 300.0 ± 96.2 (day 28), and BM MSC increased from 87.6 ± 12.1 (day 14) 126.6 ± 19.4 (day 21) to 183.2 ± 34.0 (day 28) (Figure 6.16D). For both MSC types, day 28 was found to have significantly higher nucleus counts than all other time points (one-way ANOVA, Tukey's multiple comparisons test, $P<0.001$, see Figure 6.16D), day 21 was significantly increased compared to day 4 and day 7 (one-way ANOVA, Tukey's multiple comparisons test, $P<0.05$, see Figure 6.16D)

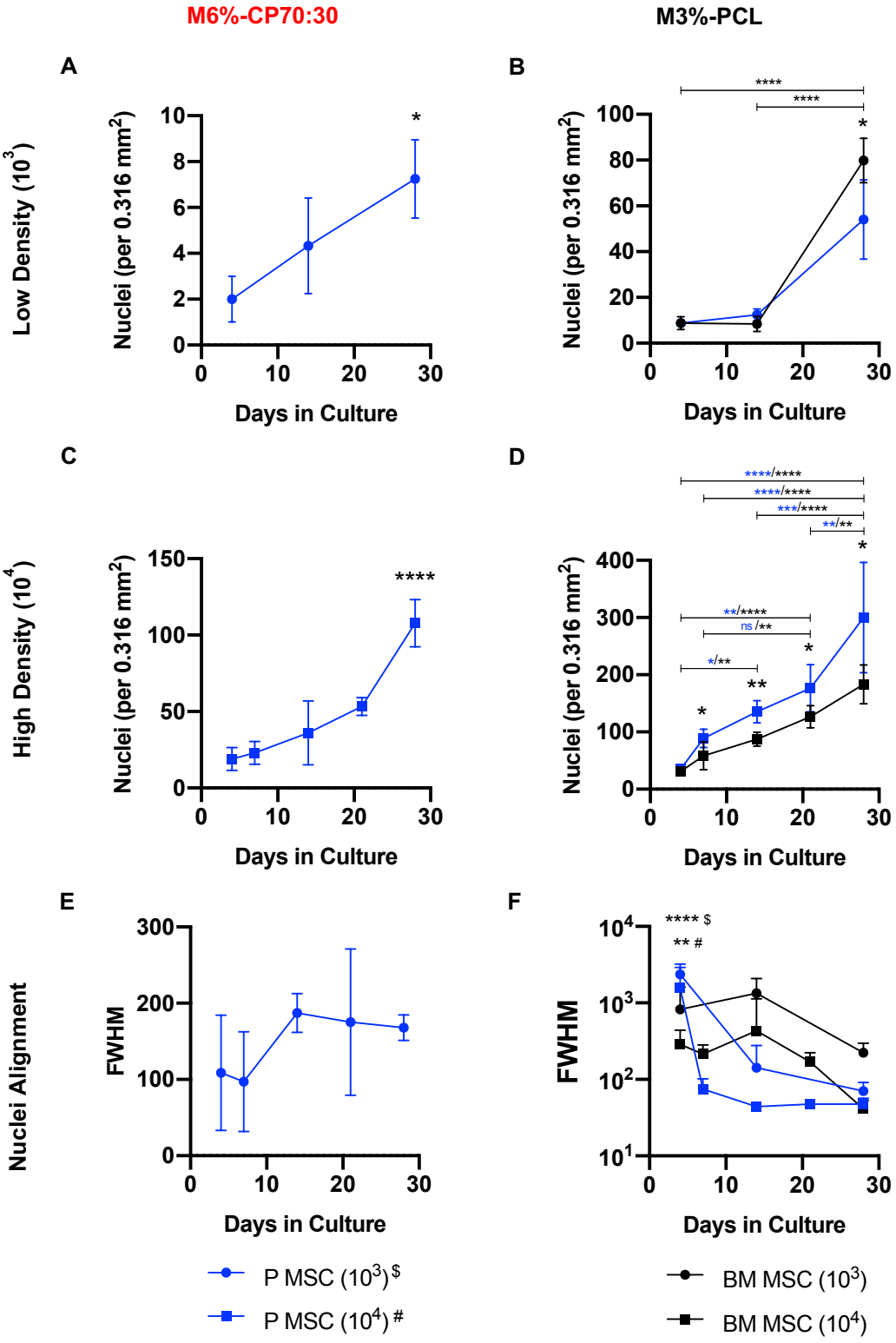

Figure 6.16: Quantification of MSC proliferation and alignment on M6%-CP70:30 and M3%-PCL. Confocal images and Gaussian distribution of the frequency distribution histograms (shown in Figure 6.13-6.15) were further quantified for nucleus count and 'full width at half maximum' (FWHM) values, respectively. Proliferation of periosteum (P) MSC onto M6%-CP70:30 and P MSC and bone marrow (BM) MSC onto M3%-PCL at, **A-B)** low cell density (10^3) and **C-D)** high cell density (10^4). **E-F)** Quantified FWHM values to show cellular alignment over time on M6%-CP70:30 and M3%-PCL. Mean values

plotted ± SD, based on n=5 images. Unpaired t-test, P<0.05 (BM MSC vs P MSC) * (P<0.05), one-way ANOVA, Tukey's multiple comparisons test, P<0.05 (time point comparison) * P<0.05, ** P<0.005, *** P<0.001, **** P<0.0001. B) Blue stars – periosteum MSC, black stars – BM MSC. C) Significance day 4 vs all other time points, $ P MSC (10^3) # P MSC (10^4).

and day 14 was significantly increased compared to day 4 (one-way ANOVA, Tukey's multiple comparisons test, P<0.05), see Figure 6.16D).

It was surprising that the cellular attachment onto M6%-CP70:30 was lower in comparison to M3%-PCL as it was hypothesised that the presence of collagen would enhance cellular attachment. The attachment and proliferation of periosteum MSCs was compared between the two free surface electrospun membranes. M3%-PCL supported significantly higher initial cellular attachment on day 4 for both cell densities (unpaired t-test, P=0.001 (10^3), P=0.01 (10^4)). In addition, proliferation on M3%-PCL was significantly higher at all time points for the lower cell density (unpaired t-test, P=0.004 (day 14), P=0.001 (day 28) and for the higher cell density (unpaired t-test, P=0.0006 (day 7), P=0.001 (day 14), P=0.003 (day 21), P=0.02 (day 28)). It was shown in Chapter 5 that collagen solubilised into solution when incubated with PBS. The majority of this was lost from M6%-CP70:30 in the first 24 hours, during initial cellular attachment. Therefore, initial attachment could be impeded by this loss of collagen from the membrane.

6.3.2.4 Nuclei Alignment onto M6%-CP70:30 and M3%-PCL

Frequency distribution of nucleus angle was plotted for every individual image, nonlinear Gaussian distribution curves were also plotted and from this FWHM was quantified to show the distribution of the data (Figure 6.16E-F). Normal distribution of nucleus angle was not possible for day 4 and day 14, low cell density for M6%-CP70:30, most likely due to the low number of cells quantified, thus FWHM was not quantified. However, FWHM was quantified for the high cell density M6%-CP70:30 constructs, whereby the values ranged from 97.2 to 187.2 for all the time points, and was shown to not change significantly over time (Figure 6.16E), thus increased alignment of nuclei with time was not seen.

In comparison, a clear picture was seen when quantified for periosteum MSCs on M3%-PCL, whereby FWHM was shown to significantly drop (one-way ANOVA, Tukey's multiple comparisons test, 10^4 $P<0.006$, 10^3 $P<0.0001$) after day 4 for the rest of the time points for both cell densities (Figure 6.14 and Figure 6.16). When looking at BM MSC alignment on M3%-PCL, the reduction of FWHM was delayed in comparison to periosteum MSCs and was seen after day 14, whereby the high cell density (10^4) alignment was shown to match both cell densities for periosteum MSCs. However, even though FWHM for the low cell density BM MSCs was shown to reduce at day 28, this was not as prominent as the rest, confirmed visually (Figure 6.15C and Figure 6.16F). However, none of the differences for either cell density for BM MSC over the time course were shown to be significant (one-way ANOVA, Tukey's multiple comparisons test, $P<0.05$).

To compare the two free surface electrospun membranes, it was apparent that M3%-PCL provided a favourable surface for periosteum MSCs to attach, proliferate and align onto in comparison to M6%-CP70:30. However, it should be noted that with a high enough seeding density, proliferation of periosteum MSCs can be seen on M6%-CP70:30. This reduction in cellular attachment onto M6%-CP70:30 is postulated to be due to the initial 'burst' release of collagen when the membrane is placed in solution.

With respect to comparison of periosteum and BM MSCs growth onto M3%-PCL it was shown that both MSC types have similar initial cellular attachment, however, periosteum MSCs proliferate at a significantly higher rate at all following time points in comparison to BM MSCs at a high cell density. Alignment of MSCs was also positively influenced by increased cell density, irrespective of the cell type. In addition, at the low cellular density, similar growth rates were seen at day 14, however, by day 28 BM MSCs were shown to have significantly higher cellular content.

6.3.3 Functional Testing of Barrier Membrane Purpose

Following confirmation that MSCs are able to attach and proliferate onto M3%-PCL and M6%-CP70:30, albeit in different ways, it was imperative to ascertain the 'barrier function' of said membranes. A key specification for the free surface electrospun membranes was to be able to act as barrier to cell migration. Periosteum MSCs were used as the cell type of choice to test whether MSCs could migrate through the membranes and laser cut samples were used as positive controls that would allow for MSC migration through the holes. A serum gradient was created, whereby, periosteum MSCs were serum starved overnight and then 10^5 cells, suspended in 100 µL of serum free DMEM, were placed onto the top of both free surface electrospun membranes, which were contained within a MINUSHEET® tissue carrier (Figure 6.2). The MINUSHEET® tissue carrier would then float on top of StemMACS media (serum containing), which would then create a serum gradient, driving periosteum MSCs from the top of the barrier membrane to the bottom. This assay was set up to ascertain whether periosteum MSCs could be 'driven' to migrate through the free surface electrospun membranes, or whether these membranes posed a barrier to migration.

Clear attachment of periosteum MSCs onto the top side of M3%-PCL was seen, with the original free surface electrospun membrane at day 1 (Figure 6.17A & D), as well as the laser cut samples (Figure 6.17G & J). However, lower levels of attachment were shown in the areas close to the laser cut holes in comparison to the rest of the membrane. Over the next two time points (day 4 and day 7) clear proliferation was seen on the original M3%-PCL membrane (Figure 6.17B-C & E-F), while proliferation onto the laser cut membrane, close to the holes was less apparent (Figure 6.17H-I & K-L).

When imaging from the bottom of the M3%-PCL construct there were no apparent nuclei to image at day 1 for either the original or the laser cut membrane (Figure 6.18A, D, G & J). For the original M3%-PCL this was continued for day 4 and day 7, where at day 7 there was evidence of staining for DAPI, however, this was not consistent with the staining seen for a nucleus so was taken as potential fluorescence imaged from the top side of the membrane (Figure 6.18B-C & E-F). In contrast, the laser cut M3%-PCL

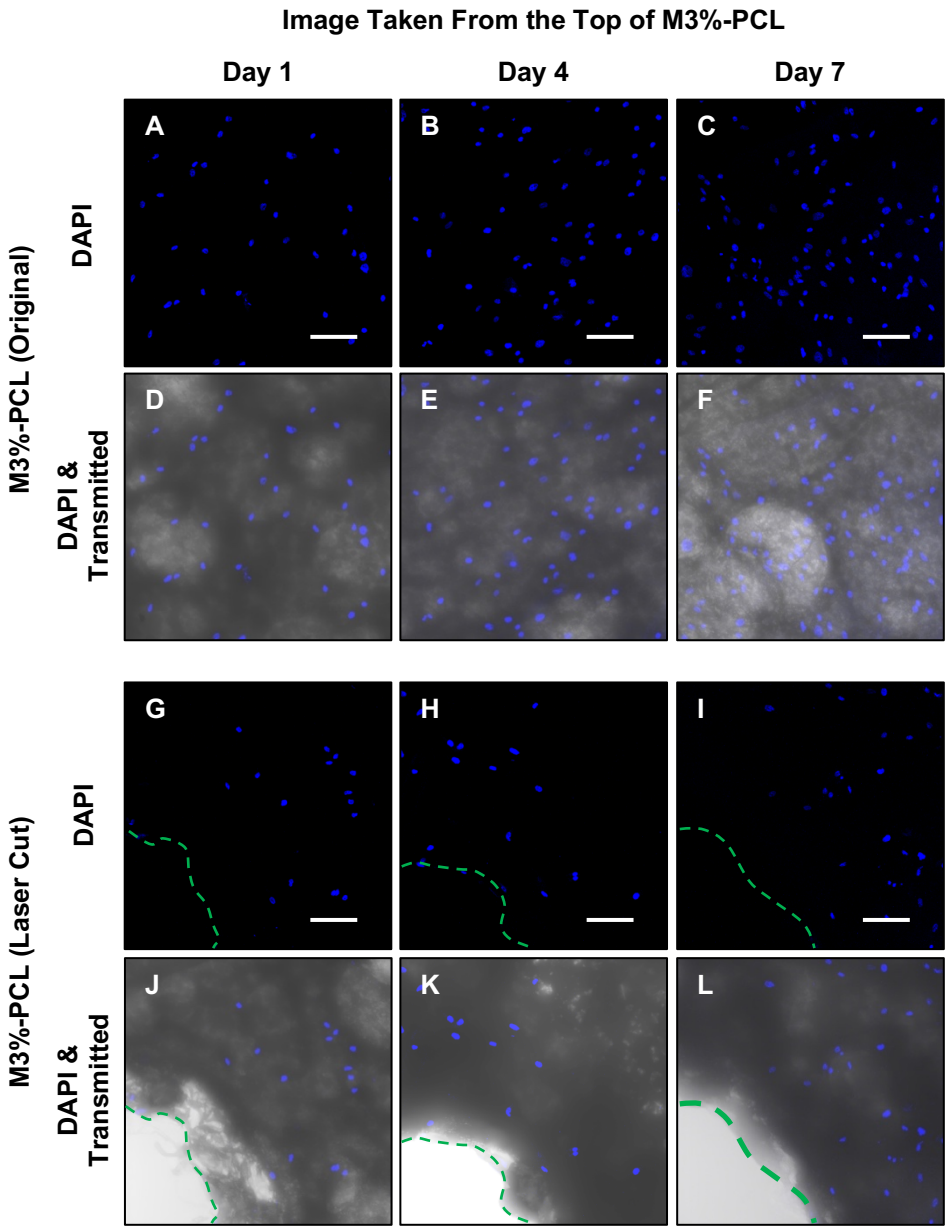

Figure 6.17: Prevention of MSC migration through M3%-PCL using a modified transwell assay to test barrier function, imaging from the top of the membrane. Confocal microscopy images of DAPI stained membrane:MSC constructs, imaged from the 'top', where the MSCs were seeded onto. DAPI images and DAPI merge with transmitted light imaging of the underlying membrane. Three time points were taken over a week. **A-F)** The original M3%-PCL and **G-L)** M3%-PCL with laser cut holes, as a positive control for MSC migration. Images taken at x20, scale bar represents 100 µm. Green dash line to show the outline of the laser cut hole.

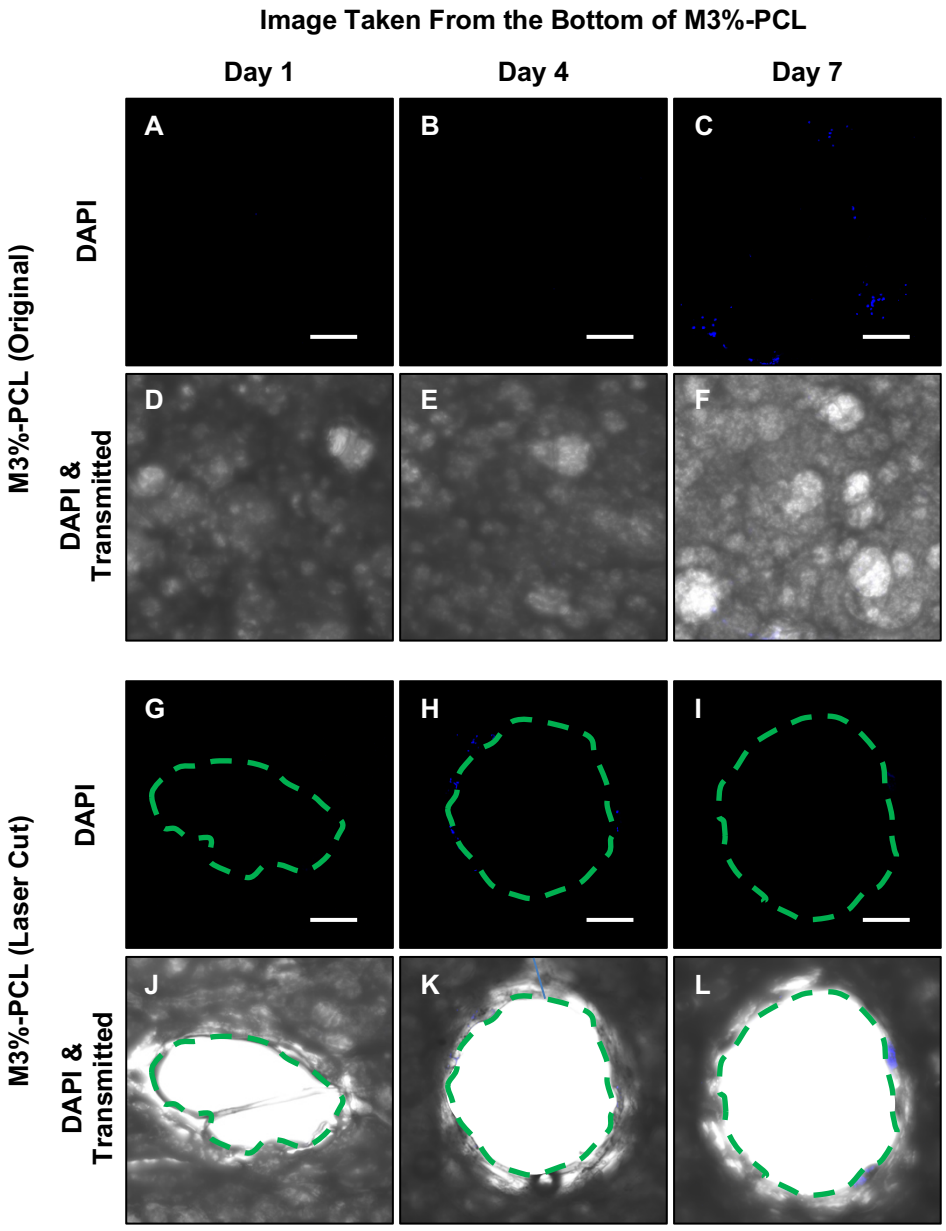

Figure 6.18: Prevention of MSC migration though M3%-PCL using a modified transwell assay to test barrier function, imaging from the bottom of the membrane. Confocal microscopy images of DAPI stained membrane:MSC constructs, imaged from the 'bottom', to ascertain whether MSCs were able to migrate through the membrane or laser cut holes. DAPI images and DAPI merge with transmitted light imaging of the underlying membrane. Three time points were taken over a week. **A-F)** The original M3%-PCL and **G-L)** M3%-PCL with laser cut holes, as a positive control for MSC migration. Images taken at x10, scale bar represents 100 μm. Green dash line to show the outline of the laser cut hole.

showed evidence of DAPI staining surrounding the edge of the laser cut hole at day 7 (Figure 6.18I&L).

Again, M6%-CP70:30 showed cellular attachment and proliferation on the top side of the membrane over the course of a week (Figure 6.19A-F), the laser cut membranes showed lower cellular attachment visually near to the hole, as with M3%-PCL (Figure 6.19G-L). With respect to imaging from the bottom of the membrane there was evidence of DAPI staining in both experimental conditions (Figure 6.20). However, as found with previous imaging of M6%-CP70:30 (Figure 6.13), there were areas of positive DAPI staining that did not appear morphologically as nuclei, thus were assumed to be nucleus fragments.

To conclude, both membranes showed evidence of cellular attachment and proliferation onto the top side of the membranes, however, cellular attachment appeared lower when in close proximity to the laser cut holes. In addition, for both membrane types and experimental conditions, evidence of periosteum MSCs was not found on the bottom side of the membrane. Where there was evidence of nuclei, it was on the edge of the laser cut hole. Therefore, it would appear that both membranes act as a barrier to periosteum MSC migration through the thickness of the material for up to a week, with or without the addition of laser cut holes to the membrane.

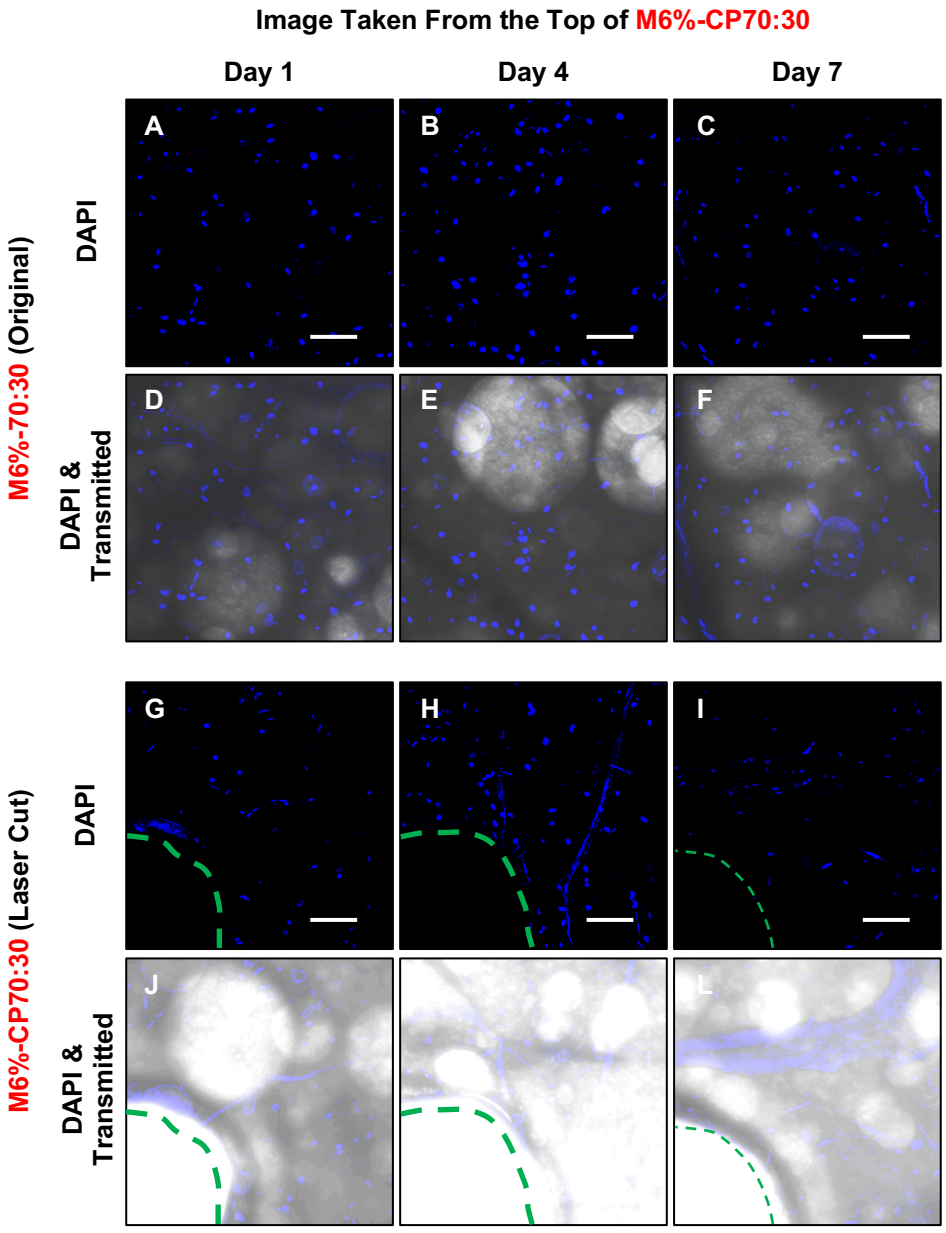

Figure 6.19: Prevention of MSC migration though M6%-CP70:30 using a modified transwell assay to test barrier function, imaging from the top of the membrane. Confocal microscopy images of DAPI stained membrane:MSC constructs, imaged from the 'top', where the MSCs were seeded onto. DAPI images and DAPI merge with transmitted light imaging of the underlying membrane. Three time points were taken over a week. **A-F)** The original M6%-CP70:30 and **G-L)** M6%-CP70:30 with laser cut holes, as a positive control for MSC migration. Images taken at x20, scale bar represents 100 µm. Green dash line to show the outline of the laser cut hole.

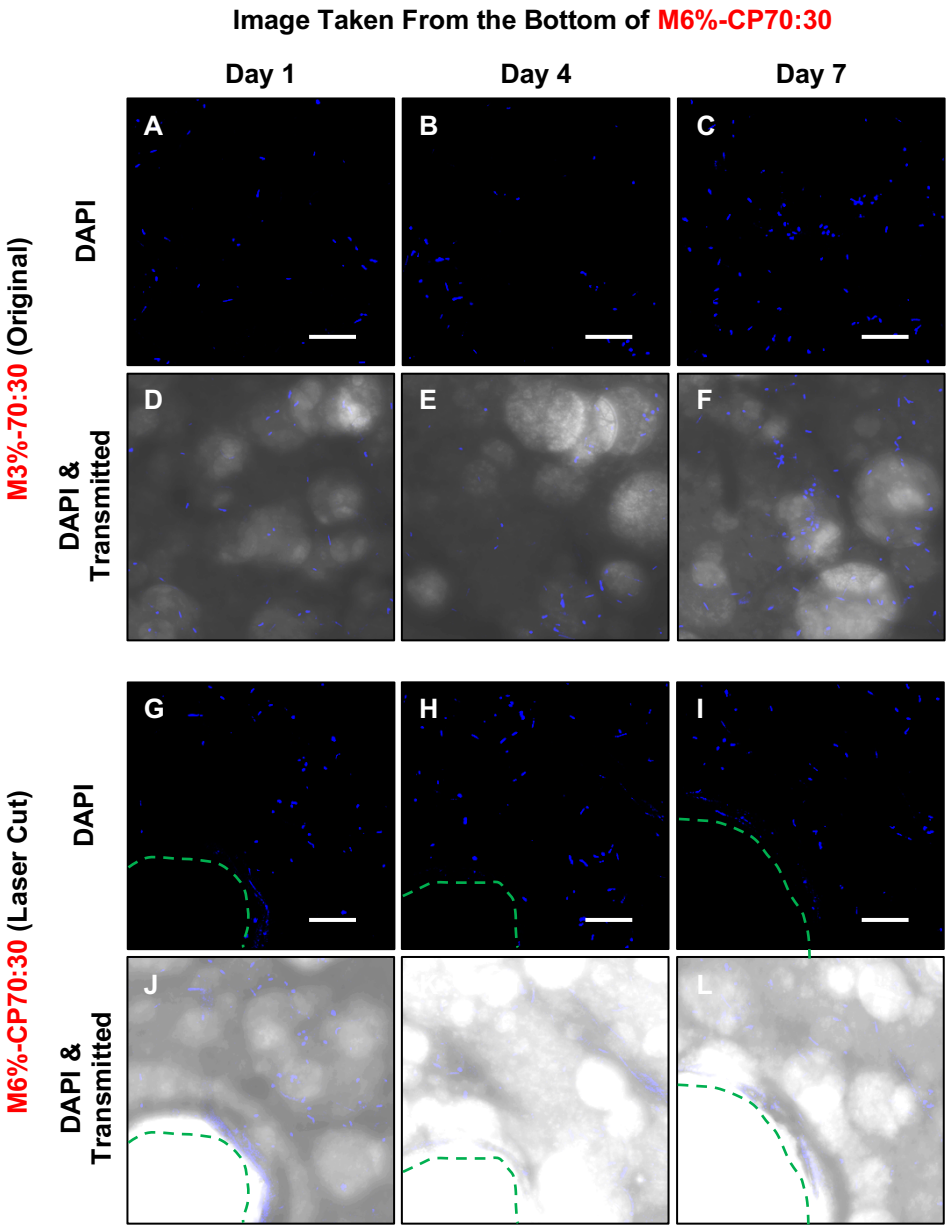

Figure 6.20: Prevention of MSC migration though M6%-CP70:30 using a modified transwell assay to test barrier function, imaging from the bottom of the membrane. Confocal microscopy images of DAPI stained membrane:MSC constructs, imaged from the 'bottom', to ascertain whether MSCs were able to migrate through the membrane or laser cut holes. DAPI images and DAPI merge with transmitted light imaging of the underlying membrane. Three time points were taken over a week. **A-F)** The original M6%-CP70:30 and **G-L)** M6%-CP70:30 with laser cut holes, as a positive control for MSC migration. Images taken at x20, scale bar represents 100 µm. Green dash line to show the outline of the laser cut hole.

6.4 Discussion

Investigation into cellular interactions with membranes suited to CSBD repair has so far revolved around BM MSCs or osteoblast cell lines. This provided a niche in the surrounding research to compare and contrast the cellular interactions and proliferation patterns of donor matched patient samples of periosteum and BM MSCs with the novel manufacturing process of the free surface electrospun membranes developed in Chapter 5. In addition, current assessments of the 'barrier' functionality of membranes have been rudimentary thus far, so a functional assessment into the barrier to cell migration of said membranes was carried out *in vitro*. Furthermore, an emerging live cell imaging technology, phase holographic imaging, was utilised to compare cell morphology, migration and proliferation patterns of donor matched periosteum and BM MSCs to gain further insight into the differences in colony formation as shown discovered in Chapter 4. Furthermore, this data was used to see whether or not it could predict MSC behaviour on 3D surfaces, the free surface electrospun membranes.

6.4.1 Live Cell Imaging of Periosteum and Bone Marrow MSCs

The use of live cell imaging (phase holographic imaging) allowed for a deeper insight into the hour by hour changes to MSCs during *in vitro* culture. Previous perceptions of MSC morphology have been developed from 'static' snapshots of *in vitro* cultures using time point microscopy. Which provides information on morphology only at the time of imaging. However, live cell imaging has revealed the variability in not only cell morphology, but cell migration patterns.

When comparing 'NP' with P0 cultures of periosteum derived cells, which were imaged for 25 hours on day 5 and day 18 in culture, respectively, the 'NP' cells were shown to be thicker, with a higher surface area. This is suggestive that time in culture results in reduced cell size, which is supported in part by Kawase et al. (2016), who showed a large reduction in periosteum derived cell (>passage 2) thickness (approximate 0.7 μm vs 0.1 μm) and a maintenance of cell surface area. However, this data is of the whole culture population, as opposed to this chapter which splits cells based on morphological differences (dividing, flat and spindle). Thus, the trends seen in

Kawase et al. (2016), would be confounded by the 'dividing cell' within the cell population that show increased cell thickness and reduced cell surface area. Despite this difference in approaches of analysis, the results are comparable.

When looking at the cells as a whole population there were no differences seen between the two periosteum culture types (NP and P0), with respect to cell migration patterns. This indicates that over the first two weeks in culture (as in CFU-F assays, Chapter 4) migratory behaviours do not change with time at a similar cell confluence. Therefore, early passage cultures (for periosteum) can be taken as a surrogate to indicate native periosteum MSC behaviour.

The influence of the effect of confluence on cell morphology and cell migration was not investigated. Future work would aim to compare 'low confluence' areas of cultures as in this Chapter to 'higher confluence', which would be more representative of the central areas of growing colonies. It has already been shown over 24 hours, that as MSCs proliferate or migrate in the field of view cell migration plateaus and cell directness becomes more random. Therefore, with higher levels of confluence, this trend is expected to be more apparent, which would show how cells behave at the start of colony formation compared to an established colony. However, it should be noted that cell tracking becomes more difficult with increased confluence as it is harder to distinguish between individual cells. In addition, as little difference was seen between the early cultures of periosteum cells, future work would look at comparing these cultures to a much later passage (e.g. >passage 5) to see if this is sustained in culture. This is particularly relevant as BM MSC proliferation rates are shown to considerably reduce beyond P0.

In addition, proliferation rates of MSCs are thought be to affected by contact inhibition, whereby the presence of MSCs nearby inhibits proliferation (Fossett & Khan 2012), which could factor in the reduced size of colonies seen with periosteal CFU-F plates within Chapter 4. Therefore, another future direction would be to investigate the influence of confluence on the incidence of cell division. The HoloMonitor software creates a cell division hierarchy when cell tracking, allowing for cells to be tracked immediately post cell division, again

opening up the possibility to track whether cell migration speed depends on the individual cell's maturity.

As a whole population, BM MSCs (P0 comparison) were significantly more migratory, shown through increased cell motility, in comparison to periosteum MSCs. This was surprising as it was predicted that the larger BM CFU-F colonies were formed due to BM MSCs being less migratory than periosteum MSCs, with a preference to stay static and proliferate. Interestingly MSC migration is known to be negatively influenced by cell adhesion (Qu 2019). Anecdotally, periosteum MSCs were found to be more adhesive than BM MSCs to tissue culture plastic, which made trypsinisation (0.05%) difficult, therefore the trypsin level was increased to 0.01%. This is suggestive that periosteum MSCs migration could have been impeded by the increased adhesion to the underlying tissue culture plastic, however, this is just speculative and would need to be investigated in more detail.

Mean cell migration was used to split apart the cell populations into 'migratory' and 'non migratory' cells (</> 100 µm mean migration), to show the variation in cell migration in a field of view. This again showed that the BM migratory cells were more motile than their periosteum counterparts, shown through increased velocity. However, it should be noted that the migratory cells of P0 periosteum made up a larger percentage of the overall population (58%) compared to P0 BM (37%). This is suggestive that even though the 'migratory cells' within periosteum migrate over a smaller distance and at a slower speed (20 µm/h, compared to 32 µm /hr (BM)), there was a greater proportion of 'migratory cells', in comparison to BM. This is the first time that the speed at which periosteum MSCs migrate at has been quantified, however, Kallifatidis et al. (2008) reports human BM MSC migration speed at 15 µm/h, approximately half the speed of the donor quantified in this Chapter.

The distinct differences in colony formation shown in Chapter 4 showed that periosteum forms a smaller and more homogenous in size colonies, opposed to BM which are much larger and heterogenous. Up to P0, both MSC types showed a similar time per PD (Figure 4.2), however, going forward into long term *in vitro* culture, BM MSC proliferation rate slowed in comparison to periosteum. Therefore, when looking at early *in vitro* growth of cells, MSCs

from both tissue sources proliferate at a similar rate as a whole population. However, BM MSCs appear more heterogenous, with respect to colony formation and have been shown to have a subpopulation of cells that are more migratory than those in periosteum. Future work in linking migration to effects on proliferation rate is needed to complete picture.

Currently, mean cell migration was split to </> 100 μm, however to ascertain the true heterogeneity of MSC migration, this could be separated further into <50 μm, 50-100, 100-150 and >150 μm. This would reveal more distinct migration patterns, where the two extremes (<50 μm and >150 μm) would be of particular interest. Here it is predicted that highly migratory cells (>150 μm) would migrate in a more exaggerated way than shown in this Chapter, with more 'purpose' or higher directness in comparison to the non-migratory cells (<50 μm). This could also be used to investigate whether migration is linked to proliferation.

Due to time constraints and the length of this thesis, investigation into the full extent of the Holographic imaging data was not able to be explored. However, a good basis of analysis has been carried out which has formed the guidelines for further work in this area. As previously mentioned a main area to investigate would be the influence increasing confluence on cell morphology, proliferation and migratory patterns. This is particularly important when assessing colony formation, colonisation of a tissue culture flask or biomaterial as MSCs will have low confluence at the beginning and then proliferate, thus increasing confluence. With respect to CFU-F colony formation there is a particularly stark difference in confluence from the centre of a colony to the colony edge, to the areas in between individual colonies. As colonies are round and have a central point, it is clear that there is some directional cell migration away from the colony centre to the less confluent areas.

The main limitations to this body of work have been that data on uncultured (NP) BM MSCs was not possible and that only one donor has been assessed. In addition, not all parameters were able to be assessed due to time constraints. There are approximately 40 individual output parameters that are quantified, so the real power of this data has not been fully explored. A limited number of parameters were investigated based on their link to cell morphology

and migration. The results using cell motility and therefore cell velocity showed the most exciting results, with respect to BM MSCs covering more ground at a faster speed however, this does not mean that cell migration has no importance, as its use comes in the form of being a bench mark for splitting cells into migratory and non-migratory fractions.

To come full circle, the implication of this data on predicting how MSCs will interact with the developed free surface electrospun membranes was considered. Petecchia, Usai, et al. (2017) used holographic imaging to investigate differences in MSC growth onto treated glass as well as on a coating of TiO_2. Here, the TiO_2 coating was shown to be favourable as the cells were larger, which they attributed to favourable cell adhesion due to cell spreading (Petecchia, Usai, et al. 2017). Based purely on the Holographic imaging results, it could be predicted that BM MSCs would migrate on the membranes more than periosteum MSCs, however as proliferation rates were not investigated a prediction on populating of the free surface electrospun membranes cannot be made. In addition, passage 3 MSCs were used during cell attachment assays on the free surface electrospun membranes, which have been subjected to more time *in vitro*, thus proliferation data from Chapter 4 may provide a more likely predictor. Herein, periosteum MSCs were shown to be more proliferative at this stage than BM MSCs.

However, there are multiple factors at play here, with not only the tissue source of MSC used, but the passage grown onto the material, density of cells in a certain area, as well as the underlying material itself. This Chapter has shown that periosteum MSCs grown onto two materials of apparent similar morphology (fibre diameter, alignment and pore size) show completely different cell morphologies. A more spread out cell shape could be seen on the collagen containing membrane, M6%-CP70:30 in comparison to the PCL control membrane, M3%-PCL, however, the influence of confluence could not be ruled out in having an effect due to the lower initial cell attachment seen on M6%-CP70:30. In agreement with this was work carried out by Tejeda-Montes et al. (2014), whereby rat MSCs were grown onto various biomaterials with differing topographies, where cell morphology was affected by different

physical or biomolecular signals from the underlying biomaterials, designed to influence MSC adhesion and/or mineralisation.

6.4.2 MSC Growth onto M6%-CP70:30 and M3%-PCL

It has been shown that both periosteum and BM MSCs are able to attach and proliferate onto M3%-PCL and periosteum MSCs onto M6%-CP70:30, albeit to differing degrees. Initial attachment (day 4) of periosteum MSCs and BM MSCs onto M3%-PCL was shown to be similar at both cell densities. Clear proliferation of both MSC types was seen on M3%-PCL, BM MSC showed higher proliferation at the low cell density by day 28, however, periosteum MSC was significantly more proliferative from day 7 to day 28 at the higher cell density. Thus, M3%-PCL is supportive of the two main MSC types that the membrane would come into contact with *in vivo*. In contrast, M6%-CP70:30 showed significantly reduced cell attachment of periosteum MSCs at both cell densities, when compared to M3%-PCL. As a result, proliferation onto M6%-CP70:30 was not as high as that of M3%-PCL. This was unexpected as the addition of collagen to the free surface electrospun membrane was hypothesised to enhance MSC attachment and proliferation.

In a similar study, PCL and collagen-PCL (70:30 ratio as in Chapter 5) electrospun membranes were shown to be favourable materials for mouse osteoblast adhesion and proliferation, whereby the collagen-PCL membrane was potentially more favourable for initial attachment and proliferation (Ren et al. 2017). Rabbit BM MSCs were grown onto a PLLA and collagen bilayer electrospun membrane interestingly, favourable cellular attachment and spreading was seen on PLLA in comparison to collagen, where only a few cells were able to be imaged (Cai et al. 2010). Chong et al. (2007) developed a Gelatin-PCL (50:50 ratio) electrospun membrane, which supported fibroblast growth onto it *in vitro*, however, comparisons were not made to a PCL membrane, therefore differences in attachment and growth could not be concluded.

It is known that substrate stiffness (elastic modulus) as well as the substrate itself can effect cellular behaviour (Trappmann et al. 2012), the M6%-CP70:30 not only contained collagen but was also significantly stiffer compared to

M3%-PCL (16.5 MPa compared to 4.8 MPa). However, human MSCs have been shown to respond to increased stiffness (0.5 kPa to 115 kPa) with increased ‘adhesive cell area’, however this response was not seen when using a different material with increasing stiffness (0.1 kPa to 800 kPa), suggestive that MSC response to stiffness or underlying material is not uniform (Trappmann et al. 2012). With respect to cell surface area, periosteum MSCs were shown to be more ‘spread’ when grown onto M6%-CP70:30 than when compared to a more spindle or elongated morphology onto M3%-PCL. Future work could include quantifying cell surface area to confirm this, however, a low density of cells in the field of view would be needed to be able to identify individual cells.

Phipps et al. (2011) compared electrospun PCL membranes to PCL-Collagen-HA membranes and collagen only membrane. Here, little cellular attachment was seen on the collagen membrane, whereas PCL and PCL-Collagen-HA membranes supported BM MSCs, with proliferation onto PCL-Collagen-HA being significantly higher. To ascertain the reason behind the poor cellular attachment of the collagen membrane, the membrane was incubated with culture media for 24 hours to produce ‘conditioned media’. MSCs were grown onto PCL using the conditioned media and improvements to cellular attachment and spreading were shown, suggestive that the soluble factors released from the collagen membrane were not an impediment to cellular interactions with the PCL scaffold (Phipps et al. 2011).

As with the aforementioned study, crosslinking of the collagen within the membrane was not carried out, therefore, as shown in Chapter 5, collagen is known to solubilise and be released from M6%-CP70:30 when hydrated. In particular 50% of the membrane’s collagen content is solubilised within the first 24 hours, during which cellular attachment is being carried out. Therefore, it could be hypothesised that this ‘burst’ release of collagen from M6%-CP70:30 impeded initial MSC attachment, future work would address this by incubating M6%-CP70:30 for up to 24 hours (this could be titrated) prior to MSC seeding to ascertain whether this has an effect. As seen in Phipps et al. (2011) conditioned media from incubation of M6%-CP70:30 could be used during an MSC attachment study onto M3%-PCL in order to prove whether

the soluble factors released from this membrane effect cellular attachment. Based on the outcomes of this work it may be prudent to investigate cross-linking collagen to reduce the 'burst' release (see Future Works, Section 7.4).

When imaging M6%-CP70:30 using confocal microscopy, there were 'flecks' of DAPI positivity that did not appear morphologically like a nuclei (oval shaped and larger) or to overlap with areas of actin filaments. These areas were not attributed to the inherent auto-fluorescence of M6%-CP70:30, as were not present on 'cell free' membranes post quenching. Therefore, these areas could be genuine DAPI staining; DAPI binds to adenine-thymine regions of DNA and fluoresces upon binding with DNA (Kubista, Aakerman & Norden 1987) and is not a 'live/dead' marker, so will fluoresce when bound to dead or dying cells. The source of collagen used in this study was in-house rat tail collagen, solubilised in 17.4 mM acetic acid (Bell, Ivarsson & Merrill 1979; Tronci, Russell & Wood 2013). There were no steps taken during this process to remove or degrade the cellular content of the rat tail tendons. The area within rat tail tendons covered by cells has been shown to reduce with age from 40% (5 days) to 2% (6 months) (Craig et al. 1989). Therefore, future experiments should confirm whether there is a certain level of DNA within the collagen source in addition to the inclusion of a live/dead cell marker to investigate if the DNA fragments could be from apoptotic MSCs. However, when culturing MSCs *in vitro*, cell death results in the cell debris floating, so the assumption could be made that if there were dead MSCs following attachment to M6%-CP70:30, they would be detached from the membrane and be washed off as part of the staining regime. Furthermore, the use of atelocollagen or GMP grade collagen, which would not contain DNA fragments could mitigate this issue (Tronci et al. 2016; Liang et al. 2018).

It should be noted that the seeding density used in this Chapter was 1-2 log fold smaller than that of all the comparative literature, the cell densities used were 2.5 x 10^2 cells per cm^2 or 2.5 x 10^3 cells per cm^2, compared to 1-2.8 x 10^4 cells per cm^2 (Cai et al. 2010; Phipps et al. 2011; Ji et al. 2013; Ren et al. 2017). This is important for the future clinical uses of these membranes, as the next step would be to investigate the interactions of 'clinical' sources of MSCs, that come in the form of BMA or ex-plant periosteum tissue. Therefore,

developing a membrane that supports cellular attachment and proliferation at low cell seeding densities is of utmost importance due to the known lower frequency of MSCs in BMA or ex-plant periosteal tissue, shown in Chapter 4.

6.4.2.1 MSC Alignment onto M3%-PCL and M6%-CP70:30

It was unexpected to find periosteum and BM MSC alignment onto M3%-PCL as the current literature has pointed towards alignment being driven by fibre alignment or the formation of longitudinal grooves, as seen by Stachewicz et al. (2015) and Shi et al. (2014), respectively. The potential importance of cellular alignment with respect to periosteum regeneration has been discussed previously, where it has been shown that collagen fibres as well as cells within the periosteum align along the longitudinal axis of the bone (Foolen et al. 2008; Shi et al. 2014). Therefore, the significance of M3%-PCL providing both periosteum and BM MSCs with the support to align, without the underlying fibres being aligned themselves, should not be understated. It was first thought that the alignment seen at the higher cell density (2.5×10^3 cells per cm^2) could be due to the increasing cell confluency seen by both MSC types proliferating quickly. As a result, the cell density was lowered 1 log fold to see if the compact nature of the MSCs was causing alignment to occur. Here it was shown that BM MSC alignment was influenced by cell seeding density, but periosteum MSC alignment was ‘slowed down’ but by day 28 showed comparable alignment to the higher seeding density.

Upon closer inspection of confocal imaging from similar randomly aligned electrospun membranes from the literature, there is potential evidence of MSC or osteoblast alignment, seen through similar alignment of actin fibres that was shown in this Chapter. However, none of the articles have quantified, drawn conclusions or even commented on this (Wang et al. 2011; Phipps et al. 2011; Caballero et al. 2014; Gong et al. 2019). Thus, this Chapter has shown a novel insight into the differing interactions of two sources of MSCs with underlying substrates that has previously not been discussed.

M6%-CP70:30 has been shown to support periosteum MSC attachment and proliferation, preferentially at a higher seeding density, the morphology on said membrane was clearly more spread out than that of M3%-PCL. However,

there is room for improvement of this membrane with respect to cellular attachment that future work would aim to address. In contrast, M3%-PCL clearly supports periosteum and BM MSC attachment and proliferation, to a greater extent than M6%-CP70:30 (with respect to periosteum MSCs). Clear alignment of both MSC types was shown and MSC spreading was not as pronounced as on M6%-CP70:30. The importance or consequences of the difference in cell spreading between the two developed membranes has yet to be ascertained, future work into potential gene expression differences as well as influences on osteogenic differentiation potential is needed.

Limitations to this work include the lack of testing of BM MSCs with M6%-CP70:30, due to time constraints this was not investigated. Also, cell attachment assays were only carried out using one donor, ideally this would be repeated using multiple donors to confirm that trends in attachment and proliferation are not confined to this donor.

6.4.3 Functional Barrier Membrane Testing

As discussed in Section 6.1.3, the current testing of the ‘barrier’ function of membranes has revolved around assumptions made on fibre diameter or pore size. This was carried out in Chapter 5, showing a particularly small mean pore size of 1.4 µm and 0.4 µm for M3%-PCL and M6%-CP70:30 respectively. Some studies have ultilised confocal imaging to image cell penetration into materials. This Chapter developed a novel assay to functionally test the free surface electrospun membrane’s ability to provide a block to cell migration. By creating a serum gradient across the membranes this formed a ‘cue’ for periosteum MSCs to migrate towards the serum containing media at the bottom of the well, therefore forcing the MSC to attempt to migrate through the membrane or in the case of the positive controls, the laser cut holes.

It was shown that periosteum MSC attachment was lower surrounding the laser cut holes for the positive control in comparison to the original membranes, this was unexpected, however could be attributed to the size of the holes or the melted edges of the holes. At approximately 280 µm (M6%-CP70:30) and 500 µm (M3%-PCL), there could have been fluid flow through the laser cut hole, from the top of the membrane to the media at the bottom of

the well or vice versa. However, as this assay was set up in ‘static’ culture conditions, once the plate was placed in the incubator there would be little to no fluid disturbance during cellular attachment, as in the previously discussed cell attachment assay. Despite this, there was no evidence of cellular presence on the bottom of either of the membranes; the DAPI staining on the bottom of M6%-CP70:30 was attributed to cellular debris as previously described due to staining morphology.

Unfortunately, because the positive control membranes, with laser cut holes, did not show evidence of cellular attachment to the bottom of the membranes, future work would need to be carried out to optimise this assay to have true evidence of experimental conditions in which periosteum MSCs will be able to migrate through a ‘hole’ or pore made in the membranes. The reasons for the positive control not working as was hoped could be due to the size of the pore itself, being too big to encourage cellular migration or that the serum gradient was not maintained due to this, resulting in there being no ‘stimuli’ to drive migration to the bottom of the membranes. MSC migration has been investigated using Transwell migration inserts, with 8 μm diameter pores (Ponte et al. 2007), which is known to maintain a gradient, either due to the reduced pore size or the barrier created by the polymer it is formed from, opposed to the permeable free surface electrospun membranes. Therefore, future work to form smaller holes in the membranes is needed.

This assay is an attempt to drive cell migration through the free surface electrospun membranes, where previous studies have grown cells on top of a membrane, but not provided a stimulus to drive migration, as detailed in Section 6.1.3 (Ekaputra et al. 2011; Vaquette & Cooper-White 2011; Phipps et al. 2012). Future work would aim to investigate how the free surface electrospun membranes, and the laser cut membranes, act as a ‘filter’. This is of importance for two reasons, firstly to address the issue of estimating how long the serum gradient is maintained during the barrier function assay. The second reason is to assess whether nutrients or proteins can pass through the membrane. This is of particular importance as the membrane should act as a barrier to cellular migration or infiltration, however, the blockage of fluid or nutrient transfer could be detrimental during bone repair.

6.5 Conclusions

Live cell imaging of early *in vitro* culture of periosteum and BM MSCs showed how heterogenous MSC morphology is over a 25 hour period, which has been previously unseen. Distinct differences were seen in migration patterns of BM MSCs, which were shown to be more motile and migratory than periosteum MSCs. However, this information on migration of MSCs was not a predictor to MSC interactions onto the free surface electrospun membranes, future investigation into proliferation behaviours is needed for this.

The cellular attachment and proliferation of MSCs was shown to be improved through the use of M3%-PCL, compared to M6%-CP70:30. However, future work is needed to ascertain whether potential xenogenic DNA content from the rat tail collagen or the known release of collagen from the membrane could drive this. Periosteum MSCs have been shown to align on M3%-PCL with ease at low and high seeding densities, whereas BM MSC takes longer to align and preferentially at a higher seeding density. A novel ‘barrier function’ assay has been developed, showing that both membranes act as a barrier to cellular penetration and infiltration. However, further work is needed to generate smaller holes, to maintain a serum gradient for this assay.

Chapter 7: General Discussion

7.1 Summary of Research

The aim of this study was to investigate periosteum as a source of MSCs to be utilised during CSBD repair in comparison to the current gold standard MSC source, BM. In addition, the production of a biodegradable membrane, to wrap around a bone defect to act as a barrier to cellular infiltration and support periosteal regrowth during CSBD repair. The following section will summarise the findings of this thesis that have been discussed in detail in Chapter's 3-6. Subsequent sections will look to deliberate whether this thesis has managed to answer the main questions it set out to; firstly, if periosteum is a preferable MSC source to BM and secondly, based on the product specification set out in Chapter 5 (Figure 5.1), was a biodegradable barrier membrane appropriate for CSBD repair developed? Finally, a summary of future works and reflection on the project will be presented.

The histological architecture of porcine and rare samples of human periosteum were investigated (Chapter 3), whereby human periosteum was more vascular, with blood vessels of larger diameter than porcine. Porcine periosteum was chosen as the animal to model human periosteum, due to the proven use of *in vivo* porcine models for bone regeneration and CSBD repair models (McGovern, Griffin & Hutmacher 2018). Periosteum was shown to mainly consist of collagen, in line with current literature (Evans, Chang & Knothe Tate 2013; Evans et al. 2013). However, minimal evidence of elastin content was found in adult human periosteum, in contrast to the generalised known description of periosteum based on canine palate periosteum elastin content (Squier, Ghoneim & Kremenak 1990). Human periosteum samples were often harvested without the presence of the cambium layer, despite this MSC candidate CD271 staining was also found in the fibrous layer, suggestive that the cambium layer did not need to be intact to harvest MSCs.

In line with recent literature, MSCs were collagenase digested from 'clinically relevant' samples of human periosteum (Cuthbert et al. 2013) and compared to donor matched BM MSCs (Chapter 4). Periosteum MSCs were found at a significantly higher percentage and formed significantly smaller, homogenous

in size colonies and proliferate at a faster rate after the first passage *in vitro* when compared to donor matched BM MSCs. Expression of SUSD2 (Sivasubramaniyan et al. 2013) and MSCA-1 (Sobiesiak et al. 2010) was variable on periosteum and BM MSCs, however CD146 expression was negative on periosteum MSCs, in line with findings of Sacchetti et al. (2007), but CD146 expression was variable on BM MSCs (Tormin et al. 2011; Churchman et al. 2017), thus a differential marker was not found.

Osteogenic and chondrogenic differentiation potential was found to be similar between the two MSC types, however, subjectable to donor variance. However, adipogenic differentiation was found to be significantly reduced in periosteum MSCs, potentially linked to a failure to induce upregulated PPAR-γ gene expression (Rosen et al. 2012), which is a key molecule responsible for initiating the cascade for adipocyte differentiation.

A novel cell imaging technique (phase holographic imaging) was used to live cell image and track periosteum and BM MSCs over a period of 25 hours. A snapshot of periosteal cultures after 4 days (NP) and 18 days (P0) in culture showed no differences in migratory patterns of the cells, however, the percentage of dividing cells reduced for P0 cultures. This was to be expected and consistent with the literature on the reduction in the proportions of highly-proliferative cells with increased time in culture (Churchman et al. 2017). In contrast, when comparing P0 cells from periosteum and BM, BM MSCs were shown to be significantly more migratory and motile.

Two free surface electrospun membranes have been produced, one consisting of PCL (M3%-PCL) and the other of collagen and PCL (M6%-CP70:30). Both membranes were shown to have similar morphologies, however, the pore sizes of M6%-CP70:30 were significantly smaller at 0.4 μm verses 1.4 μm (M3%-PCL). Both are considerably smaller than estimated MSC size (prior to culture) of 10 μm (Tormin et al. 2011) indicating that a barrier membrane was produced (Chapter 5). A ‘burst’ release of collagen from M6%-CP70:30, following 24 hour PBS incubation, was shown and the process of electrospinning and contact with HFIP resulted in degradation of the collagen helical structure. The early release of collagen could have affected periosteal MSC attachment, which was shown to be significantly

lower than with M3%-PCL. Periosteum MSCs attach, proliferate and align onto M3%-PCL, irrespective of seeding density, however BM MSCs showed increased alignment with increased seeding density. M6%-CP70:30 did not provide a surface for periosteum MSC alignment, however, cell morphology was distinctly more spread out compared to on M3%-PCL, this could be result of the presence of collagen or the increased space on the membrane for cell spreading due to reduced cellular attachment and proliferation.

The barrier function of the free surface electrospun membrane was partly assumed based on the membrane's small pore size, mentioned above. A novel assay to functionally test the ability of the membranes to act as a barrier to cell migration was carried out, where periosteum MSCs were shown to favour remaining on the top side of the material, which they were seeded onto rather than migrate through the material or laser cut holes. However, in the case of laser cut pores, which were relatively large, this could be due to the serum gradient not being maintained to create a 'driver' of migration or due to the nature of the laser cut holes not being conducive to cell migration. Regardless of this, spontaneous migration through the membranes was not seen confirming that both M3%-PCL and M6%-CP70:30 function as barrier membranes.

7.2 Is Periosteum Preferable to Bone Marrow as an MSC Source?

To conclude whether periosteum is preferable to BM as a source of MSCs for CSBD repair is a complicated and nuanced discussion. Both sources were investigated as they are easily accessible from the surgical field (periosteum) or an established addition procedure carried out during current CSBD repair (P. Hernigou et al. 2014), whereas the use of lipoaspirates would not only require an additional incision but also additional surgical training. Performance of MSCs during *in vitro* experiments for MSC enumeration, proliferation and differentiation capacities must be compared as the first step in the development of novel bone reconstruction procedures based on minimally-manipulated cells.

For the first time, this thesis was able to obtain donor matched samples of ‘clinically relevant’ human periosteum and iliac crest BMA, donated from patients undergoing orthopaedic surgery. As a result, *in vitro* donor matched comparisons of the two ‘clinically relevant’ sources of MSCs were able to be carried out. It was shown that despite these samples often not containing the osteogenically important cambium layer, 2% of all cells, liberated during a collagenase digest, were MSCs. Therefore, showing that harvesting using a scalpel, opposed to a periosteal elevator (Brownlow et al. 2000), although not achieving perfect periosteum removal, still provides a tissue sample highly rich in MSCs. This is in contrast to BMA, which showed 4 log fold lower MSC concentration in relation to total cell count, which was particularly variable in MSC quantity, known to be effected by aspiration technique (Cuthbert et al. 2012).

Periosteum and BM MSCs showed similar proliferation rates during early *in vitro* culture (<P0), however, periosteum MSCs were shown to be more proliferative (based on PD rates) at later passages. BM MSCs grown for less than 3 weeks *in vitro* were shown to be more migratory than donor matched periosteum MSCs. However, periosteum MSCs populated M3%-PCL at a significantly higher rate, cell alignment was more pronounced, and at an earlier stage in comparison to BM MSCs. Both MSC types showed similar cell phenotypes and had variable outcomes during osteogenic and chondrogenic differentiation assays, in contrast periosteum MSCs showed significantly lower adipogenic potential, which could be attributed to not all periosteal progenitors having a ‘trilineage’ function (Stich et al. 2017).

This confirms the potential variance of the MSC sources (De Bari et al. 2008) and points to their differing importance for bone regeneration, whereby periosteum could be considered as a more proliferative MSC source, with lower adipogenic potential, but BM as a more migratory, with higher adipogenic potential, source. It may be this reason that both sources, in conjunction with endosteal MSCs are recruited and required for uneventful fracture healing (Mercurio et al. 2012).

To conclude based on the data that this thesis has produced, it is inconclusive which MSC source can be considered to be preferable. It was hypothesised

that in comparison to donor matched bone marrow MSCs, periosteum derived MSCs would be found at significantly higher levels, be more proliferative, migratory, osteogenic and chondrogenic. However, it has only been proven that periosteum MSCs are found at higher levels and more proliferative (after P4), but show similar osteogenic and chondrogenic capacity, are less migratory (from one donor) and show a tendency to align spontaneously on a polymer based biomaterial. Conversely, bone marrow MSCs were shown to have greater adipogenic capacity, form larger and heterogenous colonies and migrate more at higher speeds.

To take the discussion forward to how periosteum can realistically be used during surgery in the future, there are two main drawbacks of its use in comparison to BMA. Firstly, the surgeon would be limited by the size of periosteum sample that could be harvested; typical weights harvested in this thesis were 0.1-0.5g, equating to approximately 0.25 cm^3 (0.5 x 0.5 x 1 cm) size piece of tissue. Larger sized periosteum samples or multiple samples risk damage to the underlying bone, however, due to the apparent high numbers of MSCs in these samples, this might not be necessary. This is where the main advantage of BMA lies, surgeons can either aspirate large volumes of BMA (up to 60 mL), followed by centrifugation to concentrate MSC numbers (BMAC) (El-Jawhari et al. 2017) or take multiple small volume draws from different areas to prevent dilution of BMA in peripheral blood (De Filippo et al. 2019; Hernigou et al. 2013; J. Hernigou et al. 2014; Cuthbert et al. 2012). Here, it has been found that the development of specific aspiration techniques can provide an enriched MSC population (De Filippo et al. 2019), thus allowing for ‘clinically relevant’ numbers of MSCs to be harvested for use in surgery.

The second drawback to periosteum is the ‘form’ that it is in, this thesis used collagenase digest to liberate MSCs from the tissue, which would not be an appropriate technique for use in orthopaedic surgery, as this is considered to be ‘more than minimally manipulated’ (Gee 2018). Again, this shows an advantage of BMA over periosteum, which as a liquid is easy to maintain sterility within blood tubes or syringes as well as being able to saturate absorbent collagen based scaffolds, mix with autograft or hard bone scaffolds (El-Jawhari et al. 2016; Kouroupis et al. 2013). Thus, the current *in vitro*

method to circumvent this for periosteum samples would be to macerate the tissue into small pieces and allow for MSC outgrowth from this. Although, compared to the collagenase-based release method, this will take time and it is unlikely that cells from the centre of the tissue would be able migrate out (Uematsu et al. 2013). However, this is unlikely to be the case *in vivo*, as locally-available collagenase enzymes may enable some considerable 'loosening' of the extracellular matrix within the tissue fragments thus allowing an easier liberation and egress of periosteal MSCs for the scaffold's colonisation.

As this thesis showed, BMA is not perfect and is a highly variable source of MSCs for bone regeneration, but significant research, as discussed above, has been put into improving aspiration technique and uses of it during surgery, therefore, logically the same is needed to take periosteum forward as an appropriate supply of MSCs in the future. As mentioned, an ability of periosteal MSCs to colonise and align on biocompatible membranes used as 'barriers' and graft containment devices, as shown in this thesis, may represent an important key characteristic in favour of periosteal tissue as a source of MSCs in complex bone reconstruction procedures.

It is proposed that the main hurdle to overcome for periosteum samples' use in surgery is that it is not a liquid, like BMA. The future aims of this project would work towards the utilisation of MSCs within the surgical theatre, with 'minimal manipulation', allowing for shorter regulatory routes. This can be achieved using tissue processing devices based on mechanical tissue disaggregation. For example, an Italian company (Human Brain Wave) has developed a machine that could do this, the Rigenera®, that finely macerates soft tissue, using 600 single use blades, like skin biopsies, adipose tissue and cartilage, and resuspends the liberated cell-containing micro-grafts in sterile saline for future intended use. As this is a purely mechanical manipulation method to disaggregate tissue, this would be considered equivalent to 'minimal manipulation', accepted by FDA standards (Gee 2018).

Recent papers have covered its successful use in humans through creating skin micro-grafts (from skin biopsies) for complex wound care (Giaccone et al. 2014; Marcarelli et al. 2017), cartilage micro-grafts (from ear skin and cartilage

biopsies) for knee chondral injuries and nasal valve collapse (Fernández & Luengo 2019; Ceccarelli et al. 2017). Of particular interest was the use of Rigenera® to obtain MSCs from adipose tissue, whereby cells were shown to be viable *in vitro*, proliferative and phenotypically similar to MSCs derived from the gold standard, enzymatically digested adipose tissue (De Francesco et al. 2018). In addition, utilisation of the Rigenera® protocol to dissociate MSCs from dental pulp or periodontal ligaments has been shown, whereby the micro-graft suspension was loaded onto a collagen sponge for the use in oral surgery (Graziano et al. 2013; Barbier et al. 2018). This is of particular interest to this thesis as ideally the 'micro-graft' solution would be combined with the developed free surface electrospun membranes or in conjunction with autograft as bone defect filler.

The aforementioned studies show the potential of the production of 'micro-grafts' in a saline suspension, through use of the Rigenera® protocol, from multiple soft tissue types to deliver viable cells, similar to that of cells derived from enzymatically digested tissue. Unfortunately, this avenue could not be investigated during this PhD, due to the multidisciplinary nature of the project, whereby the barrier membrane was also being developed concurrently. Therefore, investigation into efficiency of this new 'minimally manipulative' technique for MSC liberation from periosteum samples, in comparison to collagenase digest would be pertinent, where a simple comparative CFU-F assay could be carried out to compare MSC content. In addition, it should be investigated how the micro-grafts would be absorbed by, and populate the free surface electrospun membranes developed during this thesis.

As it stands, it cannot be definitively concluded from the work of this thesis that periosteum is a preferable MSC source to BMA as significantly increased osteogenic potential was not shown, merely equivalence, however, the converse is also true. Further work to compare BMA to periosteum 'micro-grafts' to simulate potential uses during surgery with respect to MSC quantification, native osteogenic potential and growth onto the developed free surface electrospun membranes is needed.

7.3 Development of a Biodegradable Barrier Membrane for CSBD Repair

The development of a barrier membrane for CSBD was clinically led to ensure the production of a material that suits not only the needs of the surgeons, but can also be upscaled for future commercialisation, as well as achieving the required 'biological functions'. The success of this endeavour has been summarised in Table 7.1, whereby whether the original product specification, set out in Table 5.1, has been achieved is specified, this will now be discussed.

Through taking a clinically led approach, the barrier membrane was developed with surgical scenario functionality in mind. Free surface electrospinning was not only utilised as the manufacturing procedure due to its potential for future upscale manufacturing, but as it also produces ample-sized nonwovens, that can be cut to the shape needed by the surgeon. This, allows for the production of a material than can be customisable in the surgical theatre based on CSBD size. In addition, the literature surrounding the use of free surface electrospinning for tissue engineering applications is under represented in comparison to needle based methods, thus adding an additional layer of novelty to the manufacturing process. The choice of PCL as a base scaffold was informed by its extensive use in tissue engineering applications as well as its well-described biodegradation profile *in vivo* (Woodruff & Hutmacher 2010). Similarly, collagen incorporation was considered from the outset, based on perceived cell homing capabilities and similarity to the *in vivo* structure of periosteum. Both membranes, have shown good handling capabilities and tensile strength, however differed with respect to interactions with liquids, whereby, M6%-CP70:30 was shown to be more 'absorbent' following water contact angle measurement.

It was defined by the clinical supervisor, that the membranes degradation profile should amount to approximately 12 weeks *in situ*, once implanted. This thesis did not directly quantify the degradation profile of the membranes, however, the materials, PCL and collagen, for the membranes were chosen based on their known degradation properties (Woodruff & Hutmacher 2010). Future work into ascertaining an *in vitro* and *in vivo* degradation profile would aim to ratify this, covered in Section 7.4.4.

Table 7.1: Assessment on whether the barrier membrane product specification (as set out in Figure 5.1) was achieved, and the future *in vitro* or *in vivo* improvements needed.

Specification	Currently Achieved	Future *in vitro* and *in vivo* Improvements
Clinical Functionality		
Surgical handling capability	Good tensile strength & easy to handle.	Further tensile testing on hydrated membranes. Develop and test thicker samples.
Customise size and shape	Customisable due to free surface electrospinning.	
Degradation profile (12 weeks)	In theory, through use of non-crosslinked collagen and biodegradable PCL.	Degradation work to be carried out, *in vitro* and *in vivo.*
Membrane Architecture		
Prevent soft tissue invasion	100 µm thick samples may be thick enough, similar to human P.	Upscale manufacture to bath solution to achieve thicker samples
Containment capability	MSCs unable to migrate through membrane. MSC growth onto the membranes possible.	Investigate interactions with grafting material, BMA & ex-plant P 'micro-grafts'
Bio-compatibility	Successful MSC growth, lower attachment on M6%-CP70:30	Improve M6%-CP70:30 attachment, could be due to collagen solubilisation or HFIP. Use of atelocollagen to circumvent issue
Cell Homing Capability		
Replicate Human Periosteum	Nonwoven fibre allows for MSC attachment, proliferation and alignment. Collagen, abundant in native P, can be incorporated (M6%-CP70:30). No bilayer, however might not be needed as single layer acts to cell home and blocks infiltration.	*In vivo* investigation is needed to monitor provisional tissue formation around the membrane, and subsequent tissue remodelling into a P-like structure.
Collagen Architecture	Collagen can be incorporated, but 50% of it solubilises out of membrane quickly.	Crosslinking of collagen or use of atelocollagen
Thickness (0.1-1 mm)	P thickness is variable so cannot match thickness, should depend on handling and barrier function.	Thicker samples can be obtained by folding or bath spinning, more collagen may be retained on thicker membranes (test *in vitro*).

Table 7.1 (continued):

Specification	Currently Achieved	Future *in vitro* and *in vivo* Improvements
Bilayer Functionality	Not achieved, but cambium hard to determine in older patients, and barrier achieved with one layer.	
Support Periosteum Regrowth	P MSC shown to migrate and proliferate on both membranes.	Improve M6%-CP70:30 attachment.

P – periosteum

When embarking on the development of a barrier membrane that would contain grafting material and MSCs to the defect site, whilst simultaneously blocking cellular infiltration from surrounding soft tissue, skeletal muscle, the negative connotations to this were also considered. Investigation into whether cells from skeletal muscle contribute to bone regeneration, and whether therefore 'blocking' access of said cells into the defect site could negatively affect bone repair was carried out.

Bone regeneration is impaired not only by compromised periosteum and bone, but also when the surrounding skeletal muscle is injured (Gustilo, Mendoza & Williams 1984; Reverte et al. 2011). *In vivo* animal models have shown that myogenic lineage cells are present in the fracture callus during open fracture, but not closed fractures (Liu et al. 2011) and when skeletal muscle is physically blocked from the fracture site, through the use of a PTFE barrier (non-porous), healing was impaired when the periosteum was stripped (Harry et al. 2008). This suggests that skeletal muscle can aid in bone regeneration in the case of open fracture or compromised periosteum, therefore, this notion should be not forgotten about when designing future *in vivo* studies for the use of the free surface barrier membranes. In addition, a systematic review has been carried out to ascertain whether there is a subset of cells resident in human skeletal muscle that showed the ISCT MSC phenotype and could contribute to bone healing (Owston, Giannoudis & Jones 2016). Evidence for resident cells conforming to the ISCT MSC phenotype (Dominici et al. 2006) that are capable of *in vivo* bone formation, however the full implications of blocking skeletal muscle is currently unknown.

However, there is *in vivo* evidence of porous barrier membranes aiding CSBD repair, suggestive that a porous membrane is needed (Cai et al. 2010). As a result of this it would have been prudent to know if the free surface electrospun membranes acted as a barrier to nutrient transfer, as discussed in Chapter 6, however time constraints prevented this. The MINUSHEET® tissue carriers would be utilised as in the barrier assay, however instead of a serum gradient across the membrane, a known amount of Albumin would added to the top, with simulated body fluid (SBF) at the bottom of the well. This would allow for samples of the SBF to be taken over time and the concentration of Albumin to be calculated from a BSA standard. Albumin has a molecular mass of 66.5 kDa, which is larger than certain important molecules that would need access to the defect site. This includes VEGF, PDGF, BMPs and TGF-β, all of which are fundamental to revascularisation and angiogenesis of the defect site (De Witte et al. 2018), these growth factors vary from 20-55 kDa, dependent on which cleaved form is used, thus Albumin would be a good model nutrient.

7.3.1 Future Uses of Free Surface Electrospun Membranes in Surgery

M3%-PCL and M6%-CP70:30 are similar in many ways, thickness, fibre and pore size diameter and barrier functionality, but there are also important differences, due to the presence or absence of collagen, with respect to material stiffness, liquid absorbance and cellular attachment. All of these attributes are important to consider when deciding the potential uses of each free surface electrospun membrane during surgical repair of CSBDs, summarised in Figure 7.1.

As previously discussed a debrided CSBD site would be filled with varying mixtures of autograft, synthetic bone scaffolds, BMA or BMA and growth factors, dependent on surgeons preference and the clinical scenario, e.g. elderly patient, bone infection, non-union etc. Therefore, both of the free surface electrospun membranes will come into contact with the above materials to varying degrees. With respect to the use of autograft, it is probably that MSCs will migrate out and onto the membranes, thus whatever membrane is used should support this.

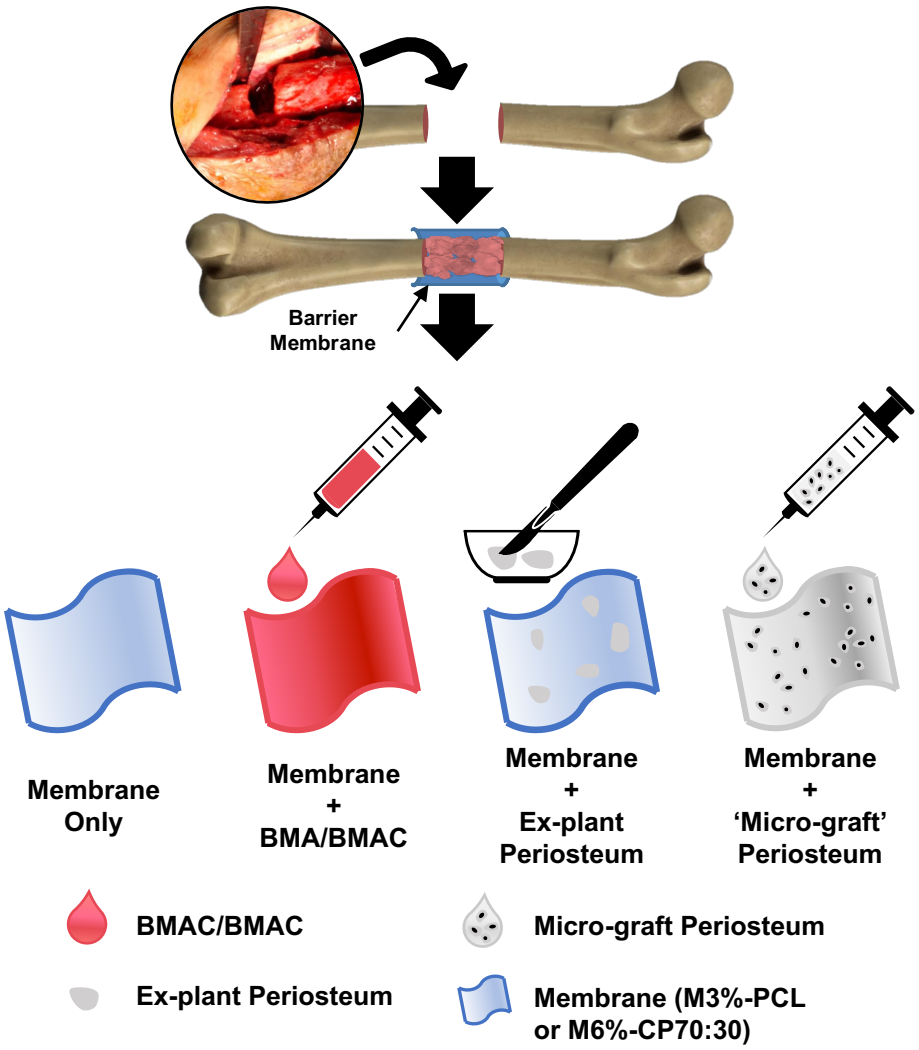

Figure 7.1: Schematic of the proposed uses of the free surface electrospun membranes for critical size bone defect (CSBD) repair, via a 'hybrid graft'. CSBDs will be debrided and filled with autograft or a combination of synthetic bone graft and bone marrow aspirate (BMA) or BMA concentrate (BMAC). The defect site will be wrapped in M3%-PCL (PCL) or M6%-CP70:30 (Collagen-PCL) membranes, either on its own, soaked in BMA/BMAC, with ex-plant periosteum pieces attached or soaked in 'micro-graft' periosteum, generated through the Rigenera® protocol. *Insert:* photograph of tibial bone defect, taken during surgery, with the patient's consent and ethical approval (see Appendix 5).

The first, and most simple use of the membranes would be to use it 'bare', purely as a containment factor for the grafting material and barrier to soft tissue invasion. The aforementioned interactions with MSCs from autograft as well as from periosteum from the fracture ends would be possible, on the 'inside' of the membrane, suggestive of a co-existence of periosteum and BM MSCs. Based on this it would be logical to use M3%-PCL, as the stronger and cheaper material to develop, unless the solubilisation of collagen immediately

following implantation can act as a ‘cue’ to induce cellular attachment after the ‘burst release’. However, this still needs to be investigated *in vitro*.

The second option would be to load BMA or BMAC directly onto the membranes to be absorbed, prior to implantation, thus M6%-CP70:30 would be preferable for this due to its enhances absorbance ability. However, the cellular attachment capabilities of this membrane need to be improved, through crosslinking and use of atelocollagen. Here, BMA or BMAC will cover both sides of the membrane, ‘releasing’ growth factors into the defect site, whilst MSCs present will attach onto the membrane.

The final two options involve the utilisation of periosteum as a source of MSCs, here ex-plant periosteum can be macerated and added to the membrane, or use of the Rigenera® protocal to produce periosteum ‘micro-grafts’ that could be absorbed by the membrane. This would allow for periosteum MSCs to attach and proliferate onto the membranes, in theory in combination with periosteum MSCs migrating out the fracture ends, aligning along the long axis of the bone (M3%-PCL).

The original hypothesis of this thesis was that a collagen containing barrier membrane would outperform the polymer only control, unfortunately this was not the case. Even though all of the above options could use either membrane, M3%-PCL is preferable (apart from its inferior absorbance), due to it being cheaper to manufacture (collagen is expensive), approval for use in humans (GMP grade PCL used) and superior MSC attachment and proliferation.

As described above, the only considered ‘improvement’ of the collagen-PCL blended membrane had over M3%-PCL was its noticeable improved liquid absorbance. However, this was counteracted by significantly lower cellular attachment onto M6%-CP70:30, potentially caused by the ‘burst’ release of collagen, which is also partially denatured, from the membrane in the first 24 hours once hydrated. Therefore, as it stands M6%-CP70:30 is an inferior membrane in comparison to M3%-PCL, especially when considering future commercialisation, whereby collagen would result in increased manufacturing costs. To improve on this future work is needed to improve cellular attachment of M6%-CP70:30 to make the use of collagen worthwhile. However, it should

be noted that the superior absorbance capability of M6%-CP70:30 may be necessary for use in conjunction with BMA or periosteum ‘micro-grafts’.

7.4 Future Directions

The body of research carried out for this thesis covered a diverse range of research areas, which have all bought about interesting results or leads that due to time constraints could not be carried out. The following section details the future directions for each research strand covered in this thesis.

7.4.1 Histological Evaluation of Periosteum

This project gained access to rare ‘clinically relevant’ samples of human periosteum, harvested from donors undergoing trauma orthopaedic surgery. Further histological investigation into the type of immune cells found within areas of inflammation using IHC as well as identifying the true nature of the ‘muscle like’ and ‘tendon like’ areas found within periosteum is imperative. These unexpected ‘ectopic’ tissues may represent an aberrant tissue repair response to periosteal microdamage from activated muscle-resident MSCs (Owston, Giannoudis & Jones 2016). If true, this provides further evidence that graft containment and creating a barrier from the neighbouring muscle tissue is indeed and an important practical consideration. Staining for calcium deposition, through von Kossa or Alizarin Red stains would answer the question of whether or not the ‘muscle like’ areas are mineralised, and would give further insight into the nature of these areas. There is a specific marker for tendons called Tenascin-C, which is predominantly expressed in tendons (adults) and dense connective tissue within embryos (Midwood et al. 2016). However, there is evidence of Tenascin-C expression at sites of inflammation and trauma (Midwood & Orend 2009). This could pose an issue when identifying tendon within human periosteum samples as there could be cross over of ‘tendon like’ areas with areas of inflammation (shown in Chapter 3). In addition, as periosteum samples are harvested from close to areas of trauma, it could be postulated that Tenascin-C could be expressed in periosteum as a response to said trauma.

A limitation in using the ‘clinically relevant’ samples of human periosteum was that orientation of the samples was difficult to determine. Samples were stripped from the underlying bone and commonly lacked the cambium layer, which would allow for correct orientation. Therefore, obtaining human cadaveric or amputation samples would allow for a source of periosteum with the underlying bone and therefore cambium still intact. This would allow for a more accurate evaluation of the architecture of human periosteum, as well as providing ‘control’ samples to the ‘clinically relevant’ samples from close to fracture site. This would ascertain whether ‘muscle-like’ and ‘tendon-like’ areas are formed as a response to trauma or part of the native periosteum structure. However, further ethical approval would need to be obtained for this body of work.

The porcine periosteal work was limited through only evaluating a small cross section of the porcine femur, nevertheless, it uniquely showed the variability in thickness of periosteum around the femur circumference. Following on from this, it would be prudent to have further validated the variance of periosteal thickness around the circumference of the bone by taking multiple cross sections along the length of the porcine femur. Therefore, allowing for analysis on the changes in periosteum architecture, vascularity and thickness throughout the length of the femur and in relation to the adjacent muscle mass. The decalcification process was, however, lengthy (approximately a year) and obtaining more samples within the time constraints of the project was not possible.

With respect to how such a comprehensive study would inform membrane design, it is likely to show that periosteum thickness is variable not only in cross section, but longitudinally, therefore again showing that an exact match in thickness of the membrane to periosteum would be impossible in most cases. Therefore, the thickness of the membrane would ideally be based on its ability to be handled well and to block cell migration. A variation of membrane thicknesses could be developed for use in different types of bones, e.g. load bearing vs non load bearing or large vs small bone diameter.

7.4.2 Comparison of MSCs from Bone Marrow and Periosteum

As with human periosteal histology, increased donor numbers to allow for increased sample numbers for each experiment is always needed. There were also a low number of female donors, so this would allow for differences with age or gender to be investigated. Information on how many cells, volume of BMA or volume of periosteum 'micro-graft' to be load onto biomaterials needs future investigation and whether or not this needs to be adjusted to donor age is an important consideration, due to the known reduction in osteogenesis of BM MSCs with age. Here, the CFU-F assay could be modified to investigate colony formation onto M6%-CP70:30 or M3%-PCL, instead of tissue culture plates.

Holographic imaging was utilised as a rudimentary indication of how periosteum and BM MSCs form colonies. A main limitation of this work was the inability to 'track' a migratory cells' path once it moved out of the field of view. However, PHI, the company that developed this microscope are developing software to be able to knit together large fields of view in order to remedy this issue. Therefore, in the future it would be possible to track cell migration over a wider area as well as potentially image the formation of a whole colony in real time.

Further investigation into the current data collected from live cell imaging would be carried out, the software has 40 outputs based on quantification of cell morphology, migratory and proliferation patterns, all of which could not to be investigated due to time constraints of the project. Of particular interest are the proliferation habits of MSCs, through tracking the cells, a hierarchy of cell division can be quantified and changes in migration or morphology based on cell division could be explored. In addition, carrying out experiments using multiple matched donors of BM and periosteum MSCs would also reveal if there are distinct donor variability differences in migratory patterns; this would also be compared to a late passage culture to see how migratory patterns change with *in vitro* age. The use of live cell imaging for imaging of cellular

growth onto biomaterials is possible if the substrate is transparent, unfortunately limiting the potential for this to thin substrate coatings.

Osteogenic differentiation appeared to be variable from both BM and periosteum MSC sources, therefore further investigation using time points over an extended period of time would assess peak Ca^{2+} deposition and differentiation of periosteum MSCs. In addition, a time course would be set up for ALP staining, with bi weekly time points for up to 3 weeks to ascertain at what time following osteogenic induction do periosteum MSCs show peak ALP production and whether or not this is different to BM MSCs.

As mentioned, the use of cultured MSCs in a surgical setting requires increased regulatory approval. Ideally this thesis would have been able to work towards ascertaining the osteogenic potential of minimally-manipulated BMA (non lysed), non-digested periosteum (ex-plant) and the aforementioned periosteal 'micro-grafts', as a move towards investigating periosteum's potential use in a surgery setting. Therefore, a future direction would be to quantify osteogenic potential of BMA and ex-plant periosteum. Here, BMA or 'minced' periosteum would be plated into dishes and subjected to osteogenic differentiation, alongside separate dishes with StemMACS media as comparison. If NCC count was high enough, a time course could be carried out to determine the length of time it takes to see detectable Ca^{2+} deposition as well as the effect of minimal culture.

Combining both for a co-culture osteogenic experiment would be an interesting development, despite *in vitro* co-culture experiments of Chapter 4 not showing a synergistic increase in osteogenic potential, as this set of experiments would work to prove whether the use of periosteum on its own or in conjunction with BMA is a viable option for use during surgery.

7.4.3 Further Development of Free Surface Electrospun Barrier Membranes

Tensile strength of the free surface electrospun membranes is important as it eludes to how easily surgeons can handle the membrane, as well as how well the membrane can withstand mechanical forces following implantation. Tensile testing of M3%-PCL and M6%-CP70:30 was carried out in 'dry'

samples, however as this material will be used ‘wet’, either through addition of MSC suspensions or once *in situ*. Therefore, ascertaining the tensile properties following hydration as well as following incubation for a set amount of time (e.g. after 3 weeks in PBS) would provide information on how the tensile properties of the membranes change with hydration and time, providing preliminary data that would need to be backed up by *in vivo* degradation studies.

One of the main advantages to using free surface electrospinning is in its potential to upscale manufacture. Developing the process from using a small scale spike electrode to that of a bath solution would allow for larger samples of material to be made. However, as the current equipment (NS-LAB 200, Elmarco) has an uncovered bath, allowing for solvent evaporation and therefore changes in solution concentration, applying for funding to upgrade this equipment to a contained system would be ideal. Investigation into alternative solvent systems would be prudent, due to the toxic nature of HFIP and its known effect on further degradation of helical collagen. A recent study used acetic acid to electrospin collagen and PCL nano-fibres (Chakrapani et al. 2012), which should be tested as an alternate to HFIP.

7.4.4 Functional Testing of Electrospun Barrier Membranes

Knowing the degradation profile of the free surface electrospun membranes is important to the membranes’ *in vivo* function, the ideal degradation profile would be approximately 12 weeks. Therefore, an *in vitro* ‘mass loss’ study of both M3%-PCL and M6%-CP70:30 would be carried out, whereby the membranes would be incubated at 37°C with PBS or collagenase to simulate breakdown of the membranes *in vivo*. However, ideally an *in vivo* study would also be carried out to test for biocompatibility and also to provide a more precise investigation into membrane degradation *in vivo*. This could be carried out using a subcutaneous pocket study. Based on the above investigations, if degradation is too slow, the use of a lower molecular weight PCL could be investigated (Woodruff & Hutmacher 2010).

Initial cellular attachment onto M6%-CP70:30 was found to be considerably lower when compared to M3%-PCL. This is hypothesised to be due to the

‘burst’ release of collagen from the membrane during the first 24 hours once hydrated. This theory could be tested through incubation M6%-CP70:30 in PBS or culture media for 24 hours prior to MSC attachment to see if this results in improved cellular attachment.

If improvement to M6%-CP70:30 cellular attachment was not achieved by this, functionalisation of the membrane would be considered. Collagen has been functionalised with 4-vinylbenzyl (collagen-4VBC), which can be UV cured to produce a crosslinked structure (Liang et al. 2018), which could be more resistant to solubilisation of collagen once hydrated.

In addition, comparisons of the two developed membranes could be made with respect to the ability of the free surface electrospun membranes to support osteogenic differentiation of BM or periosteum MSCs. Here the cellular attachment assay carried out in Chapter 6 would be taken forward to use osteogenic media instead with a time course of 2-4 weeks whereby Ca^{2+} deposition could be quantified using the Calcium assay showed in Chapter 4, in addition to confocal imaging to show cell morphology changes during differentiation onto the membranes.

As previously discussed, investigation into the utilisation of ex-plant periosteum is imperative to ascertaining whether periosteum should be used during orthopaedic surgery. As the electrospun membrane will be used to wrap around a defect site, it could also be covered in ex-plant periosteal tissue during surgery prior to implantation. Therefore, *in vitro* testing would be carried out to show whether periosteum MSCs can migrate out of the ex-plant tissue and populate the electrospun membranes as further *in vitro* simulation of how the membranes would behave *in vivo*.

Improvements to the barrier function assay could be made through producing smaller pore sizes that would also form a serum gradient to be maintained. Also, SEM imaging of the top and bottom of the membrane would be used in addition to confocal imaging to further ascertain whether MSCs were able to migrate to the bottom of the membrane.

Long term future projections for this piece of work would include further *in vivo* studies, starting with the aforementioned subcutaneous pocket model, to corroborate that the free surface electrospun membranes are biocompatible

in vivo as well as ascertaining *in vivo* degradation times of said membranes. Following this, a segmental defect *in vivo* model (porcine or ovine study) would be used to test the 'functional' use of M6%-CP70:30 and M3%-PCL as a barrier, wrapping around the CSBD site. This would be in comparison to various controls: 'empty defect', 'gold standard', defect filled with bone grafting material and also between the two membranes to see if one simulates increased bone regeneration compared to the other.

7.5 Final Conclusion

This multidisciplinary project has uncovered interesting insights into the histological architecture of periosteum, the *in vitro* nature of donor matched periosteum and BM MSCs as well as a developing two free surface electrospun membranes, suitable for use in CSBD repair. A debate over the ideal MSC source or use of collagen within the free surface electrospun membrane has been started, whereby future work is needed into the use of 'minimally manipulated' forms of periosteum and BMA and improvement of cellular attachment of M6%-CP70:30.

Appendices

Appendix 1: Details of Reagents, Solutions, Consumables and Equipment

Appendix 1.1: Reagents used throughout Research Methodology

Reagents	Manufacturer
1,1,1,3,3,3-Hexafluoro-2-propanol (HFIP)	Flurochem
4′,6-diamidino-2-phenylindole (DAPI)	Sigma
Acetic Acid (Glacial)	Sigma
Acetone	Sigma
Acid Alcohol (1%)	Atom Scientific
AdipoDIFF	Miltenyi Biotec
Alizarin Red	Sigma
Ammonium Chloride	Stem Cell Technologies
Ammonium Hydroxide	Sigma
β-Mercaptoethanol	Sigma
Boric Acid	Sigma
Bovine Serum Albumin (BSA)	Sigma
Calcium Liquid Assay	Sentinel Diagnostics
CFSE CellTrace™ Proliferation Kit	Thermo Fisher
ChondroDIFF	Miltenyi Biotec
Citrate Concentrate	Sigma
Citric Acid (anhydrous)	Sigma
Collagenase (600 U/mL)	Miltenyi Biotec
Dako EnVision+ Immunostaining kit	Agilent
Disodium tetraborate dehydrate	Sigma
Distilled H_2O (dH_2O)	-
Dulbecco's Modified Eagle Medium (DMEM) low glucose	Gibco
Dimethyl Sulfoxide (DMSO)	Sigma
DNase	Qiagen
DPX Mounting Media	Sigma
Eosin	Sigma
Ethanol (EtOH)	Fisher Scientific
Ethylenedinitrilotetra acetic Acid (EDTA)	Sigma
Fast Blue RR Salt Capsules	Sigma
Fetal Calf Serum (FCS)	BioSera
Formaldehyde (37.5%)	Fisher Scientific
Galpore™ Wetting Fluid	Porometer
Haematoxylin (Harris)	Fisher Scientific
Haematoxylin (Wiegert's) – Solution A & B	VWR International

Appendix 1.1 (continued): Reagents used throughout Research Methodology

Reagents	Manufacturer
Human IgG	Sigma
Hydrochloric Acid (HCl)	Sigma
Isopropanol	Sigma
L-cysteine	Sigma
Magnesium Sulphate	Sigma
Methanol	Sigma
Methyl Blue	Atom Scientific
Mouse Serum	Sigma
Naphthol AS-MX Phosphate	Sigma
Nile Red	Sigma
Nuclease Free Water	Ambion
Oil Red O	Sigma
Optimal Cutting Temperature (OCT) compound	VWR
OsteoDIFF	Miltenyi Biotec
Oxalic acid	Sigma
Papain	Sigma
Paraffin Wax	Sigma
Penicillin Streptomycin (PS)	Thermo Fisher
Phalloidin-FITC	Thermo Fisher
Phosphate Buffered Saline (PBS)	Sigma
PicoGreen Assay	Thermo Fisher
Picric Acid (saturated, aqueous)	Fisher Scientific
Poly (ε-caprolactone) (PCL) (M_n: 80,000g mol^{-1})	Sigma
Potassium Chloride (KCl)	Sigma
Potassium Permanganate	Atom Scientific
RL Buffer	Norgen-Biotek
Saponin	Sigma
Single Cell RNA Purification Kit	Norgen-Biotek
Sodium Azide	Sigma
Sodium Chloride (NaCl)	Sigma
Sodium Heparin (1000 U/mL)	Wockhardt UK Ltd
Sodium Hydroxide (NaOH)	Fisher Scientific
Sodium phosphate dibasic	Sigma
Sodium dihydrogen phosphate	Sigma
StemMACS media	Miltenyi Biotec
Sulphated GAG Assay	Biotec
TaqMan Gene Expression Master Mix	Applied Biosystems
Tris base	Sigma
TrueVIEW™ Autofluorescence Quenching Kit	Vector Laboratories
Toluidine Blue	Sigma
Trypan Blue Solution (0.4%)	Sigma

Appendix 1.1 (continued): Reagents used throughout Research Methodology

Reagents	Manufacturer
Trypsin (0.5%)	Sigma
Tween 20	Sigma
Ultra-Pure Water	Sigma
Xylene	Sigma

Appendix 1.2: Details of solutions used throughout Research Methodology

Reagents	Chapter Used	Details of Reagent Solutions
Acetic Acid (17.4 mM)	5	1 mL Acetic Acid in 1L dH_2O
Acid Alcohol (1%)	4	1 mL HCl in 100 mL 70% EtOH (diluted in dH_2O)
Acidified Water (0.5 M)	4	2.87 mL Glacial Acetic Acid added slowly to 25 mL dH_2O, topped up to 100 mL
Alizarin Red (40 mM)	4	342 mg Alizarin Red in 25 mL dH_2O, pH to 4.1 using Ammonium Hydroxide
Borate Buffer (10 mM)	4	1.91 g disodium tetraborate dehydrate dissolved in 500 mL dH_2O, adjust pH to 8.8 with 1 M boric acid
Boric Acid (1 M)	4	6.183 g boric acid in 100 mL dH_2O
Citrate Buffer (10 mM/L)	3	1.92 g citric acid in 1 L of dH_2O, adjust to pH 6.0 using NaOH, add 0.5 mL Tween 20
Citrate Fixative	4	2 mL citrate concentrate to 98 mL dH_2O, diluted 2 parts to 3 with acetone
Collagenase (600 U/mL)	4	Used at 1 g of tissue to 5 mL of collagenase
DAPI	4 & 6	Aliquoted into vials at concentration 100 mg/mL in PBS
DAPI Buffer	4	Final concentration: 0.5 mg/mL, 20 mL of FACS buffer to 1 vial of DAPI
Differentiation Media (AdipoDIFF, ChondroDIFF, OsteoDIFF)	4	Add 1% PS (1 mL for 100 mL bottle)
DNase	4	Mixed with RDD Buffer (5:35 µL)
Ethylenedinitrilotetra acetic Acid (EDTA) (0. 5 M)	4	250 g EDTA powder dissolved in 1750 mL of dH_2O, adjusted to pH 7 using NaOH pellets
Electrospinning solution 3%-PCL	5	0.3 g PCL in 10 mL HFIP

Appendix 1.2 (continued): Details of solutions used throughout Research Methodology

Reagents	Chapter Used	Details of Reagent Solutions
Electrospinning solution 6%-CP50:50	5	0.6 g (0.3 g Collagen, 0.3 g PCL) in 10 mL HFIP
Electrospinning solution 6%-CP60:40	5	0.6 g (0.36 g Collagen, 0.24 g PCL) in 10 mL HFIP
Electrospinning solution 6%-CP70:30	5	0.6 g (0.42 g Collagen, 0.18 g PCL) in 10 mL HFIP
Electrospinning solution 6%-CP80:20	5	0.6 g (0.48 g Collagen, 0.12 g PCL) in 10 mL HFIP
Ethanol (100%, 75%, 50%, 25%)	3-6	Diluted in dH_2O
FACS Buffer	4	500 mL PBS + 0.1% BSA (0.5 g) + 0.01% Sodium Azide (1 mL of 5% stock solution) + 0.5 M EDTA (200 µL)
Fast Blue Stain	4	Dissolve 1x Fast Blue RR salt capsule in 48 mL 37°C dH_2O, protected from light. Add 2 mL Naphthol AS-MX
Flow Cytometry Blocking Buffer	4	10% mouse serum (300 mL) + 1% human IgG (100 mL) + 1100 mL FACS Buffer
Formaldehyde (3.75%)	3 & 6	Stock solution 37.5%, dilute 1 in 10 dH_2O
Freezing Media	4	90% FCS with 10% DMSO
HCl (0.5 M)	4	26.5 mL HCl and 473.5 mL dH_2O
Masson's Trichrome Solutions	3	1% (w/v) Methyl Blue, Wiegert's Haematoxylin (Solution A & B), 1% Acid Alcohol, Ponceau Fuchsin and Phosphotungstic Acid (1%)
Methylene Blue (1% w/v)	4	1g methylene blue dissolved in 100 mL of 10 mM borate buffer (pH 8)
Nile Red/DAPI staining solution	4	0.2% Saponin in PBS, with 1 µg/mL Nile Red and 1 µg/mL DAPI
Oil Red	4	0.5% in isopropanol (50 mg in 10 mL) diluted upon use (3:2 Oil Red to water and filter twice)
Papain Digest Solution	4	0.125 mg/mL papain with 100 mL sodium phosphate buffer, 5 mM EDTA and 1 mM L-cysteine
Phalloidin-FITC	6	Diluted 1:1000 with PBS, protected from light and stored at -20°C
Phosphate Buffered Saline (PBS)	3-6	1 tablet dissolved in 200 mL dH_2O
Picro Sirius Red (0.1%)	3 & 5	0.25g Sirius red in 250 mL saturated aqueous picric acid

Appendix 1.2 (continued): Details of solutions used throughout Research Methodology

Reagents	Chapter Used	Details of Reagent Solutions
Rat Tail Collagen (in house)	5 & 6	Tendons stripped from 50 frozen rat tails, collagen solubilised in 17.4 mM acetic acid (see Section 5.2.1)
RNA Lysis Buffer	4	1:100 β-Mercaptoethanol with RL buffer (Norgen)
RT Master Mix	4	RT Buffer, dNTP Mix, RT Random Primers, Multiscribe Reverse Transcriptase, RNase Inhibitor, Nuclease Free Water (see Table 4.3)
Scott's Tap Water	3	3.5 g sodium bicarbonate, 20 g magnesium sulphate in 1 litre of dH_2O
Sodium Hydroxide (0.1 M)	5	4 g NaOH to 1 L dH_2O
Sodium Phosphate Buffer (50 mM)	4	3 ml of 1M sodium phosphate dibasic (1.42 g in 10 mL) with 7 ml of sodium dihydrogen phosphate (1.56 g in 10mL) in 200 mL dH_2O (pH 6.5).
StemMACS MSC Expansion Media	4 & 6	Add 1% PS (5 mL) to 500 mL bottle
Supplemented DMEM Media	4 & 6	*Supplemented DMEM media (used in tissue culture:* 10% FCS (50 mL), 1% PS (5 mL) in 500 mL of low glucose DMEM media *Low Serum DMEM media (used in CFSE experiment, Section 4.2.8):* 1% FCS and 1% PS in low glucose DMEM media
Tris-buffered Saline	3	16 g NaCl, 0.4 g KCl and 6 g Tris base dissolved in 800 mL dH_2O, adjust to 7.4 pH with HCl and make up to 1 L with dH_2O
Toluidine Blue (1%)	4	1 g Toluidine blue to 100 mL 50% Isopropanol (diluted in dH_2O)
Trypsin (0.1%)	4 & 6	5 mL Trypsin (0.5% stock solution) with 20 mL PBS
Tween 20 (0.1%)	6	1 µL Tween 20 in 1000 µL dH_2O

Appendix 1.3: Details of consumables used throughout Research Methodology

Consumables	Manufacturer
Bijoux (5 mL)	Star Lab
Cell Strainer (70 µm)	BD Falcon
Centrifuge Bottles (1000 mL)	Beckman Coulter
Cryo Boxes	Starstedt
Cryovials (1.8 mL)	Nunc
Cuvette (1 cm)	Applied Photophysics
EDTA Blood Tubes (Vacutainer)	BD Biosciences
Filter (0.22 µm, 0.4 µm)	Millex
FACS tubes	Corning
Falcon Tubes (15 mL, 50 mL)	Corning
Flat bottom well plates – (6, 12, 24, 48, 96 well)	Corning
Histology Cassettes	Scientific Laboratory Supplies
Histology Slide Covers	Thermo Scientific
HoloLids - 24 well plate lids	Phase Holographic Imaging
Lumox Multiwell 24 well plate	Sarstedt
Microtome Blades (CellEdge R+)	Cell Path
MicroAmp™ 384 PCR Plate	Applied BioSystems
MicroAmp™ Optical Adhesive Film	Applied BioSystems
Mr Frosty Freezing Container	Thermo Scientific
Non Tissue Culture Treated Plates (6, 12 well)	CellStar, BioOne
PCR Tubes and Caps	Star Lab
Pipette Tips (10 µL, 200 µL, 1000 µL)	Rainin
Polypropylene Thermally Bonded Spunbond Fabric	Elmarco
Round Bottom Flasks	Martin Christ
RNA Elution Tubes	Norgen-Biotek
Safe-lock Tubes (0.5 mL, 1.5 mL)	Eppendorf
Scalpel (Blade sizes 10 and 22)	Swann Morton
SEM Specimen Stubs and Mounts	Agar Scientific
Single Cell RNA Spin Column	Norgen-Biotek
Stripette (5 mL, 10 mL, 25 mL)	Corning
SuperFrost Plus Histology Slides	Thermo Scientific
Tissue Culture Flasks (T25, T75 and T150)	Corning
Tubes and Tethered Cap with O-Ring	Star Lab
Tissue Culture Round Dishes (100 mm or 60 mm diameter)	Corning

Appendix 1.4: Details of equipment used throughout Research Methodology

Equipment	Manufacturer
AAP Chirascan Circular Dichroism Spectropolarimeter	Applied Photophysics
Agar Auto Sputter Coater	Agar Scientific
Attune 2 Laser System Flow Cytometer	Applied Biosystems
Attune Cytometric Software	Applied Biosystems
Centrifuge 5415D and 5810R	Eppendorf
Centrifuge (Ultra) J-26 XP	Beckman
CKX41/BX45 Microscopes	Olympus
Class II Laminar Flow Biological Safety Cabinet	Nuaire
CO_2 Incubator InCuStage (37°C, 5% CO_2)	Sanyo
Confocal Microscope – DM6 CS	Leica Camera AG
Confocal Microscope Software – LAS X	Leica Camera AG
Contact Angle Goniometer (CAM 200)	KSV Instruments, Ltd
Cryostat (CM1520)	Leica Biosystems
CS2200 Dental X-Ray Machine	Carestream Dental
Epsom 3590 Photo Scanner	Epsom
FACS DIVA software	BD BioSciences
Freeze Dryer (Alpha 2-4 LD Plus)	Christ Martin
Freezer (-20°C)	Liebherr
Freezer (-80°C)	New Brunswick Scientific
Fridge (2-4°C)	Zanussi
Gilson Pipette	Gilson
Haemocytometer (BS7.48)	Hawksley
Hitachi SEM (5-3400N)	Hitachi
Hitachi SEM (5-3400N) Software	Hitachi
HoloMonitor M4 Base Unit Microscope	Phase Holographic Imaging
HoloMonitor M4 Software	Phase Holographic Imaging
Hot Plate (SH3)	Stuart Scientific
Hot Plate Stirrer (PC-351)	Corning
ImageJ Software	ImageJ
Infinity 1 Camera	Lumenera
Infinity Image Acquisition software	Lumenera
LSR II Flow Cytometer	BD BioSciences
Mechanical Tube Spinner	VWR
Microtome – RM2235	Leica

Appendix 1.4 (continued): Details of equipment used throughout Research Methodology

Equipment	Manufacturer
Microscope (AxioCam MRc5)	Zeiss
Microscope (L5200B)	GX Microscope
Microwave	
NanoDrop Spectrophotometer ND-100	NanoDrop
NanoSpider NS Lab	Elmarco
pH Meter	Jenway
Plate Reader (Mithras LB 940)	Berthold
Porolux 100FM	Porometer
ProGage Thickness Tester	Thwing-Albert Instrument Company
QuantStudio TM 7 Flex Real-Time PCR System	Applied BioSystems
Thermocycler – Verti 96 well	Applied Biosystems
Tissue Processor – ASP200	Leica
Titan - Tensile Testing Machine	James Heal
Vortex	Star Lab
Water bath (SUB6)	Grant
Water Bath (H11210)	Leica
Weighing Scale (AL54)	Mettler Toledo
X-Ray Machine (CS2200)	Carestream Health
ZenPro Software	Zeiss
Zwick Machine - Tensile Testing Machine	Zwick/Roell

Appendix 2: Histological Tissue Processing Protocol

Appendix 2.1: Tissue processing protocol for iliac crest bone and periosteum samples, post fixation. All steps were carried out at 37°C, apart from those denoted with *, which were carried out at 65°C.

Step	Solution and Reagents	Time (hour:min)
1	70 % Ethanol	0.30
2	80 % Ethanol	0.30
3	90 % Ethanol	0.30
4	95 % Ethanol	0.30
5	100 % Ethanol	1:00
6	100 % Ethanol	1:00
7	100 % Ethanol	1:30
8	Xylene	1:00
9	Xylene	1:30
10	Xylene	1:30
11	Paraffin Wax*	1:00
12	Paraffin Wax*	1:00
13	Paraffin Wax*	1:00

Appendix 3: Antibody Conjugates for Flow Cytometry

Appendix 3.1: Antibody Conjugates used for flow cytometry (LSRII). APC – Allophycocyanin, FITC – Fluorescein isothiocyanate, PE - R-phycoerythrin, PECy7 - PE/Cyanine7

Target	Fluorophore	Clone	Manufacturer
Positive Markers			
CD73	PE	AD2	Miltenyi Biotec
CD90	PECy7	SE10	BD Biosciences
CD105	FITC	SN6	Bio-Rad
CD105	PE	REA794	Miltenyi Biotec
Negative Markers			
CD14	FITC	TÜK4	Miltenyi Biotec
CD19	PE	HIB19	BD Biosciences
CD34	APC	581	BD Biosciences
CD45	PECy7	HI30	BD Biosciences
HLA-DR	VioGreen	REA805	Miltenyi Biotec
Test Markers			
CD271	APC	LNGFR	Miltenyi Biotec
SUSD2	APC	W5C5	BioLegend
MSCA-1	PE	W8B2	Miltenyi Biotec
CD146	PE	P1H12	BD Biosciences
Isotype Controls (all raised in Mouse)			
IgG1	APC	IS11-12E4.23.30	Miltenyi Biotec
IgG1	FITC	MOPC-21	BD Biosciences
IgG1	PE	MOPC-21	BD Biosciences
IgG1	PECy7	MOPC-21	BD Biosciences
IgG2a	FITC	MCA1210	Bio-Rad
IgG1	VioGreen	MOPC-21	Miltenyi Biotec

Appendix 3.2: Flow cytometry antibody details with the Attune system FITC – Fluorescein isothiocyanate, PE - R-phycoerythrin, PerCP-vio – peridinin chlorophyll protein-vio 700. All antibodies purchased from Miltenyi Biotec apart from, * Bio Rad, ** BD Biosciences

Antibody	Fluorochrome	Volume (µL)	Clone
Isotype Controls (all raised in mouse)			
IgG1	PE	10.0	MCA1210*
IgG1	FITC	10.0	MCA1210*
IgG1	VioGreen	2.0	MOPC-21**
IgG1	PerCP-Vio	2.0	MOPC-21**
Negative Markers			
CD14	VioGreen	2.0	REA599
CD19	VioGreen	2.0	LT19
CD34	VioGreen	2.0	AC136
CD45	VioGreen	2.0	REA747
HLA-DR	VioGreen	2.0	REA805
Positive Markers			
CD73	PE	10.0	AD2
CD90	PerCP-Vio	10.0	REA897
CD105	FITC	10.0	43A4E1

Appendix 4: TaqMan Probes Used for Real Time PCR

Appendix 4.1: TaqMan Probes used for real time PCR experiments

Assay ID	Gene Symbol	Synonyms
Hs99999909_m1	HPRT1	Hypoxanthine phosphoribosyltransferase 1
Hs00609452_g1	BGLAP	Bone gamma-carboxyglutamate (gla) protein (Osteocalcin)
Hs00231692_m1	RUNX2	Runt-related transcription factor 2
Hs00264051_m1	COL2A1	Collagen, type II, alpha 1
Hs00165814_m1	Sox9	SRY (sex determining region Y) – box 9
Hs00609791_m1	FABP4	Fatty acid binding protein 4
Hs01115513_m1	PPAR-γ	Peroxisome proliferator-activated receptor-gamma

Appendix 5: Ethical Approval

NHS
Health Research Authority

NRES Committee Yorkshire & The Humber - Leeds East
Yorkshire and Humber REC Office
First Floor, Millside
Mill Pond Lane
Meanwood
Leeds
LS6 4RA

Tel: 0113 3050108
Fax:

12 April 2012

Prof Peter Giannoudis
Consultant
Department of Trauma and Orthopaedics
St James's University Hospital
LS9 7TF

Dear Prof Giannoudis

Study title:	**Biological properties of Mesenchymal Stem Cells in Fracture Healing**
REC reference:	**06/Q1206/127**
Amendment number:	**3/1**
Amendment date:	**11 April 2012**

Thank you for submitting the above amendment, which was received on 12 April 2012. It is noted that this is a modification of an amendment previously rejected by the Committee (our letter of 22nd February 2012 refers).

The modified amendment has been considered on behalf of the Committee by the Vice-Chair.

Ethical opinion

I am pleased to confirm that the Committee has given a favourable ethical opinion of the modified amendment on the basis described in the notice of amendment form and supporting documentation.

Approved documents

The documents reviewed and approved are:

Document	Version	Date
Parental Agreement - Consent Form	1.1	23 March 2012
Participant Consent Form: Patient Consent Form 16 - 17 years old	1.0	23 March 2012
Participant Consent Form: Children Assent Form	1.0	01 February 2012
Participant Information Sheet: Patient Information Sheet 16 - 17 years old	1.0	23 March 2012
Participant Information Sheet: Parental Information Sheet	1.1	23 March 2012
Participant Information Sheet: Children Information Sheet	1.1	23 March 2012
Protocol	6.0	19 December 2011
Modified Amendment		11 April 2012

Appendix 6: Presentations, Conferences and Publications

Details of the conferences attended throughout the PhD, with oral and poster presentations and details of first author and co-author articles published during this time.

Oral Presentations

- **British Orthopaedic Research Society** (BORS), University of Leeds, 2018 – *A Collagen-Based Soft Tissue Barrier Membrane with Periosteal Mesenchymal Stem Cell Homing Capability for Bone Defect Repair*
- **UK Society for Biomaterials** (UKSB), University of Bath, 2018 – *A Collagen-Based Soft Tissue Barrier Membrane with Periosteal Mesenchymal Stem Cell Homing Capability for Bone Defect Repair*
- **European Society of Tissue Regeneration in Orthopaedics and Traumatology**, ESTROT, University of Leeds, 2017 - *Investigating Co-Culture of Periosteal and Bone Marrow MSCs onto Bone Scaffolds for Critical Size Bone Defect Repair*

Poster Presentations

- **Tissue and Cell Engineering Society** (TCES), University of Keele, 2018 – *A Collagen-Based Barrier Membrane for Bone Defect Repair,*
- **STEM for Britain**, Portcullis House, Westminster, 2018 – *Development of a Collagen Barrier Membrane for Large Bone Defect Repair*
- **European Chapter Meeting of Tissue Engineering and Regenerative Medicine International Society** (TERMIS-EU), Davos, Switzerland, 2017 - *Investigating Co-Culture of Periosteal and Bone Marrow Mesenchymal Stem Cells onto Bone Scaffolds for Critical Size Bone Defect Repair*
- **TCES,** 2015-2016
- **Joint Centre of Doctoral Training Conference (CDT)**, 2015-2018 – awarded best poster prize 2016
- **MSC Conference**, 2015-2017
- **BORS**, University of Glasgow, 2016 - *Investigating the Potential of Periosteal Cells for Critical Size Bone Defect Repair*

Research Articles

- Moisley, K., El-Jawhari, J., **Owston, H.**, Tronci, G., Russell, S., Jones, E., Giannoudis, P. 2019. *Optimising Proliferation and Migration of Mesenchymal Stem Cells Using Platelet Products: A Rational Approach to Bone Regeneration.* Journal of Orthopaedic Research. *DOI 10.1002/jor.24261*
- Sivasubramaniyan, K., Ilas, D., Harichandan, A., Bos P., Santos, D., de Zwart, P., Koevoet, W., **Owston H.**, Bühring H., Jones, E., van Osch, G. 2018. *Bone Marrow-Harvesting Technique Influences Functional Heterogeneity of Mesenchymal Stem/Stromal Cells and Cartilage Regeneration*. American Journal of Sports Medicine. 46(14):3521-3531
- Aldridge, A., Desai, A., **Owston, H.**, Jennings, L, Fisher, J., Rooney, P., Kearney, J., Ingham, E. and Wilshaw, S. 2017. *Development and characterization of a large diameter decellularised vascular allograft.* Cell Tissue Bank. 19(3):287-300

Reviews

- **Owston, H.**, Giannoudis, P. and Jones, E. 2016. *Do skeletal muscle MSCs in humans contribute to bone repair? A systematic review*. Injury. 47(suppl 6):S3-S15
- Altaie, A., **Owston, H.** and Jones, E. 2016. *Use of platelet lysate for bone regeneration – are we ready for clinical translation?* World Journal for Stem Cells. 8(2):47-55

References

AGHEB, M. et al. 2017. Novel electrospun nanofibers of modified gelatin-tyrosine in cartilage tissue engineering. *Materials Science and Engineering C*. **71**,pp.240–251.

AL-QTAITAT, A., R.C. SHORE and J.E. AARON 2010. Structural changes in the ageing periosteum using collagen III immuno-staining and chromium labelling as indicators. *Journal of Musculoskeletal Neuronal Interact*. **10**(1),pp.112–123.

ALDRIDGE, A. et al. 2013. Assay validation for the assessment of adipogenesis of multipotential stromal cells-a direct comparison of four different methods. *Cytotherapy*. **15**(1),pp.89–101.

ALEXANDER, D. et al. 2009. Cellular Physiology Biochemistry and Biochemistr y LNGFR Induction During Osteogenesis of Human Jaw Periosteum-derived Cells. *Cellular Physiology and Biochemistry*. **24**(1),pp.283–290.

ALEXANDER, D. et al. 2010. MSCA-1/TNAP Selection of Human Jaw Periosteal Cells Improves their Mineralization Capacity. *Cell Physiol Biochem*. **26**(1),pp.1073–1080.

ALEXANDER, D. et al. 2015. Phenotypic Characterization of a Human Immortalized Cranial Periosteal Cell Line. *Cellular Physiology and Biochemistry*. **35**(1),pp.2244–2254.

ALLEN, M.R. and D.B. BURR 2005. Human femoral neck has less cellular periosteum, and more mineralized periosteum, than femoral diaphyseal bone. *Bone*. **36**(2),pp.311–316.

ALLEN, M.R., J.M. HOCK and D.B. BURR 2004. Periosteum: Biology, regulation, and response to osteoporosis therapies. *Bone*. **35**(5),pp.1003–1012.

ÁLVAREZ-VIEJO, M., Y. MENÉNDEZ-MENÉNDEZ and J. OTERO-HERNÁNDEZ 2015. CD271 as a marker to identify mesenchymal stem cells from diverse sources before culture. *World Journal of Stem Cells*. **7**(2),pp.470–476.

ANTONOVA, E. et al. 2013. Tibia shaft fractures: Costly burden of nonunions. *BMC Musculoskeletal Disorders*. **42**(1),pp.14–24.

ARAFAT, M.T. et al. 2015. Biomimetic wet-stable fibres via wet spinning and diacid-based crosslinking of collagen triple helices. *Polymer*. **77**,pp.102–112.

AUBIN, J. 2001. Regulation of Osteoblast Formation and Function. *Reviews in Endocrine & Metabolic Disorders*. **2**(1),pp.81–94.

BADYLAK, S. and T. GILBERT 2008. Immune response to biologic scaffolds materials.pdf. *Seminars in Immunology*. **20**(1),pp.109–116.

BALL, M.D. et al. 2011. Human periosteum is a source of cells for orthopaedic tissue engineering: A pilot study. *Clinical Orthopaedics and Related Research*. **469**(11),pp.3085–3093.

BARBIER, L. et al. 2018. Autologous dental pulp mesenchymal stem cells for inferior third molar post-extraction socket healing: A split-mouth randomised clinical trial. *Medicina oral, patologia oral y cirugia bucal*.

23(4),pp.e469–e477.

DE BARI, C. et al. 2008. A biomarker-based mathematical model to predict bone-forming potency of human synovial and periosteal mesenchymal stem cells. *Arthritis and Rheumatism*. **58**(1),pp.240–250.

DE BARI, C., F. DELL'ACCIO, J. VANLAUWE, J. EYCKMANS, Ilyas M. KHAN, et al. 2006. Mesenchymal multipotency of adult human periosteal cells demonstrated by single-cell lineage analysis. *Arthritis and Rheumatism*. **54**(4),pp.1209–1221.

DE BARI, C., F. DELL'ACCIO, J. VANLAUWE, J. EYCKMANS, Ilyas M KHAN, et al. 2006. Mesenchymal Multipotency of Adult Human Periosteal Cells Demonstrated by Single-Cell Lineage Analysis. *Arthritis & Rheumatism*. **54**(4),pp.1209–1221.

BATTULA, V.L. et al. 2009. Isolation of functionally distinct mesenchymal stem cell subsets using antibodies against CD56, CD271, and mesenchymal stem cell antigen-1. *Haematologica*. **94**(2),pp.173–184.

BELL, E., B. IVARSSON and C. MERRILL 1979. Production of a tissue-like structure by contraction of collagen lattices by human fibroblasts of different proliferative potential in vitro. *Proceedings of the National Academy of Sciences of the United States of America*. **76**(3),pp.1274–8.

BELLOTTI, C. et al. 2016. Detection of mesenchymal stem cells senescence by prelamin A accumulation at the nuclear level. *SpringerPlus*. **55**(1),pp.1427–1435.

BERNARDO, M.E., F. LOCATELLI and W.E. FIBBE 2009. Mesenchymal Stromal Cells. *Annals of the New York Academy of Sciences*. **1176**(1),pp.101–117.

BIGHAM, a. S. et al. 2011. Evaluation of osteoinduction properties of the demineralized bovine foetal growth plate powder as a new xenogenic biomaterial in rat. *Research in Veterinary Science*. **91**(2),pp.306–310.

BIRK, D. and R. MAYNE 1997. Localization of collagen types I, III and V during tendon development. Changes in collagen types I and III are correlated with changes in fibril diameter. *European Journal of Cell Biology*. **72**(4),pp.352–361.

BISSERET, D. et al. 2015. Periosteum: Characteristic imaging findings with emphasis on radiologic-pathologic comparisons. *Skeletal radiology*. **44**(3),pp.321–38.

BOSKEY, A.L. 2013. Bone composition: relationship to bone fragility and antiosteoporotic drug effects. *BoneKEy Reports*. **2**(447),pp.1–11.

BOSKEY, A.L. and R. COLEMAN 2010. Aging and Bone. *Journal of Dental Research*. **89**(12),pp.1333–1348.

BOURQUE, W.T., M. GROSS and B.K. HALL 1993. Expression of four growth factors during fracture repair. *The International journal of developmental biology*. **37**(4),pp.573–579.

BROWNLOW, H.C. et al. 2000. Anatomical effects of periosteal elevation. *Journal of Orthopaedic Research*. **18**(3),pp.500–502.

BROWNLOW, H.C., A. REED and A.H.R.W. SIMPSON 2001. Growth factor expression during the development of atrophic non-union. *Injury*. **32**(7),pp.519–524.

BUCKWALTER, J., M. GLIMCHER and R. BECKER 1995. Bone biology. *Journal of Bone and Joint Surgery (American Volume)*. **77**,pp.1256–1275.

BÜHRING, H.-J. et al. 2009. Phenotypic characterization of distinct human bone marrow-derived MSC subsets. *Annals of the New York Academy of Sciences*. **1176**(1),pp.124–134.

CABALLERO, M. et al. 2014. Osteoinduction of Umbilical Cord and Palate Periosteum- Derived Mesenchymal Stem Cells on Poly-Co-Glycolytic Acid Nano-Microfibers. *Annals of Plastic Surgery*. **72**(Suppl 2),pp.S176–S183.

CAETANO-LOPES, J., H. CANHÃO and J.E. FONSECA 2007. Osteoblasts and bone formation. *Acta reumatológica portuguesa*. **32**(2),pp.103–110.

CAI, Y.Z. et al. 2010. Electrospun nanofibrous matrix improves the regeneration of dense cortical bone. *Journal of Biomedical Materials Research - Part A*. **95**(1),pp.49–57.

CALORI, G. et al. 2011. The use of bone graft substitutes in large cancellous voids: Any specific needs? *Injury*. **42**(SUPPL 2),pp.S55–S63.

CALORI, G.M. et al. 2007. Risk factors contributing to fracture non-unions. *Injury*. **38**(Suppl 2),pp.S11-8.

CECCARELLI, G. et al. 2017. In vitro and in vivo studies of alar-nasal cartilage using autologous micro-grafts: The use of the Rigenera® protocol in the treatment of an osteochondral lesion of the nose. *Pharmaceuticals*. **10**(2),pp.1–10.

CHAKRAPANI, V.Y. et al. 2012. Electrospinning of Type I Collagen and PCL Nanofibers Using Acetic Acid. *Journal of Applied Polymer Science*. **125**(1),pp.3221–3227.

CHANG, H. and M. KNOTHE TATE 2012. Concise Review : The Periosteum : Tapping into a Reservoir of Clinically Useful Progenitor Cells. *Stem Cells: Translational Medicine*. **1**(1),pp.480–491.

CHEN, D. et al. 2012. Co-culturing mesenchymal stem cells from bone marrow and periosteum enhances osteogenesis and neovascularization of tissue-engineered bone. *Journal of tissue engineering and regenerative medicine*. **6**(1),pp.822–832.

CHEN, D. et al. 2011. Superior mineralization and neovascularization capacity of adult human metaphyseal periosteum-derived cells for skeletal tissue engineering applications. *International Journal of Molecular Medicine*. **27**(14),pp.707–713.

CHEN, D. et al. 2015. Synergetic effects of hBMSCs and hPCs in osteogenic differentiation and their capacity in the repair of critical-sized femoral condyle defects. *Molecular Medicine Reports*. **11**(2),pp.1111–1119.

CHEN, K. et al. 2015. Decellularized periosteum as a potential biologic scaffold for bone tissue engineering. *Acta Biomaterialia*. **19**(1),pp.46–55.

CHEN, L. et al. 2008. Paracrine Factors of Mesenchymal Stem Cells Recruit Macrophages and Endothelial Lineage Cells and Enhance Wound Healing. *PLoS ONE*. **3**(4),p.e1886.

CHEN, L. et al. 2019. Three-Dimensional Co-Culture of Peripheral Blood-Derived Mesenchymal Stem Cells and Endothelial Progenitor Cells for

Bone Regeneration. *Journal of Biomedical Nanotechnology*. **15**(2),pp.248–260.

CHO, T.-J., L.C. GERSTENFELD and T.A. EINHORN 2002. Differential temporal expression of members of the transforming growth factor beta superfamily during murine fracture healing. *Journal of bone and mineral research*. **17**(3),pp.513–520.

CHONG, E.J. et al. 2007. Evaluation of electrospun PCL/gelatin nanofibrous scaffold for wound healing and layered dermal reconstitution. *Acta Biomaterialia*. **3**(3),pp.321–330.

CHURCHMAN, S.M. et al. 2017. Predicting the Remaining Lifespan and Cultivation-Related Loss of Osteogenic Capacity of Bone Marrow Multipotential Stromal Cells Applicable across a Broad Donor Age Range. *Stem Cells International*. **2017**(Article ID 6129596),pp.1–10.

CHURCHMAN, S.M. et al. 2012. Transcriptional profile of native CD271+ multipotential stromal cells: evidence for multiple fates, with prominent osteogenic and Wnt pathway signaling activity. *Arthritis and Rheumatism*. **64**(8),pp.2632–43.

COLNOT, C. et al. 2003. Altered fracture repair in the absence of MMP9. *Development*. **130**(17),pp.4123–4133.

COLNOT, C. 2011. Cell Sources for Bone Tissue Engineering: Insights from Basic Science. *Tissue Engineering Part B: Reviews*. **17**(6),pp.449–457.

COLNOT, C. 2009. Skeletal cell fate decisions within periosteum and bone marrow during bone regeneration. *Journal of Bone and Mineral Research*. **24**(2),pp.274–282.

CRAIG, A.S. et al. 1989. An estimate of the mean length of collagen fibrils in rat tail-tendon as a function of age. *Connective Tissue Research*. **19**(1),pp.51–62.

CURTIS, E.M. et al. 2016. Epidemiology of fractures in the United Kingdom 1988-2012: Variation with age, sex, geography, ethnicity and socioeconomic status. *Bone*. **87**(3),pp.19–26.

CUTHBERT, R. et al. 2015. Examining the Feasibility of Clinical Grade CD271+ Enrichment of Mesenchymal Stromal Cells for Bone Regeneration. *PloS One*. **10**(3),pp.1–17.

CUTHBERT, R. et al. 2013. Induced periosteum a complex cellular scaffold for the treatment of large bone defects. *Bone*. **57**(2),pp.484–492.

CUTHBERT, R. et al. 2012. Single-platform quality control assay to quantify multipotential stromal cells in bone marrow aspirates prior to bulk manufacture or direct therapeutic use. *Cytotherapy*. **14**(4),pp.431–440.

DAHLIN, C., L. ANDERSSON and A. LINDE 1991. Bone augmentation at fenestrated implants by an osteopromotive membrane technique. A controlled clinical study. *Clinical Oral Implants Research*. **2**(1),pp.159–165.

DEFRATES, K. et al. 2018. Protein-Based Fiber Materials in Medicine: A Review. *Nanomaterials*. **8**(7),pp.457–483.

DHANDAYUTHAPANI, B. et al. 2011. Polymeric Scaffolds in Tissue Engineering Application: A Review. *International Journal of Polymer Science*. **2011**(2),pp.1–19.

DIMITRIOU, R. et al. 2011. Complications following autologous bone graft harvesting from the iliac crest and using the RIA: A systematic review. *Injury*. **42**(SUPPL 2),pp.S3–S15.

DIMITRIOU, R. et al. 2012. The role of barrier membranes for guided bone regeneration and restoration of large bone defects: current experimental and clinical evidence. *BMC Medicine*. **10**(81),pp.1–24.

DIMITRIOU, R., E. TSIRIDIS and P. V. GIANNOUDIS 2005. Current concepts of molecular aspects of bone healing. *Injury*. **36**(12),pp.1392–1404.

DOMINICI, M. et al. 2006. Minimal criteria for defining multipotent mesenchymal stromal cells. The International Society for Cellular Therapy position statement. *Cytotherapy*. **8**(4),pp.315–317.

DWEK, J.R. 2010. The periosteum: What is it, where is it, and what mimics it in its absence? *Skeletal Radiology*. **39**(4),pp.319–323.

EKAPUTRA, A.K. et al. 2011. The three-dimensional vascularization of growth factor-releasing hybrid scaffold of poly (e-caprolactone)/collagen fibers and hyaluronic acid hydrogel. *Biomaterials*. **32**(32),pp.8108–8117.

EL-JAWHARI, J.J. et al. 2016. Collagen-containing scaffolds enhance attachment and proliferation of non-cultured bone marrow multipotential stromal cells. *Journal of Orthopaedic Research*. **34**(4),pp.596–606.

EL-JAWHARI, J.J. et al. 2017. The CD45lowCD271high Cell Prevalence in Bone Marrow Samples May Provide a Useful Measurement of the Bone Marrow Quality for Cartilage and Bone Regenerative Therapy. *Journal of Bone and Joint Surgery (American Volume)*. **99**(15),pp.1305–1313.

EVANS, S.F. et al. 2013. Periosteum, bone's "smart" bounding membrane, exhibits direction-dependent permeability. *Journal of Bone and Mineral Research*. **28**(3),pp.608–617.

EVANS, S.F., H. CHANG and M.L. KNOTHE TATE 2013. Elucidating Multiscale Periosteal Mechanobiology: A Key to Unlocking the Smart Properties and Regenerative Capacity of the Periosteum? *Tissue Engineering Part B: Reviews*. **19**(2),pp.147–159.

EYCKMANS, J., G.L. LIN and C.S. CHEN 2012. Adhesive and mechanical regulation of mesenchymal stem cell differentiation in human bone marrow and periosteum-derived progenitor cells. *Biology Open*. **1**(11),pp.1058–68.

EYRE-BROOK, A. 1984. The periosteum: its function reassessed. *Clinical Orthopaedics and Related Research*. **189**(1),pp.300–7.

FAN, W. et al. 2010. Structural and cellular features in metaphyseal and diaphyseal periosteum of osteoporotic rats. *Journal of Molecular Histology*. **41**(1),pp.51–60.

FAN, W., R. CRAWFORD and Y. XIAO 2008. Structural and cellular differences between metaphyseal and diaphyseal periosteum in different-aged rats. *Bone*. **42**(4),pp.81–89.

FEHRER, C. and G. LEPPERDINGER 2005. Mesenchymal stem cell aging. *Experimental Gerontology*. **40**(1),pp.926–930.

FERNÁNDEZ, A.D. and A.B. LUENGO 2019. Biostimulation of Knee Cartilage Using Autologous Micro-Grafts: A Preliminary Study of the Rigenera Protocol in Osteochondral Lesions of the Knee. *Rehabilitation Science*.

3(1),pp.8–12.

FERREIRA, A.M. et al. 2016. Impact of Collagen/Heparin Multilayers for Regulating Bone Cellular Functions. *ACS Applied Materials & Interfaces*. **8**(44),pp.29923–29932.

FILGUEIRA, L. 2004. Fluorescence-based Staining for Tartrate-resistant Acidic Phosphatase (TRAP) in Osteaclasts Combined with Other Fluorescent Dyes and Protocols. *Journal of Histochemistry and Cytochemistry*. **52**(3),pp.411–414.

FILION, T.M. and J. SONG 2013. A Sulfated Nanofibrous Mesh Supporting the Osteogenic Differentiation of Periosteum-Derived Cells. *Journal of Biomaterials and Tissue Engineering*. **3**(4),pp.486–493.

DE FILIPPO, C.M. et al. 2019. Isolation of clinically relevant concentrations of bone marrow mesenchymal stem cells without centrifugation. *Journal of Translational Medicine*. **17**(1),pp.1–10.

FOOLEN, J. et al. 2008. Collagen orientation in periosteum and perichondrium is aligned with preferential directions of tissue growth. *Journal of Orthopaedic Research*. **26**(9),pp.1263–1268.

FOSSETT, E. and W.S. KHAN 2012. Optimising Human Mesenchymal Stem Cell Numbers for Clinical Application:A Literature Review. *Stem Cells International*. **2012**(Article ID 465259),pp.1–5.

DE FRANCESCO, F. et al. 2018. A non-enzymatic method to obtain a fat tissue derivative highly enriched in adipose stem cells (ASCs) from human lipoaspirates: Preliminary results. *International Journal of Molecular Sciences*. **19**(7),pp.2061–2063.

FRANCHI, M. et al. 2007. Collagen structure of tendon relates to function. *TheScientificWorldJournal*. **7**,pp.404–420.

FREY, S.P. et al. 2013. Immunohistochemical and Molecular Characterization of the Human Periosteum. *The Scientific World Journal*. **2013**(Article ID 341078),pp.1–8.

FROUM, S., S.-C. CHO and L. PARIENTE 2012. *A Surgical Protocol for Guided Bone Regeneration Procedures: Using Absorbable Membranes to Minimize and Treat Complications*.

GARG, N., S. GAUR and S. SHARMA 1993. Percutaneous autogenous bone marrow grafting in 20 cases of ununited fracture. *Acta Orthop Scand*. **64**(6),pp.671–2.

GEE, A. 2018. Regulation of Regenerative Medicine Products. *Adv Exp Med Biol*. **1098**(1),pp.189–198.

GERSTENFELD, L., D. CULLINANE, et al. 2003. Fracture healing as a post-natal developmental process: Molecular, spatial, and temporal aspects of its regulation. *Journal of Cellular Biochemistry*. **88**(5),pp.873–884.

GERSTENFELD, L., T.J. CHO, et al. 2003. Impaired fracture healing in the absence of TNF-alpha signaling: the role of TNF-alpha in endochondral cartilage resorption. *Journal of Bone and Mineral Research*. **18**(9),pp.1584–1592.

GERSTENFELD, L. et al. 2006. Three-dimensional reconstruction of fracture callus morphogenesis. *The journal of histochemistry and cytochemistry : official journal of the Histochemistry Society*. **54**(11),pp.1215–1228.

GIACCONE, M. et al. 2014. A New Medical Device, Based on Rigenera Protocol, in the Management of Complex Wounds. *Journal of Stem Cells Research, Reviews and Reports*. **1**(3),pp.3–5.

GIANNOUDIS, P. V, H. DINOPOULOS and E. TSIRIDIS 2005. Bone substitutes: an update. *Injury*. **36**(Suppl 3),pp.S20–S27.

GIANNOUDIS, P. V, T.A. EINHORN and D. MARSH 2007. Fracture healing: The diamond concept. *Injury*. **38**(Suppl 4),pp.S3–S6.

GONG, M. et al. 2019. Core-sheath micro/nano fiber membrane with antibacterial and osteogenic dual functions as biomimetic artificial periosteum for bone regeneration applications. *Nanomedicine: Nanotechnology, Biology and Medicine*. **17**(1),pp.124–136.

GOODING, C.R. et al. 2006. A prospective, ranomised study comparing two techniques of autologous chondrocyte implantation for osteochondral defects in the knee: Periosteum covered versus type I/III collagen covered. *Knee*. **13**(3),pp.203–210.

GRANERO-MOLTÓ, F. et al. 2012. Regenerative Effects of Transplanted Mesenchymal Stem Cells in Fracture Healing. *Stem Cells*. **27**(8),pp.1887–1898.

GRAZIANO, A. et al. 2013. Periodontal tissue generation using autologous dental ligament micro-grafts: case report with 6 months follow-up. *Annals of Oral and Maxillofacial Surgery*. **1**(2),pp.20–25.

GREGORY, C. et al. 2004. An Alizarin red-based assay of mineralization by adherent cells in culture: comparison with cetylpyridinium chloride extraction. *Analytical Biochemistry*. **329**(1),pp.77–84.

GUSTILO, R., R. MENDOZA and D. WILLIAMS 1984. Problems in the management of type III (severe) open fractures: a new classification of type III open fractures. *Journal of Trauma*. **24**(8),pp.742–6.

HAK, D.J. et al. 2014. Delayed union and nonunions: Epidemiology, clinical issues, and financial aspects. *Injury*. **45**(SUPPL 2),pp.S3–S7.

HARRY, L.E. et al. 2008. Comparison of the Healing of Open Tibial Fractures Covered with Either Muscle or Fasciocutaneous Tissue in a Murine Model. *Journal of Orthopaedic Research*. **26**(1),pp.1238–1244.

HASS, R. et al. 2011. Different populations and sources of human mesenchymal stem cells (MSC): A comparison of adult and neonatal tissue-derived MSC. *Cell communication and signaling : CCS*. **9**(1),p.12.

HE, Q., C. WAN and G. LI 2007. Concise review: multipotent mesenchymal stromal cells in blood. *Stem cells*. **25**(1),pp.69–77.

HENRICH, D. et al. 2016. Establishment and characterization of the Masquelet induced membrane technique in a rat femur critical-sized defect model. *Journal of Tissue Engineering and Regenerative Medicine*. **10**(10),pp.E382–E396.

HERNIGOU, J. et al. 2014. Understanding bone safety zones during bone marrow aspiration from the iliac crest: the sector rule. *International Orthopaedics*. **38**(11),pp.2377–2384.

HERNIGOU, P. et al. 2013. Benefits of small volume and small syringe for bone marrow aspirations of mesenchymal stem cells. *International Orthopaedics*. **37**(11),pp.2279–2287.

HERNIGOU, P. et al. 2014. Morbidity of graft harvesting versus bone marrow aspiration in cell regenerative therapy. *International Orthopaedics*. **38**(9),pp.1855–1860.

HERNIGOU, P. et al. 2005. The use of percutaneous autologous bone marrow transplantation in nonunion and avascular necrosis of bone. *Journal of Bone and Joint Surgery (British Volume)*. **87**(7),pp.896–902.

HERRING, S.W. and P. OCHAREON 2016. The Periosteum of the Zygomatic Arch: Vascularization and Growth. *Anatomical Record*. **299**(12),pp.1661–1670.

HO, W. et al. 2006. The behavior of human mesenchymal stem cells in 3D fibrin clots: dependence on fibrinogen concentration and clot structure. *Tissue engineering*. **12**(6),pp.1587–1595.

HONCZARENKO, M. et al. 2005. Human Bone Marrow Stromal Cells Express a Distinct Set of Biologically Functional Chemokine Receptors. *Stem Cells*. **24**(4),pp.1030–1041.

HOSOYA, A. et al. 2005. Effects of fixation and decalcification on the immunohistochemical localization of bone matrix proteins in fresh-frozen bone sections. *Histochemistry and Cell Biology*. **123**(6),pp.639–646.

HOSSAIN, N. and M. BARRY 2011. Focus on Management of traumatic bone loss. *Journal of Bone and Joint Surgery (British volume)*,pp.1–3.

IPPOLITO, G.D. et al. 1999. Age-Related Osteogenic Potential of Mesenchymal Stromal Stem Cells from Human Vertebral Bone Marrow. *Journal of Bone and Mineral Research*. **14**(7),pp.1115–1122.

IROKAWA, D. et al. 2017. Clinical outcome of periodontal regenerative therapy using collagen membrane and deproteinized bovine bone mineral: a 2.5-year follow-up study. *BMC Research Notes*. **10**(1),pp.1–8.

ISENBERG, B.C. and J.Y. WONG 2006. Building structure into engineered tissues. *Materials Today*. **9**(12),pp.54–60.

ITO, T. et al. 2008. FGF-2 increases osteogenic and chondrogenic differentiation potentials of human mesenchymal stem cells by inactivation of TGF-?? signaling. *Cytotechnology*. **56**(1),pp.1–7.

IVIGLIA, G., S. KARGOZAR and F. BAINO 2019. *Biomaterials, current strategies, and novel nano-technological approaches for periodontal regeneration*.

JACKSON, W.M., L.J. NESTI and R.S. TUAN 2010. Potential therapeutic applications of muscle-derived mesenchymal stem and progenitor cells. *Expert Opin Biol Ther.* **10**(4),pp.505–517.

JÄGER, M. et al. 2011. Bridging the gap: Bone marrow aspiration concentrate reduces autologous bone grafting in osseous defects. *Journal of Orthopaedic Research*. **29**(2),pp.173–180.

JHA, B.S. et al. 2011. Electrospun Collagen: A Tissue Engineering Scaffold with Unique Functional Properties in a Wide Variety of Applications. *Journal of Nanomaterials*. **2011**,pp.1–15.

JI, W. et al. 2013. Incorporation of stromal cell-derived factor-1a in PCL/gelatin electrospun membranes for guided bone regeneration. *Biomaterials*. **34**(3),pp.735–745.

JIN JIN, H. et al. 2013. Comparative Analysis of Human Mesenchymal Stem

Cells from Bone Marrow, Adipose Tissue, and Umbilical Cord Blood as Sources of Cell Therapy. *International Journal of Molecular Sciences*. **14**(9),pp.17986–18001.

JING, D. et al. 2013. Characterisation of Human Mesenchymal Stem Cells: Expansion in a 3-L, Single-Use, Stirred-Tank Bioreactor. *BioProcess International*. **11**(Suppl 3),pp.S30–S36.

JONES, E.A. et al. 2002. Isolation and Characterization of Bone Marrow Multipotential Mesenchymal Progenitor Cells. *Arthritis and Rheumatism*. **46**(12),pp.3349–3360.

JUNG, R.E. et al. 2013. Long-term outcome of implants placed with guided bone regeneration (GBR) using resorbable and non-resorbable membranes after 12-14 years. *Clinical Oral Implants Research*. **24**(10),pp.1065–1073.

JUNG, S. and J. KLEINHEINZ 2014. Adult Mesenchymal Stem Cells in Current Tissue Engineering Concepts *In*: *Cells and Biomaterials in Regenerative Medicine*., pp. 103–118.

JUNQUEIRA, L., G. BIGNOLAS and R. BRENTANI 1979. Picrosirius staining plus polarization microscopy, a specific method for collagen detection in tissue sections. *The Histochemical Journal*. **11**(4),pp.447–455.

KADERLY, R. 1991. Primary bone healing. *Seminars in Veterinary Medicine and Surgery (Small Animals)*. **6**(1),pp.21–25.

KALLIFATIDIS, G. et al. 2008. Improved lentiviral transduction of human mesenchymal stem cells for therapeutic intervention in pancreatic cancer. *Cancer Gene Therapy*. **15**(4),pp.231–240.

KARSDAL, M. 2016. *Biochemistry of Collagens, Laminins and Elastin*.

KAWASE, T. et al. 2016. Non-invasive, quantitative assessment of the morphology of γ-irradiated human mesenchymal stem cells and periosteal cells using digital holographic microscopy. *International Journal of Radiation Biology*. **92**(12),pp.796–805.

KHOJASTEH, A. et al. 2017. Bone engineering in dog mandible : Coculturing mesenchymal stem cells with endothelial progenitor cells in a composite scaffold containing vascular endothelial growth factor. *Journal of Biomedical Materials Research B Applications of Biomaterials*. **105**(7),pp.1767–1777.

KIM, K., S. PARK and G. IM 2014. Osteogenic differentiation and angiogenesis with cocultured adipose-derived stromal cells and bone marrow stromal cells. *Biomaterials*. **35**(17),pp.4792–4804.

KISIEL, A. et al. 2012. Isolation, characterization, and in vitro proliferation of canine mesenchymal stem cells derived from bone marrow, adipose tissue, muscle, and periosteum. *American Journal of Veterinary Research*. **73**(8),pp.1305–1317.

KITAORI, T. et al. 2009. Stromal cell-derived factor 1/CXCR4 signaling is critical for the recruitment of mesenchymal stem cells to the fracture site during skeletal repair in a mouse model. *Arthritis and Rheumatism*. **60**(3),pp.813–23.

KNIGHT, M.N. and K.D. HANKENSON 2013. Mesenchymal Stem Cells in Bone Regeneration. *Advances in wound care*. **2**(6),pp.306–316.

KNOTHE TATE, M.L. et al. 2016. Periosteum mechanobiology and mechanistic insights for regenerative medicine. *BoneKEy Reports*. **5**(857),pp.1–6.

KOMORI, T. 2010. Regulation of Osteoblast Differentiation by Runx2. *Advances in Experimental Medicine and Biology*. **658**(1),pp.43–9.

KOUROUPIS, D. et al. 2013. Native multipotential stromal cell colonization and graft expander potential of a bovine natural bone scaffold. *Journal of Orthopaedic Research*. **31**(12),pp.1950–8.

KOVAR, F.M. and G.E. WOZASEK 2011. Bone graft harvesting using the RIA (reaming irrigation aspirator) system - a quantitative assessment. *Wien Klin Wochenschr*. **123**(9–10),pp.285–290.

KUBISTA, M., B. AAKERMAN and B. NORDEN 1987. Characterization of interaction between DNA and 4',6-diamidino-2-phenylindole by optical spectroscopy. *Biochemistry*. **26**(14),pp.4545–4553.

KUROSE, T. et al. 2006. Distribution and change of collagen types I and III and elastin in developing leg muscle in rat. *Hiroshima Journal of Medical Sciences*. **55**(3),pp.85–91.

KUZNETSOV, S.A. et al. 2001. Circulating skeletal stem cells. *The Journal of cell biology*. **153**(5),pp.1133–40.

LEE, C.H., A. SINGLA and Y. LEE 2001. Biomedical applications of collagen. *International Journal of Pharmaceutics*. **221**(1),pp.1–22.

LEE, D.W. et al. 2015. The role of two different collagen membranes for dehiscence defect around implants in humans. *Journal of Oral Implantology*. **41**(4),pp.445–449.

LEHMANN, W. et al. 2005. Tumor necrosis factor alpha (TNF-a) coordinately regulates the expression of specific matrix metalloproteinases (MMPS) and angiogenic factors during fracture healing. *Bone*. **36**(2),pp.300–310.

LERNER, U.H. 2012. Osteoblasts, Osteoclasts, and Osteocytes: Unveiling Their Intimate-Associated Responses to Applied Orthodontic Forces. *Seminars in Orthodontics*. **18**(4),pp.237–248.

LI, Y. et al. 2015. Fibrin gel as an injectable biodegradable scaffold and cell carrier for tissue engineering. *Scientific World Journal*. **2015**(Article ID 685690),pp.1–10.

LIANG, H. et al. 2018. Monomer-Induced Customization of UV-Cured Atelocollagen Hydrogel Networks. *Frontiers in Chemistry*. **6**(1),pp.1–14.

LIN, T.W., L. CARDENAS and L.J. SOSLOWSKY 2004. Biomechanics of tendon injury and repair. *Journal of Biomechanics*. **37**(6),pp.865–877.

LIN, Z. et al. 2014. Periosteum: biology and applications in craniofacial bone regeneration. *Journal of dental research*. **93**(2),pp.109–16.

LIU, R. et al. 2011. Myogenic progenitors contribute to open but not closed fracture repair. *BMC Musculoskeletal Disorders*. **12**(1),pp.288–296.

LOI, F. et al. 2016. Inflammation, fracture and bone repair. *Bone*. **86**(1),pp.119–130.

LUKAS, D., A. SARKAR and P. POKORNY 2008. Self-organization of jets in electrospinning from free liquid surface: A generalized approach. *Journal of Applied Physics*. **103**(8),pp.1–7.

LUNDGREN, D. et al. 1994. The use of a new bioresorbable barrier for guided

bone regeneration in connection with implant installation. *Clinical Oral Implants Research*. **5**(1),pp.177–184.

LV, F.-J. et al. 2014. Concise Review: The Surface Markers and Identity of Human Mesenchymal Stem Cells. *Stem Cells*. **32**(6),pp.1408–1419.

LYNN, A.K., I. V YANNAS and W. BONFIELD 2004. Antigenicity and Immunogenicity of Collagen. *Journal of Biomedical Materials Research B Applications of Biomaterials*. **71**(2),pp.343–354.

MA, S. et al. 2014. Guided bone regeneration with tripolyphosphate cross-linked asymmetric chitosan membrane. *Journal of Dentistry*. **42**(12),pp.1603–1612.

MA, T. 2010. Mesenchymal stem cells: From bench to bedside. *World Journal of Stem Cells*. **2**(2),pp.13–17.

MAFI, R. et al. 2011. Sources of adult mesenchymal stem cells applicable for musculoskeletal applications - a systematic review of the literature. *The Open Orthopaedics Journal*. **5**(Suppl 2),pp.242–248.

MAINI, L. et al. 2000. The Ilizarov method in infected nonunion of fractures. *Injury*. **31**(7),pp.509–517.

MALIZOS, K.N. and L.K. PAPATHEODOROU 2005. The healing potential of the periosteum. *Injury*. **36**(Suppl 3),pp.S13–S19.

MAO, N. 2016. *Methods for characterisation of nonwoven structure, property, and performance*. Elsevier Ltd.

MARCARELLI, M. et al. 2017. Rigenera protocol in the treatment of surgical wound dehiscence. *International Wound Journal*. **14**(1),pp.277–281.

MARSELL, R. and T. EINHORN 2011. The Biology of Fracture Healing. *Injury*. **42**(6),pp.551–555.

MARTINEZ, C. et al. 2007. Human bone marrow mesenchymal stromal cells express the neural ganglioside GD2: a novel surface marker for the identification of MSCs. *Blood*. **109**(10),pp.4245–4248.

MASQUELET, A. and T. BEGUE 2010. The Concept of Induced Membrane for Reconstruction of Long Bone Defects. *Orthopedic Clinics of North America*. **41**(1),pp.27–37.

MCGOVERN, J.A., M. GRIFFIN and D.W. HUTMACHER 2018. Animal models for bone tissue engineering and modelling disease. *Disease Models and Mechanisms*. **11**(4),pp.1–14.

MERCURIO, A.D. et al. 2012. Effects of extensive circumferential periosteal stripping on the microstructure and mechanical properties of the murine femoral cortex. *Journal of Orthopaedic Research*. **30**(4),pp.561–568.

MEYER, M., H. BALTZER and K. SCHWIKAL 2010. Collagen fibres by thermoplastic and wet spinning. *Materials Science and Engineering: C*. **30**(8),pp.1266–1271.

MIDWOOD, K.S. et al. 2016. Tenascin-C at a glance. *Journal of Cell Science*. **129**(23),pp.4321–4327.

MIDWOOD, K.S. and G. OREND 2009. The role of tenascin-C in tissue injury and tumorigenesis. *J Cell Commun Signal*. **3**(3–4),pp.287–310.

MILLS, L.A., S.A. AITKEN and A.H.R.W. SIMPSON 2017. The risk of non-union per fracture: current myths and revised figures from a population of over 4 million adults. *Acta Orthopaedica*. **88**(4),pp.434–439.

MILLS, L.A. and A.H.R.W. SIMPSON 2013. The relative incidence of fracture non-union in the Scottish population (5.17 million): a 5-year epidemiological study. *BMJ Open*. **3**(e002276),pp.1–6.

MINUTH, W.W. and L. DENK 2012. Supportive development of functional tissues for biomedical research using the MINUSHEET® perfusion system. *Clinical and Translational Medicine*. **1**(1),pp.22–36.

MOCHIZUKI, T. et al. 2006. Higher chondrogenic potential of fibrous synovium- and adipose synovium-derived cells compared with subcutaneous fat-derived cells: Distinguishing properties of mesenchymal stem cells in humans. *Arthritis and Rheumatism*. **54**(3),pp.843–853.

MOORE, S.R., S. MILZ and M.L. KNOTHE TATE 2014. Periosteal thickness and cellularity in mid-diaphyseal cross-sections from human femora and tibiae of aged donors. *Journal of Anatomy*. **224**(2),pp.142–149.

MUSCHLER, G.F. et al. 2003. Spine Fusion Using Cell Matrix Composites Enriched in Bone Marrow-Derived Cells. *Clin Orthop Relat Res*. **1**(407),pp.102–118.

MUSCHLER, G.F., C. BOEHM and K. EASLEY 1997. Aspiration to obtain osteoblast progenitor cells from human bone marrow: the influence of aspiration volume. *Journal of Bone and Joint Surgery (American Volume)*. **79**(11),pp.1699–709.

NAKAMURA, A. et al. 2009. Osteocalcin secretion as an early marker of in vitro osteogenic differentiation of rat mesenchymal stem cells. *Tissue Eng Part C Methods*. **15**(2),pp.169–80.

NAKAMURA, Y. et al. 2010. Isolation and characterization of endosteal niche cell populations that regulate hematopoietic stem cells. *Blood*. **116**(9),pp.1422–1432.

NAUNG, N.Y., E. SHEHATA and J.E. VAN SICKELS 2019. Resorbable Versus Nonresorbable Membranes: When and Why? *Dental Clinics of North America*. **63**(3),pp.419–431.

NAUTH, A. et al. 2015. Bone graft substitution and augmentation. *Journal of Orthopaedic Trauma*. **29**(12),pp.S34–S38.

NESTI, L.J. 2008. Differentiation Potential of Multipotent Progenitor Cells Derived from War-Traumatized Muscle Tissue. *Journal of Bone and Joint Surgery (American Volume)*. **90**(11),pp.2390–2398.

NICOLAIDOU, V. et al. 2012. Monocytes Induce STAT3 Activation in Human Mesenchymal Stem Cells to Promote Osteoblast Formation. *PLoS ONE*. **7**(7),pp.1–16.

NOORT, W.A. et al. 2011. Human versus porcine mesenchymal stromal cells: phenotype, differentiation potential, immunomodulation and cardiac improvement after transplantation. *Journal of Cellular and Molecular Medicine*. **16**(8),pp.1827–1839.

OGISO, B. et al. 1991. Fibroblasts Inhibit Mineralised Bone Nodule Formation by Rat Bone Marrow Stromal Cells In Vitro. *Journal of Cellular Physiology*. **146**(1),pp.442–450.

OMAR, O. et al. 2019. Barrier membranes: More than the barrier effect? *Journal of Clinical Periodontology*. **46**(S21),pp.103–123.

ORYAN, A., S. ALIDADI and A. MOSHIRI 2013. Current concerns regarding healing of bone defects. *Hard Tissue*. **2**(2),pp.1–12.

OWSTON, H., P.V. GIANNOUDIS and E. JONES 2016. Do skeletal muscle MSCs in humans contribute to bone repair? A systematic review. *Injury*. **47**(Suppl 6),pp.S3–S15.

OZAKI, A. et al. 2000. Role of fracture hematoma and periosteum during fracture healing in rats: interaction of fracture hematoma and the periosteum in the initial step of the healing process. *Journal of Orthopaedic Science*. **5**(1),pp.64–70.

PANAGIOTIS, M. 2005. Classification of non-union. *Injury*. **36**(Suppl 4),pp.S30–S37.

PANTELI, M. et al. 2015. Biological and molecular profile of fracture non-union tissue: current insights. *Journal of Cellular and Molecular Medicine*. **19**(4),pp.685–713.

PAT, S. et al. 2016. Heavily carbon doped GaAs nanocrystalline thin film deposited by thermionic vacuum arc method. *Journal of Alloys and Compounds*. **657**(1),pp.711–716.

PERSANO, L. et al. 2013. Industrial upscaling of electrospinning and applications of polymer nanofibers: A review. *Macromolecular Materials and Engineering*. **298**(5),pp.504–520.

PETECCHIA, L., F. VITI, et al. 2017. A biophysical approach to quantify skeletal stem cells trans-differentiation as a model for the study of osteoporosis. *Biophysical Chemistry*. **229**(1),pp.84–92.

PETECCHIA, L., C. USAI, et al. 2017. Biophysical characterization of nanostructured TiO2 as a good substrate for hBM-MSC adhesion, growth and differentiation. *Experimental Cell Research*. **358**(2),pp.111–119.

PHILIPPART, P. et al. 2014. *In Vivo* Production of Mesenchymal Stromal Cells After Injection of Autologous Platelet-Rich Plasma Activated by Recombinant Human Soluble Tissue Factor in the Bone Marrow of Healthy Volunteers. *Tissue Engineering Part A*. **20**(1–2),pp.160–170.

PHILLIPS, A. 2005. Overview of the fracture healing cascade. *Injury*. **36**(Suppl 3),pp.S5–S7.

PHIPPS, M.C. et al. 2012. Increasing the pore sizes of bone-mimetic electrospun scaffolds comprised of polycaprolactone, collagen I and hydroxyapatite to enhance cell infiltration. *Biomaterials*. **33**(2),pp.524–534.

PHIPPS, M.C. et al. 2011. Mesenchymal stem cell responses to bone-mimetic electrospun matrices composed of polycaprolactone, collagen I and nanoparticulate hydroxyapatite. *PLoS ONE*. **6**(2),pp.1–8.

PONTE, A.L. et al. 2007. The In Vitro Migration Capacity of Human Bone Marrow Mesenchymal Stem Cells: Comparison of Chemokine and Growth Factor Chemotactic Activities. *Stem Cells*. **25**(7),pp.1737–1745.

POPOWICS, T.E., Z. ZHU and S.W. HERRING 2002. Mechanical properties of the periosteum in the pig, Sus scrofa. *Archives of Oral Biology*. **47**(10),pp.733–741.

QU, F. 2019. Cell migration: implications for repair and regeneration in joint disease. *Nature Reviews Rheumatology*. **15**(1),pp.167–179.

RADTKE, C.L. et al. 2013. Characterization and osteogenic potential of equine muscle tissue– and periosteal tissue–derived mesenchymal stem cells in comparison with bone marrow– and adipose tissue–derived mesenchymal stem cells. *American Journal of Veterinary Research*. **74**(5),pp.790–800.

RAJENDRAN, R. et al. 2013. Regenerative potential of dental pulp mesenchymal stem cells harvested from high caries patient's teeth. *J Stem Cells*. **8**(1),pp.25–41.

REN, K. et al. 2017. Electrospun PCL/gelatin composite nanofiber structures for effective guided bone regeneration membranes. *Materials Science and Engineering C*. **78**(1),pp.324–332.

REVERTE, M.M. et al. 2011. What is the effect of compartment syndrome and fasciotomies on fracture healing in tibial fractures? *Injury*. **42**,pp.1402–1407.

REYA, T. et al. 2001. Stem cells, cancer, and cancer stem cells. *Nature*. **414**(1),pp.105–111.

RIBEIRO, N. et al. 2014. A biocomposite of collagen nanofibers and nanohydroxyapatite for bone regeneration. *Biofabrication*. **6**(3),pp.1–10.

RICARD-BLUM, S. 2011. The Collagen Family. *Cold Spring Harbor Perspectives in Biology*. **3**(1),pp.1–19.

ROBERTS, S.J. et al. 2015. Uncovering the periosteum for skeletal regeneration: The stem cell that lies beneath. *Bone*. **70**(1),pp.10–18.

ROSEN, C.J. et al. 2012. Marrow Fat and the Bone Microenvironment: Developmental, Functional, and Pathological Implications. *Critical Reviews™ in Eukaryotic Gene Expression*. **19**(2),pp.109–124.

ROTHAMEL, D. et al. 2005. Biodegradation of differently crosslinked collagen membranes: An experimental study in the rat. *Clinical Oral Implants Research*. **16**(3),pp.369–378.

ROZBRUCH, S.R. et al. 2008. Limb lengthening and then insertion of an intramedullary nail: a case-matched comparison. *Clinical orthopaedics and related research*. **466**(12),pp.2923–32.

RUBIO-AZPEITIA, E. and I. ANDIA 2014. Partnership between platelet-rich plasma and mesenchymal stem cells : in vitro experience Corresponding author : *Muscles, ligaments and tendons journal*. **4**(1),pp.52–62.

SACCHETTI, B. et al. 2007. Self-renewing osteoprogenitors in bone marrow sinusoids can organize a hematopoietic microenvironment. *Cell*. **131**(2),pp.324–336.

SAKAGUCHI, Y. et al. 2005. Comparison of Human Stem Cells Derived From Various Mesenchymal Tissues Superiority of Synovium as a Cell Source. *Arthritis & Rheumatism*. **52**(8),pp.2521–2529.

SAKAGUCHI, Y. et al. 2009. Suspended cells from trabecular bone by collagenase digestion become virtually identical to mesenchymal stem cells obtained from marrow aspirates. *Stem Cells*. **104**(9),pp.2728–2735.

SAMPAIO DE MARA, C. et al. 2011. Periosteum as a source of mesenchymal stem cells: the effects of TGF-β3 on chondrogenesis. *Clinics*. **66**(3),pp.487–92.

SANTOS, A., A.D. BAKKER and J. KLEIN-NULEND 2009. The role of

osteocytes in bone mechanotransduction. *Osteoporosis international*. **20**(6),pp.1027–1031.

SCHEMITSCH, E.H. 2017. Size Matters: Defining Critical in Bone Defect Size! *Journal of Orthopaedic Trauma*. **31**(Suppl 10),pp.S20–S22.

SCHENK, R. and E. HUNZIKER 1994. Histologic and ultrastructural features of fracture healing C. Brighton, G. Friedlander, & J. Lane, eds. *Bone Formation and Repair*. **1**(1),pp.117–145.

SCHENK, R.K. et al. 1997. Healing pattern of bone regeneration in membrane-protected defects: a histologic study in the canine mandible. *The International Journal of Oral & Maxillofacial Implants*. **9**(1),pp.13–29.

SCHNEIDER, D. and B. SCHULTRICH 1998. Elastic modulus: A suitable quantity for characterization of thin films. *Surface and Coatings Technology*. **98**(1–3),pp.962–970.

SCOTTI, C. et al. 2013. Engineering of a functional bone organ through endochondral ossification. *Proceedings of the National Academy of Sciences of the United States of America*. **110**(10),pp.3997–4002.

SEAGRAVE, R. et al. 2014. Utilizing reamer irrigator aspirator (RIA) autograft for opening wedge high tibial osteotomy: A new surgical technique and report of three cases. *Int J Surg Case Rep*. **5**(1),pp.37–42.

SHAO, J., W. ZHANG and T. YANG 2015. Using mesenchymal stem cells as a therapy for bone regeneration and repairing. *Biological Research*. **48**(62),pp.1–7.

SHAPIRO, F. 1988. Cortical bone repair. The relationship of the lacunar-canalicular system and intercellular gap junctions to the repair process. *Journal of Bone and Joint Surgery (American Volume)*. **70**(7),pp.1067–81.

SHI, S., M. KIRK and a J. KAHN 1996. The role of type I collagen in the regulation of the osteoblast phenotype. *Journal of bone and mineral research*. **11**(8),pp.1139–45.

SHI, X. et al. 2014. Periosteum-Mimetic Structures Made from Freestanding Microgrooved Nanosheets. *Advanced Materials*. **26**(1),pp.3290–3296.

SHIBUYA, N. and D.C. JUPITER 2015. Bone Graft Substitute. *Clinics in Podiatric Medicine and Surgery*. **32**(1),pp.21–34.

SIAR, C.H. et al. 2011. Subcutaneous reactions and degradation characteristics of collagenous and noncollagenous membranes in a macaque model. *Clinical Oral Implants Research*. **22**(1),pp.113–120.

SIBOV, T.T. et al. 2012. Mesenchymal stem cells from umbilical cord blood: parameters for isolation, characterization and adipogenic differentiation. *Cytotechnology*. **64**(5),pp.511–521.

SIEGEL, G. et al. 2013. Phenotype, donor age and gender affect function of human bone marrow-derived mesenchymal stromal cells. *BMC Medicine*. **11**(146),pp.1–20.

SIMPSON, A.H. 1985. The blood supply of the periosteum. *Journal of anatomy*. **140**(4),pp.697–704.

SINCLAIR, S. and K. BURG 2011. Effect of osteoclast co-culture on the differentiation of human mesenchymal stem cells grown on bone graft granules. *Journal of Biomaterials Science, Polymer Edition*. **22**(4–

6),pp.789–808.

SIVAKUMAR, R. et al. 2016. Management of Large Bone Defects in Diaphyseal Fractures by Induced Membrane Formation by Masquelet's Technique. *Journal of Orthopaedic Case Reports*. **6**(3),pp.59–62.

SIVASUBRAMANIYAN, K. et al. 2013. Prospective Isolation of Mesenchymal Stem Cells from Human Bone Marrow Using Novel Antibodies Directed Against Sushi Domain Containing 2. *Stem Cells and Development*. **22**(13),pp.1944–1954.

SMITH, B.D. and D. a. GRANDE 2015. The current state of scaffolds for musculoskeletal regenerative applications. *Nature Reviews Rheumatology*. **11**(4),pp.213–222.

SOBIESIAK, M. et al. 2010. The Mesenchymal Stem Cell Antigen MSCA-1 is Identical to Tissue Non-specific Alkaline Phosphatase. *Stem Cells and Development*. **19**(5),pp.669–677.

SPICER, P.P. et al. 2012. Evaluation of bone regeneration using the rat critical size calvarial defect. *Nature protocols*. **7**(10),pp.1918–29.

SQUIER, C.A., S. GHONEIM and C.R. KREMENAK 1990. Ultrastructure of the periosteum from membrane bone. *J. Anat*. **171**(1),pp.233–239.

STACHEWICZ, U. et al. 2015. 3D imaging of cell interactions with electrospun PLGA nanofiber membranes for bone regeneration. *Acta Biomaterialia*. **27**(1),pp.88–100.

STICH, S. et al. 2017. Characterization of single cell derived cultures of periosteal progenitor cells to ensure the cell quality for clinical application. *PLoS ONE*. **12**(5),pp.1–17.

STOLZING, A. et al. 2008. Age-related changes in human bone marrow-derived mesenchymal stem cells : Consequences for cell therapies. *Mechanisms of Ageing and Development*. **129**(1),pp.163–173.

TAN, H. et al. 2015. The systemic influence of platelet-derived growth factors on bone marrow mesenchymal stem cells in fracture patients. *BMC Medicine*. **13**(1),pp.6–16.

TARCHALA, M. et al. 2018. A pilot study: Alternative biomaterials in critical sized bone defect treatment. *Injury*. **49**(3),pp.523–531.

TEJEDA-MONTES, E. et al. 2014. Bioactive membranes for bone regeneration applications: Effect of physical and biomolecular signals on mesenchymal stem cell behavior. *Acta Biomaterialia*. **10**(1),pp.134–141.

THÉBAUD, N.B. et al. 2012. Whatever their differentiation status , human progenitor derived – or mature – endothelial cells induce osteoblastic differentiation of bone marrow stromal cells. *Journal of Tissue Engineering and Regenerative Medicine*. **6**(1),pp.E51–E60.

TOHMA, Y. et al. 2017. Reg gene expression in periosteum after fracture and its in vitro induction triggered by IL-6. *International Journal of Molecular Sciences*. **18**(11),pp.1–15.

TORMIN, A. et al. 2011. CD146 expression on primary nonhematopoietic bone marrow stem cells is correlated with in situ localization. *Blood*. **117**(19),pp.5067–5077.

TRAPPMANN, B. et al. 2012. Extracellular-matrix tethering regulates stem-cell fate. *Nature Materials*. **11**(7),pp.642–649.

TRONCI, G. et al. 2016. Protease-sensitive atelocollagen hydrogels promote healing in a diabetic wound model in a diabetic wound model. *Journal of Materials Chemistry B*. **4**(1),pp.5475–5485.

TRONCI, G., S.J. RUSSELL and D.J. WOOD 2013. Photo-active collagen systems with controlled triple helix architecture. *Journal of Materials Chemistry B Materials in Biological Medicine*. **1**(30),pp.3705–3715.

TURBAK, A. 1993. *Nonwovens: Theory, Process, Performance, and Testing*. Tappi Pr.

TZIOUPIS, C. and P. V GIANNOUDIS 2007. Prevalence of long-bone non-unions. *Injury*. **38**(Suppl 2),pp.S3–S9.

UEMATSU, K. et al. 2013. Application of stem-cell media to explant culture of human periosteum: An optimal approach for preparing osteogenic cell material. *Journal of Tissue Engineering*. **4**(1),pp.1–12.

UMRATH, F. et al. 2018. Comparative Study of MSCA-1 and CD146 Isolated Periosteal Cell Subpopulations. *Cellular Physiology and Biochemistry*. **51**(3),pp.1193–1206.

UNDALE, A.H. et al. 2009. Mesenchymal stem cells for bone repair and metabolic bone diseases. *Mayo Clinic proceedings. Mayo Clinic*. **84**(10),pp.893–902.

UPPAL, H.S. et al. 2013. The viability of cells obtained using the Reamer-Irrigator-Aspirator system and in bone graft from the iliac crest. *Bone and Joint Journal*. **95 B**(9),pp.1269–1274.

UTVÅG, S., O. GRUNDNES and O. REIKERAOS 1996. Effects of periosteal stripping on healing of segmental fractures in rats. *Journal of Orthopaedic Trauma*. **10**(4),pp.279–84.

UYAR, T. and E. KNY 2017. *Chapter 3 - Biomedical applications of electrospinning, innovations, and products*.

VAQUETTE, C. and J.J. COOPER-WHITE 2011. Increasing electrospun scaffold pore size with tailored collectors for improved cell penetration. *Acta Biomaterialia*. **7**(6),pp.2544–2557.

VARMA, S., J.P.R.O. ORGEL and J.D. SCHIEBER 2016. Nanomechanics of Type I Collagen. *Biophysical Journal*. **111**(1),pp.50–56.

VEIS, A., J. ANESEY and J. COHEN 1961. The Long Range Reorganization of Gelatin to the Collagen Structure. *Archives of Biochemistry and Biophysics*. **94**(1),pp.20–31.

VOLETI, P.B., M.R. BUCKLEY and L.J. SOSLOWSKY 2012. Tendon Healing: Repair and Regeneration. *Annual Review of Biomedical Engineering*. **14**(1),pp.47–71.

WALKER, P.A. et al. 2010. Effect of Needle Diameter and Flow Rate on Rat and Human Mesenchymal Stromal Cell Characterization and Viability. *Tissue engineering. Part C*. **16**(5),pp.989–997.

WANG, J. et al. 2016. Biodegradable polymer membranes applied in guided bone/tissue regeneration: A review. *Polymers*. **8**(4),pp.1–20.

WANG, P. et al. 2011. Nanofibrous electrospun barrier membrane promotes osteogenic differentiation of human mesenchymal stem cells. *Journal of Bioactive and Compatible Polymers*. **26**(6),pp.607–618.

WANG, T., X. ZHANG and D.D. BIKLE 2017. Osteogenic Differentiation of

Periosteal Cells During Fracture Healing. *Journal of Cellular Physiology*. **232**(5),pp.913–921.

WEIR, C. et al. 2008. Mesenchymal Stem Cells: Isolation, Characterisation and In Vivo Fluorescent Dye Tracking. *Heart, Lung and Circulation*. **17**(5),pp.395–403.

WEISS, S. et al. 2009. The systemic angiogenic response during bone healing. *Archives of Orthopaedic and Trauma Surgery*. **129**(7),pp.989–997.

WIESE, A. and H.C. PAPE 2010. Bone defects caused by high-energy injuries, bone loss, infected nonunions, and nonunions. *The Orthopedic Clinics of North America*. **41**(1),pp.1–4.

WILLERSHAUSEN, I. et al. 2014. Non-cross-linked collagen type I/III materials enhance cell proliferation: In vitro and in vivo evidence. *Journal of Applied Oral Science*. **22**(1),pp.29–37.

DE WITTE, T.-M. et al. 2018. Bone tissue engineering via growth factor delivery: from scaffolds to complex matrices. *Regenerative Biomaterials*. **5**(4),pp.197–211.

WOODRUFF, M.A. and D.W. HUTMACHER 2010. The return of a forgotten polymer : Polycaprolactone in the 21st century. *Progress in Polymer Science*. **35**(10),pp.1217–1256.

YANG, L. et al. 2008. Mechanical properties of single electrospun collagen type I fibers. *Biomaterials*. **29**(8),pp.955–962.

YIN, H., F. PRICE and M.A. RUDNICKI 2013. Satellite Cells and the Muscle Stem Cell Niche. *Physiological Reviews*. **93**(1),pp.23–67.

YOSHIMURA, H. et al. 2007. Comparison of rat mesenchymal stem cells derived from bone marrow, synovium, periosteum, adipose tissue, and muscle. *Cell and Tissue Research*. **327**(3),pp.449–462.

YU, N. et al. 2017. Live tissue imaging to elucidate mechanical modulation of stem cell niche quisecence. *Stem Cells Translational Medicine*. **6**(1),pp.285–292.

ZEUGOLIS, D.I. et al. 2008. Electro-spinning of pure collagen nano-fibres - Just an expensive way to make gelatin? *Biomaterials*. **29**(15),pp.2293–2305.

ZIMMERMANN, G. and A. MOGHADDAM 2011. Allograft bone matrix versus synthetic bone graft substitutes. *Injury*. **42**(Suppl 2),pp.S16–S21.